UNIVERSITÀ DEGLI STUDI DI PALERMO

PhD Course in Chemical, Environmental, Biomedical, Hydraulic and Materials Engineering
Dipartimento di Ingegneria
Settore Scientifico Disciplinare (ING-IND/26)

Modelling of Electrodialysis with Bipolar Membranes processes using hybrid model supported by Artificial Neural Networks

PhD Candidate:
Giovanni Virruso

Firmato digitalmente da
GIOVANNI VIRRUSO
CN = GIOVANNI VIRRUSO
C = IT

PhD Course Coordinator:
Prof. Giorgio D. M. Micale

Supervisor:
Prof. Giorgio D. M. Micale

Firmato digitalmente da: Giorgio Domenico Maria Micale
Organizzazione: UNIVERSITA' DEGLI STUDI DI PALERMO/80023730825
Data: 01/12/2024 12:54:39

Co-Supervisors:
Prof. I. David L. Bogle
Prof. Andrea Cipollina
Dr. Andrea Culcasi
Prof. Alessandro Tamburini

XXXVII CYCLE

GRADUATION YEAR 2024

Table of Contents

List of Figures

List of Tables

Abstract

Electrodialysis with bipolar membranes appears to be a promising process for the simultaneous production of acid and alkaline solutions. This process can be integrated into circular economy approaches for waste streams valorisation or utilised alone, especially in remote areas, to reduce transportation, storage and handling of these hazardous chemicals. However, there is a lack of information on large-scale units in real operational environments, and, as a result, there are no validated modelling tools that can be used for its design, optimisation, simulation and control. The aim of the present PhD thesis is to design and test a semi-industrial electrodialysis with bipolar membranes unit and develop versatile modelling tools that can be adopted for the above-mentioned application. The experimental investigation focused on evaluating well established and new process configurations and operational schemes, as well as testing the process inside an integrated treatment chain to valorise a seawater brine. The collected data were utilised to develop the modelling tools. Firstly, a model with a first principles approach was obtained and validated to simulate large-scale units also with complex stack configuration (i.e., internal staging). The model was subsequently modified to account also for nonstationary operations. In addition, the possibility of adopting innovative modelling tools was considered. For the first time, artificial neural network models were used to simulate the Electrodialysis with bipolar membranes process. Finally, the combination of first principles and data-driven models was considered to develop innovative hybrid models with superior performance compared to the two types of models used alone. The obtained results can guide the selection of the most appropriate process configuration depending on the applications, while the proposed models can be selected as realisable tools to predict the process behaviour depending on the application.

Introduction

The research for innovative and sustainable processes has been promoted in the last years by governments to accelerate the transition towards a more suitable society. One of the driving ideas is to recover valuable material from waste streams produced by industrial activities with circular economy approaches. Electrodialysis with Bipolar Membranes has emerged in recent years as an interesting way to *in situ* produce acid and base streams. These chemicals are widely employed across different industrial sectors from within the chemical industry to the water treatment and food industries. Moreover, this process enables the use of waste saline streams as feed, thus allowing to convert them into useful chemicals. For this reason, this technology can play a key role in circular economy approaches which aim to recover valuable products from exhaust salt solutions.

The present PhD thesis aims to extensively characterize the Electrodialysis with Bipolar Membranes technology and to develop reliable simulation tools, considering traditional first principles as well as innovative data-driven and hybrid approaches, to compressively describe its behaviour.

Particularly, the present PhD thesis is divided into 6 different chapters which are briefly described below.

Chapter 1 shows interesting fields in which Electrodialysis with Bipolar Membranes can play a key role in improving the sustainability of industrial processes. In Chapter 2, the Electrodialysis with Bipolar Membranes process is introduced considering its historical developments, working principle, industrial applications and new research challenges. Chapter 3 describes the design and construction of an Electrodialysis with Bipolar Membranes pilot plant and its extensive characterization from an experimental point of view. Chapter 4 deals with the modelling of the Electrodialysis with Bipolar

Membrane process adopting first principles approaches. A multi-scale model is developed and validated with data obtained from the Electrodialysis with Bipolar Membranes pilot plant. Both steady-state and transient conditions are considered, and useful analyses are carried out to study the process potential. In Chapter 5, innovative modelling approaches, such as artificial neural networks, are utilised to describe the behaviour of the Electrodialysis with Bipolar membranes process in both steady-state and transient operations, proving their effectiveness in describing complex nonlinear processes. Chapter 6 evaluates the possibility of combining first-principles and data-driven approaches into hybrid models to improve prediction performance. The results obtained from the hybrid models are compared with the other modelling approaches. The research activities conducted in this thesis work are part of the Horizon 2020 Water-Mining project [1].

A graphical outline of the thesis chapters is depicted in Figure 1.

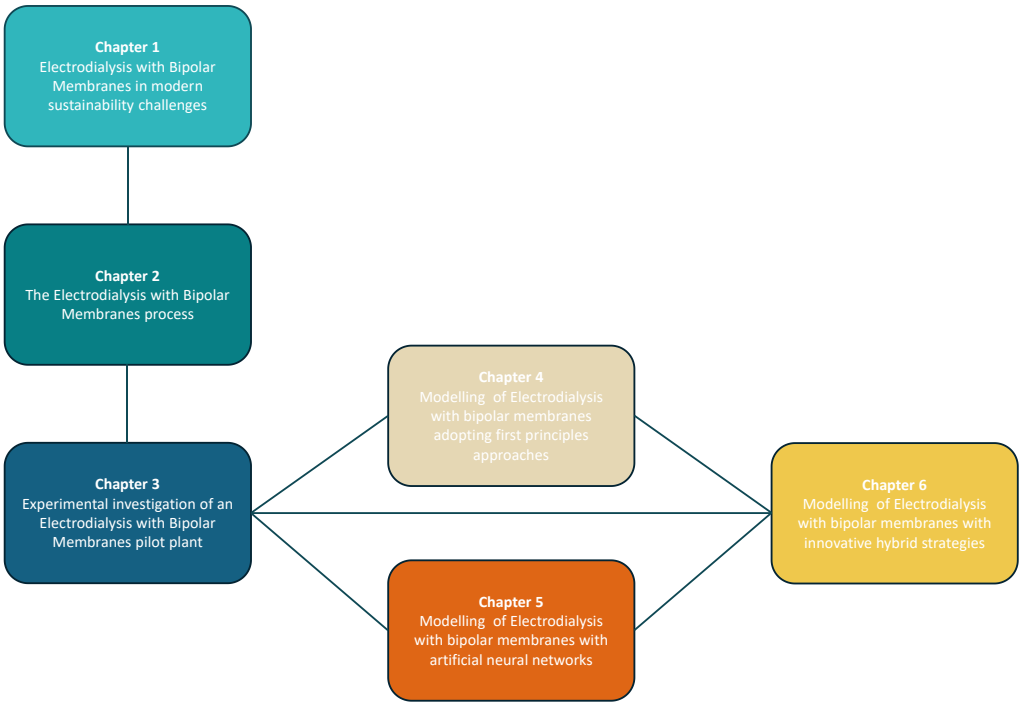

Figure 1. PhD thesis graphical outline

1. *The role of Electrodialysis with bipolar membranes in modern sustainability challenges*

The transition towards a more sustainable society has been promoted in the last decades to mitigate the effects of climate change and environmental degradation. These effects, produced by anthropogenic activities, are causing severe problems such as food safety issues, drying up of areas, ice and iceberg melting, animal extinction, and plant damage [2]. In this context, the European Union is playing a leading role in the current world scenario, enacting stricter policies to eliminate, as far as possible, or reduce pollution and emissions arising from human activities as well as promoting widespread use of renewable energy sources [3]. In the industrial context, this has led to the search for innovative sustainable technologies, capable of reducing energetic and environmental impact, and/or to the promotion of circular economy concepts which aim to reduce the disposal of waste streams.

An emerging process which has gained attention from both academic institutions and industrial companies for the useful streams produced and wide versatility in different fields is Electrodialysis with Bipolar Membranes (EDBM) [4]. EDBM produces acid and base aqueous solutions starting from the corresponding salt solution, through the application of electrical energy. A conceptual representation of the EDBM process is shown in Figure 2. Several applications have been proposed to prove the benefits of this technology in different contexts of modern sustainability challenges. These applications are reported below grouped into three main sections: i) integration into circular economy approaches for wastewater treatment; ii) in situ production of chemicals reagents; iii) coupling with renewable energy resources to exploit variable energy sources.

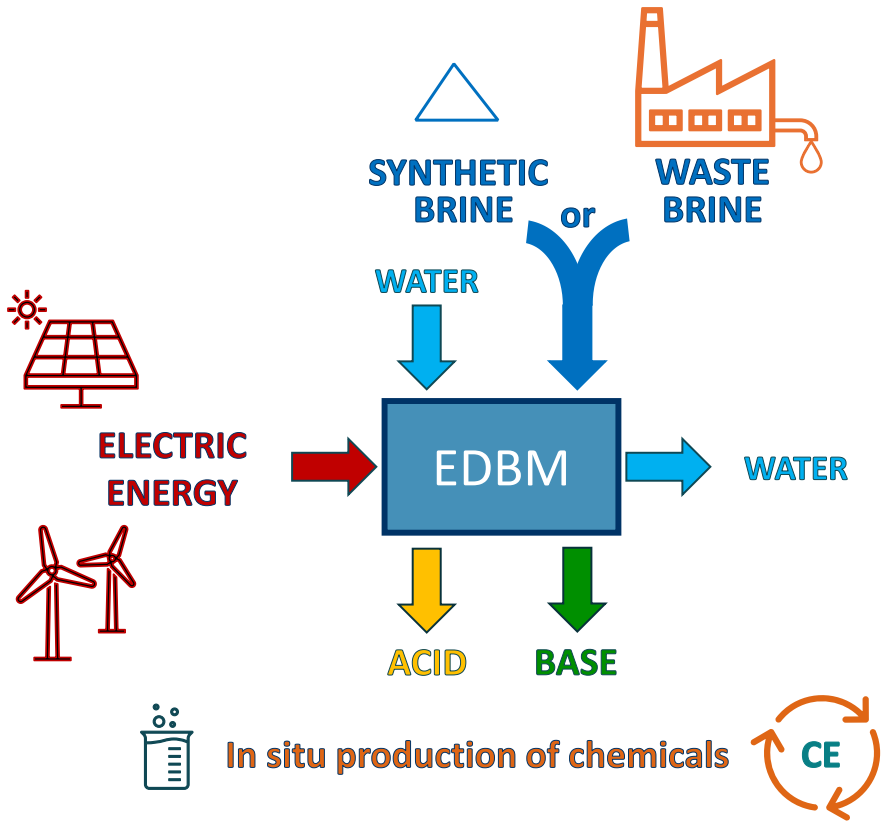

Figure 2. Conceptual diagram of Electrodialysis with Bipolar Membranes (EDBM) process operation.

1.1 Integration into circular economy approaches for wastewater treatment

The adoption of circular economy strategies for wastewater management is promoted by governments (i) to minimize volumes discharged and their associated environmental impact [5], (ii) to reduce water consumption [6] and (iii) to face the increasing resource demand [7]. To this aim, minimal liquid discharge (MLD) [8] and zero liquid discharge (ZLD) [9] have been proposed to improve the sustainability of industrial processes. MLD strategies target the recovery of water up to 95%, whilst in ZLD an entire water recovery could be achieved [10]. Another difference between the two strategies lies in the treatment approach: ZLD is obtained focusing on primary thermally driven technologies and membrane-based processes, whereas mainly the latter

are used in MLD strategies [8], [10]. In general, MLDs are preferred to reduce capital investment and energy consumption arising from thermal processes [11].

The recovery of valuable resources such as salts, minerals and chemicals, that can be sold or reused *in-situ,* represents a prerequisite to widespread MLD and ZLD treatment chains. High-purity salts or mixture of salts, used in food industries and agriculture, respectively, can be easily recovered by adopting thermally driven phase-change-based processes [12], [13]. However, different technologies such as reactive precipitation or selective absorption/adsorption are necessary for precious resources recovery (e.g., magnesium, lithium, chrome and boron) [14], [15], [16]. In these cases, chemical reagents such as acid and base solutions are required for the precipitation and regeneration phases. In the field of seawater desalination, which aims to produce fresh water in drought-affected areas, a waste-concentrated salt solution, known as brine, is produced [17]. $Mg(OH)_2$ and $Ca(OH)_2$ can be precipitated from desalination brine injecting a sodium hydroxide solution (1 mol L^{-1}) in innovative crystallizers [18]. Electroplating wastewaters contain chrome ions which can be recovered by adopting ion exchange resins (silica-supported pyridine resin) [16]. In this process, sodium hydroxide or hydrochloric acid (1 mol L^{-1}) is used as a desorption solution, while a lower concentration of hydrochloric acid (0.1 mol L^{-1}) is adopted for resin regeneration. Salt lake brines contain a significant amount of lithium and boron, which account for 66 % and 50 % of the world reservation [19]. Many efforts have been dedicated to their simultaneous recovery. Recently, Lu et al. [20] observed that lithium-ion sieves and boron-chelating resins can achieve this goal. For the regeneration processes of sieves and resins 0.3 mol L^{-1} HCl is needed.

This information proves the importance of employing acid and alkaline solutions in recovering high value-added materials. However, the purchase of these chemicals can

affect the economic feasibility of ZLD and MLD strategies. Alternatively, Electrodialysis with Bipolar Membranes (EDBM) can be used to produce chemicals, starting also from waste saline streams [21]. In this way, significant benefits can be achieved from both economic and environmental improvements.

Several works have been published in the literature demonstrating the effectiveness of integrating EDBM in circular economy contexts for wastewater valorisation. Adiba et al. [22] proposed two distinct integrated chains for the treatment of high-salinity (NaCl and Na_2SO_4) streams, emulating coal mining wastewaters from Bulianta (China). The integrated chains, adopting a ZLD strategy, combine membrane-based technology, such as Reverse Osmosis (RO), NanoFiltration (NF), Electrodialysis (ED) and EDBM, as well as an evaporative/crystallization unit. The objective of the chains is to valorise the waste brine into pure salts and mixed of salts. The produced chemicals by EDBM are utilized for pretreatment processes and cleaning procedures of the membrane units. The pretreatment step aims to remove ions, such as F^-, Mg^{2+} and Ca^{2+}, as well as to correct the brine pH, which exhibits a mild alkalinity. The two suggested combinations differ for the salt solution sent as feed to EDBM and for the salt produced. In the first chain, the NF permeate, mainly containing monovalent ions, is concentrated through an ED step and then used as feed for EDBM. This leads to the production of sodium hydroxide and hydrochloric acid via EDBM. The NF retentate is evaporated and the dissolved ions crystallised into pure sodium sulphate and a salt mixture. This chain results suitable, from an economic point of view, for treating wastewaters streams with a higher NaCl content with respect to Na_2SO_4. In the second chain, the NF retentate, containing monovalent and bivalent ions, is once again concentrated by ED and sent to EDBM, which produces sodium hydroxide and a mixture of hydrochloric and sulphuric acids. The NF permeate is concentrated through an RO,

which produces fresh water, while the RO retentate is evaporated, leading to the production of pure sodium chloride. This second alternative results more appropriate for wastewaters containing mainly Na_2SO_4. Jiang et al. [23] suggested an MLD strategy, integrating RO, ED and EDBM, for valorising cold-rolling wastewater. Specifically, the chain is able to accomplish a concentration of the salt solution, through RO and two stages of ED, along with the production of fresh water (RO permeate). Two pretreatment steps, using ion-exchange resins (IEX) are adopted prior to RO and EDBM units for removing bivalent cations. The concentrated salt solution and the produced water are, in turn, converted into chemicals (i.e., sodium hydroxide and sulfuric acid) via EDBM, which represent the only products of the chain. The work of Zhao et al. [24] presented an MLD valorisation strategy for mine water generated during coal production. The integrated chain is composed of Ultra Filtration (UF), RO, Selectrodialysis (SED) and EDBM. The UF unit is employed to remove impurities such as colloids and suspended particles. The SED is used to remove Mg^{2+} and Ca^{2+} prior to EDBM, while the fraction containing the bivalent cations is concentrated through an RO unit before a precipitation step. Overall, the chain generates a sodium hydroxide solution, a mixture of sulfuric and hydrochloric acids, and a mixture of precipitated magnesium and calcium hydroxides.

All these examples demonstrate the versatility of EDBM in being integrated into circular economy contexts for the valorisation of wastewater streams, thanks to its valuable products. These chemicals are required by other units for pre-treatment, precipitation and cleaning, ensuring the circularity of the treatment process.

1.2 In situ production of chemicals reagents

In the current industrial scenario, sodium hydroxide and hydrochloric acid represent two of the most widely used bulk chemicals. They are used in different industrial sectors as solutions, with concentrations in the range 1–30 wt.%.

Sodium hydroxide, also known as caustic soda, is produced worldwide utilizing the traditional chlor-alkali process [25]. In 2021, the use of sodium hydroxide was approximately 9.000 kton throughout Europe [26]. Pulp and paper industry, organic and inorganic chemical industries, as well as textile and aluminium sectors represent the main industrial sectors in which sodium hydroxide is adopted, accounting overall for 65% of the total production [27]. Concentrated solutions, between 10–30 wt.%, are usually employed for these applications. On the other end, several important fields utilize lower-concentrated NaOH solutions. Water treatment and food industries accounted for 5.1% and 6.4%, respectively, of the applications of caustic soda in Europe in 2021 [26]. In water treatment industry sodium hydroxide is adopted for pH corrections [28], cleaning procedures [29] and the regeneration of ion-exchange resins [30]. These applications require concentrations in the range 1–4 wt.%. In food industries, caustic soda is used for cleaning procedures, pH corrections and for the production of starches and derivatives [31]. Recently, it was reported that pre-treating the vinegar residue with a 3 wt.% NaOH solution beneficially enhances methane production by 54% during anaerobic digestion [32]. In the field of CO_2 capture, sodium hydroxide is considered an attractive absorbent thanks to the conversion in sodium carbonate, which guarantees high stability, minimal environmental impact, and low cost [33]. The concentration of sodium hydroxide solutions used to this end is in the range 1–5 wt.% [34].

Aqueous solutions of hydrochloric are commonly obtained from the organic chlorination sector, primarily from vinyl chloride production [27]. Among the main applications there are: chloride manufacture, mineral dissolution, pickling and etching of metals, alkaline stream neutralization, brine acidification, regeneration process, cleaning procedures as well as production of plastics, cosmetics and detergents [27], [35], [36]. The pickling process is widely adopted in the steel manufacturing industry to remove

oxidized layers from steel surfaces, using hydrochloric acid as removing agent. In this sector, HCl solutions with concentrations between 1.5 and 17 wt.% are usually employed [37]. Leaching processes, which focus on aluminium recovery from water treatment plant sludges, adopt hydrochloric acid as a solvent with concentrations between 1–4 mol L^{-1}, to achieve leaching efficiencies between 72–80% [38]. In the food industry, HCl is employed as a food additive (known as E 507) with a low concentration to produce corn syrups, gelatin, hydrolysed vegetable protein, and soy sauces [35]. For ion exchange resin regeneration, 4 wt.% hydrochloric acid solutions are usually employed, especially for strong acid cation exchange resins [39].

Acid and base solutions are often used in conjunction. Indeed, when an alkaline solution is utilized, it is necessary to have an acid solution, and vice-versa; to perform pH control, neutralization of effluents, and cleaning processes.

Sodium hydroxide and hydrochloric acid, as commodities, are produced in large volumes in specific areas and must be concentrated to reduce their volume before being shipped worldwide. However, these chemicals require careful handling, due to the hazards they pose to human health, rising environmental and social concerns. Moreover, concentration and transportation costs significantly contribute to the overall cost of the final products. In remote areas, such as islands and peripheral regions, this issue is exacerbated. All these aspects highlight the need to produce hydrochloric acid and sodium hydroxide *in situ*, reducing transportation, handling, and storage costs as well as the associated concerns. Electrodialysis with bipolar membranes represents one of the most promising technologies to address these challenges, as it allows the simultaneous production of hydrochloric acid and sodium hydroxide from sodium chloride solutions [40]. Moreover, its modular nature enables the adaptation of productivity to meet industry requirements.

1.3 Coupling with renewable energy sources to exploit variable energy

The production of acids and bases via electrodialysis with bipolar membranes has been widely proposed in the literature as an attractive option for the *in situ* production of chemicals in circular economy approaches for waste streams valorisation or more traditional industrial contests. Due to the significant energy burden associated with the EDBM process, the possibility of powering the process with renewable energy sources (RESs) has been suggested. In this way, a reduction in carbon footprint and cost of the produced chemicals can be achieved. A few works investigate this coupling in literature, although promising results have been found, regarding the coupling of EDBM with solar panels. Herrero-Gonzalez et al. [41] realised a PV-EDBM system, coupling a lab-scale EDBM stack (A_m=0.01 m^2) with a photovoltaic solar simulator. A SCADA system was adopted to control the plant, which was operated in a semi-batch configuration. More in detail, the outlet flowrates were controlled through an on-off control, which was based on the pH of the acid solution and on the conductivity of the saline solution. The authors found a significant reduction in the specific energy consumption of the acid from 7.3 kWh kg^{-1}, employing a fixed current density, to 4.4 kWh kg^{-1}, using a variable current density and the designed control system. In another work, Herrero-Gonzalez et al [42] developed a simulating tool using existing literature models to evaluate the techno-economic feasibility of the integrated PV-EDBM system for chemicals production, adopting a discontinuous operating mode. The system was analysed using irradiation and temperature data from Lampedusa Island (Italy). Interestingly, the authors observed a 20% reduction in the levelized cost of sodium hydroxide (equal to 210 € ton^{-1}) compared to the use of electrical grid mix. These results raise the interest in coupling EDBM with fluctuating energy sources, such as RES or in smart-grid contexts, for example, for peak-

shaving, thanks to its adaptability in working in transitory regimes maintaining high performance.

2. *The Electrodialysis with Bipolar membrane process*

This chapter details the Electrodialysis with bipolar membranes (EDBM) process, starting from the historical developments and reaching the latest developments as well as the research challenges. In addition, working principles, industrial applications, process configuration, and key performance indicators will be covered.

2.1 Historical developments

Electrodialysis with bipolar membranes is an elctro-membrane process, which enables a mass separation operation. For this purpose, ion-exchange membranes (IEMs) are employed. These membranes, carrying electrical charges, selectively control the transport of charged species (i.e., ions) from a neutral mixture [40]. The first studies on membrane systems date back to the mid-18th century when Abbe Nollet observed osmosis through a membrane in the form of a pig bladder [43]. In the 19th century, Ostwald studied the properties of semipermeable membranes, discovering that they are impermeable for both cations and anions [44]. A few years later, the concept of membrane potential, arising from the different ion concentrations between a membrane and an aqueous solution, was proved by the work of Donnan [45]. A milestone step towards the widespread of the Electrodialysis (ED) process was the suggestion of the multi-cell arrangement, which foresaw the alternation of cation-selective and anion-selective membranes [46]. This configuration enables to minimize the irreversible energy losses at the electrodes over a certain number of compartments. The first industrial-scale application of electrodialysis has been proposed for brackish water desalination. In 1962, more than twenty industrial-scale desalination plants were in operation in the United States [47]. Vincent J. Frilette [48], in 1956, introduced the concept of the *bipolar membrane*, referring to a layered membrane composed of a cation-exchange layer and an

anion-exchange layer. His work described the preparation and characterization of these membranes as well as proposed a multi-chamber arrangement, alternating bipolar membranes with cation-exchange membranes for acid and base production from the corresponding salt. This represents the beginning of the Electrodialysis with bipolar membrane process (EDBM). In 1977, the three chambers configuration, the most widespread EDBM arrangement, was presented to keep acid, base and salt solution separated [49]. Moreover, an economic evaluation proved the attractiveness of this technology compared to electrolysis for acid and base generation. The first industrial-scale EDBM plant was installed in 1988 at Washington Steel (Pennsylvania) for acid regeneration from pickling liquor [50]. With the introduction of EDBM, a completely new area of application was opened up [40].

2.2 Working principle

This paragraph explains the working principles of electro-membrane processes. Conventional electrodialysis ED is first introduced due to the similarities with EDBM. Then the EDBM is comprehensively described, focusing also on the different stack configurations presented so far in the literature.

2.2.1. The Electrodialysis process

Electrodialysis is an electrical-driven process in which ions are selectively transported between solutions [51]. The key components in electro-membrane processes are ion-exchange membranes (IEM). Two different types of IEM can be distinguished: cation-exchange membranes (CEMs) and anion-exchange membranes (AEMs). The former contains negatively charged functional groups in the polymeric matrix and allows the selective passage of cations, whilst the latter presents positively charged groups and permits the selective passage of anions [52]. IEMs resemble ion-exchange resins in sheet

form (100-200 μm thick in dry form) with high swelling capability [40]. In Figure 3 a typical ED stack is depicted showing the transport of ionic species. The stack consists of alternating series of AEMs and CEMs, separated by polymeric spacers and placed between two electrodes. The spacers allow the creation of the channels in which the solutions flow, with a velocity in the range of 1-10 cm s^{-1} [53]. When an electric potential difference is established between the electrodes an ionic current flows through the active membrane area of IEMs. This current is given by the migration of anions towards the anode (i.e., positively charged electrode) and the migration of cations towards the cathode (i.e., negatively charged electrode). Anions easily permeate through the AEM but are retained by CEM, and *vice versa* for cations. The net result of ion migration is the solution concentration in alternate channels, separated by depleted ones. These channels are commonly referred to as concentrate and dilute, respectively. The repetitive unit of an ED stack, known as cell pair, is composed of two different channels (i.e., dilute and concentrate) and two opposite charged membranes (i.e., CEM and AEM). An industrial-scale stack can reach up to several hundreds of installed cell pairs [54].

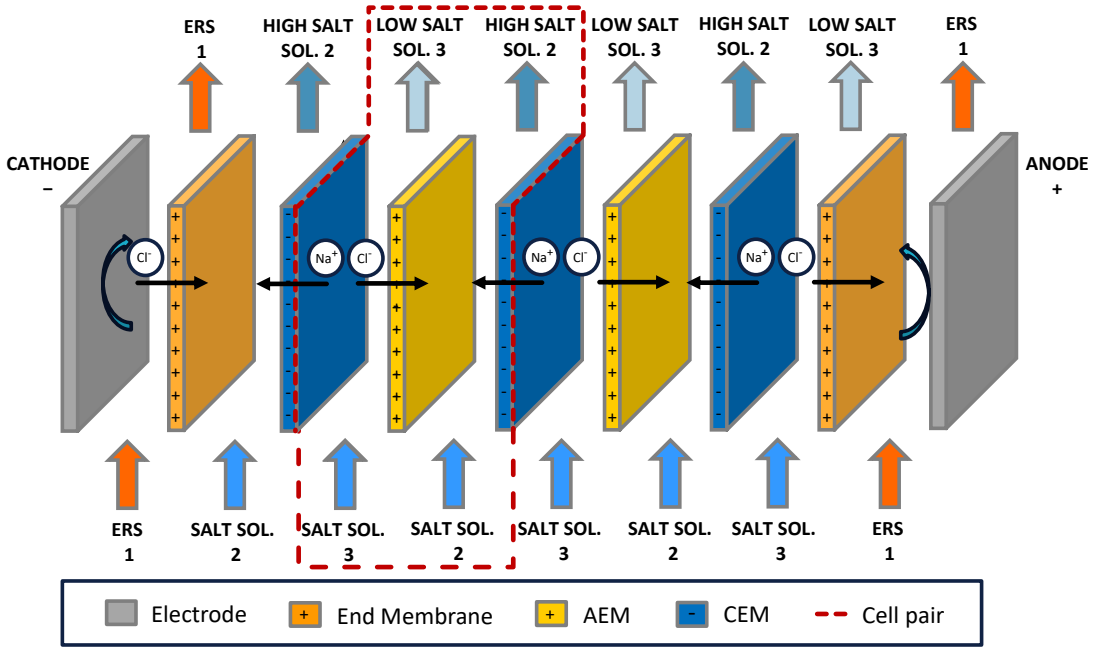

Figure 3. Schematic representation of key elements and working principle of an Electrodialysis (ED) stack. The three compartments present in the stack are shown:1 ERS, 2 concentrated, 3 diluted. ERS: electrode rinse solution.

2.2.2. *The Electrodialysis with bipolar membranes process*

Adding a bipolar membrane to the conventional ED process leads to electrodialysis with bipolar membranes (EDBM) technology. This process combines selective ion transport between solutions through ion-exchange membrane, typical of ED, with the generation of protons and hydroxide ions, allowed by bipolar membranes (BPMs). These special IEMs consist of overlapping two different charged layers joined together: a cation-exchange layer (CEL) and an anion-exchange layer (AEL) [55]. The region between the two ion-exchange layers is called the interlayer or transition region. When an electric field is applied, the electrolyte concentration is deceased in this region and the water dissociation reaction takes place, to maintain the ionic current. This reaction is promoted by employing weak acid or base catalysts [56]. The generated protons and hydroxide ions along with the ions coming from a salt solution are utilized to produce the corresponding acid and base solutions. The schematic representation illustrating the acid and base production in an EDBM unit is reported in Figure 4.

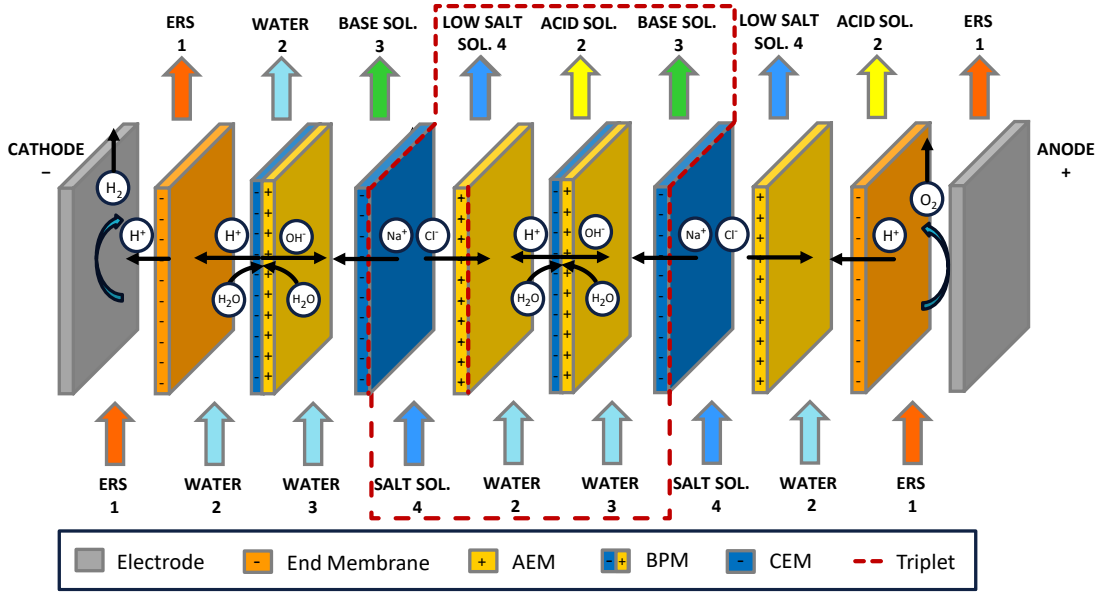

Figure 4. Schematic representation of the key elements and working principle of an Electrodialysis with bipolar membranes (EDBM) stack. The four compartments present in the stack are shown: 1 ERS, 2 acid, 3 base, 4 salt. ERS: electrode rinse solution.

Monopolar and bipolar membranes are stacked together between two electrodes, ensuring that the AEL of the bipolar membrane faces the CEM. The channel formed between the monopolar membranes (i.e., CEM and AEM) is the salt channel, while the channels on both sides of the BPM are the acid and base channels, bounded by CEL and AEM as well by AEL and CEM, respectively [57]. The repetitive unit of an EDBM consists of three compartments and three different membranes and it is called a triplet [58]. The net result of the process is the concurrently acid and base production and salt solution desalination.

In the electrodic compartments, redox reactions take place on the electrode surfaces to convert electricity into an ionic current. In general, a salt is dissolved into water to increase the conductivity of these compartments, but it remains chemically inert from a reaction point of view, while the reaction involves water.

2.3 Industrial applications

In the last decades, EDBM has been suggested for a variety of applications in different industrial fields. In all applications, the water-splitting capability of BPMs, which enables to generate acids and bases, is exploited.

The production of inorganic acid and base streams from the corresponding salts represents the oldest application for which EDBM has been proposed. An elevated number of salt solutions has been reported in the literature, ranging from sodium chloride [59] and sodium sulphate, widely investigated, to sodium phosphate [60] and ammonium nitrate [61], reported in a few works. However, these applications did not reach the industrial scale due to some membrane limitations, affecting the concentration reached and salt contamination of the produced chemicals. This affects the attractiveness and affordability of selling these products in the market. On the other hand, in the field of environmental protection, EDBM demonstrated its strength. Often these salts are

produced in industrial contests as result of reactions, neutralisation and regeneration processes, and need to be disposed of [40]. In these cases, EDBM can be used to valorise these waste streams, producing acid and base that can be reused *in situ* with less strict concentrations and purity requirements compared to the market. The first reported industrial application of EDBM was related to the recovery of hydrofluoric and nitric acids from a potassium nitrate and potassium fluoride stream obtained from a stainless-steel pickling liquor. An economic evaluation was conducted demonstrating a cost reduction in the pickling process and a pay-back period of the EDBM unit lower than 4 years [62].

Regarding organic acid production, EDBM has been demonstrated to be an attractive complement to fermentation processes. Indeed, EDBM enables to covert the organic salt into the desired acid products and, at the same time, produces a base stream that can be employed to control the pH in the fermentation process [63]. Lactic acid can be manufactured either by microbial fermentation or by chemical synthesis [64]. A racemic mixture of lactic acid is produced in the chemical synthesis route, while optical pure L- or D-lactic acid stereoisomers are synthesised in the fermentation process. Calcium lactate is obtained by fermentation processes and must be treated with a strong acid [65]. To this aim, a two-compartment EDBM (i.e., using CEM and BPM) has been used due to the size of the organic anion, which slowly migrates through AEM. In addition, the EDBM process has been utilized for the production of acetic acid [66], citric acid [67], glutamic acid [68], salicylic acid [69] and amino acids [70], [71].

In the field of waste air stream treatment, to remove harmful substances, EDBM has been adopted to regenerate the absorption media [72]. Acid and base scrubbers are usually adopted to remove NO_x, SO_2 and amines, leading to the production of salt solutions. The recovery of sodium hydroxide used in coal-burning power plants to absorb

SO_2 from exhausted gases has been studied to a large extent. Two main processes have been reported in the literature using two different EDBM stack configurations [40]. The first process utilizes sodium hydroxide to absorb SO_2 in the form of $NaHSO_3$. The latter is oxidised leading to Na_2SO_4. A three-camber EDBM unit is employed to produce sodium hydroxide, which is recirculated to the scrubber, and sulfuric acid is produced as a byproduct. The second process, known as Soxal^{TM}-process, adopts Na_2SO_3 as an absorbing medium to remove SO_2 [73]. The absorption process produces a solution of $NaHSO_3$ and Na_2SO_4, thanks to the oxygen present in the fuel gas. A two-chamber EDBM stack, adopting bipolar and cationic membranes, is used to produce Na_2SO_3 and H_2SO_3 in the alkaline and acid compartments, respectively. The sodium sulphite is recirculated to the scrubber while the solution containing sulphurous acid is further treated to generate sulphuric acid or elementary sulphur.

In food industry, EDBM has been interestingly adopted to inhibit undesired oxidation processes in apple juice industry and to separate soybean protein from other components avoiding denaturation phenomena [50]. To produce high-quality unclarified apple juice, preserving sensory and nutrient quality, it is necessary to reduce the pH to a value of 2 and then restore its initial value (i.e., 3.5) [74]. In this way, polyphenol oxidases can be irreversibly inhibited. The adoption of acid and base solutions to adjust the pH induces dilution effects along with salt formation. which significantly affects the juice flavour. Tronc et al. [75] introduced the use of two EDBM stages to accomplish this pH change that inactivates polyphenol oxidases. For both stages, the adopted stack is composed of four different compartments: three of which are fed with a KCl solution and the other one containing the row juice. In this stack configuration, the position of AEM and CEM is reversed to allow a replacement of ions with the same charge. Specifically, in the first stage the row juice is introduced in the chamber bounded by CEL and CEM,

where protons are introduced and potassium ions are removed thus, a pH reduction is promoted. In the second stage, the juice is sent to the camber bounded by AEL and CEM to generate hydroxide ions and, at the same time, transfer to the adjacent compartment chloride ions. This second stage restores the original pH, equal to 3.5. The soya protein is extensively utilised in the food industry to improve the nutritional value and functional properties of food [76]. A procedure has been developed to precipitate soy proteins using EDBM. A two-compartment (i.e., using BPMs and CEMs) EDBM stack is adopted sending the protein solution into the acid chamber. The generated protons lead the solution to the isoelectric point (in the pH range 4.2–4.6) to selectively separate proteins by precipitation [77]. After the precipitation step, in which more than 90% of the protein content is recovered, and the removal of by-products, it is possible to resolubilize the proteins utilising the sodium hydroxide produced in the base chamber of EDBM. Therefore, the production of soy protein does not use any external chemicals to adjust the pH, since they are produced by EDBM and used in different stages.

2.4 Process configurations

This section describes the process configurations largely utilised for EDBM in different industrial fields.

The closed-loop configuration, also known as batch mode, is a discontinuous operating mode in which each solution, contained in its tank, is continuously passed through the EDBM stack to accomplish a certain degree of conversion. Overall, an increase in acid and base concentrations and a reduction of the salt concentration in their respective tanks are observed over time, until the desired concentration is reached. In this configuration, the process duration depends on the solution volumes and on the current density applied to the stack. A schematic representation of the closed-loop configuration is given in Figure 5a.

The open-loop configuration, also known as once-through, is a continuous operating mode which employs different solution tanks for inlet and outlet streams. Each solution is continuously withdrawn from its inlet tank, passes through the stack to accomplish a certain degree of conversion, and then it is sent to the outlet tank where the solution is stored. The chemical concentrations reached along with the brine depletion achieved depend on the current density applied to the stack and on the solution flowrates, which determine the residence time. Due to the reduced conversion obtained with this process configuration, several stacks can be used in series, or a certain acid and base concentration could be used in the inlet tanks instead of water.

The feed and bleed configuration is a continuous operating mode that enables to extend the residence time of the solutions within the stack, recirculating a portion of the outlet flowrate back to the inlet. The desired outlet concentration could be produced starting from water (demineralised water or reverse osmosis permeate), by adjusting the recirculated flow fraction. In some cases, the feed and bleed configuration could be adopted for the chemical lines (i.e., acid and base), and it is known as partial feed and bleed, or for all the main compartments (i.e., acid, base and salt), depending on the availability of the brine. Schematic representations of partial and whole feed and bleed configuration (indicated as feed and bleed) are shown in Figure 5c, d.

The fed-batch configuration consists of two phases. In the first phase, the system works in closed-loop mode for all compartments, usually with a small volume for acid and base solutions. In this way, a rapid increase in the chemical concentrations could be obtained. In the second phase, which starts when the required concentration is reached, a makeup water flowrate is added to the acid and base tanks, with a value that depends on the applied current density. This makeup of water is provided to keep roughly constant

the chemical concentrations while their volumes increase. A schematic representation of the fed-batch configuration is reported in Figure 5e.

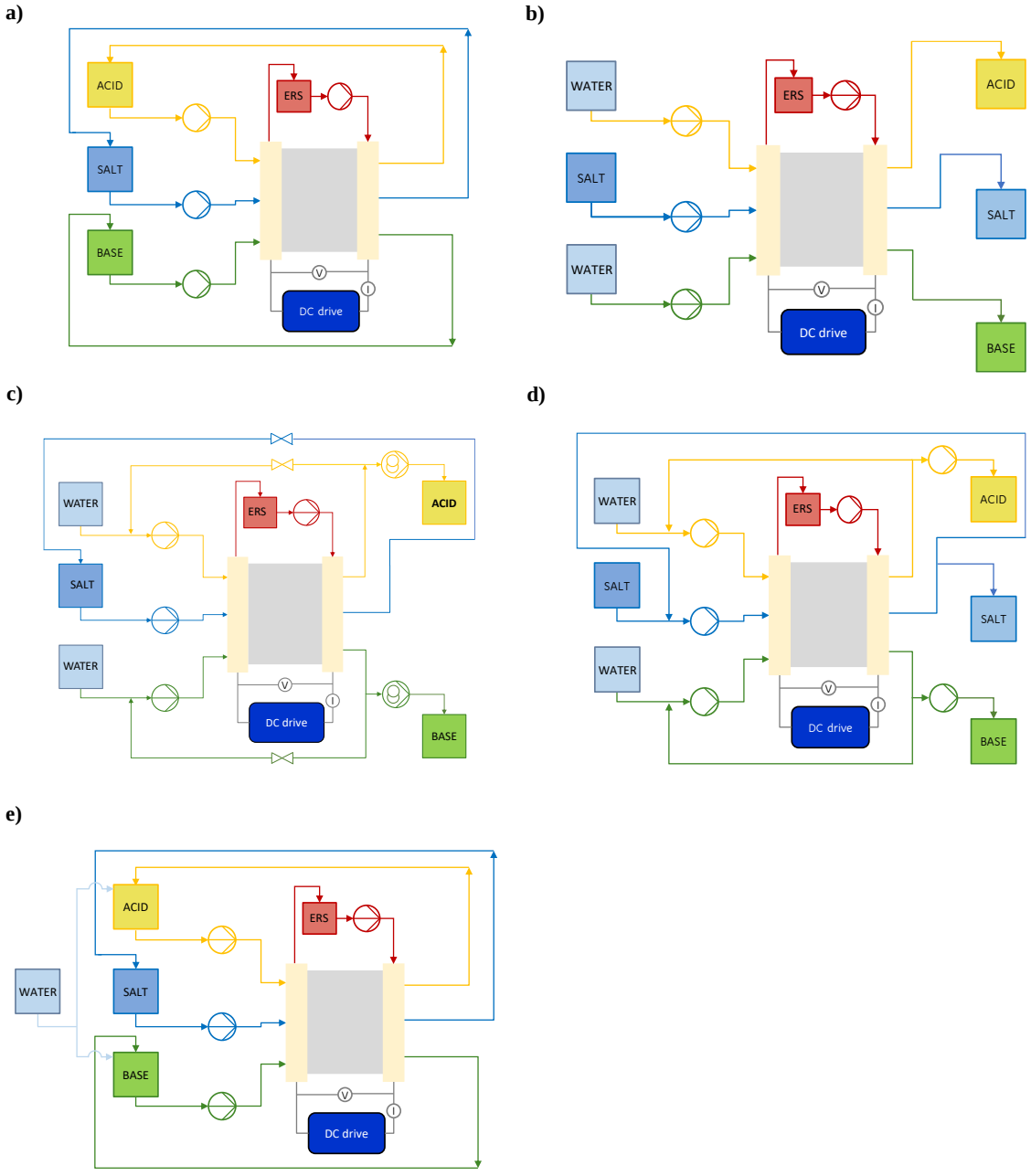

Figure 5. Schematic representation of the principal electrodialysis with bipolar membranes (EDBM) process configurations: a) closed-loop (discontinuous); b) open-loop (continuous); c) partial feed and bleed (semi-continuous); feed and bleed (continuous); e) fed-batch (discontinuous).

2.5 Performance indicators and multi-ionic transport parameters

This section deals with the description of the data analysis used to characterize EDBM behaviour. Firstly, the main Key Performance Indicators (KPI) of the EDBM process are introduced. Then, the parameters used to evaluate the transport of different ions in the case of multi-ionic salt solution are shown.

2.5.1. Overall EDBM KPIs

Current efficiency (CE), often referred as current utilization, is expressed as a percentage. It represents the fraction of the total current supplied to the stack that is converted into in either OH^- or H^+ in the alkaline or acidic compartment, respectively. Equations (1) and (2) are used for a discontinuous and a continuous mode of operation, respectively.

$$CE(discontinuous) = \frac{1000(Vt_{p,t}\ C_{p,t} - Vt_{p,0}\ C_{p,0})\ F}{N_{tr}\ \int_0^t i\ A_m\ dt} 100 \quad (1)$$

$$CE(continuous) = \frac{(Q_{p,out}\ C_{p,out} - Q_{p,in}\ C_{p,in})\ F}{60\ N_{tr}\ i\ A_m} 100 \quad (2)$$

where t is the process time in seconds, the subscripts t and 0 mean at time t and at the beginning of the test, respectively, the subscripts *in* and *out* refer to the inlet and outlet, respectively, and the subscript p indicates the product (i.e., acid or base). $Vt_{p,t}$, $Vt_{p,0}$ are the corresponding volumes of the solutions in the tanks (m^3); $C_{p,t}$, $C_{p,0}$, $C_{p,out}$ and $C_{p,in}$ are the concentrations (mol L^{-1}); Q_p is the flowrate of the product solution (L min^{-1}). F is Faraday's constant (i.e., 96,485 C mol^{-1}), N_{tr} is the triplet number (–), A_m is the membrane active area (m^2), and i (A m^{-2}) is the electric current density provided to the stack.

Specific Energy Consumption (SEC), expressed in kWh kg^{-1}, indicates the electrical energy that must be supplied to the EDBM stack to produce 1 kg of desired

product, i.e., the acid or base solute. Equations (3) and (4) are adopted for a discontinuous and a continuous mode of operation, respectively.

$$SEC(discontinuos) = \frac{\int_0^t U_{ext}\ i\ N_{packs}\ A_m\ dt}{3.6 \times 10^6\ (V_{p,t}\ C_{p,t} - V_{p,0}\ C_{p,0})\ M_p} \quad (3)$$

$$SEC(continuos) = \frac{U_{ext}\ i\ N_{packs}\ A_m}{60\ (Q_{p,out}\ C_{p,out} - Q_{p,in}\ C_{p,in})\ M_p} \quad (4)$$

where U_{ext} is the external electric potential (V) applied to the stack, N_{packs} represents the number of cell packs installed in the stack (–) and M_p is the molar mass of the desired product (g mol^{-1}).

Specific Productivity (SP), expressed in ton y^{-1} m^{-2}, provides the tons of chemicals, i.e., acid or base solution, produced in a working year, considered equal to 8,000 h, per unit of total membrane area installed in the EDBM stack. Equations (5) and (6) are employed for discontinuous and continuous modes of operation, respectively.

$$SP = \frac{2.88 \times 10^4\ (Vt_{p,t}\ C_{p,t} - Vt_{p,0}\ C_{p,0})\ M_p}{3\ A_m\ N_{tr}\ t} = \frac{0.096\ M_p\ CE\ \int_0^t i\ dt}{F\ t} \quad (5)$$

$$SP = \frac{0.48\ (Q_{p,out}\ C_{p,out} - Q_{p,in}\ C_{p,in})\ M_p}{3\ A_m\ N_{tr}} = \frac{0.096\ M_p\ CE\ i}{F} \quad (6)$$

where all other symbols have the same meaning as defined in the previous equations.

Yield (τ_p), expressed as a percentage, represents the ratio between the produced quantity of acid or base to the initial or inlet amount of NaCl. Equations (7) and (8) are used for discontinuous and continuous modes of operation, respectively.

$$\tau_p = \frac{Vt_{p,t}\ C_{p,t} - Vt_{p,0}\ C_{p,0}}{Vt_{r,0}\ C_{r,0}} \quad (7)$$

$$\tau_p = \frac{Q_{p,out}\ C_{p,out} - Q_{p,in}\ C_{p,in}}{Q_{r,in}\ C_{r,in}} \quad (8)$$

where the subscript *r* refers to the reagent (i.e., the salt), while all other symbols have the same meaning as defined in the previous equations.

2.5.2. Ion-specific parameters for multi-ionic solutions

The adoption of real multi-ionic salt solutions to feed the EDBM raises the need to address the description of different ions transport across the ion-exchange membranes. In the work of Filingeri et al. [78] a methodology to evaluate ion transport in multi-ionic contests was presented. It is assumed that ion species different from protons and hydroxides, are transported just through the monopolar membranes (i.e., CEM or AEM) thus, exiting from the salt compartment and entering into the acid/base channel, Figure 6. Indeed, the transport of these ions through the bipolar membrane can be neglected since the salt-limiting current is considerably smaller compared to the current density at which EDBM stacks are usually operated [79]. The salt-limiting current density represents the current density at which all salt ions are removed from the transition region.

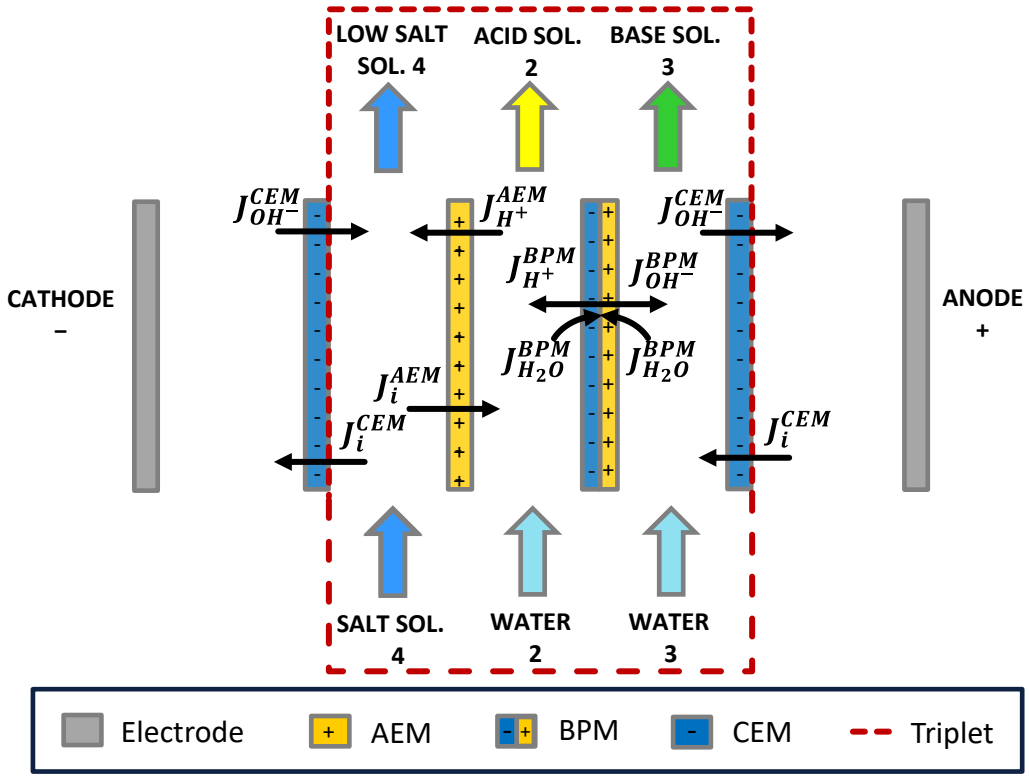

Figure 6. Simplified representation of ion fluxes in an EDBM triplet (adapted from [78]*). The subscript i indicates the generic transported ion different from protons and hydroxide ions.*

The fluxes J_i^{CEM} and J_i^{AEM}, expressed in mol m^{-2} s^{-1}, are transported from the saline solution to the base/acid, across the monopolar CEM and AEM, respectively. They are calculated as follows for a continuous operation mode:

$$J_i^{CEM} = \frac{(Q_{b,out}\, C_{i,b,out} - Q_{b,in}\, C_{i,b,in})}{60\, A_m\, N_{tr}} \quad (9)$$

$$J_i^{AEM} = \frac{(Q_{a,out}\, C_{i,a,out} - Q_{a,in}\, C_{i,a,in})}{60\, A_m\, N_{tr}} \quad (10)$$

where the subscripts *a* and *b* represent acid and base, respectively. It should be noted that the calculated fluxes include both migration and diffusion transport phenomena, representing net fluxes.

Monopolar membranes are also crossed by part of the protons and hydroxide ions, generated at the bipolar membrane interlayer, which migrates towards the oppositely charged electrode. Indeed, the fluxes of H^+ and OH^- through AEM and CEM, respectively, can be attributed to the non-ideal permselectivities of ion-exchange membranes and the partial ion-back-diffusion. Thus, resulting in a partial neutralization and pH variation in the salt channel. These fluxes, expressed in mol m^{-2} s^{-1}, are calculated as the difference between the fluxes of protons and hydroxide ions generated at the bipolar membrane, (i.e., $J_{H^+}^{BPM}$ and $J_{OH^-}^{BPM}$) and those fluxes of the two ions calculated from the experimentally measured concentration in the base and acid channels. $J_{H^+}^{AEM}$ and $J_{OH^-}^{CEM}$ are calculated for a continuous operation mode as:

$$J_{H^+}^{AEM} = J_{H^+}^{BPM} - \frac{(Q_{a,out}\, C_{H^+,a,out} - Q_{a,in}\, C_{H^+,a,in})}{60\, A_m\, N_{tr}} \quad (11)$$

$$J_{OH^-}^{CEM} = J_{OH^-}^{BPM} - \frac{(Q_{b,out}\, C_{OH^-,bout} - Q_{b,in}\, C_{OH^-,b,in})}{60\, A_m\, N_{tr}} \quad (12)$$

The protons and hydroxide ions fluxes produced in the BPM are calculated as follows:

$$J_{H^+}^{BPM} = J_{OH^-}^{BPM} = \frac{N_{packs}\, i}{F} \tag{13}$$

In this case, unitary transport numbers are considered. This assumption, although simplistic, is reasonable since low parasitic currents through manifolds and a reduced value of the salt limiting current density are expected [57].

The overall fluxes of ions, expressed in mol m^{-2} s^{-1}, across monopolar ion-exchange membranes are estimated as:

$$J_{tot}^{CEM} = \sum_i J_i^{CEM} + J_{OH^-}^{CEM} \tag{14}$$

$$J_{tot}^{AEM} = \sum_i J_i^{AEM} + J_{H^+}^{AEM} \tag{15}$$

where the subscript *i* refers to the generic ion present in the salt solution.

The dimensionless transport number is calculated for each ion i across monopolar ion-exchange membranes (i.e., CEM and AEM) as:

$$t_{i,MPM} = \frac{J_i^{MPM}}{J_{tot}^{MPM}} \tag{16}$$

the superscript *MPM* refer to CEM and AEM.

The selectivity of the monopolar ion-exchange membranes for the generic ion *i* is defined as the ratio between flux of the generic ion *i* over the inlet concentration of ion *i* in the salt compartment and the flux of the reference ion over the inlet concentration of the reference ion in the salt compartment, as follows:

$$Sel_{i/ref,MPM} = \frac{J_i^{MPM} \Big/ J_{ref}^{MPM}}{C_{i,s,in} \Big/ C_{ref,s,in}} \tag{17}$$

where subscript *ref* and *s* indicate the reference ion and the salt compartment, respectively.

Acid and alkaline streams composition is also evaluated calculating anionic and cationic purity (P), expressed in percentage and defined as follows:

$$P_{H^+,a} = \frac{C_{H^+,a,out}}{\sum_{cat} C_{i,a,out}} 100 \quad (18)$$

$$P_{Cl^-,a} = \frac{C_{Cl^-,a,out}}{\sum_{ani} C_{i,a,out}} 100 \quad (19)$$

$$P_{Na^+,b} = \frac{C_{Na^+,b,out}}{\sum_{cat} C_{i,b,out}} 100 \quad (20)$$

$$P_{OH^-,b} = \frac{C_{OH^-,b,out}}{\sum_{ani} C_{i,b,out}} 100 \quad (21)$$

where subscript *cat* and *ani* indicate cations and anions, respectively. For anions purity is possible to consider the valance of different ions through the computing of speciation (Sp), expressed in percentage and defined as:

$$Sp_{Cl^-,a} = \frac{C_{Cl^-,a,out}\ z_{Cl^-}}{\sum_{ani} C_{i,a,out}\ z_i} 100 \quad (22)$$

$$Sp_{OH^-,b} = \frac{C_{OH^-,b,out}\ z_{OH^-}}{\sum_{ani} C_{i,b,out}\ z_i} 100 \quad (23)$$

where z_i is the valence of ion *i*.

2.6 Latest developments

Besides the traditional application of electrodialysis with bipolar membranes process that has been comprehensively described in 2.3, there is a variety of innovative applications in which the advantages of this process can be interestingly used. Between them there is the possibility of creating energy storage systems (acid/base flow battery), combining with CO_2 capture systems, recovering critical raw materials such as Lithium, and promoting hydrogen production at the cathode electrode in conjunction with chemicals production.

An acid-base flow battery (ABFB) is an environmentally friendly storage system based on the reversible water dissociation process of bipolar membranes [80]. Electricity is stored in the form of pH and concentration gradient (i.e., chemical energy) in acid and base solutions [81]. During the charging phase, an electric field is applied through the electrodes and the water dissociation reaction takes place in BPMs, leading to the production of acid and base solution. In the discharging phase, no electrical energy is supplied to the system from the outside, instead a load is connected to enable the flow of current. Protons and hydroxide ions contained in the chemical streams are neutralized in the bipolar membrane interlayer, leading to the formation of water. This discharge phase is also known as forward bias or reverse electrodialysis with bipolar membranes [82]. In order to reduce CO_2 emission, thus, preventing severe effects of climate change, capture of CO_2 has been extensively studied in the last years. Sodium hydroxide is considered an attractive media for CO_2 absorption as it leads to the production of sodium carbonate, with several benefits (i.e., high stability, minimal environmental impact and low cost). Ruan et al. [83] couple an EDBM unit with a hollow fiber membrane contactor, used as an absorber. The EDBM unit is employed to convert a softened rejected brine into chemicals, mainly hydrochloric acid and sodium hydroxide. The produced alkaline stream is sent to the hollow fiber module lumen side, while a gas mixture containing CO_2 is pumped shell side. By selecting proper operating conditions for the module, removal higher than 90% can be achieved. The absorbed solution containing mainly sodium hydroxide and sodium carbonate, is used to soften the reject brine, while the acid stream produced by EDBM is employed for pH correction and cleaning process.

In recent years there has been an increase in lithium demand due to the spread of lithium batteries in a variety of applications [84]. The possibility of recovering metals from used lithium batteries or from salt solutions containing lithium ions represents a

promising approach to meet sustainability standards. Jiang et al. [85] evaluated the possibility of recovering a LiOH from a simulated lake brine adopting two chambers (i.e., CEM and BPM) EDBM unit. In addition, as a pretreatment process, an ED unit is used for concentration purposes as well as a precipitation and filtration units are employed to remove undesired compounds. Finally, a LiOH solution with purity of about 95% was obtained. EDBM appears a promising environmental-friendly and cost-effective process for producing LiOH compared with conventional processes.

Very recently. Pellegrino et al. [86], evaluated the simultaneous production of hydrogen and chemicals via EDBM, in what they called Hydrogen-EDBM (H-EDBM). Considerable high values of current density were achieved, up to 1,000 A m^{-2}, to emulate operating conditions similar to the traditional electrolyser used for hydrogen production. At 1,000 A m^{-2}, a 98% faradic efficiency for hydrogen production was obtained as well as a productivity of 18.4 mol h^{-1} m^{-2}. A levelized cost of hydrogen equal to 2.4 € kg_{H2}^{-1} was found, proving the attractiveness of H-EDBM technology.

2.7 New research challenges

The electrodialysis with bipolar membranes process has been extensively investigated at a laboratory scale in different application fields. Although few efforts have been dedicated to the process scale-up, studying situations relevant to industrial contexts. Between them the performance evaluation of different operating conditions and process configurations to extensively characterize the system, also with real brines. Moreover, in the modelling of this process, lumped or distributed parameters first principles models have been used with some adjustable parameters. These models were validated using small EDBM stacks with simple stack configurations, which limits their application in simulating industrial scale units for design and optimisation processes Lastly, adoption of this technology requires an appropriate control system, between them model predictive

control (MPC) can allow a strict control of the produced chemicals also in high transitory regimes. These control approaches require low computational demanding models that can be easily simulated and optimised, such as data-driven models. From what was said before, it follows that a significant effort should be dedicated to investigate situations which are typical of industrial contexts and propose valid models which can fully characterize the process in a variety of operating conditions and process configurations for different applications.

3. Experimental Investigation of an EDBM Pilot Plant

This section contains the results of an extensive experimental campaign conducted with an electrodialysis with bipolar membranes pilot plant. Firstly, a description of the experimental set-up is provided considering the designing and construction phases, main characteristics, installation site and the contest in which it has been realised. Secondly, information about the preparation of the solutions and analytical producers to characterize the EDBM results is provided. Then, preliminary analyses are described to investigate the system operating range and find adequate operating conditions for subsequent analyses. Moreover, the conducted experimental campaigns are reported to provide useful information for the process scale-up. Specifically, different process configurations are compared in terms of KPIs as the operating conditions vary and novel schemes for brine valorisation and water footprint reduction are suggested. Finally, two applications of EDBM in real industrial scenarios are presented: adoption of a real seawater brine (i.e., EDBM integrated into the Water Mining treatment chain) and coupling with renewable energy sources.

3.1 Experimental set-up

This section describes the Electrodialysis with bipolar membrane pilot plant utilised to conduct the experimental campaign.

3.1.1. The Water Mining project: case study 1

The EDBM pilot plant was realized within the framework of the Horizon 2020 Water-Mining Project. This project, lasting four years, started in September 2020. A total of 38 partners, between universities and companies, are involved coming from 12 different countries. The aim of the project is to implement important European legislation

(i.e., Water Framework Directive and EU Green Deal), validating innovative water resource solutions at a high Technology Readiness Level (TRL), up to 8. Specifically, these solutions combine water management services with the recovery of value-added substances mined from alternative resources, obtained from urban wastewater, seawater desalination and industrial wastewater [1]. To this aim, 6 different Case Studies are evaluated, two for each resource of interest. The Case Study 1 of the project, in which the Università degli Studi di Palermo is involved, has the objective to valorise saline streams (seawater or desalination brine) recovering fresh water, chemicals (i.e., acid and base streams), salts (i.e., sodium chloride and mixed salts) and minerals (i.e., $Mg(OH)_2$, $Ca(OH)_2$), as well as exploit waste heat, adopting Zero/Minimum Liquid Discharge (ZLD/MLD) strategies. The demonstration chain, installed on the island of Lampedusa (Italy), employs six different technologies: (i) Nano Filtration (NF), (ii) Multiple Feed Plug Flow Reactor (MF-PFR), (iii) Multiple Effect Distillation (MED), (iv) EDBM, and (v) Evaporative Ponds (EPs). A representation of the whole treatment chain is illustrated in Figure 7.

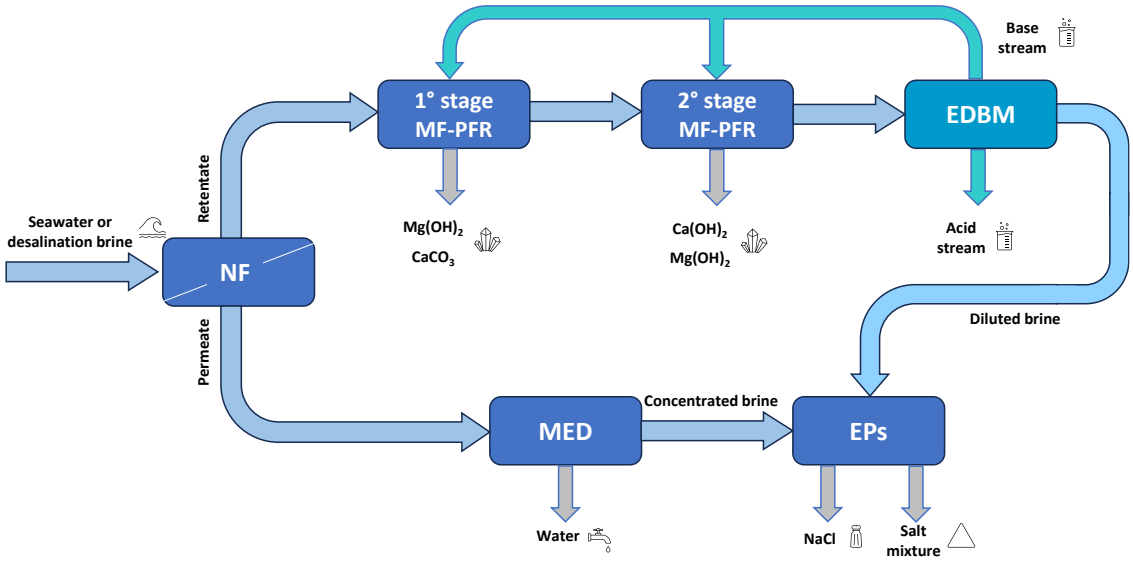

Figure 7. Schematic representation of Case Study 1 treatment chain of the European Horizon 2020 Water-Mining project.

The inlet saline feed is firstly treated into an NF unit, a membrane process which produces: i) a permeate, containing mainly monovalent ions (such as sodium, potassium and chloride) and ii) a retentate, enriched in bivalent ions (such as magnesium, calcium and sulphates). The NF retentate is sent to an innovative reactive crystallizer, known as MF-PFR, employed in two different stages. The first stage recovers a mixture of magnesium hydroxide and calcium carbonate (in a small quantity), utilising sodium hydroxide as a chemical reagent. The second stage operates at a higher pH to precipitate a mixture of calcium/magnesium hydroxide. After solid separation the resulting clarified solution underwent a polishing step with ion exchange resins (IEX) The obtained solution is sent to the downstream EDBM unit to produce two chemical streams: i) an alkaline solution, mainly containing sodium hydroxide, which is recirculated inside the chain for the precipitation steps, and ii) an acid solution, mainly containing hydrochloric acid, which is partially used for cleaning procedures or as a by-product.

The NF permeate is fed to a Multi-Effect Distillation (MED) unit to further concentrate the salty stream and to produce demineralized water. The MED unit employs low-grade heat (~80°C) supplied by the local power station, achieving a concentration factor as high as 8 [87]. The highly concentrated salt solution, produced by the MED unit, along with the diluted brine from the EDBM are directed to the Evaporative Ponds where natural evaporation is employed to crystalise sodium chloride (food grade purity) and a final mixture of other salts (mainly KCl, NaCl and Na_2SO_4).

3.1.2. The EDBM Pilot Plant

The design of the EDBM Pilot Plant was carried out utilizing both modelling and empirical approaches to define the layout of the stack, adopting 2D and 3D CAD software (i.e., Autodesck® AutoCAD and Fusion 360) to select the best arrangement of measuring instruments and control devices and employing electrical software (i.e., QElectroTech

and LTSpice XVII) to design the electrical circuits. The EDBM stack design procedure and the selection of measuring instruments and control devices can be found in the thesis works [88]. In Figure 8, the result of the design phase is shown through a 3D CAD.

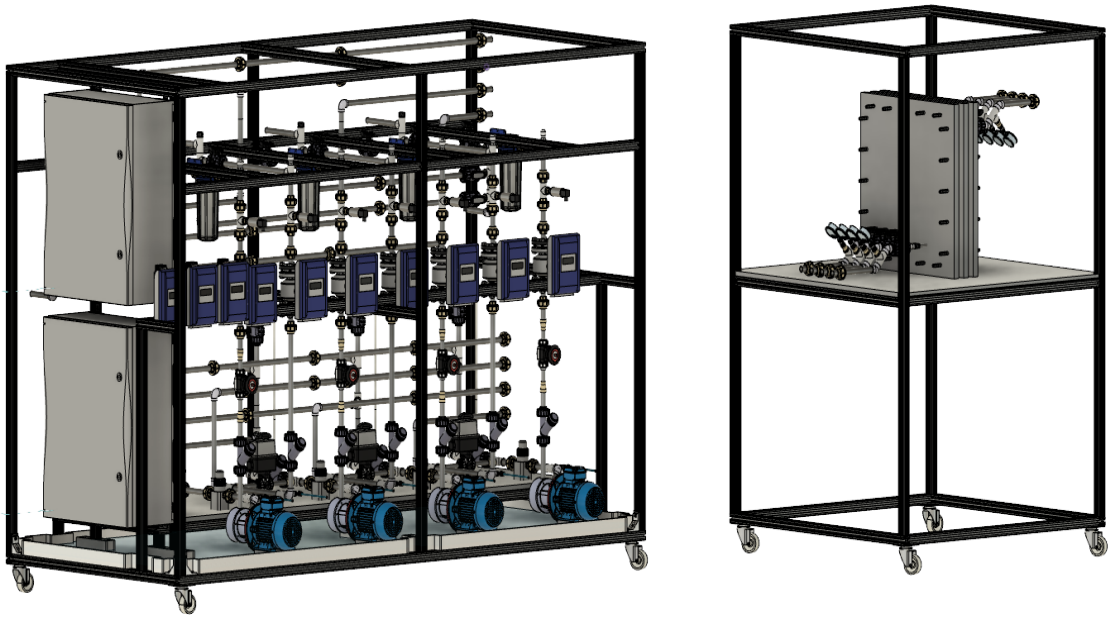

Figure 8. 3D drawing of the EDBM Pilot Plant realized with Autodesk® Fusion360. Both skid-mounted units are shown: the Pumping station and the EDBM stack unit.

The design of the electrical circuit and the construction of the pilot plant was realized, at the Università degli Studi di Palermo, during this PhD thesis work and it is briefly reported in the following paragraphs.

3.1.3. Skid-mounted unit housing auxiliary instrumentation: The pumping station

In order to house all the auxiliary instrumentation needed for the correct operation of the EDBM pilot plant, a skid-mounted unit was realized. This unit, known as a *pumping station*, was built utilizing square-based (40×40 mm) aluminium-profiled bars (METRA S.p.A.). The construction of the *pumping station* was accomplished in two phases: i) connection of the hydraulic circuit, and ii) wiring of the electrical cabinets.

The hydraulic circuit consists of four different lines, equal to the number of the solutions circulating inside the stack: acid, base, salt and electrode rinse solution (ERS). In addition, water and drain lines were connected to the main lines for cleaning and draining purposes. As described in section 2.4, acid, base and salt lines can be operated in different process configurations. This requires a flexible arrangement of these lines, with appropriate instrumentation, to permit the adoption of all these configurations in the same unit. On the other hand, the ERS solution is always operated in closed-loop mode and a simpler arrangement was considered. The hydraulic circuit connects each solution tank with the EDBM stack and *vice versa*. All the pipes and fittings were made in polypropylene (PP) with a size of 3/4 inch (FIP–Formatura Iniezione Polimeri S.p.A.). Measurement instruments were installed to monitor important process variables, such as flowrates, conductivities, temperatures, pH values and pressures. For acid, base and salt lines, the measurement instruments were installed both prior to and after the stack (i.e., inlet and outlet line) to register any variations, while in the ERS they were positioned just before the stack. For each line, a turbine pump, equipped with an external inverter, was adopted to tune the flowrate flowing inside the stack. Moreover, in acid, base and salt lines electrically actuated valves were utilized to partially recirculate the outlet flowrates to the stack inlet (i.e., feed and bleed configuration). Finally, an additional gear pump was employed in the acid and base outlet lines to strictly control them in feed and bleed mode. All the materials were selected to ensure chemical and mechanical stability. Detailed information about the measuring instruments and control devices installed in the pilot is provided in Table 1.

Table 1. Measurement instrumentations and control devices installed in the pumping station.

Element	Model	Range	Material	DN (mm)
Magnetic induction flowmeter	OPTIFLUX 4100C	0–30 l min^{-1}	PTFE	20
Conductivity meter	OPTISENS IND 1000	1–2000 mS cm^{-1}	PP	20
pH meter	SMARTPAT PH 8320	0–14	Glass AH	15
Pressure transducer	OPTIBAR P 1010 C	0–6 bar	AISI 316L	15
Turbine pump	TEOREMA PTM 2.5x6	0–3,500 rpm	PP	25
Gear pump	TEOREMA FG200−300	0-5 V	AISI 316L	3.2
Electrically actuated valve	FIP VKDIV/CE	0-100 %	PP	15

To retain coarse particles in solution before being sent to the EDBM stack, a 3/4 inch polypropylene y-strainer filter (FIPFormatura Iniezione Polimeri S.p.A.) and a cartridge filter with a 1 μm mesh (Atlas Filtri S.r.l.) were installed. To collect potential liquid leaks, 6 cm high polyvinyl chloride (PVC) basins were placed at the base of the aluminium frame. Some instantaneous snapshots are shown to illustrate the construction of the hydraulic circuit, Figure 9.

Figure 9. The construction phase of the Pumping Station, housing all the auxiliary instrumentations and control devices. a) skid-mounted structure made with aluminium bars and PVC basins; b) building of hydraulic circuits; c) view of the completed hydraulic circuits; d) installation of all the monitoring and control devices.

Two electrical cabinets were used in the pumping station to contain all the essential electrical elements, such as differential and thermal-magnetic circuit breakers, power suppliers for low-voltage devices, inverters and acquisition and command cards. Once all the necessary instruments had been selected, 2D CAD was realized to properly place them inside the electrical cabinets, Figure 10.

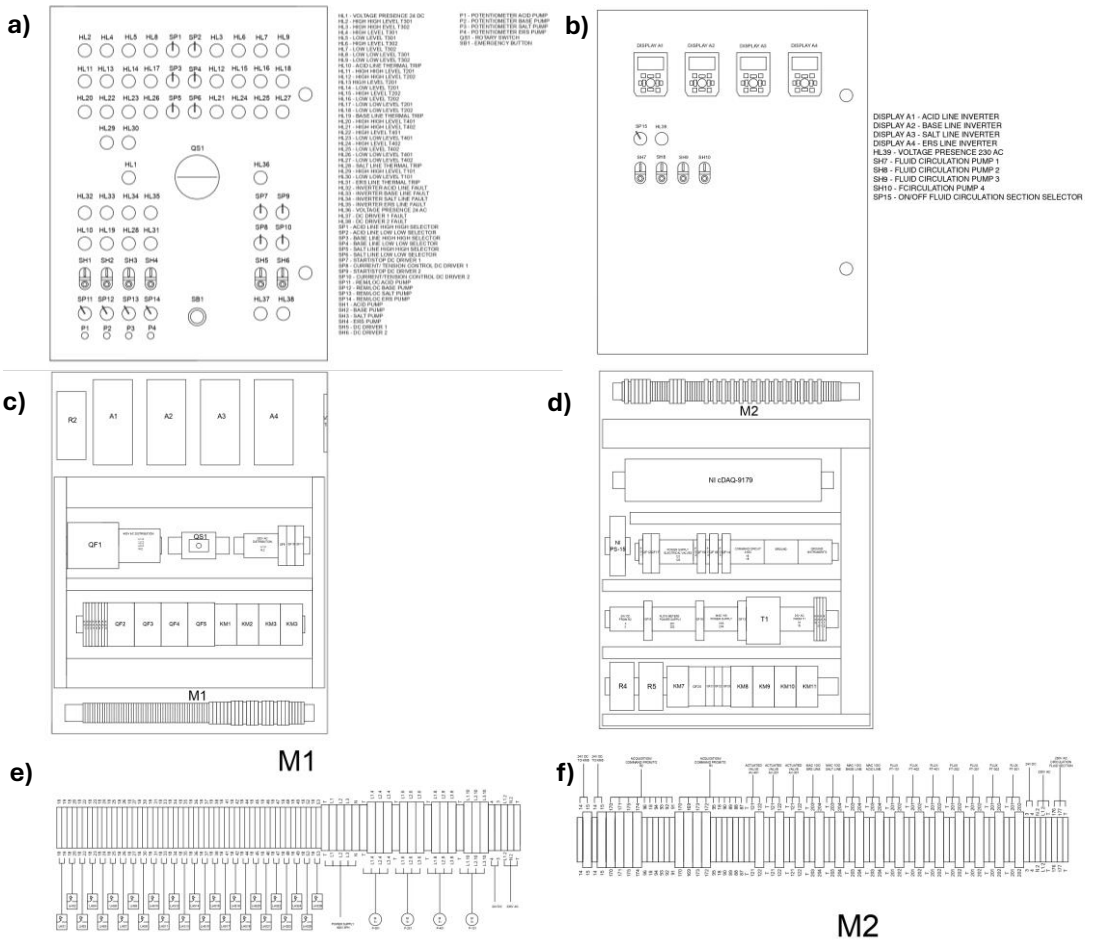

Figure 10. 2D CAD showing the layout of the electrical cabinets utilized in the pumping station. a) front view of the upper cabinet; b) front view of the lower cabinet; c) interior layout of the upper cabinet; d) interior layout of the lower cabinet; e) enlargement of the upper cabinet terminal connection box; f) enlargement of the lower cabinet terminal connection box.

Specifically, the electrical devices were divided into high voltage (i.e., 400 V and 230 V) and low voltage elements (i.e., 24 V and 12 V AC as well as 24 V and 12 V DC), and positioned into the upper and lower electrical cabinets, respectively. Several instantaneous snapshots are provided in Figure 11 to show the wiring phase of the electrical cabinets and the obtained result.

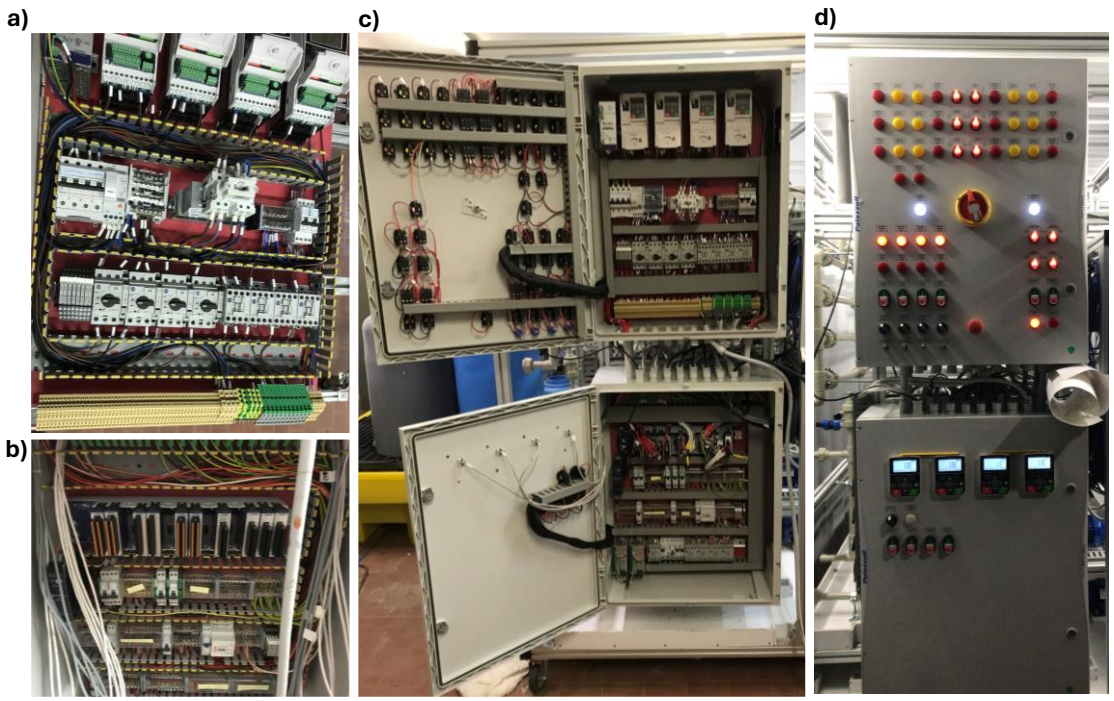

Figure 11. Wiring phase of the pumping station electrical cabinets: a) wiring of the upper cabinet; b) wiring of the lower cabinet; c) comprehensive interior view of both electrical cabinets; d) front view of both electrical cabinets.

3.1.4. Skid-mounted unit housing the stack: The EDBM stack unit

A separate skid-mounted unit was designed to house the EDBM stack. This choice comes from the need to electrically insulate the EDBM stack due to the elevated voltages and currents utilised. The structure of the skid-mounted unit was built utilizing square-based (40×40 mm) aluminium-profiled bars (METRA S.p.A.). To collect potential liquid leaks, a 6 cm high PVC basin was placed into the aluminium frame. Instantaneous snapshots regarding the construction of the skid-mounted unit housing the stack are provided in Figure 12.

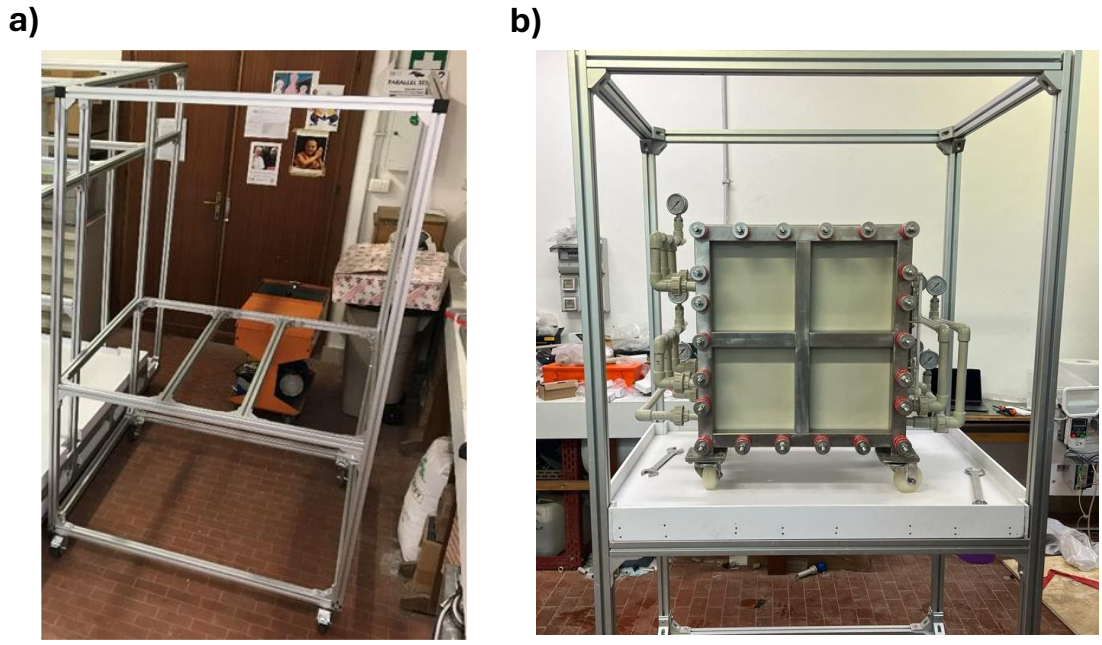

Figure 12. Construction of the skid-mounted unit containing the stack: a) aluminium frame; b) installation of the PVC basin and positioning of the EDBM stack.

3.1.4.1. EDBM stack configuration and installed membranes

The EDBM stack utilized in the pilot plant is an FT-ED 1600-3-40-2 purchased from FuMA-Tech GmbH (Germany). The unit consists of two cell packs, of 20 triplets each, allowing the unit to reach a total membrane area of 19.2 m^2. The two cell packs are arranged hydraulically in series with a common manifold, which acts as a collector for the first cell pack and as a distributor for the second one. Specifically, the entrance of the solutions to the stack is located at the bottom left side, the solutions flow through both cell packs, which are connected via a linking manifold, and the solution exit is placed at the bottom right side of the stack. The same electric potential difference is applied to both cell packs utilizing a shared anode (i.e., the positive electrode) and two distinct cathodes (i.e., the negative electrodes). A schematic representation of the EDBM stack is reported in Figure 13.

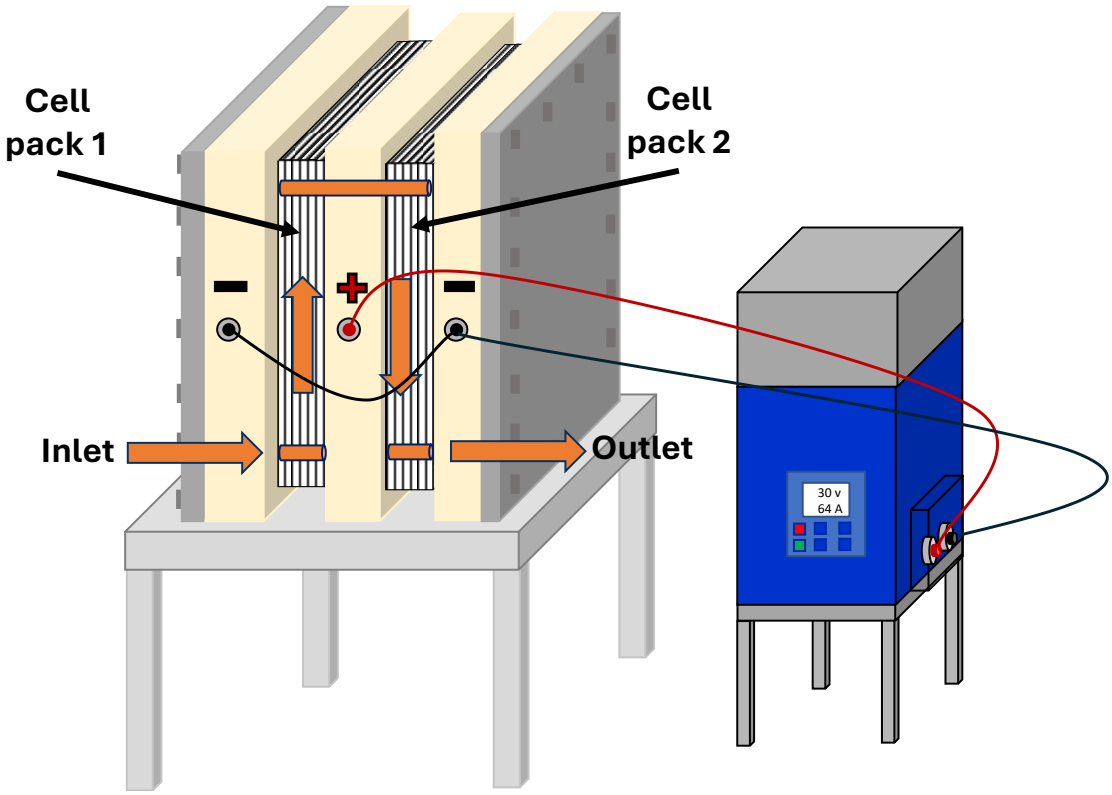

Figure 13. Schematic representation of an EDBM stack adopting an internal staging configuration with a shared anode. The orange arrows represent the three main solutions (i.e., acid, base and salt).

This stack configuration is known as internal staging with two pairs of electrodes, one of which is shared (i.e., the anode) [40]. This electrode layout decreases the capital cost of the stack, limiting the amount of material required for the most expensive electrode, i.e., the anode, compared to the adoption of two different stacks in series. The total current coming from the DC drive is split between the cell packs based on their electrical resistance, supplying a larger current fraction to the cell pack with a lower electric resistance.

The electrodes installed in the EDBM stack are dimensionally stable anode (DSA®) and stainless steel (AISI 304) as anode and cathode, respectively. The membranes installed in the EDBM stack are FUMASEP® FAB-PK as anion-exchange membrane, FUMASEP® FKB-PK as cation-exchange membrane, FUMASEP® FBM-PK as bipolar

membranes and FUMASEP® F-10150-PTFE as end-membrane. The active membrane area is 0.16 m^2 (0.345 m length and 0.454 m width). The flow of the solutions through the stack is co-current. Spacers are made from polypropylene, with a thickness of 350 μm. The number of holes in each spacer is equal to 6 with an equivalent diameter of 14.5 mm. Additional information about the ion-exchange membranes and spacers adopted in the EDBM stack is reported in Table 2.

Table 2. Main characteristics of the ion-exchange membranes installed in the EDBM stack.

	FUMASEP® FAB-PK (CEM)	**FUMASEP® FKB-PK (AEM)**	**FUMASEP® FBM-PK (BPM)**	**FUMASEP® F-10150-PTFE (end-membrane)**	**FUMATECH FT-ED 1600-3 (spacer)**
Reinforcement/ Material	PK	PK	PK	PTFE	EVO1 125°V/PP
Thickness, dry (μm)	110-140	120-150	130-160	150-200	350
Max temperature (°C)	na	40	40	na	60
Counter ion	bromide (Br-)	H^+ form	Na^+ (CEL layer) / Cl^+ (AEL layer)	H^+ form	-
pH stability range at 25 °C	0-14	0-14	na	na	0-14
Area resistance (Ω cm2)	5.0 – 9.0[a)]	<5[b)]	na	<1[c]	-
Selectivity	93-98	>98	na	>95	-
Porosity (%) (plan view/ flow direction)	-	-	-	-	64/84

3.1.5. Installation site and commissioning phase

Once the construction of the skid-mounded units had been completed, they were positioned in a 20 ft shipping container and transported to the island of Lampedusa (Italy), where the Case Study 1 demonstration treatment chain of the Water-Mining project was located. In Figure 14, the geo-localization of the installation site is shown.

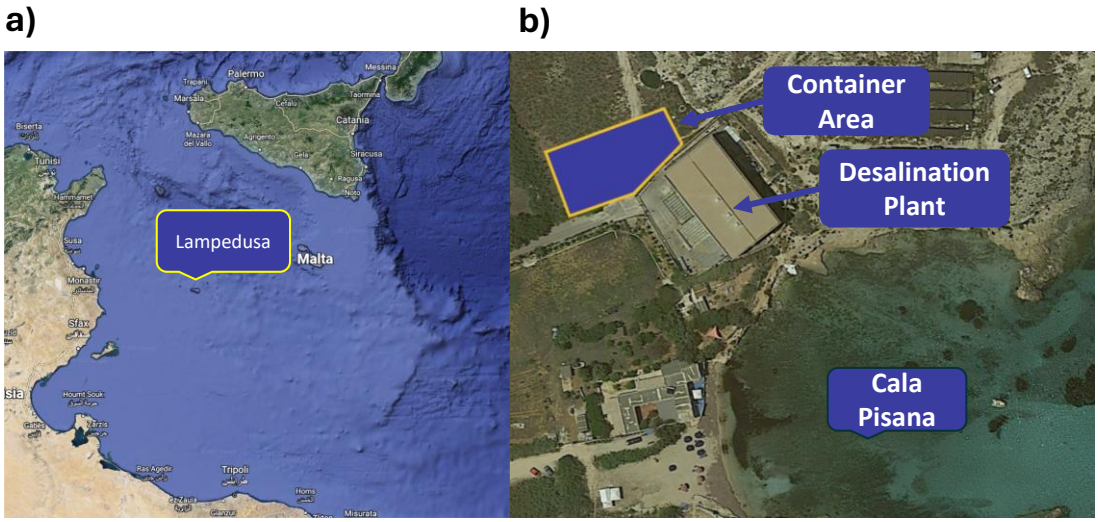

Figure 14. Geo-localization of : a) the island of Lampedusa in the Sicilian channel and b) the installation site, indicated as "Container Area". Images obtained from[89] .

The EDBM pilot plant was positioned in the container area, next to the local desalination plant, and connected to a tank farm. In detail, two high-density polyethylene (HDPE) IBC tanks, of 1 m^3 each, were utilized for the three main streams (i.e., acid, base and salt). For the ERS, a single 0.125m^3 polyethylene tank was used. In addition, two IBCs were utilized to store demineralised water and to drain the electrolytic solutions. Figure 15 shows the EDBM pilot plant and the corresponding tank farm.

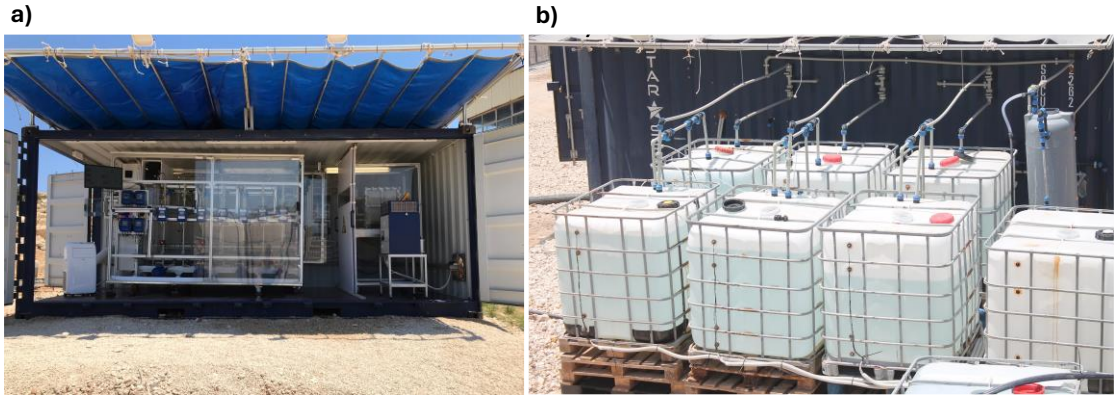

Figure 15.Instantaneous snapshots showing: a) front view of the container which houses the EDBM pilot plant; b) tank farm utilised to store the electrolytic solutions.

3.2 Solution preparation and analytical procedure

In all the tests the ERS was prepared using RO permeate (~ 350 μS cm^{-1}) and technical grade Na_2SO_4 (CR GRUPO CRIMIDESA), reaching a concentration of 0.25 mol L^{-1}. Depending on the test type, also the other solutions were prepared starting from technical grade chemicals. The artificial brine (i.e., the salt solution) was prepared by mixing reverse osmosis (RO) permeate (~ 350 μS cm^{-1}) and high-grade NaCl (>99.5% purity, Saline di Volterra S.r.l.), up to the desired concentration (often 1 mol L^{-1}). Artificial acid and base solutions were prepared for closed-loop and fed-batch tests. In closed-loop volumes of 0.3 m^3 were utilised, while in fed-batch mode 0.1 m^3 volumes were employed, with a concentration of 0.05 mol L^{-1} for both chemicals. To prepare the acid and base solutions HCl (ACS reagent 37 wt %, Honeywell, Fluka) and NaOH (technical grade, Inovyn) were, respectively mixed with RO permeate (~ 350 μS cm^{-1}). This initial concentration of 0.05 mol L^{-1} was employed to increase the conductivities of acid and base solutions preventing the application of high voltage to the stack at the beginning of the tests.

Titrations were performed with standard solutions of 0.1 mol L^{-1} HCl for the alkaline sample and of 0.05 mol L^{-1} Na_2CO_3 for the acid one, using 10 wt.% methyl orange solution (ACS dye content 85 wt.%, SIGMA-ALDRICH) as pH indicator. Sample analysis was completed by ion chromatography (Metrohm 882 compact IC plus) to measure cations and anions concentrations, using the cation (Metrosep C 4 – 250/4.0) and anion (Metrosep A Supp 5 – 250/4.0) columns, respectively. A 5.5 mmol L^{-1} H_3PO_4 solution for the cation and a mixture of 3.2 mmol L^{-1} Na_2CO_3 and 1.0 mmol L^{-1} $NaHCO_3$ for the anion were used as eluents for the two columns, respectively. Free chlorine in the ERS was measured employing N,N-diethyl-p-phenylenediamine colorimetric analysis.

3.3 Preliminary analysis

Some preliminary tests were conducted with the EDBM pilot to verify the correct functioning of the system: i) absence of leakages in the hydraulic circuit, ii) negligible internal leakage inside the stack, iii) simultaneous production of acid and base solutions, as well as to define the operative range and operating conditions for following analyses.

Firstly, the hydraulic circuit was tested, disconnecting the EDBM stack. The turbine pumps (TEOREMA PTM 2.5x6) were activated and tested at different flowrates, up to 30 L min^{-1}. In addition, manual valves were partially closed to increase the pressure of the hydraulic circuit up to 3 barg, verifying the complete absence of leaks. Secondly, an internal leakage test of the EDBM stack was conducted with water utilising the closed-loop configuration. During this test, only the pumps were activated, while the DC drive was kept off. Four different tanks, one for each solution circulating in the stack, were filled with water (approx. 100 L) and their levels were monitored. After a few hours of operation, only negligible variations (less than 1 %) were observed in the level of the tanks.

Additionally, the pilot plant was tested with artificial NaCl-containing solutions to evaluate its effectiveness in producing chemicals. Also in this case, a closed-loop configuration was utilised for all the lines, with solutions volumes of 100 L for each. tank. The initial compositions of the solution are reported in Table 3.

Table 3. Initial conditions of the solution utilised in the preliminary test.

Compartment	Acid	Base	Salt	ERS
Content	HCl	NaOH	NaCl	Na_2SO_4
Concentration (mol L^{-1})	0.05	0.05	2	0.25

During the test, the current was kept constant at 33 A, corresponding to a current density of 100 A m^{-2}. Figure 16 depicts the main results of this test in terms of external voltage and chemical concentrations over time.

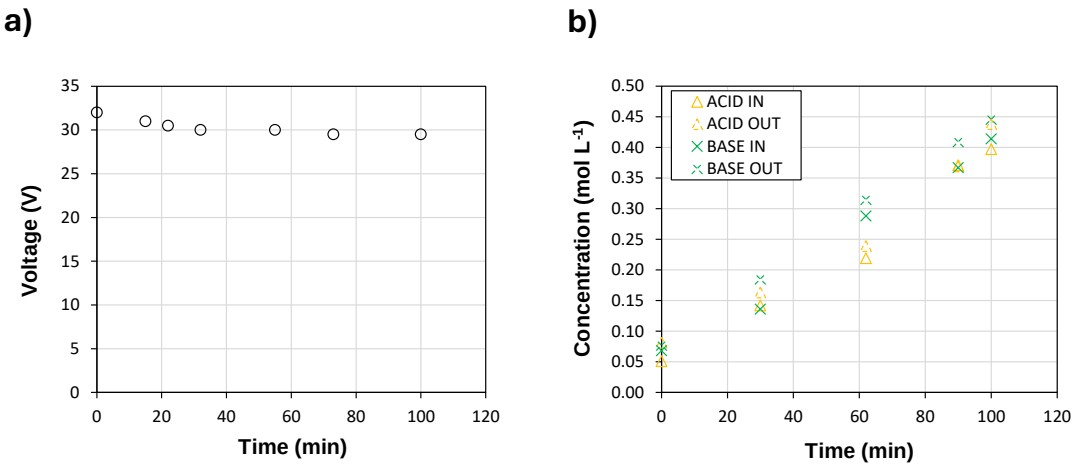

Figure 16. Preliminary test conducted in closed-loop mode at 100 A m^{-2}: a) external voltage applied to the stack and b) acid and base concentrations at the stack inlet and outlet as functions of time.

According to the graph in Figure 16a, the resulting external voltage was slightly decreasing, starting from a value of 32 V and reaching a final value of 29.5 V. Overall, the voltage decreased during the test was related to an increase in acid and base concentrations. Indeed. the latter reduces the electrical resistance of the stack. Figure 16b depicts the evolution of acid and base concentrations over time. It could be observed that acid and base concentrations higher than 0.4 mol L^{-1} were achieved in about 100 minutes.

Moreover, it should be observed that the chemical concentrations increase in a passage through the stack were limited due to the adopted current density, with values lower than 0.05 mol L^{-1}. These findings indicate that EDBM performance is promising. Indeed, the current efficiency was greater than 80%, with a Specific Energy Consumption of around 1.2 kWh kg^{-1}, for the alkaline product.

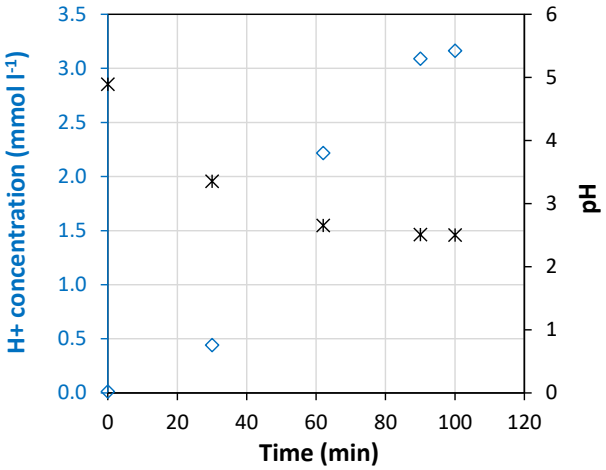

Figure 17. Protons concentration and pH of the salt tank as functions of time in a preliminary test in closed-loop mode at 100 A m^{-2}.

Finally, Figure 17 depicts the proton concentration and pH of the saline solution over time. The amount of protons diffused/migrated into the saline compartment is negligible. In detail, the H^+ concentration in the salt tank was only 3 mmol L^{-1} at the end of the test, corresponding to a pH of approximately 2.5. This demonstrates the high selectivity of the membranes and the possibility of reaching elevated current efficiency.

3.3.1. Analysis of EDBM performance in open-loop configuration

The effect of flowrates (acid, base, salt and ERS), initial concentrations in the compartments and current densities on the increase of H^+ and OH^- concentrations and KPIs was determined in open-loop configuration. The results shown in this section were published in the scientific article *Analysis of Operational Parameters in Acid and Base*

Production Using an Electrodialysis with Bipolar Membranes Pilot Plant [90]. Synthetic sodium chloride solutions were utilised in the salt chambers, while the produced hydrochloric acid and sodium hydroxide solutions were fed in the acid and base chambers, respectively. Three sets of experimental runs were carried out, employing the EDBM pilot plant described in 3.1. Table 4 summarises the operating conditions tested during the experimental campaign. Two different values of current density (i.e., 200 A m^{-2} and 400 A·m^{-2}) were employed as they result representative of the commonly utilised range of current densities (i.e., 100-600 A m^{-2}).

Table 4. Summary of the experimental conditions investigated in open-loop configuration.

Code	Current density (A·m^{-2})	Line	Inlet conc. (mol·L^{-1})	Flowrate (L·min^{-1})	Channel speed (cm·s^{-1})
T-200-I	200	Acid	0.1	2.0–7.5	0.88–3.3
		Base	0.1	2.0–7.5	0.88–3.3
		Salt	1.0	2.0–7.5	0.88–3.3
		ERS	0.25	20	4.4
T-400-I	400	Acid	0.1	2.0–7.5	0.88–3.30
		Base	0.1	2.0–7.5	0.88–3.3
		Salt	1.0	2.0–7.5	0.88–3.3
		ERS	0.25	20	4.4
T-200-F	200	Acid	0.7	2.0–8.0	0.88–3.5
		Base	0.7	2.0–8.0	0.88–3.5
		Salt	0.5	2.0–8.0	0.88–3.5
		ERS	0.25	20	4.4
T-400-F	400	Acid	0.7	2.0–7.5	0.88–3.3
		Base	0.7	2.0–7.5	0.88–3.3
		Salt	0.5	2.0–7.5	0.88 -3.3
		ERS	0.25	20	4.4
T-200-I-ERS	200	Acid	0.1	6.0	2.6
		Base	0.1	6.0	2.6
		Salt	1.0	6.0	2.6
		ERS	0.25	5.0–30	1.1–6.6
T-400-I-ERS	400	Acid	0.1	6.0	2.6
		Base	0.1	6.0	2.6
		Salt	1.0	6.0	2.6
		ERS	0.25	5.0–30	1.1–6.6

In the first set of investigated experimental conditions, constant initial concentrations were maintained (ca. 0.1 $mol \cdot L^{-1}$ of HCl and NaOH and 1 $mol \cdot L^{-1}$ of NaCl), while acid, base and salt flowrates were varied from 2 to 8 $L \cdot min^{-1}$, at constant ERS flowrate (20 $L \cdot min^{-1}$). Only in experiment T-200-F solution flowrates of 8 $L \cdot min^{-1}$ were reached, whereas in the other tests a maximum flowrates of 7.5 $L \cdot min^{-1}$ were investigated. This was due to the high pressure losses (>2 bar) that were observed at 8 $L \cdot min^{-1}$, which caused external leakages. By working at 7.5 $L \cdot min^{-1}$, the pressure losses remained below 2 bar, avoiding the presence of an external leakage. In the second set of investigated experimental conditions, higher initial chemical concentrations as well as a lower salt concentration were tested (ca. 0.7 $mol \cdot L^{-1}$ of HCl and NaOH and 0.5 $mol \cdot L^{-1}$ NaCl). In this case, the flowrates were varied within the same range. Finally, the third set of experiments was focused on studying the effect of ERS flowrate variation (from 5 to 30 $L \cdot min^{-1}$) at constant initial concentrations of the first set (ca. 0.1 $mol \cdot L^{-1}$ of HCl and NaOH and 1 $mol \cdot L^{-1}$ of NaCl) and by keeping the acid, base and salt flowrates at 6 $L \cdot min^{-1}$.

Figure 18 shows how the concentration of protons and hydroxide ions varies due to the effect of flowrates. The concentration trend is equivalent in shape for changes in acid, base and salt flowrates, Figure 18a-d. Specifically, the reduction of the concentrations follows a trend inversely proportional to the flowrates. As expected, the highest variation in the concentration was obtained at the lowest flowrate value (2 $L \cdot min^{-1}$), due to the higher residence time inside the stack. More remarkable concentration variations were obtained when lower initial concentrations were employed (T-200-I and T-400-I). In the tests T-200-F and T-400-F, higher initial concentrations led to a relevant pH gradient across the bipolar membranes generating a voltage which must be overcome to produce further chemicals. Thus, operating at the same current density

intrinsically produces a lower inlet-outlet concentration variation. Moreover, higher inlet concentrations favoured the appearance of non-ideal phenomena (such as osmosis, electro-osmosis, diffusion and parasitic currents) that reduce the EDBM performance. On the other hand, working at a higher current density (400 $A \cdot m^{-2}$) increases the final acid and base concentrations and, therefore, the variation of concentrations. This is related to the presence of the electric field, which accelerates the kinetics of water dissociation at the bipolar membrane junction, as stated by the second Wien effect [91].

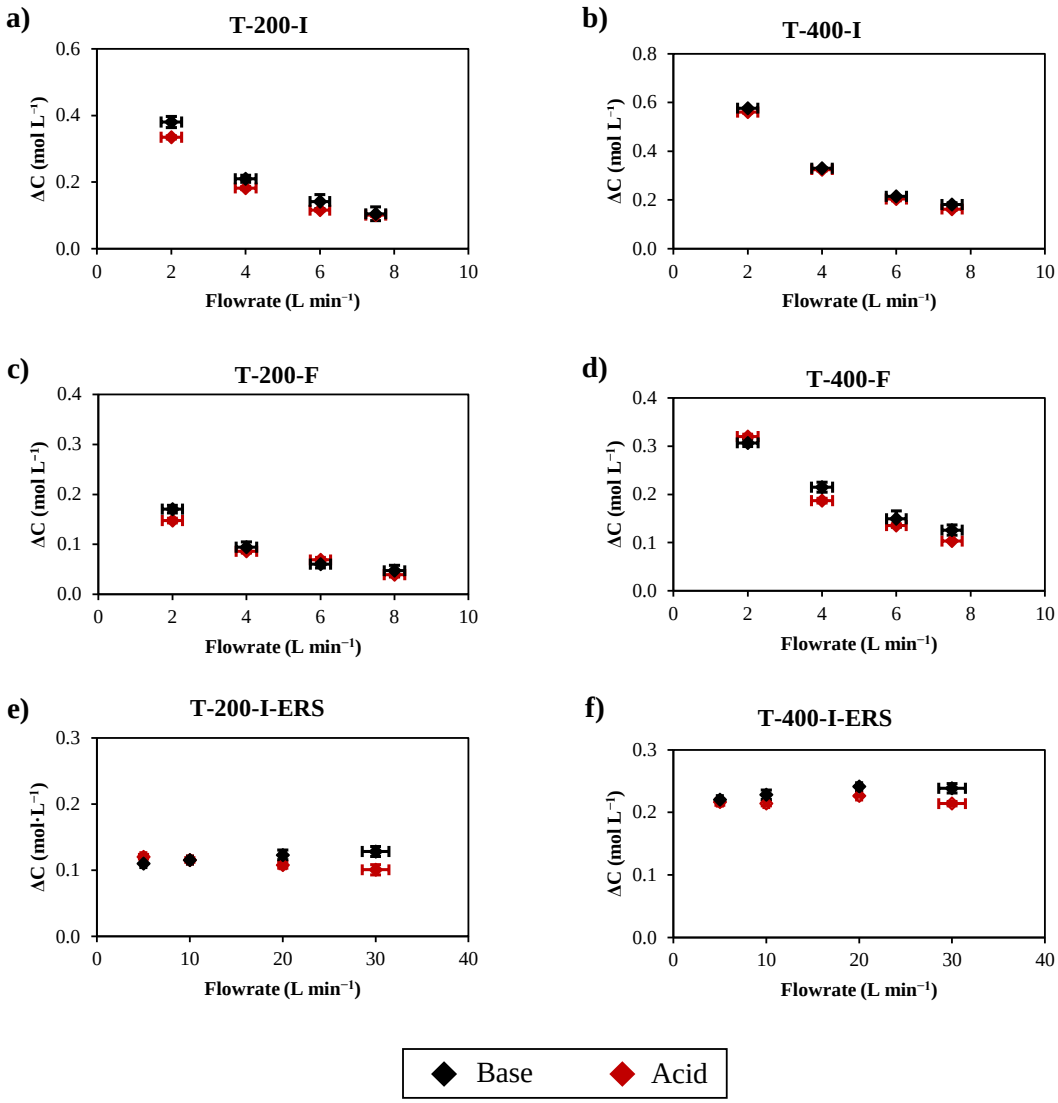

Figure 18. Values of concentration variations versus flowrate: a) T-200-I; b) T-400-I; c) T-200-F; d) T-400-F, e) T-200-I-ERS; f) T-400-I-ERS. Acid, base and salt flowrates were simultaneously changed in tests T-200-I; T-400-I; T-200-F; T-400-F, while only the ERS flowrate was varied during tests T-200-I-ERS and T-400-I-ERS.

Different concentration profiles were observed between the T-200-I-ERS (Figure 18e) and the T-400-I-ERS (Figure 18f) tests. For test T-200-I-ERS, the acid concentration slightly decreased when increasing the ERS flowrate, while the base concentration slightly increased. However, the changes throughout the test were quite limited, for both products (<0.02 mol·L−1). In test T-400-I-ERS, a maximum in the variation of concentration was also observed for both products (<0.02 mol·L−1) at 20 $L \cdot min^{-1}$, which was the flowrate recommended by the supplier for the ERS compartment. The final concentration and, therefore, the variation of concentration increased along with the current density. Almost twice the amount of concentration variation was achieved (for both NaOH and HCl) when the current density was doubled (from 200 $A \cdot m^{-2}$ in T-200-I-ERS to 400 $A \cdot m^{-2}$ in T-400-I-ERS).

In Figure 19, the trends of CE and SEC are reported for the three investigated sets of experiments. As depicted in Figure 19a, the SEC slightly decreased when the flowrates were increased in the first two sets of investigated operating conditions (T-200-I, T-400-I, T-200-F, and T-400-F). The energy supplied resulted approximately the same and the SEC variations were related to the production, which, in turn, depends on the flowrates and the variation in concentrations. Even though the variation in concentration was quite small, the production was slightly enhanced for higher flowrates, therefore, the SEC was decreased. Doubling the current density in the first set of experimental conditions (i.e., T-400-I) made the SEC 1.6–1.8 times larger, while in the second set of experiments (i.e., T-400-F) the SEC was 1.2–1.3 larger. Surprisingly, the SEC followed a quite horizontal tendency with the flowrates, except for the second set of operating conditions at higher current density (i.e., T-400-F). In this test, the SEC started from a value of 3.2 $kWh \cdot kg^{-1}$ and showed a decreasing trend as the flowrates increased. This was related to the fact that the salt solution at the stack outlet was depleted (conductivity value of approx. 4

mS·cm^{-1}), which caused: (i) an increase in the salt compartment resistance and therefore, an increase in voltage, but also (ii) a limitation of the water splitting phenomena due to the absence of counter-ions in the salt compartment that can compensate the charge balance.

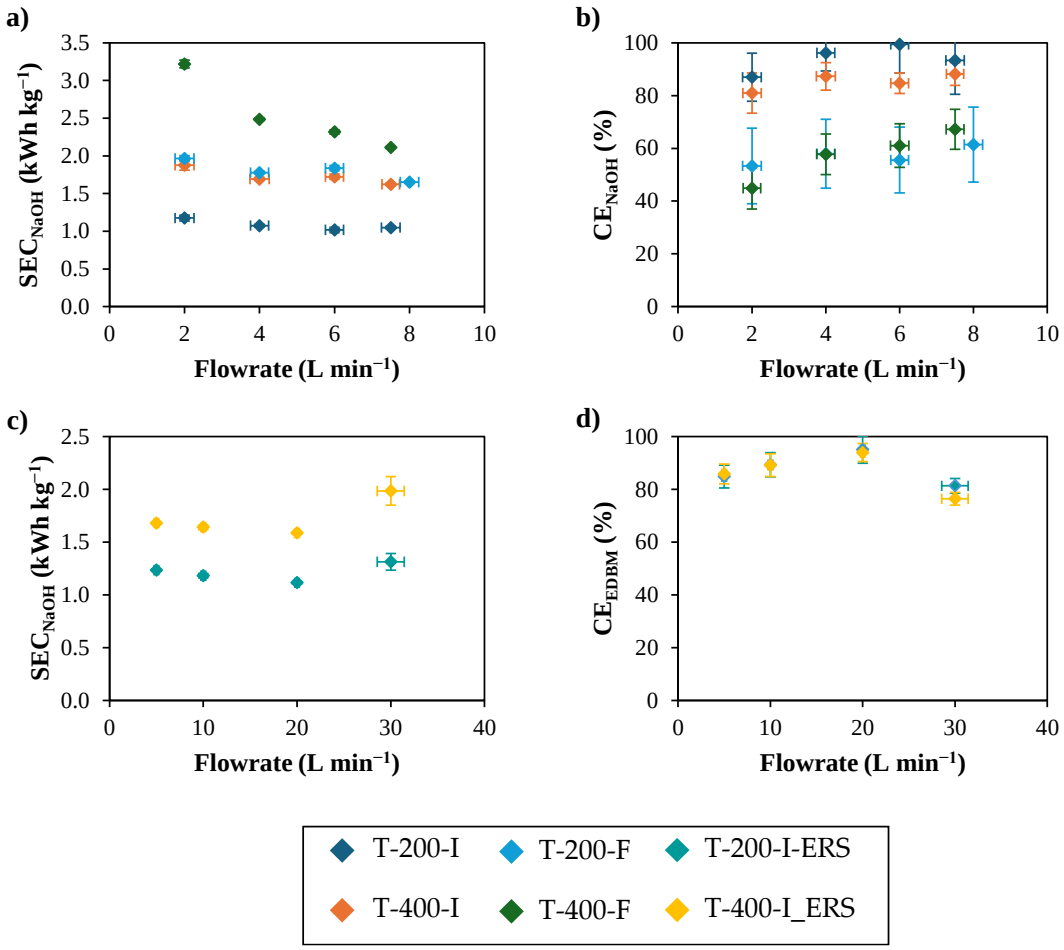

Figure 19. Trends of specific energy consumption (SEC) and current efficiency (CE)of the base product as function of flowrates. The first two sets of experiments (i.e., T-200-I, T-400-I, T-200-F and T-400-F) are shown in Figures a) and b), while the third set of experiments (i.e., T-200-I-ERS and T-400-I-ERS) are reported in Figures c) and d).

Comparing tests with the same applied current density, the SEC was 1.8 times higher for T-200-F with respect to T-200-I, and 1.2–1.4 times higher for T-400-F compared to T-400-I. The variations were more remarkable in the tests with a lower salt concentration and a higher chemical content (i.e., T-200-I and T-400-I) due to the

contribution of the ohmic resistance in the voltage. The stack resistance was higher when the concentrations in the stack were lower (i.e., T-200-I and T-400-I) thus, the energy input was increased due to a higher current and an increased resistance.

Considering the CE, Figure 19b, a small increase was observed as the flowrates increased, which was related to an increase in productivity. For the same applied current densities (T-200-I and T-200-F, or T-400-I and T-400-F) the tests of the first set of experiments had a better efficiency (1.8–2.0 times higher for T-200-I compared to T-200-F, and 1.3–1.4 times higher for T-400-I compared to T-400-F). This fact was attributed to the higher variations in the concentration obtained in the first set of experiments. Looking at the CE, when the current density was increased, a reduction of 20% was observed in the first set of experiments, while only 10% differences were observed in the second set. Both SEC and CE were slightly by the variations in concentration obtained.

Evaluating the effect of ERS flowrate on the performance indicators, a minimum in the SEC was observed for the flowrate of 20 $L \cdot min^{-1}$ (i.e., the nominal flowrate) for both T-200-I-ERS and T-400-I-ERS. The SEC increased by 1.3–1.5 times when the current density was doubled. Since the variation in concentration was doubled by changing the current density, the increase in SEC was due to the higher power consumption (ohmic losses). Similar behaviour was observed for the T-200-I-ERS and the T-400-I-ERS tests where a maximum in the CE was observed for the flowrate of 20 $L \cdot min^{-1}$. For this reason, it was decided to use this value of ERS flowrate in the subsequent experimental campaigns. The changes in CE throughout the test were <13% for T-200-I-ERS and <5% for T-400-I-ERS. The changes in the CE by doubling the current density were minimal (<5%) since twice the variation of the concentration was achieved.

3.4 Comparison between different process configurations

The EDBM pilot plant described in 3.1 was utilized to conduct a configuration comparison analysis, which results of particular interest for the industrial production of acid and base. The results reported in this paragraph were published in the scientific article *Electrodialysis with Bipolar Membranes for the Sustainable Production of Chemicals from Seawater Brines at Pilot Plant Scale* [92]. Specifically, different process configurations (i.e., closed-loop, partial feed and bleed, fed-batch) were investigated to evaluate for the first time the behaviour and performance of an up-scaled EDBM unit for producing HCl and NaOH solutions. Each of the three process configurations was tested by operating the EDBM pilot at two different current densities (i.e. either 200 or 400 A m^{-2}), fixing a target concentration of 1 mol L^{-1} of the base product. A summary of the tests conducted is presented in Table 5.

Table 5. Summary of the tests performed with the EDBM pilot plant in terms of process configurations, current density and initial conditions of the four solutions. Volumes (Vt), concentrations (C) and flowrates (Q) are expressed in m^3, mol L^{-1} and L min^{-1}, respectively.

Test	Configuration	i ($A\ m^{-2}$)	Acid Line	Base Line	Salt Line	ERS Line
1	Closed-loop	200	$Vt_{p,0} = 0.3$ $C_{p,0} = 0.05$ $Q = 5$	$Vt_{p,0} = 0.3$ $C_{p,0} = 0.05$ $Q = 5$	$Vt_{r,0} = 0.9$ $C_{r,0} = 1$ $Q = 5$	$Vt_{ERS} = 0.125$ $C_{ERS} = 0.25$ $Q = 20$
2	Closed-loop	400	$Vt_{p,0} = 0.3$ $C_{p,0} = 0.05$ $Q = 5$	$Vt_{p,0} = 0.3$ $C_{p,0} = 50$ $Q = 5$	$Vt_{r,0} = 0.9$ $C_{r,0} = 1$ $Q = 5$	$Vt_{ERS} = 0.125$ $C_{ERS} = 0.25$ $Q = 20$
3	Feed and bleed	200	$C_{p,in} = 0$ $Q_{p,out} = 0.48$ $Q_{rec} = 4.52$	$C_{p,in} = 0$ $Q_{p,out} = 0.48$ $Q_{rec} = 4.52$	$Vt_{r,0} = 0.9$ $C_{r,0} = 1$ $Q = 5$	$Vt_{ERS} = 0.125$ $C_{ERS} = 0.25$ $Q = 20$
4	Feed and bleed	400	$C_{p,in} = 0$ $Q_{p,out} = 1$ $Q_{rec} = 4$	$C_{p,in} = 0$ $Q_{p,out} = 1$ $Q_{rec} = 4$	$Vt_{r,0} = 0.9$ $C_{r,0} = 1$ $Q = 5$	$Vt_{ERS} = 0.125$ $C_{ERS} = 0.25$ $Q = 20$
5	Fed-Batch	200	$Vt_{p,0} = 0.1$ $C_{p,0} = 0.05$ $Q = 5$ $Q_{water} = 0.5$	$Vt_{p,0} = 0.1$ $C_{p,0} = 0.05$ $Q = 5$ $Q_{water} = 0.5$	$Vt_{r,0} = 0.9$ $C_{r,0} = 1$ $Q = 5$	$Vt_{ERS} = 0.125$ $C_{ERS} = 0.25$ $Q = 20$
6	Fed-Batch	400	$Vt_{p,0} = 0.1$ $C_{p,0} = 0.05$ $Q = 5$ $Q_{water} = 1$	$Vt_{p,0} = 0.1$ $C_{p,0} = 0.05$ $Q = 5$ $Q_{water} = 1$	$Vt_{r,0} = 0.9$ $C_{r,0} = 1$ $Q = 5$	$Vt_{ERS} = 0.125$ $C_{ERS} = 0.25$ $Q = 20$
7	Closed-loop	300	$Vt_{p,0} = 0.3$ $C_{p,0} = 0.05$ $Q = 5$	$Vt_{p,0} = 0.3$ $C_{p,0} = 0.05$ $Q = 5$	$Vt_{r,0} = 0.9$ $C_{r,0} = 1$ $Q = 5$	$Vt_{ERS} = 0.125$ $C_{ERS} = 0.25$ $Q = 20$
8	Closed-loop	500	$Vt_{p,0} = 0.3$ $C_{p,0} = 0.05$ $Q = 5$	$Vt_{p,0} = 0.3$ $C_{p,0} = 0.05$ $Q = 5$	$Vt_{r,0} = 0.9$ $C_{r,0} = 1$ $Q = 5$	$Vt_{ERS} = 0.125$ $C_{ERS} = 0.25$ $Q = 20$
9	Feed and bleed	300	$C_{p,in} = 0$ $Q_{p,out} = 0.75$ $Q_{rec} = 4.25$	$C_{p,in} = 0$ $Q_{p,out} = 0.75$ $Q_{rec} = 4.25$	$Vt_{r,0} = 0.9$ $C_{r,0} = 1$ $Q = 5$	$Vt_{ERS} = 0.125$ $C_{ERS} = 0.25$ $Q = 20$
10	Feed and bleed	500	$C_{p,in} = 0$ $Q_{p.out} = 1.2$ $Q_{rec} = 3.8$	$C_{p,in} = 0$ $Q_{p,out} = 1.2$ $Q_{rec} = 3.8$	$Vt_{r,0} = 0.9$ $C_{r,0} = 1$ $Q = 5$	$Vt_{ERS} = 0.125$ $C_{ERS} = 0.25$ $Q = 20$

3.4.1. Closed-loop configuration

The results of the closed-loop tests are shown in Figure 20 in terms of acid and base concentrations as well as voltage, CE and SEC as functions of time for applied current densities of 200 and 400 A m^{-2}.

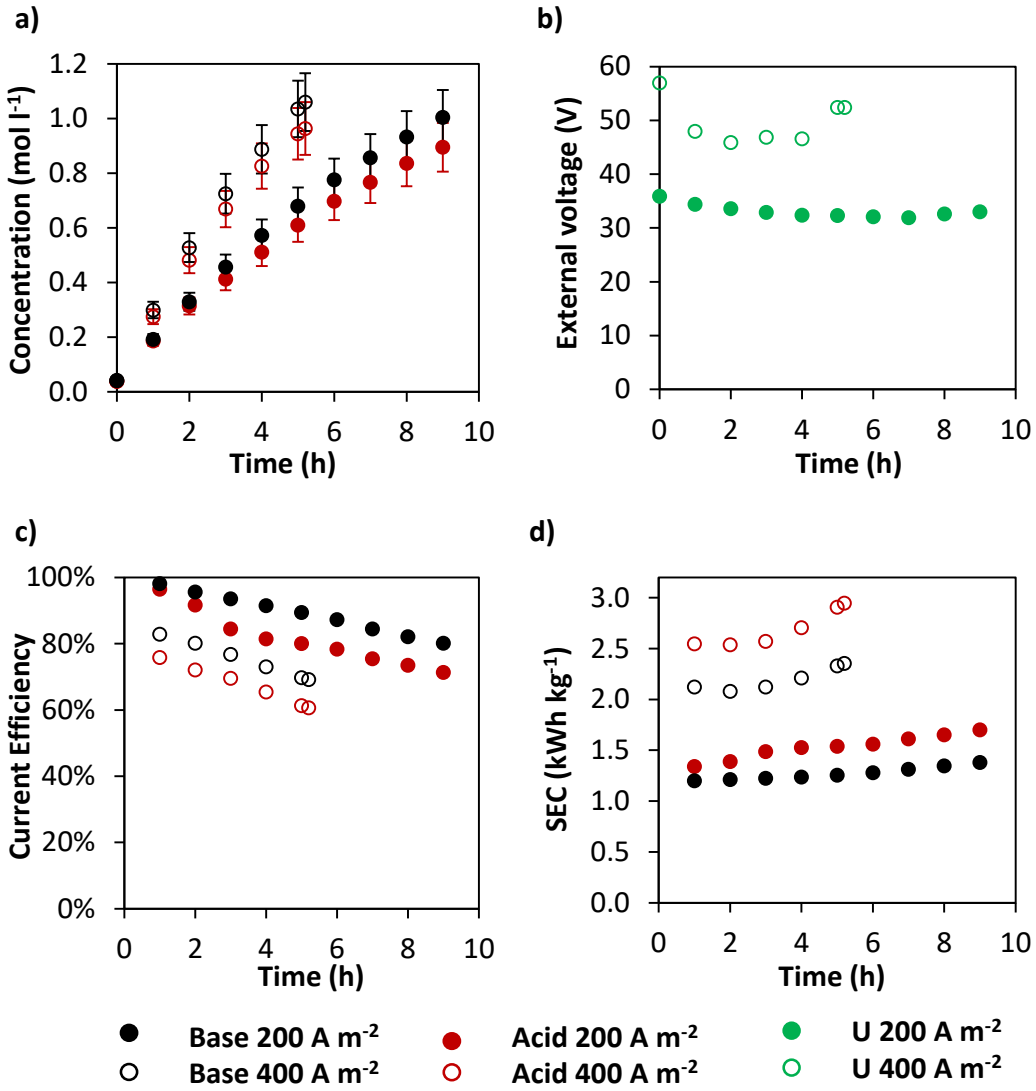

Figure 20. Time-dependent profiles of a) acid and base concentrations, b) external voltage, c) Current Efficiency, and d) Specific Energy Consumption for acid and base products for the tests performed at 200 and 400 A m^{-2}. Pilot operation mode: closed-loop (batch).

As could be observed from Figure 20a, the acid and base concentrations increased linearly with time only during the first hours of the test (about 4 hours). Then, a less-than-linear trend was observed as a result of non-ideal phenomena such as membrane

permselectivity, osmosis, diffusion, electro-osmosis and parasitic currents phenomena [93]. Mainly due to osmosis and electro-osmosis effects a volume variation of about 17%, in the acid and base tank was observed. The base concentration increased faster than the acid concentration for both the electric currents investigated. This phenomenon was mostly related to the different impacts of the acid and base diffusion phenomena in the saline solution channel. As a result of the high mobility of the protons, acid diffusion was presumably dominant. The pH in the salt channel fell down from around 9 at the beginning of the tests to less than 2 towards the end, while the pH of ERS reduced from 2.3 to 1.1, Figure 21.

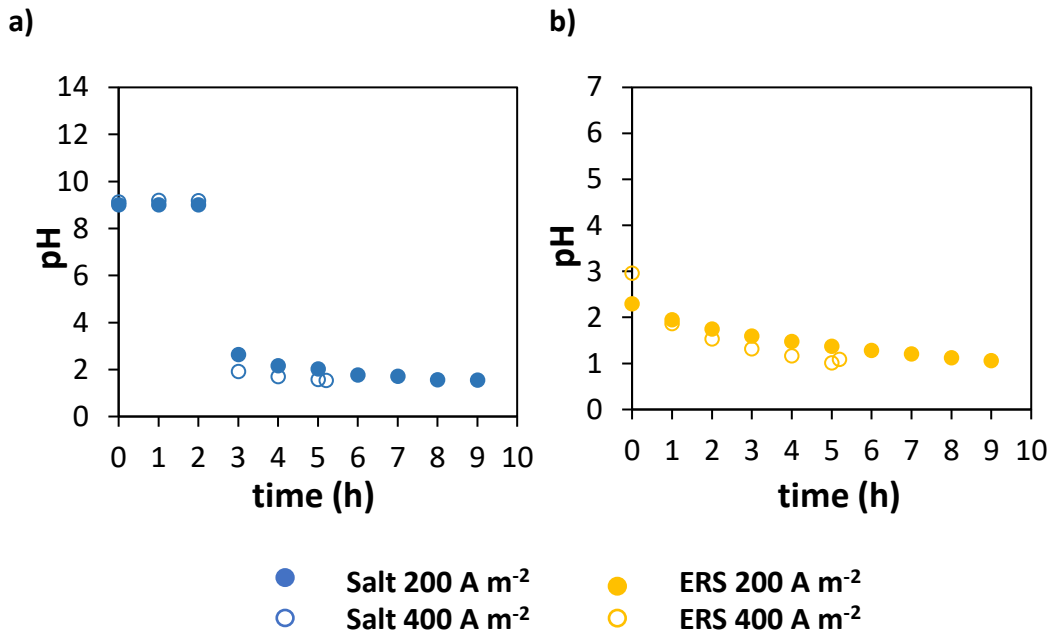

Figure 21. Dynamic trends of salt and ERS pH values for the tests conducted in closed-loop at 200 and 400 A m^{-2}.

The final concentrations reached at 200 A m^{-2} were 1 mol L^{-1} and 0.895 mol L^{-1} for the acid and base solutions, and 1.06 mol L^{-1} and 0.964 mol L^{-1} for the acid and base solutions at 400 A m^{-2}, respectively (Figure 20a). Thus, the target concentration (i.e., 1 mol L^{-1} NaOH) was met in both cases. The target was attained in 9 hours at 200 A m^{-2} and 5.2 hours at 400 A m^{-2}. At 400 A m^{-2}, the process time was approximately 0.56 times

that of the test conducted at 200 A m^{-2}. This fact proved that a slight reduction in current efficiency was obtained at a higher current density (Figure 20c). The increase in the volumes of the acid and alkaline solutions resulted in a yield of about 40%. The current efficiency showed a decreasing monotonous trend with the process time (Figure 20c). At 200 A m^{-2}, the CE was in the range of 80–100% for the base and 96–71% for the acid, while at 400 A m^{-2} resulted in the range of 83–69% for the base and 76–61% for the acid. The SEC results (Figure 20d) are directly related to the current efficiency and electric potential values. Regardless of the applied electric current, the SEC trend showed an increase over time. The SEC profile resulted almost linear in the test at 200 A m^{-2}, whereas it was non-linear at 400 A m^{-2}, with a sudden increase in slope after about 3 hours of operation. Indeed, the effect of two opposing phenomena occurred: on the one hand, a decrease in potential over time, and on the other hand, a reduction in current efficiency. The latter phenomenon prevailed, causing the SEC to rise over time. At the end of the test, the SEC values were 1.4 and 1.7 kWh kg^{-1} for acid and base, respectively, at 200 A m^{-2} and 2.35 and 2.94 kWh kg^{-1} for acid and base, respectively, at 400 A m^{-2}. The voltage showed an overall decreasing trend over time due to two opposing phenomena: a decreasing trend in the average electrical resistance of the stack and an increasing the Nernst potential. Overall, the reduction in the stack electric resistance was dominant, determining the downward trend of the electric potential. The average electric potential resulted 33 and 50 V at 300 and 400 A m^{-2}, respectively. Finally, the average Specific Productivity for the test at 200 A m^{-2} was 0.63 ton y^{-1} m^{-2} for the base and 0.51 ton y^{-1} m^{-2} for the acid. At 400 A m^{-2}, the base had an average productivity of 1.1 ton y^{-1} m^{-2}, while a lower value resulted for the acid, equal to 0.88 ton y^{-2} m^{-2}.

3.4.2. Partial feed and bleed configuration

The results relevant to the continuous steady-state operation of the EDBM pilot in partial feed and bleed mode are reported in Figure 22 for the two investigated current densities (i.e., 200 and 400 Am^{-2}). This process configuration, introduced in 2.4, utilises recirculating loops for acid and base while the salt line is operated in closed-loop. This guarantees continuous operation for a medium/short time period, depending on the quantity of salt present in the salt tank. The conducted tests lasted about 2 hours utilising a 0.9 m^3 of NaCl solution with 1 mol L^{-1} concentration. Electric conductivities were adopted as inferential variables for an online indication of the concentration obtained thus, it was possible to observe when the steady-state condition was reached (dashed lines in Figure 22). In partial feed and bleed mode, the inlet acid and base solutions were made up of reverse osmosis (RO) permeate (~ 350 μS cm^{-1}). This was possible thanks to the recirculating loops that allowed to increase the conductivity of the solution entering the stack. The target concentration of NaOH was achieved in this case by selecting appropriate operating conditions in terms of flowrates (outlet and recirculated streams) and electric current.

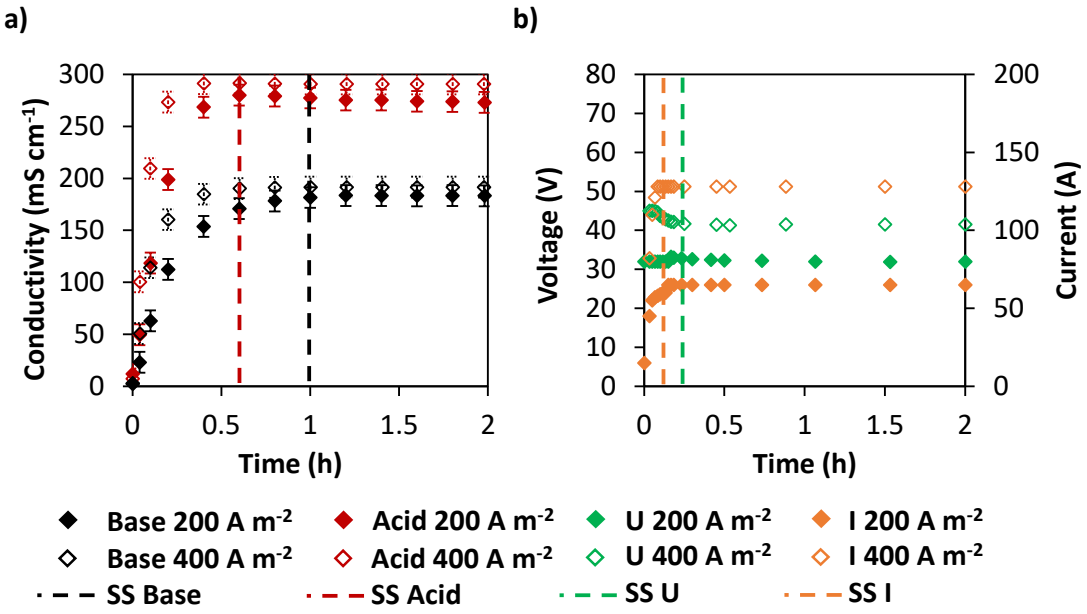

Figure 22. Time-dependent profiles of a) acid and base electric conductivities and b) external voltage and current for tests performed at 200 and 400 A m^{-2}. Vertical dashed lines indicate the end of the transient start-up of the pilot. Pilot configuration: partial feed and bleed.

In Figure 22a the start-up phases are shown until steady-state conditions are reached. Prior to the test, the stack was stored with RO permeate (~ 350 µS cm^{-1}) and a certain time was needed to replace the permeate with the salt and the produced acid and base solutions. For this reason, at the beginning of these tests, the stack was operated in potentiostatic (i.e., constant voltage) to avoid excessive voltage rise due to the low conductivity of the inlet distilled water streams. After about 0.15 hours, the electric current stabilized, due to a certain production of chemicals, and the operating mode was switched from potentiostatic to galvanostatic (i.e., constant current). The voltage remained nearly stable after this transient start-up, with a 1 V drop throughout the test, proving that the system reached a stable conditions. For both applied current densities, the desired base concentration was achieved using this configuration by suitably tuning the outlet and recirculated stream flowrates. The main performance parameters and outlet flow rates for the two current densities are summarised in Table 6.

Table 6. Summary of the main results obtained in partial feed and bleed configuration at 200 and 400 A m^{-2}.

i (A m^{-2})	**$Q_{p,out}$** (L min^{-1})	**CE** (%)		**SEC** (kWh kg^{-1})		**SP** (ton y^{-1} m^{-2})		**$C_{p,out}$** (mol L^{-1})	
	Acid/Base	Acid	Base	Acid	Base	Acid	Base	Acid	Base
200	0.48	41	60	3.0	1.8	0.3	0.48	0.68	1.01
400	1	50	66	3.3	2.1	0.74	1.06	0.8	1.06

Remarkably, the SEC at 400 A m^{-2} was only 17 % higher than at 200 A m^{-2}. Furthermore, at 400 A m^{-2}, the current efficiency is 11 % higher than at 200 A m^{-2}. Interestingly, this resulted in more than double specific productivity at 400 A m^{-2} than that obtained at 200 A m^{-2}.

3.4.3. Fed-batch configuration

Figure 23 shows the results of the fed-batch configuration in terms of concentration, current efficiency and SEC profiles for acid and base, as well as the voltage applied to the stack as a function of time. As described in 2.4, the fed-batch configuration consists of two phases: i) a standard closed-loop phase until the target concentration of base is reached; ii) a closed-loop phase with an addition of make-up water in acid and base tanks to maintain constant chemical concentrations.

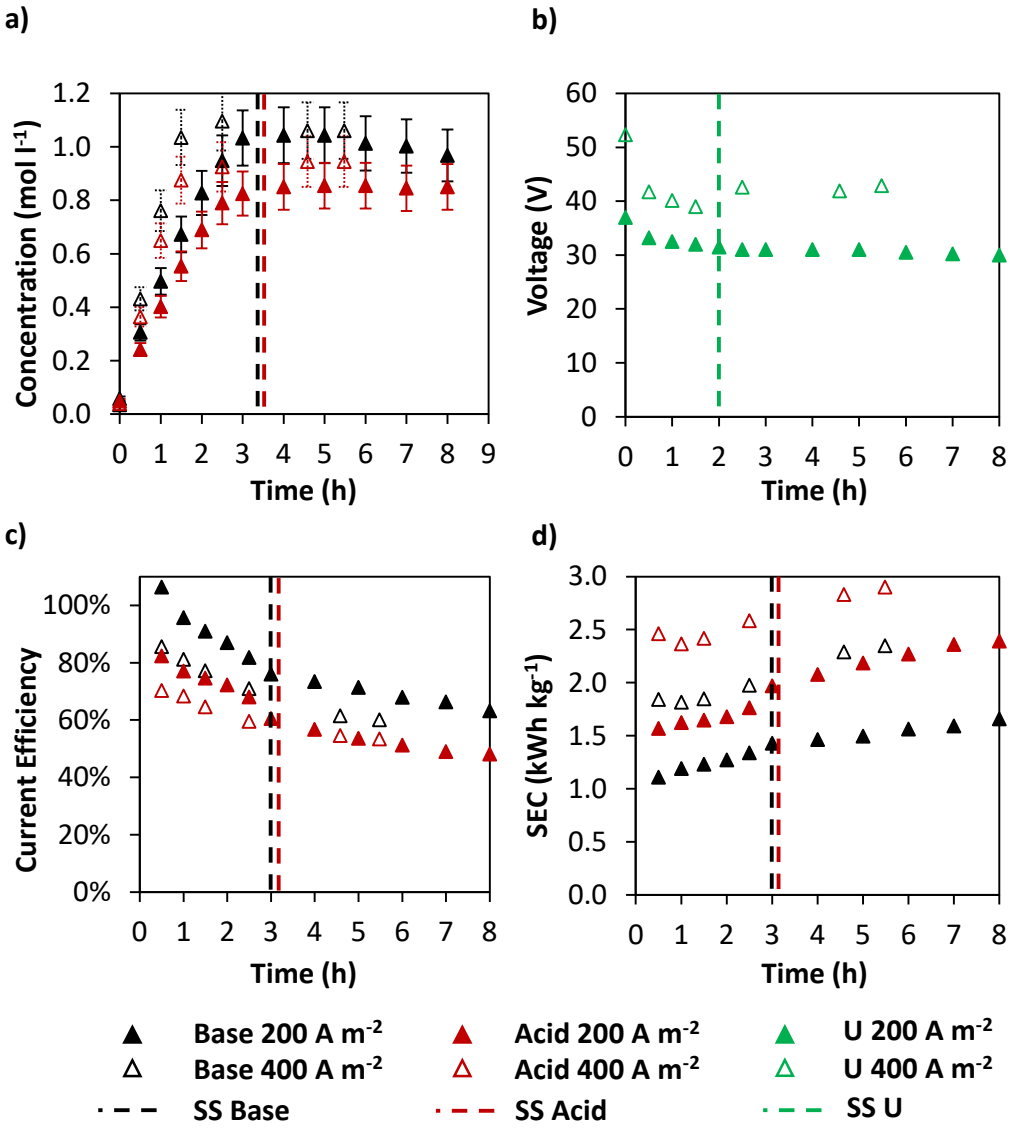

Figure 23. Time-dependent profiles of a) acid and base concentrations, b) external voltage, c) Current Efficiency, and d) Specific Energy Consumption for acid and base for tests performed at 200 and 400 A m^{-2}. Vertical dashed lines indicate the end of the closed-loop phase and the start-up of the Fed-batch phase. Pilot operation mode: Fed-batch (batch).

For both investigated current densities, the target concentration of base was reached. Precisely, 1.04 and 1.06 mol L^{-1} concentrations were observed for tests performed at 200 and 400 A m^{-2}, respectively (Figure 23a). The acid concentration reached was lower compared to the base one, with values of 0.85 and 0.95 mol L^{-1} for tests performed at 200 and 400 A m^{-2}, respectively. As mentioned for the other process configurations, this effect was related to the larger diffusion fluxes across the AEM than

the CEM, which ultimately causes a decrease in the acid current efficiency (Figure 23c). Furthermore, the higher acid concentration at 400 A m^{-2} was due to the higher applied current density. This effect was also observed for the other process configurations and could be attributed to the relative impact increase of migrative fluxes compared to diffusive ones at higher current densities. Regardless of the current density used, the make-up stream of water was sent to the acid and base tanks around the third hour of operation. Because of the small volume of solution used, concentrations rose rapidly in the first three hours of operation, as shown in Figure 23a. As a result of the diluting effect caused by the addition of make-up water, the concentration profiles for both the acid and base flattened. The water make-up flowrate was chosen to ensure that the concentration remained quasi-stationary. However, a slightly decreasing trend in concentration was observed, particularly for the base, while the acid concentration was approximately stable. At both 200 and 400 A m^{-2}, the electrical potential was somehow more stable than that obtained with the conventional closed-loop configuration (see Figure 20), especially once the water make-up enters the acid and base tanks. Since the initial conditions were the same, the starting voltage values were similar to those obtained in the closed-loop configuration. However, the average value of the electric potential was lower because the system operates at a higher concentration (i.e., lower solution resistances) for most of the test time than the conventional closed-loop configuration. Indeed, regardless of the applied current density, the system operated in quasi-steady state conditions with average concentrations of 0.89 and 1 mol L^{-1} for acid and base, respectively. The advantage of having a lower average applied voltage was offset by a decrease in current efficiency due to the increased weight of non-ideal phenomena. These phenomena are exacerbated when the system operates at high concentrations and/or concentration gradients across the membranes. At the end of the test, the current efficiency was 63.2 % and 60 % at 200 and

400 A m^{-2}, respectively, for the base and 48% and 53% at 200 and 400 A m^{-2}, respectively, for the acid (Figure 23c). The acid product showed a 22 % lower current efficiency compared to the base and an average value of 50.5%. The SEC reflected the current efficiency and voltage values (Figure 23d). Regardless of the applied current, the final SEC values were in the range 1.7–2.4 kWh kg^{-1} for the base and 2.4–2.9 kWh kg^{-1} for the acid. Despite the decrease in average applied potential, the reduction in current efficiency determined the increase in the SEC values compared to the conventional closed-loop case. Finally, the obtained SP values for the base were 0.5 and 0.96 ton y^{-1} m^{-2} at 200 and 400 A m^{-2}, respectively, and 0.35 and 0.78 ton y^{-2} m^{-2} for the acid at 200 and 400 A m^{-2}, respectively.

3.4.4. Additional tests in closed-loop and partial feed and bleed modes

From the tests conducted for each process configuration, it was observed that the fed-batch mode led to low performance at both investigated current density (i.e., 200 and 400 A m^{-2}). Consequently, it was decided to exclude this process configuration from further investigations, which aimed to map the process configuration performance in a wider range with more data points (at least three points are needed to observe a trend). Thus, closed-loop and partial feed and bleed were investigated also at 300 and 500 A m^{-2}.

The results of the additional closed-loop tests are shown in Figure 24. Concentration profiles show the same trends as those observed in Figure 20. The target concentration of base was reached for both current densities, in approximately 4 and 7.2 h for the test at 500 and 300 A m^{-2}, respectively. On the other hand, the acid concentration reached was 0.9 mol L^{-2} in both cases. The voltage decreased as a function of time for the whole test at 500 A m^{-2}, while a decreasing trend followed by a stable region was observed at 300 A m^{-2}.

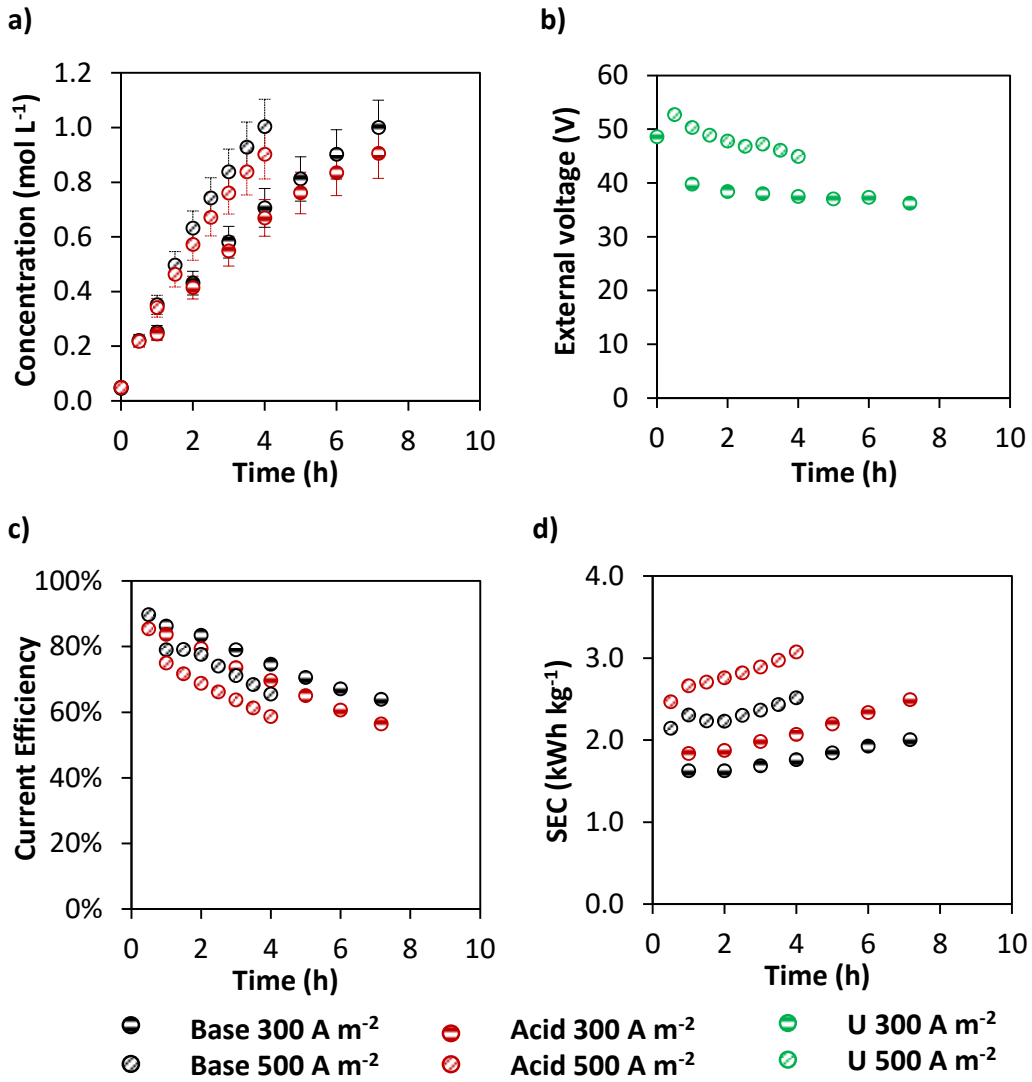

Figure 24. Time profiles of a) acid and base concentrations, b) external voltage, c) Current Efficiency, and d) Specific Energy Consumption for acid and base for tests performed at 300 and 500 A m^{-2}. Pilot operation mode: closed-loop (batch).

A significant CE reduction was observed as a function of time due to the increase of the chemical concentrations. The reduction rate was higher at 500 A m^{-2}, but, due to the lower process time, led to larger CE values (i.e., 59 % and 65 % for acid and base, respectively) compared to 300 A m^{-2}(i.e., 56 % and 64 % for acid and base, respectively). The SEC showed an increase, suggesting that the CE had a major effect on it compared to the external voltage. The obtained values were 2.0 and 2.5 kWh kg^{-1} for the base

product and 2.5 and 3.1 kWh kg^{-1} for the acidic product, at 300 and 500 A m^{-2}, respectively.

A summary of the results conducted at 300 and 500 A m^{-2} in partial feed and bleed mode is reported in Table 7.

Table 7. Summary of the results obtained in partial feed & bleed configuration at 300 and 500 A m^{-2}.

i ($A\ m^{-2}$)	**$Q_{p,out}$** ($L\ min^{-1}$)	**CE** (%)		**SEC** ($kWh\ kg^{-1}$)		**SP** ($ton\ y^{-1}\ m^{-2}$)		**$C_{p,out}$** ($mol\ L^{-1}$)	
	Acid/Base	Acid	Base	Acid	Base	Acid	Base	Acid	Base
300	0.75	46	67	3.1	1.9	0.51	0.82	0.72	1.07
500	1.2	51	62	3.6	2.6	0.94	1.3	0.84	1.05

A base concentration slightly higher than the target was obtained for both current densities, by setting the value of outlet chemicals flowrates equal to 0.75 and 1.2 L min^{-1} at 300 and 500 A m^{-2}, respectively. The obtained CE values resulted comparable with those obtained at 200 and 400 A m^{-2} for the base product (in the range 59-67 %).

3.4.5. Comparison between process configurations

This paragraph presents a comprehensive comparison analysis of the performance parameters for three investigated configurations, considering the target product (i.e. sodium hydroxide).

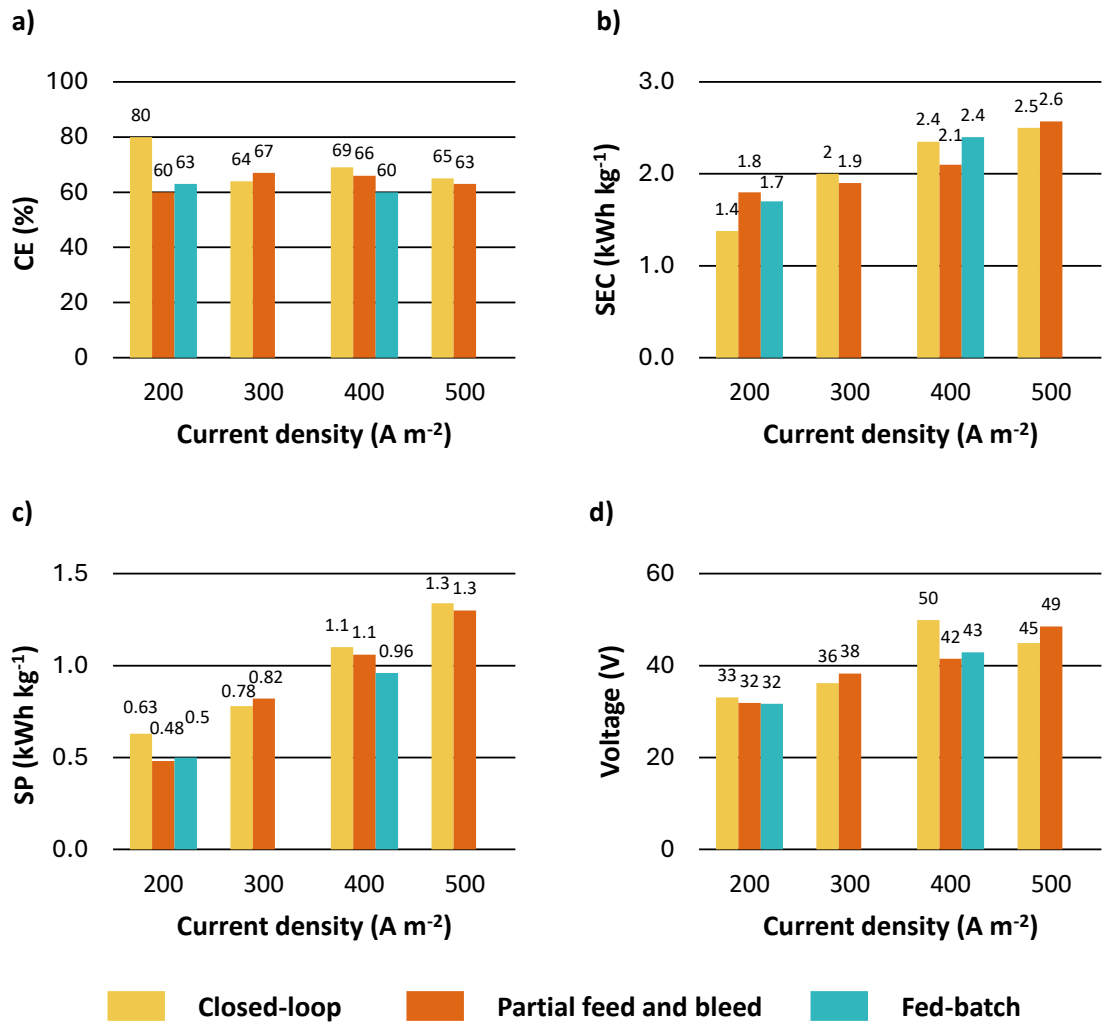

Figure 25. Performance comparison between the investigated process configurations: a) current efficiency; b) specific energy consumption; c) specific productivity; d) external voltage. The key performance indicators refer to the alkaline product at approximately 1 mol L^{-1} concentration.

From Figure 25a it could be observed how current efficiency values in the range 60-80% were found in all the tests. Except for the closed-loop at 200 A m^{-2}, all the other values resulted quite similar, with values between 60 % and 69 %. Thus, a clear trend of the current efficiency as a function of the current density was not observed due to the effect of the experimental error and of the slightly different concentration reached. The SEC showed an increasing trend as a function of the current density for each process configuration, due to the increase of the external voltage applied to the stack (Figure 25d). Values of SEC ≤ 2 were observed for current densities in the range 200-300 A m^{-2}, while

values between 2.1 and 2.6 kWh kg^{-1} were observed in the range 400-500 A m^{-2}. Specifically, at 200 the lowest value of SEC was observed for the closed-loop configuration (i.e., 1.4 kWh kg^{-1}), while at 400 A m^{-2} a reduced value was observed for the partial feed and bleed compared to the other two. As expected, the SP showed an increasing trend with the current density because of the linear dependence with the latter. Values in the range 0.5-1.3 ton y^{-1} m^{-2} were observed for the base product, with a slightly higher value for the closed-loop configuration at 200 A m^{-2} and comparable values at higher current densities.

Overall, the partial feed and bleed configuration would be preferred due to the favourable performance parameters at high current densities and the fact that operates in steady state conditions, guaranteeing more stable production and safer conditions than the discontinuous configurations, in view of a scale-up of the EDBM technology.

3.4.6. Acid product evaluation in partial feed and bleed mode

From the previous paragraph, it was found that the partial feed and bleed mode result the most promising process configuration for the EDBM process scale-up, thanks to its performance and the possibility to operate in steady-state conditions. Thus, similar to what has been done for the base product, this paragraph reports the KIPs and concentration trends as a function of the current density for the acid product to comprehensively investigate this process configuration. For the tests conducted in partial feed and bleed mode, the same outlet flowrate was utilised for the two chemicals. These flowrate values were chosen to maintain a base concentration equal to the target one (i.e., 1 mol L^{-1}), while the acid was not controlled. It was observed that the acid concentration varies significantly with the current density and, in tuns, also the KPIs. For ease of visualisation, the trends are depicted in Figure 26.

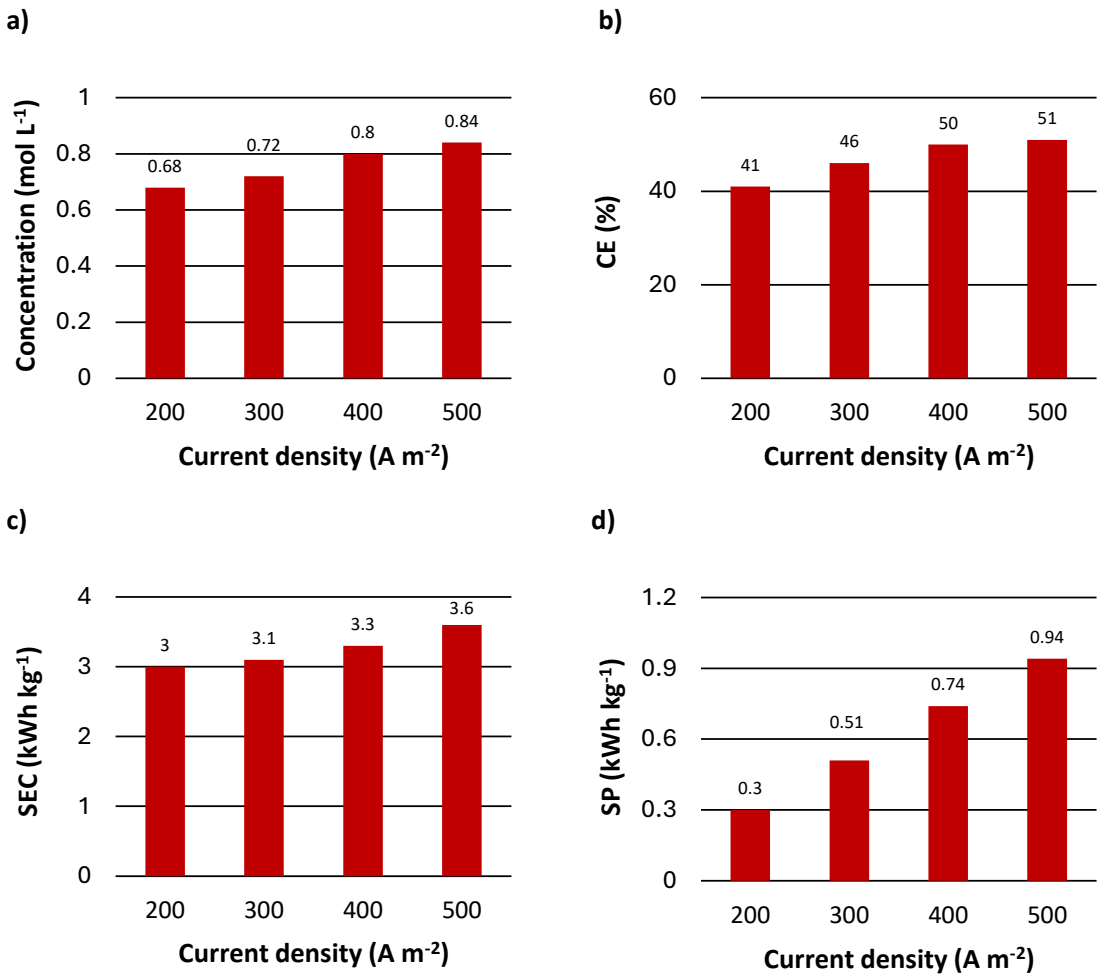

Figure 26. Acid product performance in partial feed and bleed configuration as a function of the current density: a) concentration; b) current efficiency; c) specific energy consumption; d) specific productivity.

The outlet acid concentration increased as the current density rose, from 0.68 at 200 A m^{-2} up to 0.84 at 500 A m^{-2}, while the target of 1 mol L^{-1} was kept for the base. Regarding the CE, an increase in the utilization of the current was observed for the acid at a higher current density. This increase could be attributed to the lower impact of diffusive phenomena due to the higher current density utilised and to reduced residence time inside the stack (higher inlet/outlet flowrate). The SEC showed an increasing trend with current density, despite the increase observed in the current efficiency of the acid product, with values in the range 3-3.6 kWh kg^{-1}. The SP shows a monotonous increasing trend as a function of the current density, with a value up to 0.94 ton $y^{-1}m^{-2}$ at 500 A m^{-2}.

3.5 Novel scheme for valorisation of waste brines

Electrodialysis with bipolar membrane represents a sustainable way for producing acid and base solution from brines [94], [95]. However, water and energy consumption limit the widespread of this technology. In this section, novel schemes are proposed to reduce water consumption: as a modification of the conventional feed and bleed configuration (3.5.1), or as a new process configuration (3.5.2).

When the EDBM is utilised in MLD or ZLD schemes for valorisation of waste streams, the acid and alkaline solutions are reused within the chain and their saline composition may become irrelevant, or favourable, depending on the application. Thus, the possibility of adopting saline inlet streams instead of water for the chemical compartments can be considered [96].

3.5.1. Non-conventional feed and bleed schemes: saline feed

In this paragraph, such novel operating schemes were explored as variation of the convention feed and bleed configuration. The feed and bleed is here selected instead of the partial feed and bleed configuration to prevent the progressive depletion of the salt at the stack inlet thus, guaranteeing steady operation over time. For this reason, an additional tank is used to collect the outlet salt stream from the EDBM unit (see Figure 5). Three different schemes were investigated and compared with a reference one (i.e., conventional feed and bleed configuration). Details about the investigated scenarios are reported in Table 8.

Table 8. Details of the feeding solution for the investigated schemes. "Water" refers to reverse osmosis (RO) permeate (~ 350 μS cm^{-1}), while "Salt sol." means 1 mol L^{-1} sodium chloride solution.

Scheme	Acid feed	Base feed	Salt feed
REF	Water	Water	Salt sol.
WSS	Water	Salt sol.	Salt sol.
SWS	Salt sol.	Water	Salt sol.
SSS	Salt sol.	Salt sol.	Salt sol.

The REF scheme refers to the reference feed and bleed configuration (Figure 27a), which foresees feeding the salt solution only into the salt compartment, while the acid and base compartments are fed with low conductivity water (i.e., ~ 350 μS cm^{-1}). In this layout, the main solutions exit from the EDBM are an exhausted saline solution from the saline compartment as well as acid and base solutions from their respective compartments. Generally, high-purity acid and base solutions are produced with a low salt content, which depends on its transfer from the saline to the acid and base channels due to diffusion, internal leakage, migrative effect and other undesired phenomena occurring within the stack. In the WSS scheme, shown in Figure 27b, base and salt compartments are fed with the salt solution, while the acid channel is supplied with low conductivity water (i.e., ~ 350 μS cm^{-1}). In this case, the output solutions are a depleted salt solution, an acid solution with low salt contamination and an alkaline brine, with a salt concentration similar to the inlet one. The SWS scheme (Figure 27c) is analogous to the WSS scheme. Indeed, the brine is fed into the saline and acid compartments, while low conductivity water (i.e., ~ 350 μS cm^{-1}) is provided to the base compartment. The

produced solutions are a low salt content brine, a high-purity base solution, and an acidified salt solution with reduced purity. In the SSS scenario (Figure 27d) all the compartments, except for the electrode compartment, are supplied with brine solution. In this case, the obtained solutions are a low concentrated brine as we all an acid and an alkaline brine. This scheme almost completely eliminates the water consumption of the EDBM process (except for the water needed to prepare the ERS), while, at the same time, the volume of treated brine is three times larger. In scheme WSS and SWS the water consumption is almost halved, while the brine treatment capacity of the EDBM system is doubled.

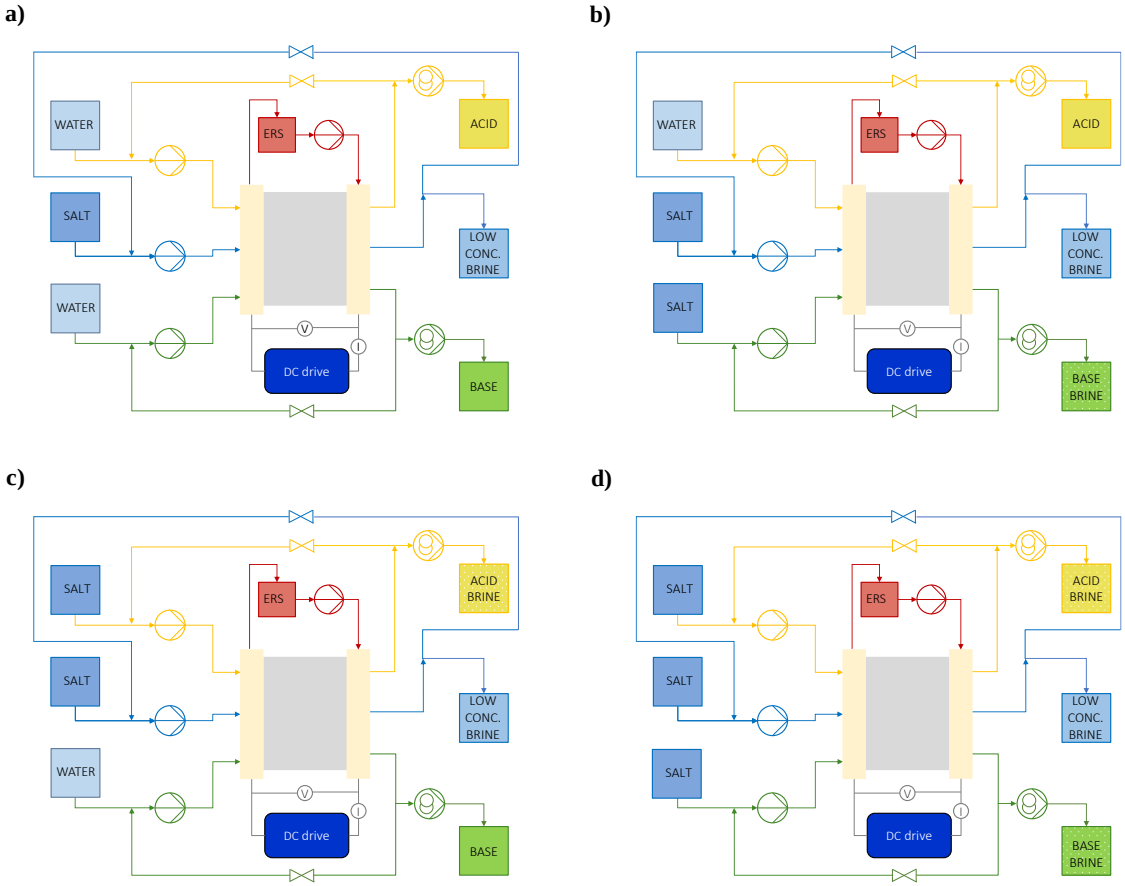

Figure 27. Tested schemes to reduce water consumption adopting the feed and bleed configuration: a) reference (REF) scheme; water-salt.salt (WSS) scheme; c) salt-water-salt (SWS) scheme; d) salt-salt-salt (SSS) scheme.

The four schemes were tested in different operating conditions to evaluate their performance. Specifically, four steady-state conditions were evaluated for each scheme

in a wide range of current densities (i.e., 200-400 A m^{-2}), chemical flowrates (i.e., 0.5-2 L min^{-1}) and salt solution flowrates (i.e., 0.75-1.5 L min^{-1}). Table 9 illustrates the investigated steady-state conditions.

Table 9. Operative conditions investigated for each scheme. The ERS compartment was operated at a constant flowrate of 20 L min^{-1} and at a concentration of sodium sulphate of 0.25 mol L^{-1}.

Steady-state	i (A m^{-2})	$Q_{a,out}$ (L min^{-1}))	$Q_{b,out}$ (L min^{-1})	$Q_{s,out}$ (L min^{-1})
A	400	2	2	1.5
B	400	1	1	1.5
C	200	1	1	0.75
D	200	0.5	0.5	0.75

It can be noted that the steady-state conditions at the two different current densities are perfectly proportional in terms of outlet flow rates. For instance, when the current density is doubled, the outlet flowrates of the three main solutions also double (steady-state A is proportional to C, while B is proportional to D). Each scheme was investigated in a single test in which the four operating conditions were evaluated. For each steady-state condition, three samples were collected and analysed by performing manual titrations. The average results from the three samples were used to compare the schemes. In the following paragraphs, the results of each scheme are firstly reported separately and then compared.

3.5.1.1. Reference (REF) scheme

Figure 28 shows the result obtained from the REF scheme. The start-up phase of the system lasted half an hour until steady-state conditions were reached. For steady-state condition A, concentration values higher than 0.5 mol L^{-1} were obtained for both

chemicals, with values of 0.53 and 0.57 mol L^{-1} for acid and base, respectively. Halving the chemical flowrate, after approximately 20 minutes, the steady-state condition B was reached, with values of acid and base concentrations well below 1 mol L^{-1}. This is due to the higher impact of non-ideal phenomena such as diffusion, parasitic currents, etc. at higher concentrations, which result in a reduction of the overall current utilisation. The base concentration reached a value of 0.88 mol L^{-1}, which is significantly higher than the corresponding acid concentration of 0.76 mol L^{-1}. This can be attributed to the higher diffusion of protons into the saline channels, producing a pH reduction of the latter and, at the same time, decreasing the number of moles available in the acid compartment. The current density was then adjusted from 400 to 200 A m^{-2} and the salt flowrate value was halved (i.e., steady-state condition C). In this case, concentration values of 0.49 and 0.54 mol L^{-1} were registered for acid and base, respectively. These concentration values result slightly lower compared to those obtained in steady-state A. Finally, steady-state D was explored halving acid and base flowrates at constant current density and salt flowrate. This resulted in significantly lower concentrations compared to the corresponding steady state at 400 A m^{-2} (i.e., steady state B). This can likely be explained by an increased influence of the diffusive flux compared to the migratory flux, due to the lower value of current density.

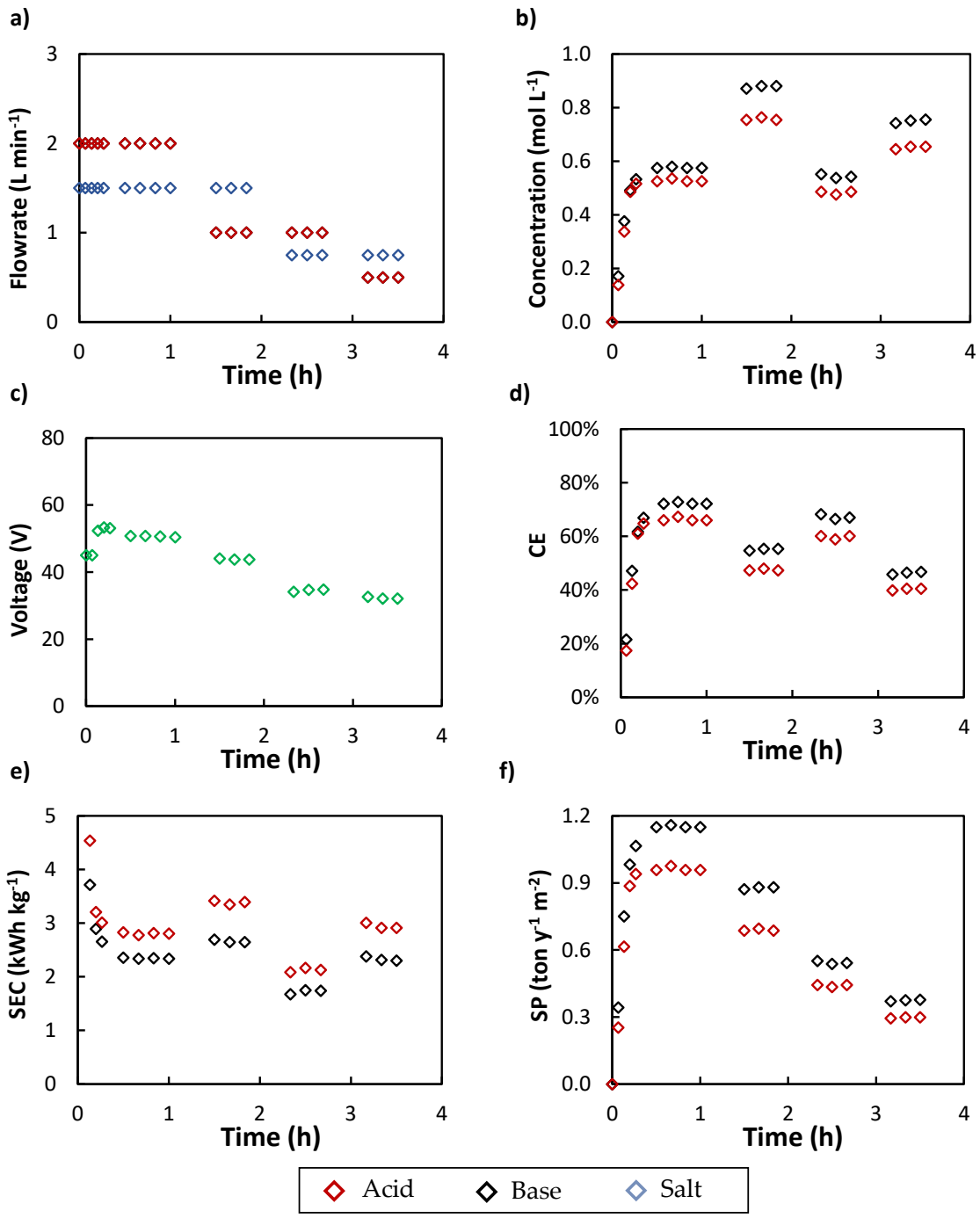

Figure 28. Representative trends of the REF scheme: a) flowrates; b) concentrations; c) external voltage; d) current efficiency; e) specific energy consumption; f) specific productivity.

The trend of the external voltage is shown in Figure 28b. In the first part of the test, during the unit startup, elevated voltage values were caused by the presence of water in both the acidic and basic channels. Once the steady-state concentration had been reached, the voltage remained almost constant throughout the sampling phase, with a

value of about 51 V in steady-state A. Moving to steady-state B, a reduction in external voltage was observed, reaching 44 V, which can be attributed to the decrease in stack resistance due to the increased concentration of both acidic and basic solutions. Halving the current density, in the last two steady-states the voltage reached values of about 35 V to 32 V, for steady-state C and D, respectively. Considering the CE the highest value where registered for steady-state A, with values of 66% and 72% for acid and base, respectively. Reducing the value of chemical flowrates, leads to lower values of 48% and 55% for acid and base, respectively. Considering the steady-states at lower current density, their CE values resulted significantly lower compared to the corresponding value at 400 A m^{-2}. In detail, reductions between 7% and 9 % were observed passing from steady-state A to C, while more pronounced reductions were registered moving from steady-state B to D, in the range 17-33 %, with a higher value for the acid product. Regarding the SEC, shown in Figure 28d, values of 2.3 and 2.8 kWh kg^{-1} were obtained for base and acid in steady state A. In steady state B, an increase in SEC was observed due to the sharp reduction in CE, which decreases more than the external voltage. The lowest values of SEC were obtained in steady-state C, with values of 2.1 and 1.7 kWh kg^{-1} for acid and base, respectively. In steady-state D, values slightly lower compared to those found for steady-state B were observed, despite the significant voltage reduction. The trends of SP can be seen in Figure 28d. The highest values were obtained in steady-state condition A for both chemicals, equal to 0.96 and 1.2 ton y^{-1} m^{-2} for acid and base, respectively. It can be seen that the SP gradually decreased, reaching the minimum values of 0.3 and 0.37 ton y^{-1} m^{-2} in steady-state D for acid and base, respectively.

3.5.1.2. Feeding one chemical compartment with a brine: WSS and SWS schemes

Following the reference scenario, two mirrored schemes were performed, with the saline solution fed first into the base compartment and into the acid compartment, referred

to as WSS and SWS schemes, respectively. The concentration and voltage trends for these two scenarios are shown in Figure 29. The concentration of acid and base reported in this paragraph refers to their protons and hydroxide ions concentration, respectively.

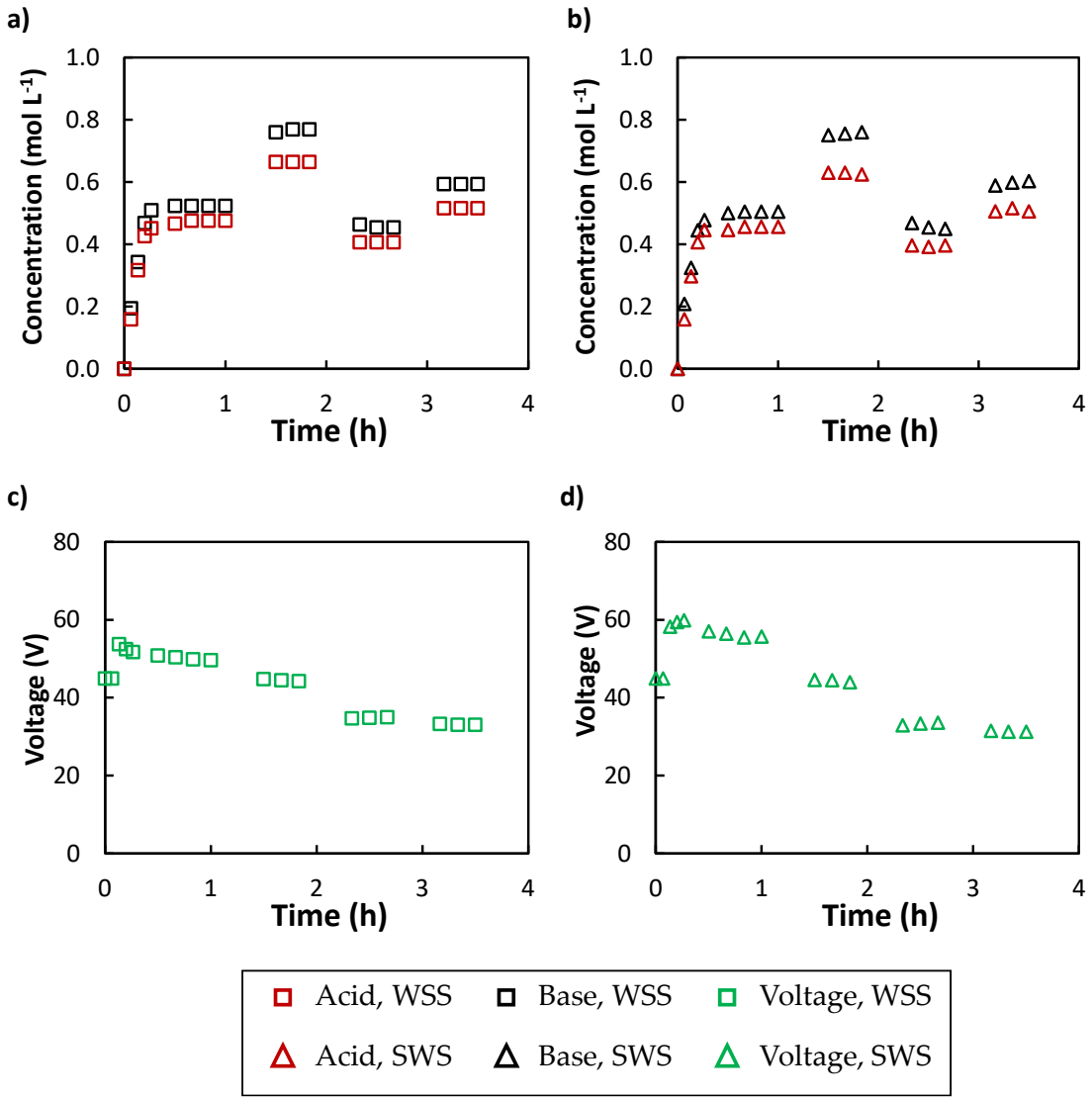

Figure 29. Acid and base concentrations in terms of protons and hydroxide ions concentrations, respectively, for a) WSS scheme and b) SWS scheme; external applied voltage trend for: c) WSS scheme and d) SWS scheme.

As can be seen, concentration and voltage trends are very similar for the two schemes. In the WSS scheme, despite the base channel being fed with the saline solution, concentrations of 0.52 mol L^{-1} for the base and 0.48 mol L^{-1} for the acid product were achieved in steady-state A. Feeding the saline solution into the acid compartment (i.e., SWS scheme), the results remained almost unchanged, with an output concentration of

0.51 mol L^{-1} for the base and concentration of 0.46 mol L^{-1} for the acid. In steady-state B, adopting the WSS scheme, a slightly higher acid concentration of 0.66 mol L^{-1} was achieved compared to the SWS scheme (i.e., 0.63 mol L^{-1}), whilst for the base product similar alkaline concentrations were reached (i.e., approximately 0.75 mol L^{-1}). In the steady-state C, almost the same concentration of acid and base were obtained between the two schemes, with values of 0.41 and 0.47 mol L^{-1} for acid and base, respectively. In steady-state D, reduced concentrations for both chemicals were observed, with concentrations below 0.6 mol L^{-1}.

Considering the external voltage trends of the stack, it can be observed that although both tests started with the same voltage of 45 V, during the initial transient phase, the SWS reached a much higher voltage than the WSS scheme. This higher value of voltage was also registered in steady-state A, with an increase of about 10%. The causes of this increased resistance in the second scenario were not related to the concentrations of acid and base, which, as seen, had very similar values in both scenarios, but rather to the conductivity of the solutions. In fact, the presence of salt in the base compartment (i.e., WSS scheme) helps to maintain a high electrical conductivity of the solutions within the stack, resulting in a reduction of the overall resistance. On the other hand, in the SWS scheme, the conductivity of the basic solution is significantly lower compared to the WSS scheme because the base compartment is fed with low-conductivity water. The presence of the brine in the acid compartments had a lower impact due to the higher conductivity of hydrochloric acid compared to sodium hydroxide (i.e., the electrical conductivity is approximately 2 times larger for the acid at the same molar concentration).

Considering the performance parameters for schemes WSS and SWS, the trends resulted qualitatively similar to the reference scenario (Figure 30). Nevertheless, slight differences

were observed between SWS and WSS schemes due to the different effects of the brine in the acid and base compartments, respectively.

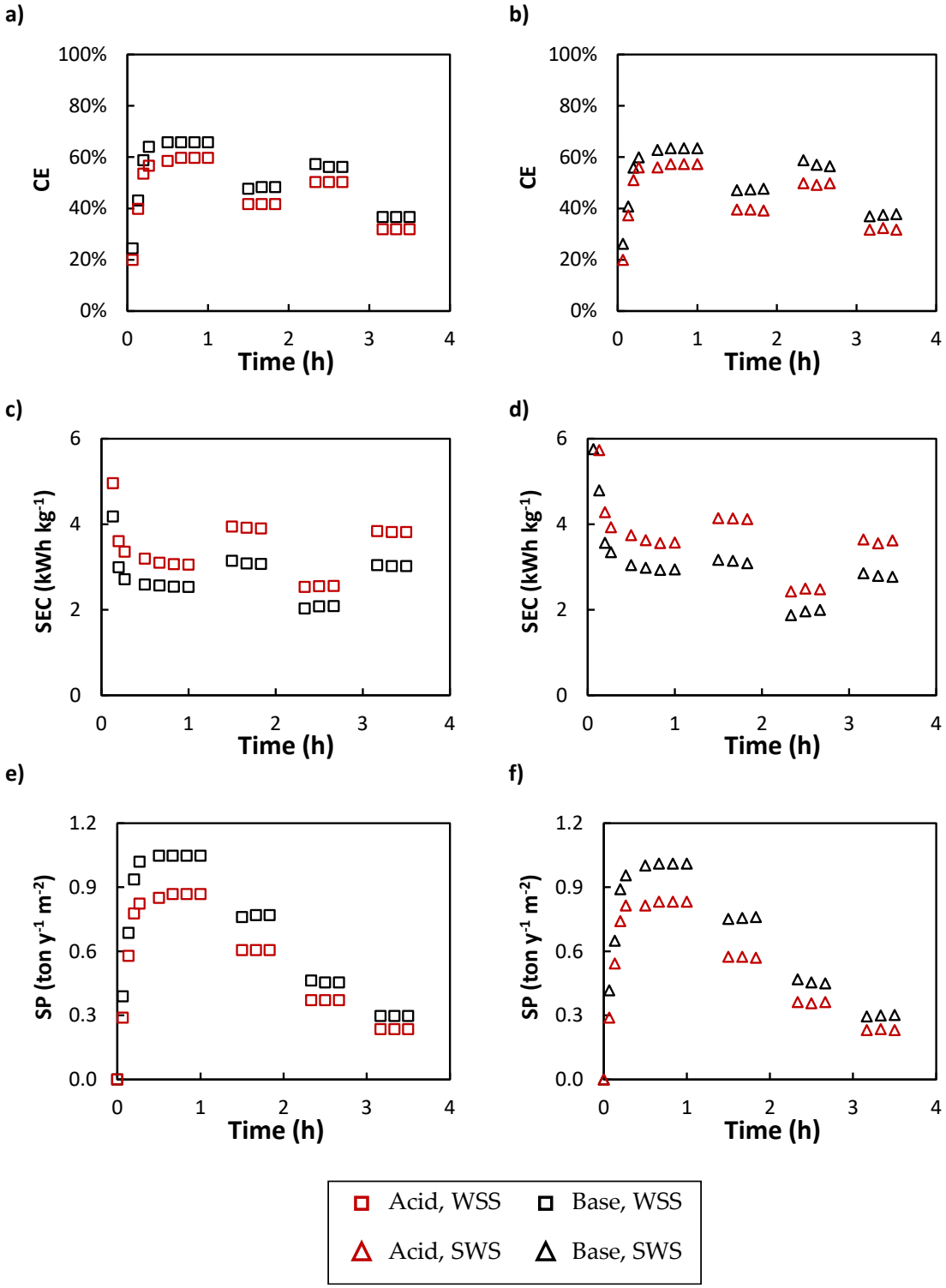

Figure 30. Representative trends of acid and base performance indicators for WSS and SWS schemes: a) current efficiency for WSS, b) current efficiency for SWS, c) specific energy consumption for WSS, d) specific energy consumption for SWS, e) specific productivity for WSS, f) specific productivity for SWS.

In steady-state A, similar CE values were obtained between the WSS and SWS schemes (Figure 30a-b), for both acid and base. Specifically, CE values in the range 63-65 % for the base and 57-60 % for the acid were found. In steady-state B, fairly low CE values (below 50 %) were obtained for both chemicals, with the acid CE dropping down to 40 % in the SWS scheme. In steady-state C, similar values between the two schemes were observed, reaching approximately 60 % for the base and 50 % for the acid. Finally, in steady-state D, CE dropped below 40 % for both products. Moreover, a more pronounced reduction in CE was observed for the base compared to the acid, with respect to steady-state B. This can be attributed to a greater acid-base neutralization effect across the membranes, which leads to a consequent reduction in CE for the base.

The trends of the SEC are shown in Figure 30c-d and, as observed for the CE, very similar values were obtained between the two schemes. However, an increase in SEC was observed in the SWS scheme due to its directly proportional to the external voltage applied to the stack. Maximum values were observed in steady-state B, with SEC values of 4.1 and 3.1 kWh Kg^{-1} for acid and base, respectively.

In terms of SP, almost overlapped values were obtained. Maximum SP values equal to 0.9 ton y^{-1} m^{-2} and 1 ton y^{-1} m^{-2} were observed for acid and base, respectively, in steady state A. Whilst minimum values of 0.2 ton y^{-1} m^{-2} and 0.3 tons y^{-1} m^{-1} were registered in steady-state D for acid and base, respectively.

3.5.1.3. Feeding both chemical compartments with a brine: SSS scheme

This section presents the results of the SSS scheme, in which the brine was fed into acidic, basic, and salt compartments. Figure 31a shows the results of the conducted test. In steady-state A, concentrations lower than 0.5 mol L^{-1} for acid and base were reached. Specifically, a base concentration of 0.45 mol L^{-1} and an acid concentration of 0.41 mol L^{-1} were achieved.

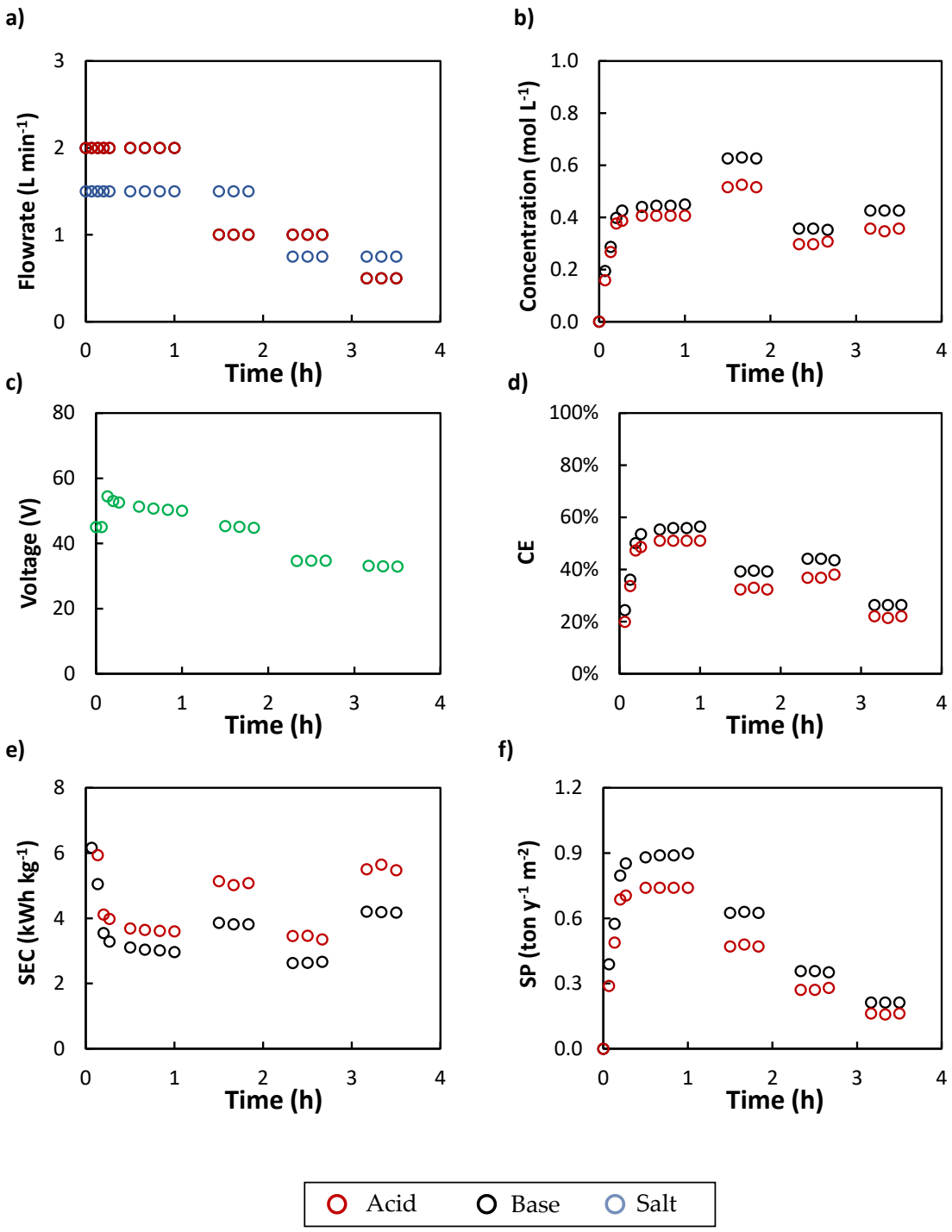

Figure 31. Representative trends of the SSS scheme: a) flowrates; b) concentrations; c) external voltage; d) current efficiency; e) specific energy consumption; f) specific productivity.

In steady-state B, a slight increase in the concentrations was observed, with values of 0.52 and 0.63 mol L^{-1} for acid and base, respectively. In the other two steady states at 200 A m^{-2} (i.e., steady-state C and D), quite low concentration values were observed. In

detail, in steady-state C, values barely above 0.3 mol L^{-1} were reached for both acid and base, while in the last steady-state D values of 0.35 and 0.43 mol L^{-1} for acid and base were found, respectively.

Looking at the external voltage (Figure 31c) at the beginning of the test, the voltage reached values slightly above 50 V, then gradually decreased throughout the test duration, reaching a minimum voltage of 33V in the last steady-state investigated (i.e., steady-state D). The obtained values were comparable with those obtained in the REF scheme, suggesting that the presence of salt did not affect significantly the resistance of the stack, leading to much lower resistance. What was observed, instead, was an almost constant voltage in the transition from one steady-state to another at fixed current density. Although the differences in acid and base concentrations between the steady states, the salt presence mitigates this effect, contributing to a higher conductivity for these compartments.

Considering the performance indicator, it can be observed from Figure 31d that values of CE higher than 60 % were never achieved for both chemicals. In addition, extremely low current efficiency values were obtained in steady-state D, with values of 21 and 26 % for acid and base, respectively. The current efficiency severely affects the specific energy consumption, with values of the latter up to 5.6 kWh kg^{-1}. From Figure 31e, it can be observed that there is a significant difference between the SEC of acid and base in all the steady states investigated. The results highlight how, in this case, the effect of current efficiency prevailed over that of voltage in determining specific consumption. Indeed, while the voltage remained close to 33 V in the steady-states at 200 A m^{-2}, the CE was extremely low, leading to a significant increase in the consumption. The values of SEC in steady-state D resulted higher than the corresponding steady-state at 400 A m^{-2}, for both chemicals, despite the halved current density.

The collapse in the current efficiency also impacted the specific productivity. In steady-state A, SP values lower than 1 ton y^{-1} m^{-2} were reached for both chemicals. The SP these values decreased over the test, reaching a specific productivity of around 0.2 ton y^{-1} m^{-1} for both acid and base in steady state D.

3.5.1.4. Comparison between non-conventional schemes

This paragraph provides a comprehensive comparison of all the innovative schemes evaluated, focusing on the product of greatest interest, sodium hydroxide. Figure 32a presents bar charts showing the concentrations obtained in all the steady-states investigated. A reduction was obtained in the hydroxide ions concentration passing from the reference (REF) feed and bleed configuration to the saline feed schemes. It could be noted that WSS and SWS schemes led to the same concentration values in all the investigated steady-states. This means that the presence of a brine in one of the compartments adjacent to the bipolar membrane leads to the same performance. An increase in the salt-limiting current density is expected due to the transport of salt ions from the chemicals compartment to the interlayer. This effect, in turn, reduces the water-splitting capability of the bipolar membrane [79]. In the SSS scheme, this effect is exacerbated because both the adjacent compartments of the bipolar membrane contain a high salt concentration. Indeed, comparing the different steady-states, more significant concentration reductions (compared to the REF scheme) were observed at low current density (i.e., steady states C and D). Specifically, percentual reductions in the range 16-35 % and 21-43 % were registered in steady-states C and D, respectively. In Figure 32b the current efficiency trend is reported. At fixed steady-state, the CE of the different schemes showed a trend similar to the corresponding base concentration. Indeed, the higher the current efficiency in a scheme, the larger the concentration reached. As expected, the CE decreases as the concentration rises and it was observed both at 200 and

400 A m^{-2}. What is worthy of note is the current efficiency increase observed at higher currents. In fact, comparing steady-states A and C as well as B and D (which are proportion to each other in terms of operating conditions) an increase in the current efficiency was observed for the investigated schemes at higher current densities. This results an interesting characteristic of the feed and bleed configuration that needs further evaluation.

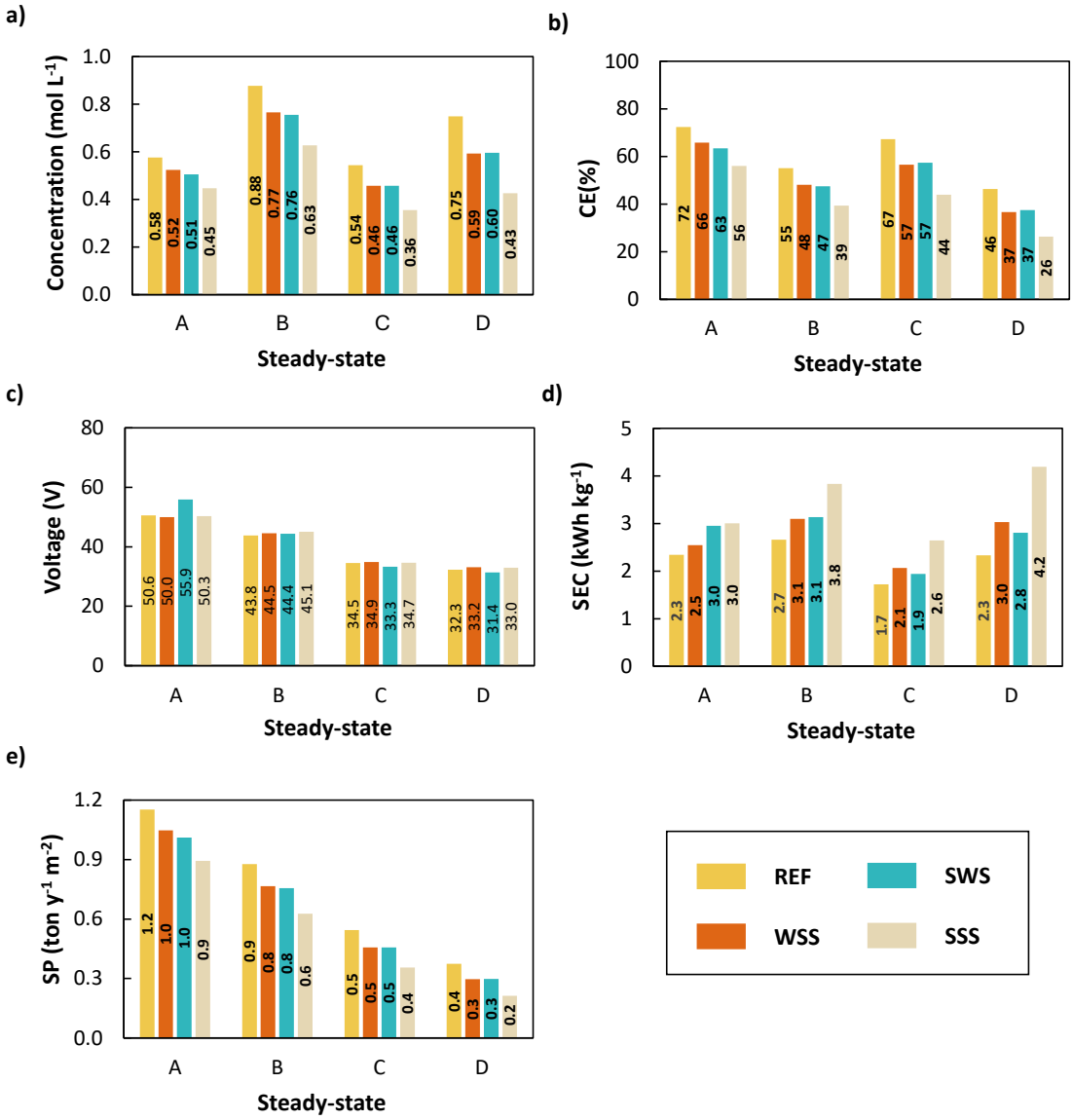

Figure 32. Comparison between the four proposed non-conventional schemes in terms of concentration and KPIs for the base product. Concentration refers to hydroxide ions present in the alkaline product.

Comparing the voltages value between the different schemes, almost constant values were observed. The only exception was the voltage in steady-state A for the SWS scheme, which showed an increase of about 10 % compared to the other schemes. This effect could be related to the lower conductivity of the base compartment due to the absence of salt and to the lower hydroxide ions concentration compared to the REF scheme. The specific energy consumption depends on the CE because the voltage remains almost unchanged. An inversely proportional trend to CE was observed with the lowest values reached in steady-state C. Whilst, the highest values were observed in steady-state B except for SSS scheme, for which a more substantial consumption was registered in steady-state D. In terms of specific productivity, significantly higher values were obtained in steady-state A for all the schemes, with values between 0.9 and 1.2 ton y^{-1} m^{-2}. These results highlight that feeding the acid and base channels with saline solution leads to a gradual decline in performance as well as in the maximum achievable concentration. However, they allowed for the identification of operating conditions where there is no significant drop in performance, which could be considered when implementing innovative layouts for EDBM to reduce water consumption and improve the brine treatment capacity. In this regard, the operating condition identified as preferable, in terms of performance parameters, is steady-state A, confirming what has already been obtained in previous studies.

3.5.2. Without Salt Discharge (WSD) configuration

A novel configuration for improving brine treatment and reducing water consumption is described here: the "Without Salt Discharge" (WSD) configuration. A schematic representation of the WSD configuration is shown in Figure 33. The EDBM unit utilises two streams as inputs: a brine in the salt compartment and water (i.e., RO permeate) in the base channels. Thus, only two inlet tanks are needed. The acid

compartment, instead, is not fed with an inlet stream containing a high salt content, but with the brine exiting from the salt compartment. In this case, the outlet salt flowrate is equal to the inlet acid flowrate. This outlet brine has already been depleted of most of its dissolved salts to produce chemicals. This innovative configuration offers significant advantages over the previous. Although it is similar to the SWS scheme in terms of water consumption reduction, an improvement in the quality of acid product can be obtained due to the reduced salt content. Additionally, recirculating the outlet salt solution within the unit eliminates the need for downstream treatment processes. Finally, this configuration prevents the loss of produced acid that would normally occur during standard operation. Indeed, due to the high mobility of the protons they pass through the AEM reaching the salt compartment. The outlet solution obtained from the salt compartment is here fed to acid one, which positively affects its overall performance, since it already contains protons at the entrance of the acid comportment.

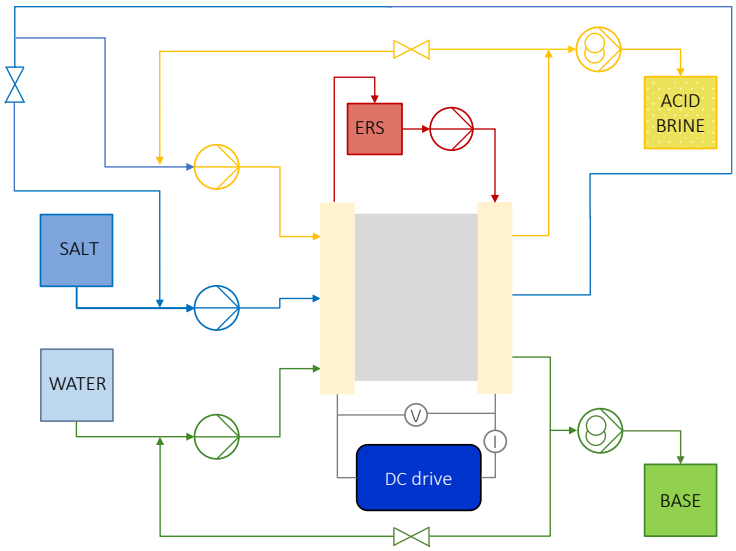

Figure 33. Schematic representation of the Without Salt Discharge (WSD) configuration. The EDBM unit presents two outputs: a base stream with high quality and an acid solution with reduced salt concentration.

The WSD was evaluated by adopting the same steady-state condition utilised for the non-conventional schemes reported in section 3.5.1. Here the value of the acid

flowrate was set equal to the salt flowrate value reported in Table 9, due to their connection. Figure 34 shows the results related to the WSD configuration.

In the first evaluated steady-state (i.e., steady-state A), reached after the system start-up phase, a current density of 400 A m^{-2} as well as an acid (equal to the salt) and base flowrate of 1.5 and 2.0 L min^{-1}, respectively, were used. An acid product concentration of 0.6 mol L^{-1} was achieved, higher than the base concentration, equal to 0.5 mol L^{-1}. Reducing the base flowrate to 1.0 L min^{-1} at fixed current density and acid flowrate (i.e., steady-state B) produced a significant increase in base product concentration, reaching more than 0.9 mol L^{-1}, at an almost fixed acid concentration (i.e., 0.6 mol L^{-1}). In general, lower acid concentrations promote higher base concentrations as the two solutions interact. In the steady-state C, a current density of 200 A m^{-2} as well as an acid and base flowrate of 0.75 and 1 L min^{-1} were employed. The concentrations reached in this case were 0.54 and 0.46 mol L^{-1} for the acid and base, respectively. In steady-state D, only the base flowrate was changed with respect to the third steady-state, to a value of 0.5 L min^{-1}. The acid concentration remained practically unchanged, while the base concentration reached a value of approximately 0.7 mol L^{-1}.

This new layout was tested in two additional steady-states compared to the non-conventional schemes to further evaluate it. Increasing the acid flow rate to 2 L min^{-1}, while maintaining a base flowrate of 1 L min^{-1}, led to an increase in base concentration to 1 mol L^{-1} at a fixed current density of 400 A m^{-2}. The acid concentration was significantly lower than the base concentration, reaching a value of 0.5 mol L^{-1}. The final investigated steady-state involved a further increase in acid flowrate, up to 2.5 L min^{-1}. As in the previous steady state, this increase had positive effects on the base concentration, increasing it by 10% compared to the previous value. This highlights the fundamental role of salt availability in EDBM process thus, the higher salt concentration

in salt chambers leads to improved performance for the chemicals. This, of course, should be balanced with the desired acid product salt content, which depends on the application of the acid brine. Current efficiency values between 45 and 68 % were observed for the base product in the investigated steady-states, while the corresponding SEC values were in the range 1.8-2.4 kWh kg^{-1}, which resulted quite low considering the concentration reached and the current density utilised. Specific productivites up to 1.1 ton y^{-1} m^{-2} were also registered in the last investigated steady-state.

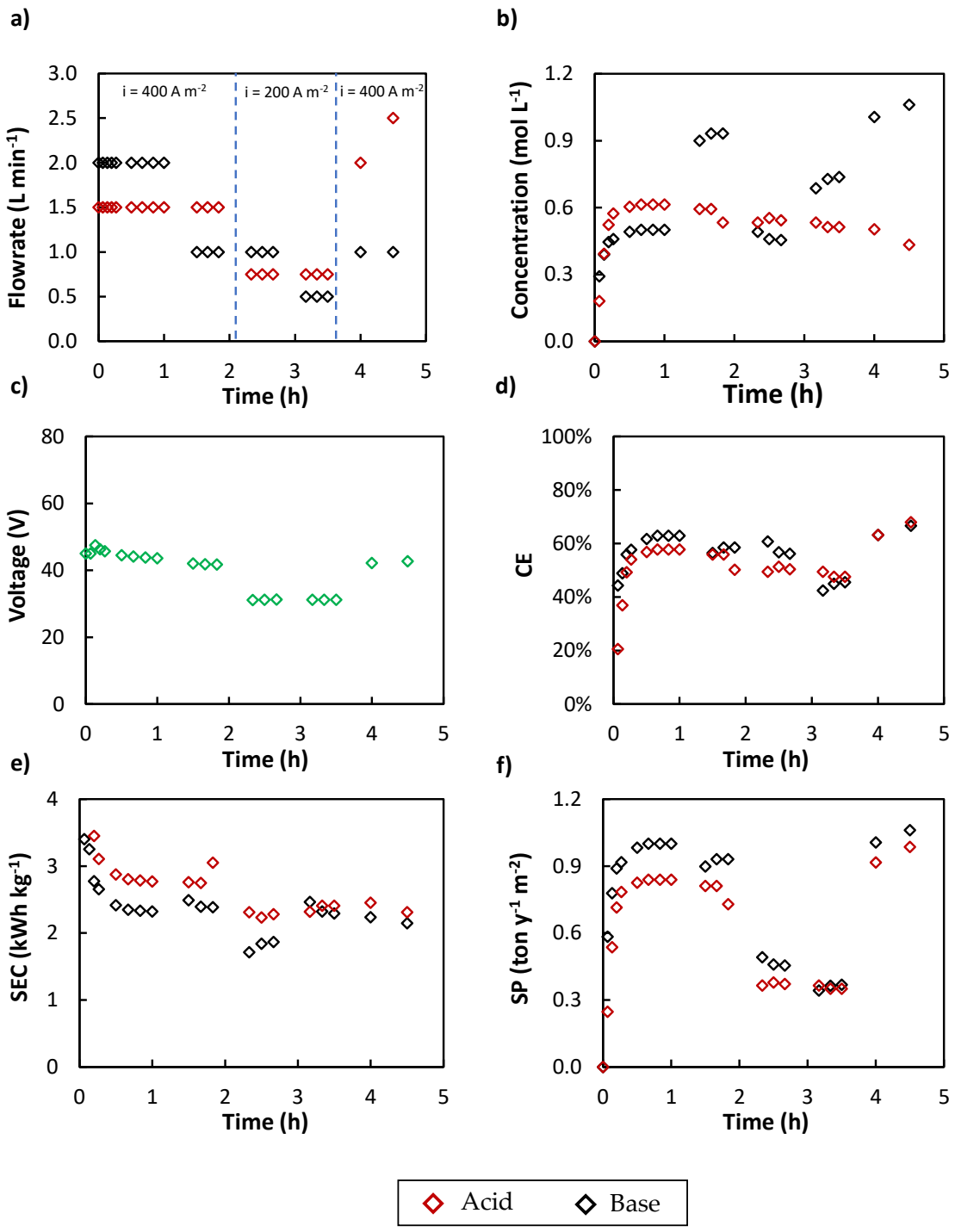

Figure 34. Representative trends of the test conducted with the SWD configuration: a) flowrates; b) concentrations; c) external voltage; d) current efficiency; e) specific energy consumption; f) specific productivity.

Comparing the WSD configuration with non-conventional schemes, a significant performance increase could be observed. Figure 35 shows the performance of the WSD configuration with respect to the corresponding non-conventional scheme (i.e., SWS) and reference scheme (i.e., REF).

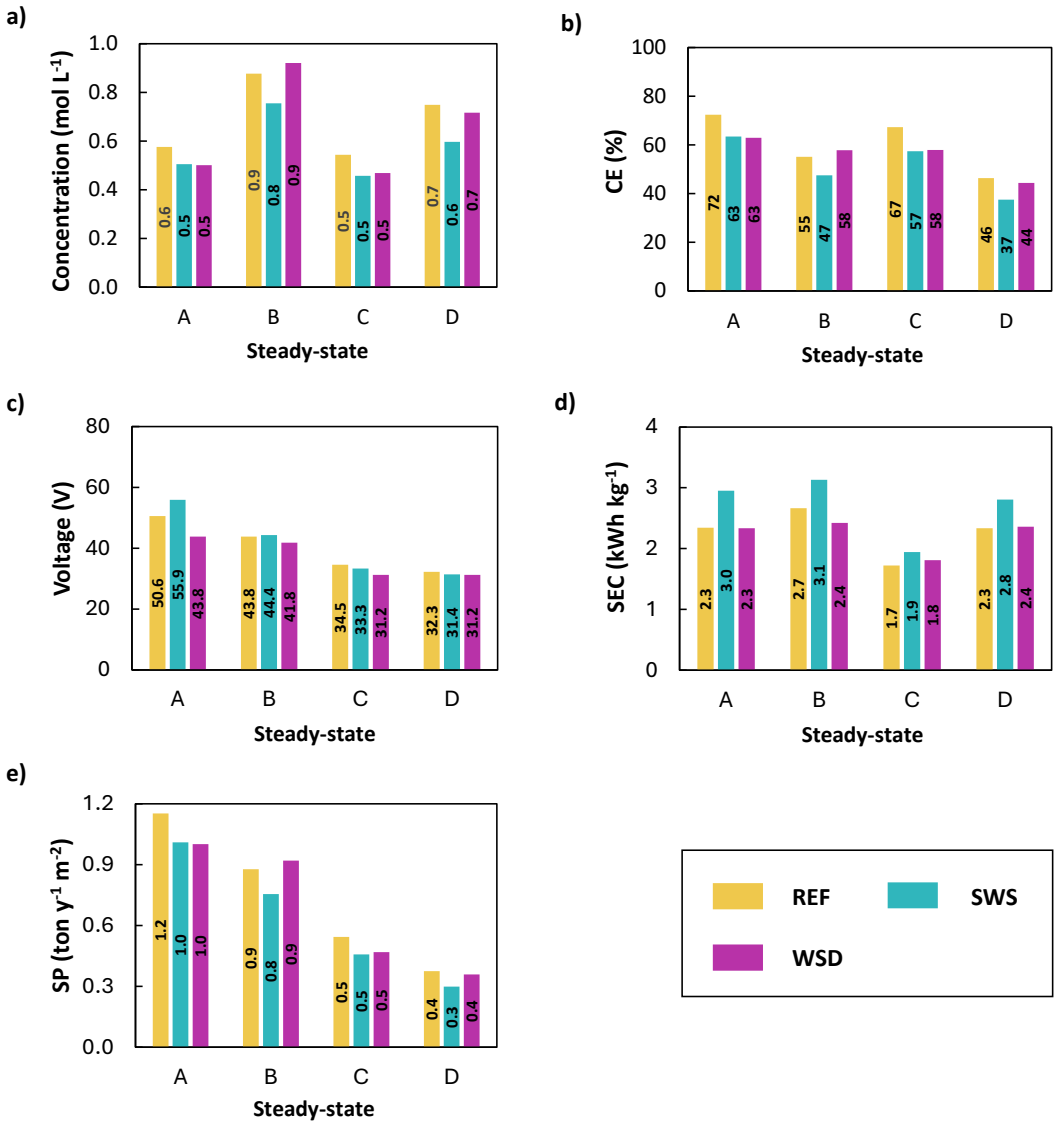

Figure 35. Comparison between the WSD configuration, salt-water-salt (SWS) non-conventional scheme and reference (REF) scheme, in terms of concentration and KPIs for the base product.

For steady-states A and B, which correspond to a lower alkaline product concentration, a similar performance was observed between the WSD configuration and the SWS scheme. The only significant difference was a SEC reduction, related to a voltage decrease in the WSD configuration (Figure 35c). The latter resulted more pronounced at higher current density (i.e. steady-state A), with a reduction of about 20%. This effect could be related to the higher acid concentration reached along with a higher salt solution conductivity due to the direct connection with the acid channels. At higher alkaline product concentrations (i.e., steady-state B and C), the WSD configuration shows

a meaningful performance enhancement, with values of concentration and KPIs perfectly comparable with the REF scheme or slightly better. The reason for this could be attributed to the lower acid concentration in the acid compartment due to the higher acid flowrate, which leads to a reduction of underside diffusive fluxes.

These results proved the attractiveness of this innovative process configuration, which can be employed in circular economy contexts that aim to valorise a brine, reducing the water consumption and reusing on site the acid product, despite its salt content.

3.6 EDBM applications in moder sustainability challenges

This section presents two examples of applying EDBM in moder sustainability challenges. Firstly, the operation of the EDBM pilot plant within the Water Mining treatment chain (see 3.1.1) is described. Here the unit is fed with a real seawater brine, pretreated by upstream units. Risk mitigation approaches adopted to guarantee continuous operation are reported. Moreover, EDBM performance, as operating conditions vary, is evaluated under two control strategies (i.e., flowrate and pressure control). Secondly, the possibility of coupling EDBM with removable energy sources is described. Specifically, a photovoltaic field is used to power the EDBM unit and the process capability to operate under transitory regimes, maintaining constant product concentration, is evaluated in normal day operations (i.e., summer and winter scenarios).

3.6.1. Testing of EDBM within the Water Mining treatment chain

As described in 3.1.1, the EDBM pilot plant is part of an integrated treatment chain realized in the framework of the European Horizon 2020 Water-Ming project [1] and installed on the island of Lampedusa (Italy). Utilising seawater to feed the chain depicted in Figure 7, the resulting composition of the salt solution fed to the EDBM unit is reported in Table 10. A synthetic sodium chloride solution, with the same electrical

conductivity, was also employed to compare the performance of the system with real and artificial solutions.

Table 10. Composition of the real and synthetic brines fed to the EDBM unit.

Brine	Average Salt concentration (mol L^{-1})					Conductivity (mS cm^{-1})
	Na^+	K^+	Cl^-	SO_4^{2-}	OH^-	
Real	0.72 ± 0.03	0.01 ± 0.001	0.52 ± 0.02	0.055 ± 0.004	0.100 ± 0.02*	67±2**
Synthetic	0.75± 0.03		0.75± 0.03			67±2**

*Corresponding to a pH in the range 12.9–13.1.
**Conductivity measured at 20°C

3.6.1.1. Process configuration and risk mitigation strategies

Aiming to evaluate the feasibility of employing the EDBM pilot plant in the treatment chain presented in Figure 7 and to study his behaviour as the operative conditions vary, the unit was tested in a long-run experience of 59 h. The EDBM pilot was operated in feed and bleed configuration (continuous operating mode) for acid, alkaline and saline streams, while the Electrode Rinse Solution (ERS) was operated in a closed-loop fashion. Figure 36 shows the Process Flow Diagram (PFD) of the EDBM plant. The total flowrates entering the stack were controlled by magnetically-driven centrifugal regenerative turbine pumps (PTM 2.5x6, Teorema S.r.l.), while the outlet flowrates from the system were controlled by gear pumps (FG200-300, Teorema S.r.l.) or electrically driven valves depending on the outlet flowrate value (1.2 L min^{-1} is split-range value). For flowrate values lower than then 1.2 L min^{-1} the gear pumps were utilised, whilst for higher values both final control elements were used [97]. Throughout the test, the acid and base compartments were fed with reverse osmosis permeate (~350 μS cm^{-1}). In the ERS compartments, a synthetic solution of sodium sulphate with a concentration of 0.25 mol L^{-1} was adopted. This solution was pumped through the stack with a constant flowrate of 20 L min^{-1} during the whole test.

It is worthy of note how the knowledge gained from previous experimental campaigns, conducted with artificial solutions, was utilized to implement safety strategies for risk prevention that could occur during long-run operations, especially with real solutions. Indeed, risk mitigation in an EDBM pilot plant is a critical aspect to ensure successful and safe operations. The strategy regarded the identification of potential hazards such as membrane fouling, voltage fluctuations, and material degradation.

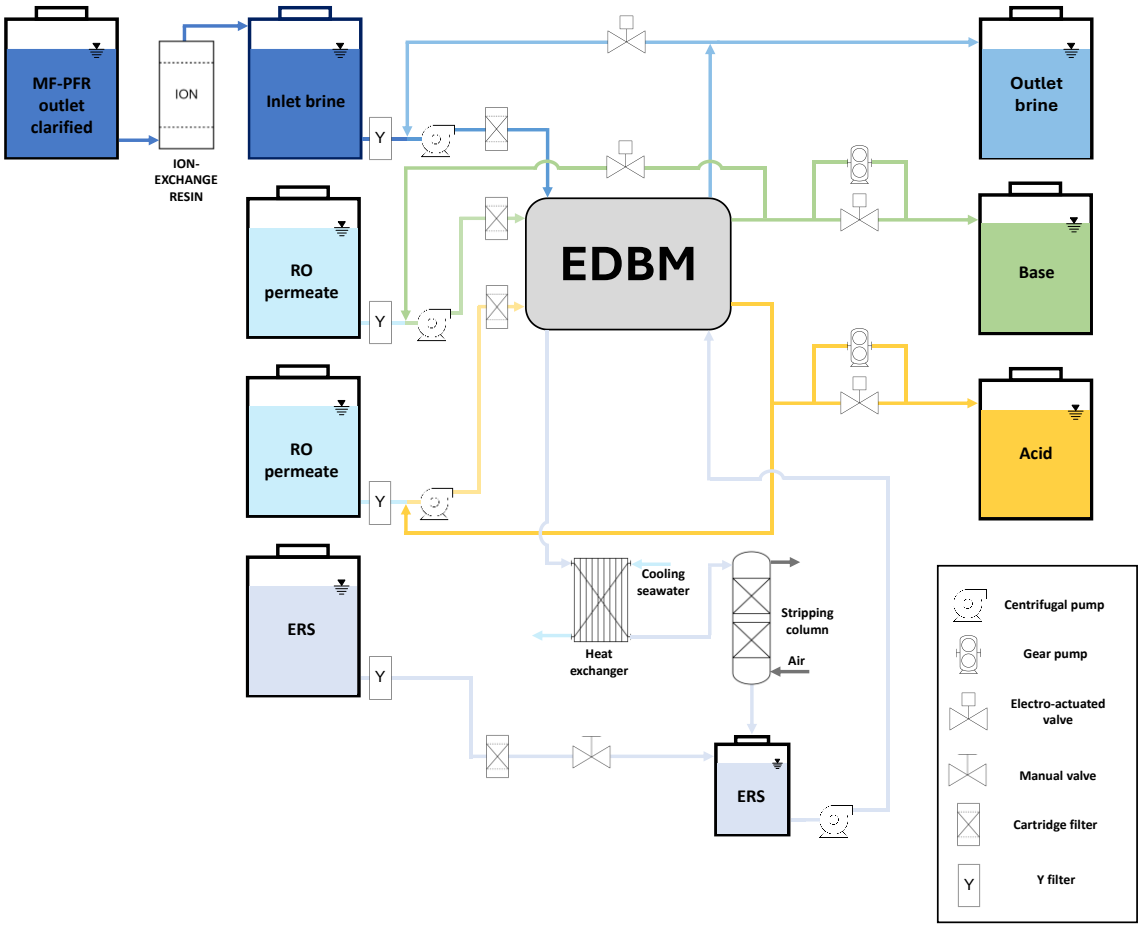

Figure 36. Process Flow Diagram (PFD) of the EDBM pilot plant.

Firstly, ion-exchange resins (IEX), Purolite® C104 Plus, were employed as a pretreatment step to ensure that the content of calcium and magnesium ions was always lower than 10 ppm ($CaCO_3$ equivalent), as suggested by the EDBM stack supplier. In fact, a higher concentration of these species could lead to scaling phenomena via

precipitation of magnesium and calcium hydroxide in the alkaline compartment causing the clogging of the channels and damaging of membranes. Subsequently, to prevent the voltage from reaching high values during transitory phases, a safety switch-off of the plant was introduced in the programmable logic controller (PLC) avoiding the voltage from exceeding 80 V, considered a safety limit. Moreover, the DC drive implements an additional safety measure to improve the electrical safety of the system. Specifically, the applied potential difference is placed between the ground potential (e.g., a voltage difference of 50 V is obtained, utilizing the anode and cathode at values of 25 V and -25V, respectively, with respect to the ground potential), to reduce the maximum absolute operating voltage of the electrodes compared to the ground potential.

To ensure the stability and optimal performance of the pilot system, a distinctive strategy was devised for the electrode rinse compartment. Indeed, a titanium plate heat exchanger, cooled by seawater, was introduced to keep the temperature in the electrochemical compartment lower than 40 °C. This was of primary importance as the temperature of the ERS tends to naturally rise, due to Joule effect dissipations, especially if operated in closed-loop mode. Uncontrolled temperature can lead to thermal degradation of membranes and spacers. Furthermore, the accumulation of small quantities of chloride ions within the ERS could generate chlorine compounds via competitive reactions at the anode surface, which may provoke long-term chemical damage to the stack components. To overcome this problem, a stripping column for the degassing of gaseous compounds, such as hydrogen, oxygen and chlorine, was installed from the ERS (Figure 36). Free chlorine content in the ERS was monitored every 2 h and the solution was replaced either when the concentration of free chlorine reached a value greater than 10 ppm or at least every 6 h. Finally, a 3/4 inch polypropylene y-strainer filter (FIP®

Formatura Iniezione Polimeri S.p.A.) and a cartridge filter with a 1 μm mesh (Atlas Filtri S.r.l.) were installed to retain coarse particles in the pilot circuit.

These integrated measures ensure the longevity and high performance of the EDBM process.

3.6.1.2. Implemented Control strategies

This section describes the two distinct control strategies adopted during the test. The flowrate control strategy is implemented to maintain equal velocities into the channels and is widely adopted in lab-scale applications [98], [99] due to its simplicity of implementation. In this case, a fixed flowrate of 5 L min^{-1} (corresponding to a channel velocity of 2.7 cm s^{-1}) was used for acid, base and salt streams. This control strategy was utilised in the previous experimental campaigns. However, due to inherent differences in pressure losses within the compartments, this results in unequal pressure distribution among the channels. This pressure difference generates convective flows between the compartments [40], which can lead to the neutralization of the produced chemicals, thus reducing the performance of the system.

The pressure control strategy allows to minimise this effect since equal inlet pressures (i.e., equal to 1 barg) are imposed in the acid, base, saline and ERS compartments (all the outlet pressures are atmospheric). This approach requires different recirculation flowrates for acid, base and salt solutions (operated in feed and bleed mode) and, consequently, different velocities within the channels to maintain the same inlet pressure. Instead for the ERS compartment, a lamination valve at the stack inlet is employed to regulate the inlet pressure. These two control strategies were investigated and compared by analysing the system performance under various operating constraints.

3.6.1.3. Test description

During the long-run test, the EDBM pilot plant performance was evaluated under different operating conditions and control strategies, employing both an artificial and a real brine. The operating conditions were varied by either acting on the current density supplied to the stack or changing the outlet flowrate of the acid, base and salt streams. The test lasted 59 h, processing approximately 6 m^3 of real brine and 500 L of synthetic solution. Three step variations in the unit operation were investigated during the test: i) from artificial to real brine, ii) from flowrate control to pressure control strategy and iii) from real to artificial brine. Table 11 summarises the different phases of the test carried out.

Table 11. Overview of the long-run test conducted with the EDBM pilot plant.

Test phase	Solution	Duration (h)	Collected samples	Control strategy
1	A	3.0	5	F
2	R	29.0	23	F
3	R	24.3	17	P
4	A	2.7	3	P
Total		59.0	48	

A = artificial brine, R = real brine, F = flowrate control mode, P = pressure control mode

Most of the test was conducted employing the real brine in order to demonstrate the stability of the system in a real operational environment. The different operating conditions are codified and summarized in Table 12. The code comes from the acid, base and salt outlet flowrates as well as the current density adopted.

Table 12. Different sets of operating conditions tested with the EDBM pilot plant.

Operating condition code	Solution	Outlet flowrate (L min^{-1})			Current density (A m^{-2})	Control strategy
		Acid	Base	Salt		
1–0.7–1.8–400*	A	1	0.7	1.8	400	F/P
1–0.7–1.8–400*	R	1	0.7	1.8	400	F
1–0.8–1.8–400*	R	1	0.8	1.8	400	F/P
1–0.8–2.3–400	R	1	0.8	2.3	400	F
1–0.8–1.8–200	R	1	0.8	1.8	200	F
1–0.8–0.9–200	R	1	0.8	0.9	200	F
2–1.6–1.8–400	R	2	1.6	1.8	400	F
2–1.6–2.3–400	R	2	1.6	2.3	400	F
1.4–1.1–1.8–400	R	1.4	1.1	1.8	400	P
1.4–1.1–2.3–400	R	1.4	1.1	2.3	400	P
1.4–1.1–1.8–200	R	1.4	1.1	1.8	200	P
1.2–1–1.8–400	R	1.2	1	1.8	400	P
1.5–1.1–1.8–400	R	1.5	1.1	1.8	400	P
1.5–1.1–2.3–400	R	1.5	1.1	2.3	400	P

A = artificial brine, R = real brine, F = flowrate control mode, P = pressure control mode.
*both flowrate and differential pressure control strategies were investigated.

3.6.1.4. Flowrate control strategy results

The EDBM pilot was operated under flowrate control strategy for the first 32 hours, employing both artificial and real brines. For this control strategy, the performance achieved with the two brines was compared. Moreover, several steady-state conditions were evaluated employing the real brine, by letting both the current density and solutions outlet flowrates to vary. In this way, the system behaviour was assessed in a wide range of operating conditions.

3.6.1.4.1. Comparison between artificial and real solutions

The comparison between artificial and real multi-ionic brines was made for a given conductivity (~ 67 mS cm^{-1} at 20 °C) of the inlet salt solutions to the EDBM unit. The operating conditions were maintained constant, keeping an outlet flowrate of acid, base and salt equal to 1.0, 0.70 and 1.8 L min^{-1}, respectively, and applying a fixed current density of 400 A m^{-2} (code 1–0.7–1.8–400).

In Figure 37, the comparison is shown in terms of KPIs, outlet concentration and measured external voltage for both acid and base products. The main differences in the transition from synthetic to real brine lie in an increase in the external voltage U_{ex} and, consequently, in the specific energy consumption for both chemicals. For the alkaline product, an increase of 3 % was observed in the current efficiency, specific productivity, and concentration, with values of 49 % of CE, 0.8 ton y^{-1} m^{-2} of SP and 1.1 mol L^{-1} of concentration, respectively. Regarding the SEC, an increase from 3.5 kWh kg^{-1} to 4.0 kWh kg^{-1} was noted for the base product. For the acid, conversely, a reduction of about 10 % in CE, SP and concentration was measured, with values of 35 % of CE, 0.52 ton y^{-1} m^{-2} of SP and 0.56 mol L^{-1} of concentration, respectively. Also in this case, the SEC showed an increase passing from 4.7 kWh kg^{-1} to 6.2 kWh kg^{-1}, moving from artificial to real brine.

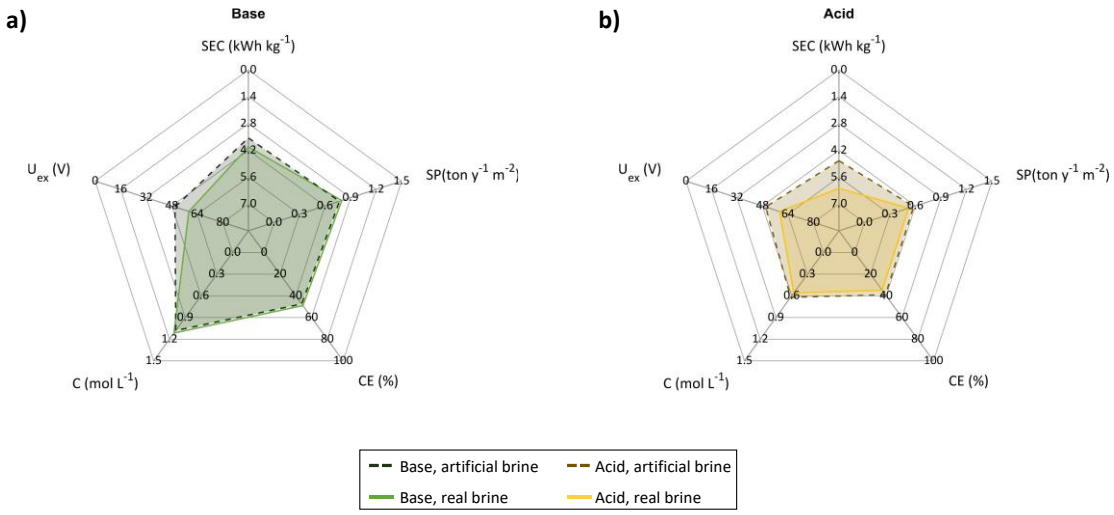

Figure 37. Spider-plots highlighting the main differences in EDBM performance when an artificial and a real salt solution are adopted, under flowrate control mode. KPIs, concentration and measured external voltage are shown for both produced chemicals. Operating condition 1–0.7–1.8–400 (i.e., acid flowrate–base flowrate–salt flowrate–current density) was used. The comparison was made at equal conductivity of the inlet salt solutions (~ 67 mS cm^{-1} at 20 °C).

The utilisation of the real brine had a beneficial effect on the alkaline product, for which the performance parameters such as CE and SP as well as the outlet concentration increased. Conversely, the SEC was mainly affected by the voltage and an increase was also observed. In general, the performance improvement could be attributed to the presence of hydroxide ions in the brine (pH of around 13). Looking at the acid product, the use of the real salt solution led to a performance reduction. Indeed, the acid channel received hydroxide ions that neutralized the produced acid, leading to a concentration reduction. This undesired effect can be tolerated since the alkaline product represents the most valuable chemical. In Figure 38a, the pH of the inlet and outlet salt solution are shown as a function of time, straddling the transition from artificial to real salt solution. All the illustrated points represent samples collected in steady-state conditions. It could be observed that the salt compartment reduced his pH in both cases, compared to the inlet pH value. When an artificial solution was employed, the pH of the salt stream went from an almost neutral pH to a value close to 2. Conversely, when the real brine was adopted, the pH decreased from 13 to 9. The acidification of the salt solution is in general an

undesired phenomenon, but in this case, it has a double beneficial effect: i) it improves the performance indicator (i.e., CE and SP) and the concentration of the base streams; ii) it reduces the outlet salt stream pH to a value closer to the neutrality so that it can be sent to the downstream processes (evaporative pounds) without any further treatment (i.e., pH correction), Figure 38b. On the other side, the increase in external voltage can be attributed to the smaller salt content of the real brine. Indeed, the comparison was made keeping the conductivity of the inlet salt stream constant, but different values of outlet conductivity were reached. This is related to the lower salt content of the real brine, which passed through the same stack, at fixed operating conditions, led to a lower outlet conductivity of the real brine. This reduction in the outlet salt concentration, produced an increase in the external voltage, as already observed in a previous work [90].

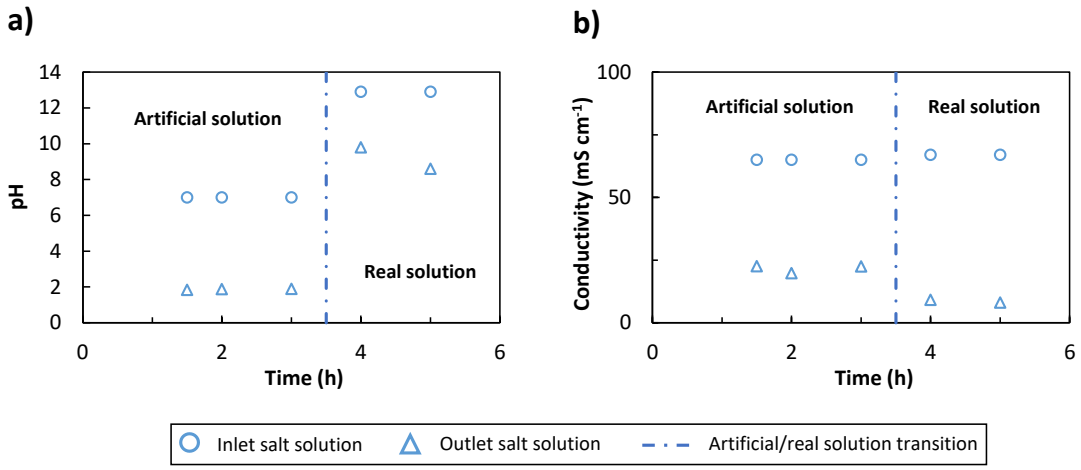

Figure 38. pH and conductivity trends for inlet and outlet salt solutions. The vertical dash-dotted line represents the transition from real to artificial solution. Operating condition 1–0.7–1.8–400 (i.e., acid flowrate–base flowrate–salt flowrate–current density) and a flowrate control mode were used.

3.6.1.4.2. Comparison between different sets of operating conditions

Following the comparison between real and artificial solutions, the flowrate control strategy was further studied evaluating different sets of operative conditions to assess the behaviour of the system when a real brine is employed. The comparison of these scenarios is reported in Figure 39.

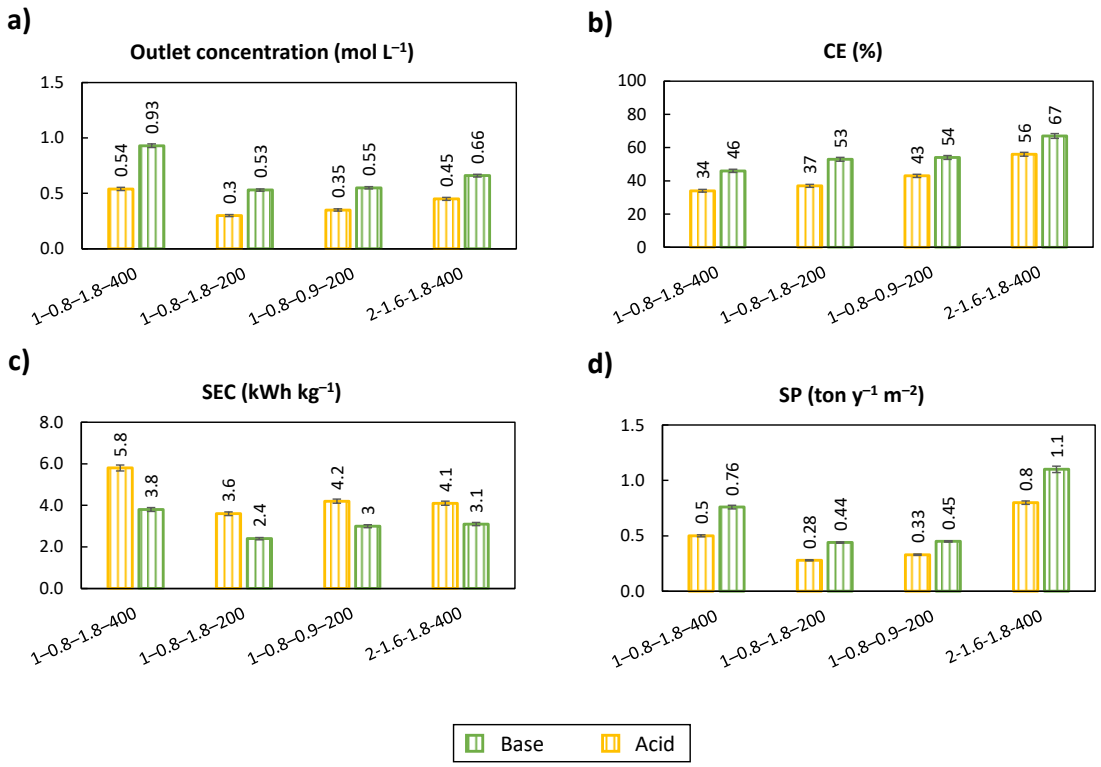

Figure 39. Values of chemical concentrations and key performance parameters recorded in the four different operating conditions under flowrate control mode, employing the real salt solution. The operating conditions are reported with the following coding: acid flowrate (L min^{-1}) – base flowrate (L min^{-1}) – salt flowrate (L min^{-1}) – current density (A m^{-2}).

In the first evaluated set of operating conditions, acid, base, and salt outlet flowrate of 1, 0.8, and 1.8 L min^{-1}, respectively were used, and a current density of 400 A m^{-2} was applied to the EDBM stack (i.e., operating condition 1–0.8–1.8–400). Under these operating conditions, values of concentration of 0.54 mol L^{-1} and 0.93 mol L^{-1} for acid and base, respectively were obtained, (Figure 39a). The corresponding current efficiency resulted quite low, and the SEC reached a value of 5.8 kWh kg^{-1} and 3.8 kWh kg^{-1} for acid and base, respectively. In the second condition, halving the current density (i.e., 1–0.8–1.8–200), lower concentrations were obtained (0.3 mol L^{-1} and 0.53 mol L^{-1} for acid and base, respectively). This resulted in an improvement of the system performance in terms of SEC and CE, with values for the alkaline product of 2.4 kWh kg^{-1} and 53%, respectively. Conversely, a significant reduction in the SP was observed

due to his proportionality to the current density and current efficiency, with values of 0.28 ton y^{-1} m^{-2} and 0.44 ton y^{-1} m^{-2} for acid and base, respectively. In the third operating condition, reducing by half also the outlet salt flowrate (i.e., 1–0.8–0.9–200) an increase of the acid concentration was observed, while the base concentration remained unchanged compared to the second case. The concentration increase in the acid line might be attributed to a passage of hydroxide ions from the salt to the acid chamber, being reduced by the lower salt flowrate. In the fourth case, doubling all the flowrates and the current density (i.e., 2–1.6–1.8–400) produced an increase of chemicals concentration to values of 0.45 mol L^{-1} and 0.66 mol L^{-1} for acid and base, respectively. Interestingly, the obtained concentration resulted significantly lower compared to the first scenario (i.e., 1–0.8–1.8–400), leading to higher performance, with values of CE between 54 % and 67 % as well as value of SP 0.8 ton y^{-1} m^{-2} and 1.1 ton y^{-1} m^{-2}, for acid and base, respectively. These results confirmed that the feed and bleed configuration shows better performance once the current density is increased and the outlet chemical concentrations are reduced, as reported also in [57], [92].

Lastly, the effect of increasing salt/acid and salt/base outlet flowrate ratio was investigated at high current density (i.e., 400 Am^{-2}). Specifically, starting from operating condition 2–1.6–1.8–400, the outlet salt flowrate was increased by 0.5 L min^{-1} (i.e., up to 2.3 L min^{-1}) and its effect on chemicals concentration and KPIs was evaluated. These results are in Figure 40, and show how outlet acid and base concentration result almost unchanged, while a significant reduction in the SEC (by 20%) was recorded. This effect was related to the higher outlet salt conductivity, which passed from 5 mS cm^{-1} to 17 mS cm^{-1}, leading to a voltage reduction from 62.5 V to 53 V.

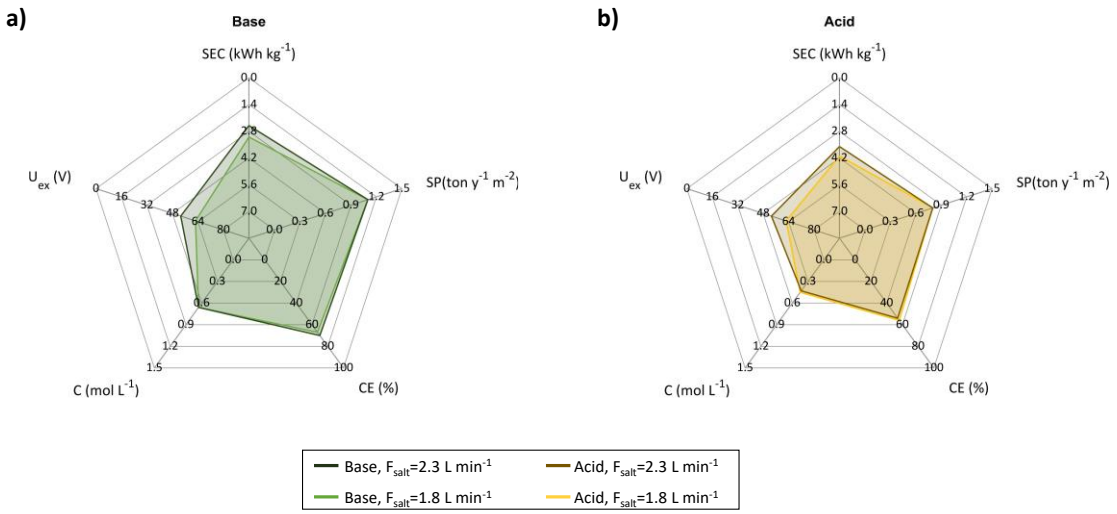

Figure 40. Effect of the outlet salt flowrate increase (+ 0.5 L min^{-1}) at high current density. Results are obtained employing the real salt solution and the flowrate control strategy.

3.6.1.5. Pressure control strategy results

The EDBM pilot was operated by adopting the pressure control strategy for 27 hours, testing both artificial and real brines. Several operating conditions were evaluated employing the real brine, to investigate the performance of the system in a wide range of operating conditions. In addition, a comparison between the two control strategies was made at fixed operating conditions, using the real salt solution. Finally, artificial and real solutions were compared under similar operating conditions.

3.6.1.5.1. Comparison between different sets of operating conditions

Several scenarios were investigated under pressure control strategy by letting operating conditions to vary. The same values of current density (i.e., 400 A m^{-2} and 200 A m^{-2}) and salt outlet flowrate (i.e., 1.8 L min^{-1} and 2.3 L min^{-1}) as in the flowrate control case were evaluated. On the other hand, higher values of acid and base outlet flowrates were considered in order to compare the system performance under similar values of outlet chemicals concentration (due to the better performance achieved). The comparison between different sets of operating conditions in terms of outlet concentration and KPIs

is presented in Figure 41. In the first evaluated set of operating conditions (code 1.4–1.1–1.8–400) values of concentration of 0.65 mol L^{-1} and 1.03 mol L^{-1} for acid and base, respectively were obtained. Improved performance indicators were obtained, with values of 71% % of CE, 1.2 ton y^{-1} m^{-2} of SP, and 2.6 kWh kg^{-1} of SEC for the alkaline product. Comparing sets of operating conditions 1.4–1.1–1.8–400 and 1.4–1.1–1.8–200, a reduction in concentration, SEC and SP in the range 40–43 % was observed for both products in the second case. Whilst, an improvement in the CE of about 18 % was registered for acid and base. Interestingly, for the base stream absolute values of 84 % of CE, 1.5 kWh kg^{-1} of SEC were obtained at 0.62 mol L^{-1} of concentration. This performance appears promising, considering the size of the unit (i.e., semi-industrial scale) and the employment of a real brine with a reduced salt content (Table 10). Decreasing the flowrate of both chemicals (i.e., 1.2–1–1.8–400) produced an increase in concentration to values of 0.77 mol L^{-1} and 1.1 mol L^{-1} for acid and base, respectively. Interestingly, the SEC showed a reduction of 8–19 % for both chemicals. This effect was mainly related to the voltage reduction which was, in turn, produced by the conductivity increase in the outlet brine (i.e., lower conversion of salt). Increasing the outlet flowrate of the acid stream of 0.1 L min^{-1} (i.e., operating condition 1.5–1.1–1.8–400) compared to operating condition 1.4–1.1–1.8–400, allowed to study the potential interaction between products. Specifically, it was possible to see whether a reduction in outlet acid concentration can have a positive effect on the base product (i.e., the pH gradient between the compartments is reduced). However, no improvements were observed for the base product, suggesting that diffusive processes did not have a high impact.

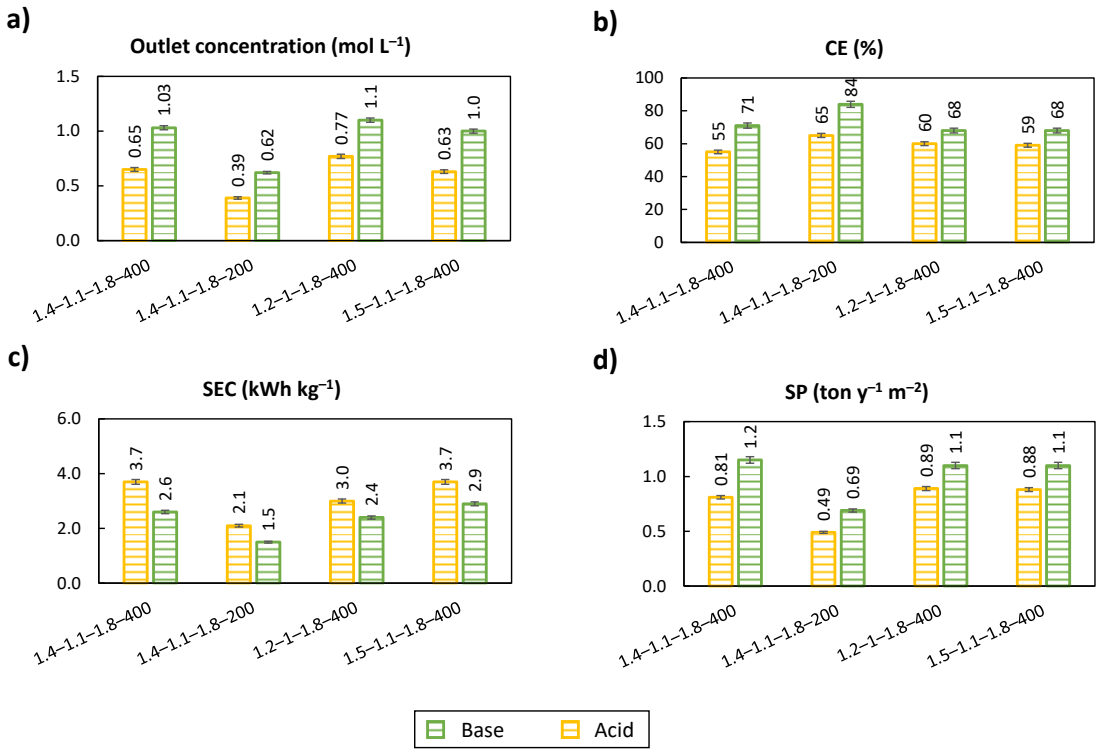

Figure 41. Concentration and KPIs as a function of different operating conditions under pressure control mode, employing a real salt solution. In the X axis the operating conditions of the EDBM unit are reported in the following form: acid flowrate (L min^{-1}) – base flowrate (L min^{-1}) – salt flowrate (L min^{-1}) – current density (A m^{-2}).

Furthermore, also for this control strategy the effect of increasing the outlet flowrate of the salt streams of + 0.5 L min^{-1} was evaluated in terms of outlet concentration and KPIs are reported in Figure 42. An increase in the performance was observed, especially for the base streams. The most meaningful effect was the SEC reduction (5–24 %) due to the higher conductivity of the outlet salt stream. These results suggested that the higher availability of the real brine had a beneficial effect on EDBM performance of the base product, while maintaining similar KPIs and almost constant concentration for the acid one.

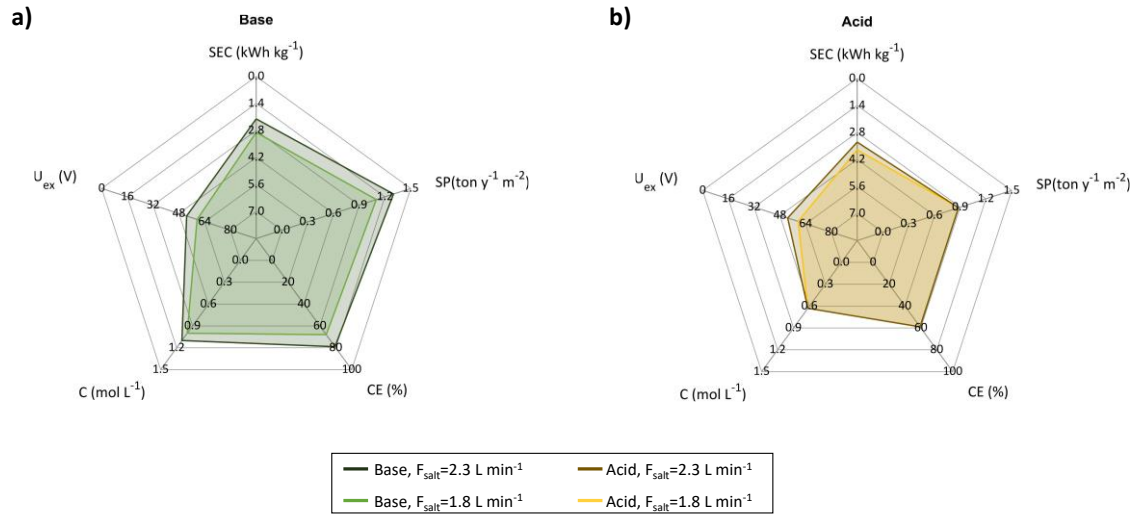

Figure 42. Effect of the outlet salt flowrate increase (+ 0.5 L min^{-1}) in performance indicators, voltage and concentration of both products, under pressure control strategy. Acid and base flowrates as well as current density were maintained constant and equal to 1.5 L min^{-1}, 1.1 L min^{-1} and 400 A m^{-2}, respectively.

3.6.1.6. Comparison between flowrate and pressure control strategies

Following the observation of better performance under pressure control strategy, a quantitative analysis is here reported. The same operating condition was evaluated utilizing the real brine. In Figure 43, the comparison between the control strategies is presented in terms of outlet concentration and KPIs. A significant performance improvement was observed moving from flowrate to pressure control. More in detail, improvements in outlet concentration and KPIs in the range 32–43 % were observed, for both acid and base products. For the base stream, a CE of 63 % and a SEC of 2.6 kWh kg^{-1} were obtained at a concentration of 1.3 mol L^{-1} under pressure control. This significant improvement in the performance was mainly related to the reduction of convective fluxes through the membranes between adjacent compartments, generated from the different pressure distributions. Although, the same geometry of the compartments (i.e., acid, base and salt) and the same volume flowrates were used, during several hours of operations meaningful differences in the pressure losses can be found. This effect is allegedly generated by deformation processes for membranes and spacers

and possible fouling phenomena. Indeed, inlet pressures of the compartment were monitored under flowrate control strategy and average values of 1.0 barg, 1.5 barg and 1.1 barg for acid, base and salt, respectively, were found during the test under flowrate control strategy.

In terms of purity, acid product quality improved significantly, passing from a cationic purity of 50% to 85%. Instead, the anionic purity of the acid product remained quite high passing from 95% to 90 % (from 90% to 80% in terms of speciation). Almost constant purities were observed for alkaline products in both control modes, with values higher than 95% for both cationic and anionic purity.

Employing the pressure control strategy allowed this undesired effect to be tackled, thus guaranteeing high performance of the EDBM.

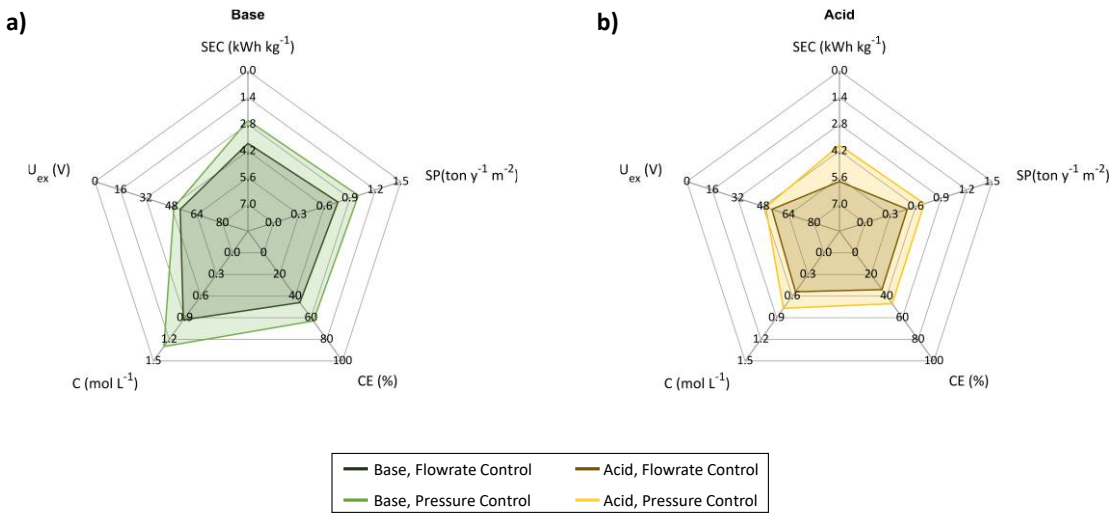

Figure 43. Comparison in terms of KPIs, concentration and external voltage between flowrate and pressure control strategies at fixed operating condition (i.e., 1–0.8–1.8–400), employing the real brine.

3.6.1.7. Comparison between artificial and real solutions

The effect of utilising artificial and real brine was also evaluated for the pressure control strategy and the results are shown in Figure 44. For the alkaline product, an improvement of all the KPIs was observed at a constant concentration of 1.3 mol L^{-1},

reaching values of 2.6 kWh kg^{-1}, 63 % and 1 ton y^{-1} m^{-2} for SEC, CE and SP, respectively, in the case of real brine. On the other hand, the acid product was negatively affected by the pH of the real brine, leading to a slight reduction in concentration and KPIs, with variation in the range of 6-10 %. These results differ from what was obtained under flowrate control strategy, where the major effect was an increase in the voltage passing to from artificial to real solution. Under pressure control mode, the voltage remained unchanged due to the outlet brine conductivity which was higher than 15 mS^{-1}.

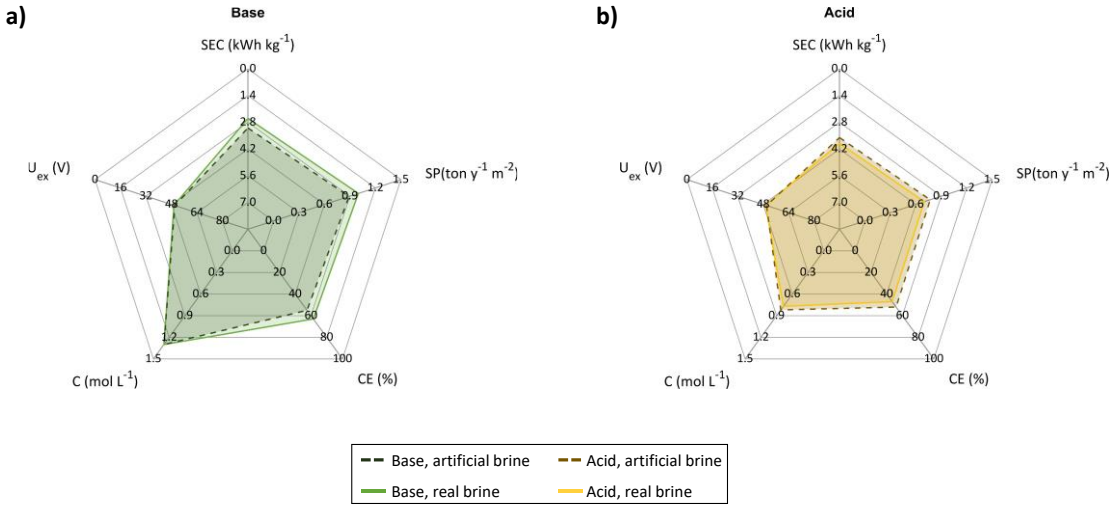

Figure 44. Comparison in terms of KPIs, concentration and external voltage between artificial (i.e., 1–0.7–1.8–400) and real brine (i.e., 1–0.8–1.8–400), under pressure control mode.

3.6.1.8. Ion transport analysis

To further assess the pilot operation with the real salt solution, an analysis of ions transport across membranes was conducted. Transport numbers and selectivity of each ion in IEMs were calculated from concentrations and flowrates of inlet and outlet streams (see section 2.5.2). This analysis is here reported only for phase 3 of the test, in which the pressure control strategy and real brine were used. Indeed, convective fluxes observed under flowrate control mode (phases 1 and 2 of the test), related to the internal passage of solution from one compartment to the adjacent ones through the membranes, would

dramatically reduce the reliability of present results. The results of the analysis are depicted in Figure 45.

For anion exchange membrane (AEM) similar values of transport number were observed for Cl^- and H^+, ranging at 400 A m^{-2} from 0.36 to 0.5, depending on the operating conditions. It should be noted that the transport of these ions takes place in opposite directions: Cl^- ions move from the salt to the acid compartment while H^+ ions go from the acid to the salt compartment. Therefore, a considerable quantity of protons was lost in the salt channel, thus reducing the CE of the acid product. When the current density was halved, the transport number of protons was reduced, reaching a value of 0.3, while the one of Cl^- increased to 0.55. This effect was mainly due to protons generation reduction in the BPM, which led to a lower concentration of protons in the acid chamber. The other ions (i.e, Na^+, K^+ and SO_4^{2-}) exhibited very low transport numbers with values lower than 0.1. This was expected due to their ion charge, in the case of cations, and the reduced concentration of SO_4^{2-} [78]. Looking at the selectivity of the AEM, which employed Cl^- as a reference ion, a value around 1 was obtained also for the SO_4^{2-} (thus indicating a similar selectivity of the AEM to Cl^- and SO_4^{2-}), whilst a reduced selectivity, lower than 0.2, was found for the cations.

Analysing the CEM behaviour, high values of Na^+ transport number in range 0.6–0.8 were observed. Hydroxide ions showed a transport number close to 0.3 at 400 Am^{-2} and it was almost halved at 200 A m^{-2}. This was confirmed by higher values of CE found at 200 A m^{-2} (i.e., 84%). For the other ions (i.e., Cl^-, SO_4^{2-}, K^+), values lower than 0.05 were observed. Regarding the selectivity of the CEM, similar values were observed between Na^+ and K^+, while for other ions it appeared negligible being lower than 0.1.

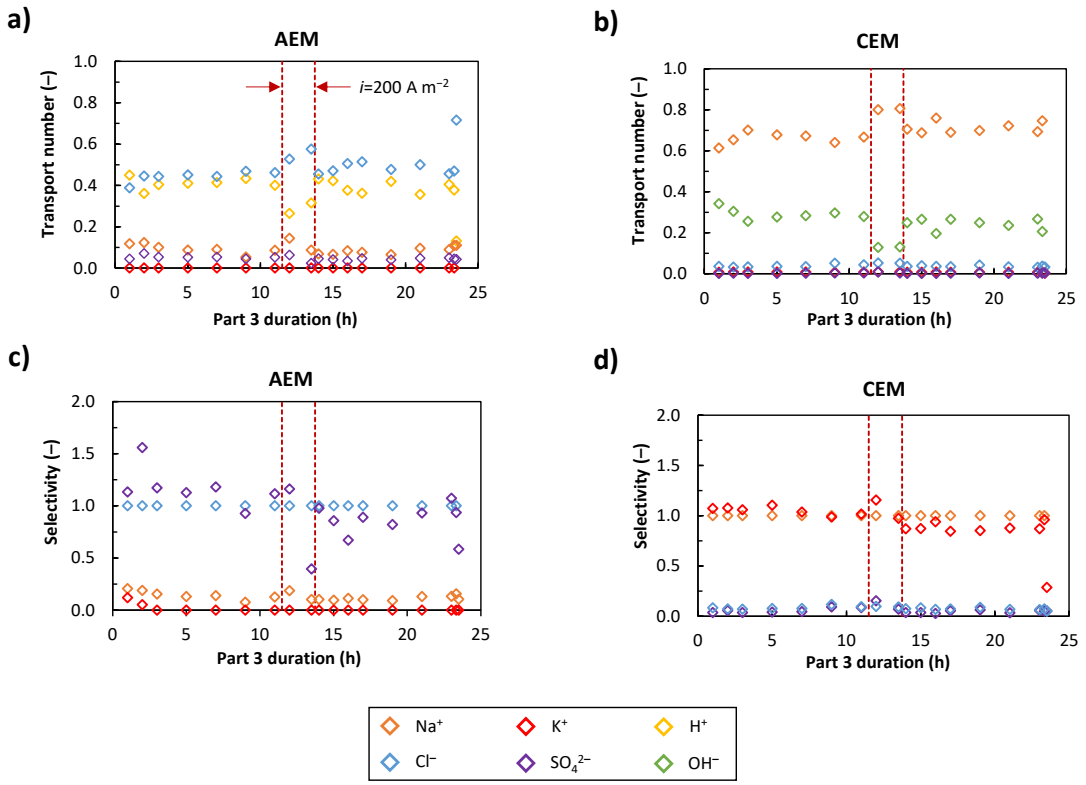

Figure 45. Transport numbers and selectivity profiles versus time under pressure control strategy and employing a real brine. Red dashed lines delimit the region in which the current density was halved from the initial value of 200 A m^{-2}, to the final one of 200 A m^{-2}. AEM= anion exchange membrane, CEM= cation exchange membrane.

3.6.2. Coupling EDBM with renewable energy sources

The electrodialysis with bipolar membranes process can benefit from coupling with renewable energy sources due to its high energy consumption and wide flexibility in working under transitory regimes. This is demonstrated by coupling the EDBM pilot plant, described in 3.1, with photovoltaic (PV-EDBM). The pilot plant was tested in a continuous process configuration (feed and bleed mode) under two different irradiation scenarios, i.e. summer and winter. In order to operate under transitory regimes, the EDBM pilot plant requires appropriate control systems to maintain the desired product quality. To this aim, advanced control systems were developed and tested firstly through Matlab's dynamic simulation toolbox (Simulink). Subsequently, the controllers were implemented in LabVIEW software and tested in the real plant mimicking a PV field. The objective of

the control system was to allow continuous operation of the equipment in highly transitory regimes, to maintain the desired concentration for both, acid and base. The results described in this section were published in a scientific article *Coupling electrodialysis with bipolar membranes with renewable energies through advanced control strategies* [97].

3.6.2.1. Uncontrolled system characterisation

The analysis of the transient behaviour of the uncontrolled system was conducted to determine its dynamic features. An extensive experimental campaign was conducted to cover the entire operating range of the EDBM stack which exhibited a non-linear behaviour. All the tests were performed by feeding 1 mol L^{-1} of sodium chloride solution in the salt compartment and RO permeate (~350 μS cm^{-1}) in the acidic and alkaline compartments. Table 13 summarises the dynamic tests performed.

Table 13. Summary of the main dynamic tests performed with the pilot scale EDBM unit.

Test	Inlet variable	Step size	Outlet variable	Purpose
1	Voltage of the inlet pump	±25% ±50%	Inlet flowrate	Design of the inlet flowrate control
2	Voltage of the inlet pump	±25% ±50%	Inlet pressure	Design of the inlet pressure control
3	Opening degree of electro-actuated valve	±25% ±50%	Outlet flowrate	Design of the outlet flowrate control
4	Voltage of the outlet pump	±25% ±50%	Outlet flowrate	Design of the outlet flowrate control
5	Outlet flowrate	±25% ±50%	Outlet conductivity	Design of composition control
6	Current density	±25% ±50%	Outlet conductivity	Disturbances study on the outlet conductivity
7	Applied Voltage	±25% ±50%	Power	Design of the DC drive control

Figure 46 shows the dynamic response of the acid and base conductivities, as a consequence of different step variations in current density and output flowrates. The tests were performed starting from two steady-state conditions at 200 and 400 A m^{-2}. It is possible to observe how disturbance of the same size led to different steady-state values and time constants for the outlet conductivities (reported in Figure 46). Moreover, a faster response of the acid was observed in most cases. To obtain a reliable relationship between the inlet and the outlet variables, all the other variables of the process were kept constant and equal to their steady-state values. All the dynamic trends were fitted using first order or first order plus dead time transfer functions. From these transfer functions, it was possible to create a linearized model of the process in a wide range of operating conditions thus, allowing the design of all plant controllers.

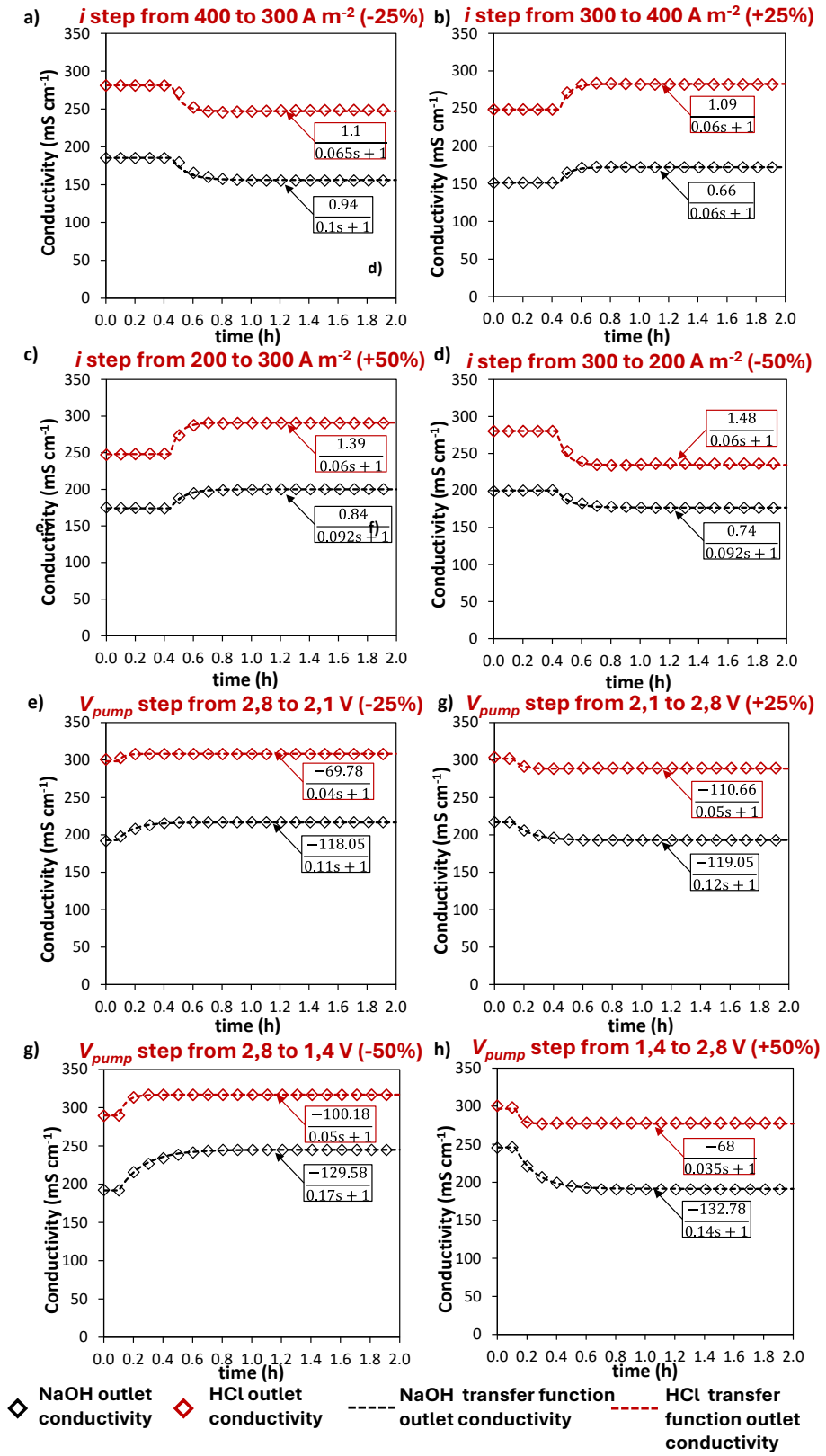

Figure 46. Dynamic response of the uncontrolled system to step variations of current density (i) and outlet flowrate (V_{pump}). Symbols: experimental data; solid line: Simulink Transfer Function trend.

3.6.2.2. Performed step tests to develop control systems

Several control systems were designed and implemented inside the Programmable Logic Controller (PLC) to allow the EDBM pilot plant to automatically operate under dynamic conditions. The study of the uncontrolled system led to the development of four advanced controllers: (i) an override solution flowrate-maximum pressure adopted to prevent issues related to clogging phenomena which could damage the stack; (ii) a product quality cascade control, where the slave controller is an outlet flowrate controller with split range logic and the master is a conductivity control; (iii) a ratio control between the salt and base solutions to guarantee the desired molar ratio; (iv) the DC drive control system for PV maximum power point tracker. The latter allows to operate the system with a variable power set-point, mimicking the real power produced by a solar field.

3.6.2.3. Sizing of the solar field

Two irradiation scenarios, representing summer (July) and winter (December) seasons in Lampedusa Island (Italy), were taken from the European PV-GIS platform [100]. From the irradiation data, a small solar field was designed adopting a commercial panel with an efficiency of 21 % (JA SOLAR, type JAM72S30-540/MR) and a surface area of 32 m^2 (i.e., peak power of 6.5kWp).

3.6.2.4. Summer scenario results

Figure 47 shows the main results of the summer scenario. Figure 47a compares the simulated power from the DC with the real power obtained from the solar field, showing a good agreement. The daily operation was limited between 6:00 and 18:00, when about 10 % of the peak maximum is available. In Figure 47b the trends of external applied voltage and current density are depicted. Their trends resulted qualitatively similar to the available power. Indeed, the DC controller acts on the voltage in order to

reproduce the trend of the available power. The EDBM unit worked in a highly transient regime, with current density ranging from 50 A m^{-2} at 6:00 up to 450 A m^{-2} at 12:00.

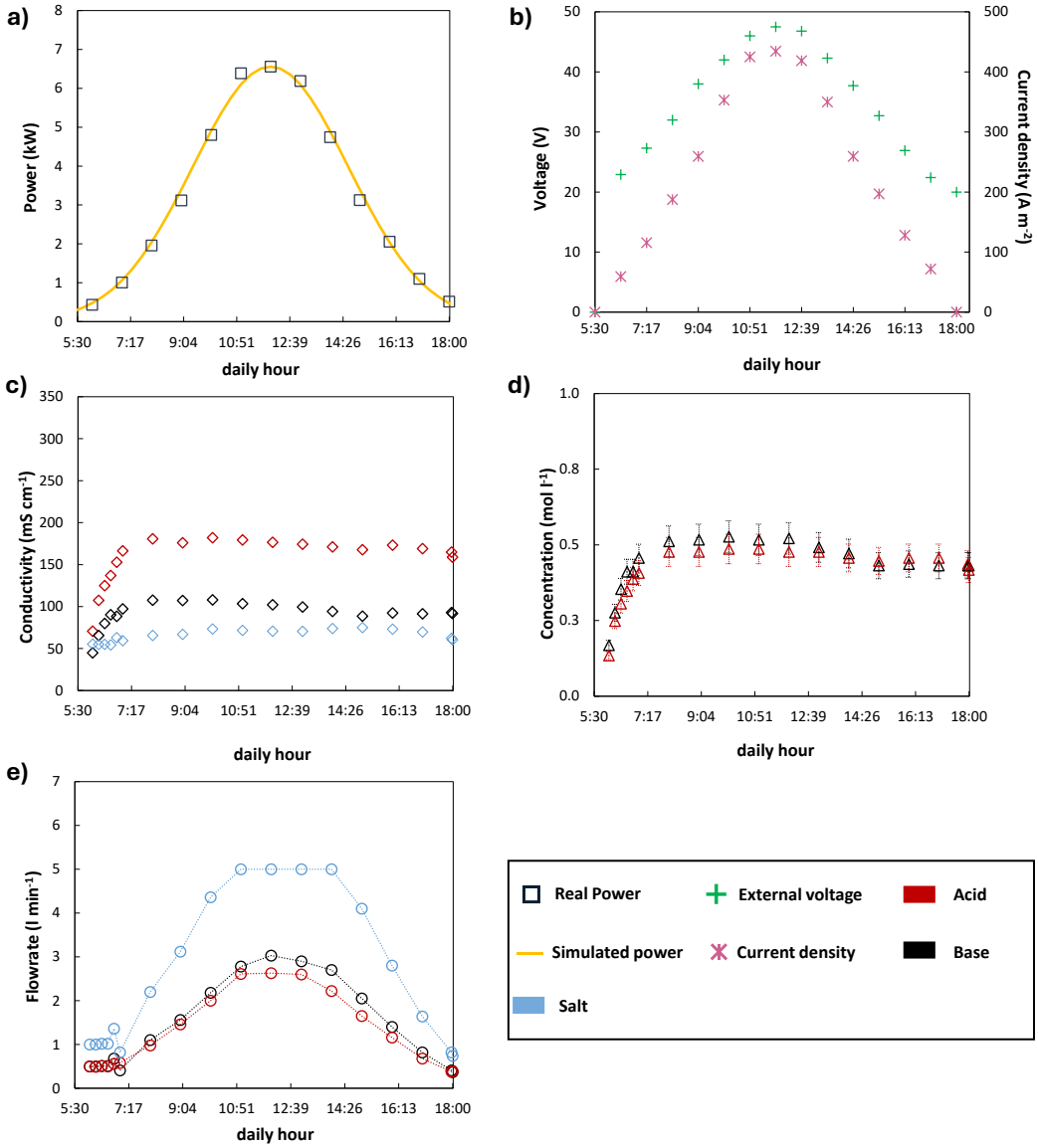

Figure 47. Trends of the main variables during the transient operation of the EDBM unit in the summer scenario: a) real and simulated PV-power, b) applied voltage and current density, c) solution conductivities, d) product concentrations, e) solution outlet flowrates.

Figure 47c shows the trends of the outlet conductivities for the acid, base and salt solutions. The chemical conductivity trends provide insights about the performance of the cascade composition control. As can be seen, an almost constant trend of chemical conductivities was registered during the daily operation (except for the start-up phase).

The controller was found capable of keeping the conductivity close to their set-points, equal to 175 mS cm^{-1} and 100 mS cm^{-1} for acid and base, respectively, which correspond to approximately 0.5 mol L^{-1} chemicals concentration. In Figure 47d the corresponding chemical concentration trends are reported. The adoption of conductivities as controlled variables (i.e., inferential variables) allowed to keep the product concentrations fairly close to the desired targets, slightly higher prior to the maximum pawer point and sightly lower after the maximum. The trend of the solution flowrates is shown in Figure 47e. The hydraulically start-up of the pilot was programmed at 5:30 to enable a membrane conditioning process, while the energy was supplied to the system at 6:00. During this initial phase, the cascade control was deactivated due to the very low values of the power. Thus, the outlet flowrate of the slave controller was fixed to a low-value of flowrate, equal to 0.5 L min^{-1}. When the conductivity values reached their set points, the cascade control system was activated, approximately at 7:00. The flowrate of the salt solution was always higher compared to the acid and base flowrates, due to the fixed ratio value of 2 (i.e., ratio control between the salt and base outlet flowrates). This control strategy limits an excessive impoverishment of the salt solution and improves acid and base productivity.

The trend of the KPIs is shown in Figure 48. The Current efficiency started from values equal to 30% and 36% for acid and base respectively, during the initial transient phase where the concentrations were very low. Once the set-point conductivities had been reached, the CE started to increase, proportionally to the current density. The maximum current efficiency values were found at the maximum power, resulting equal to 74 % and 91% for acid and base, respectively.

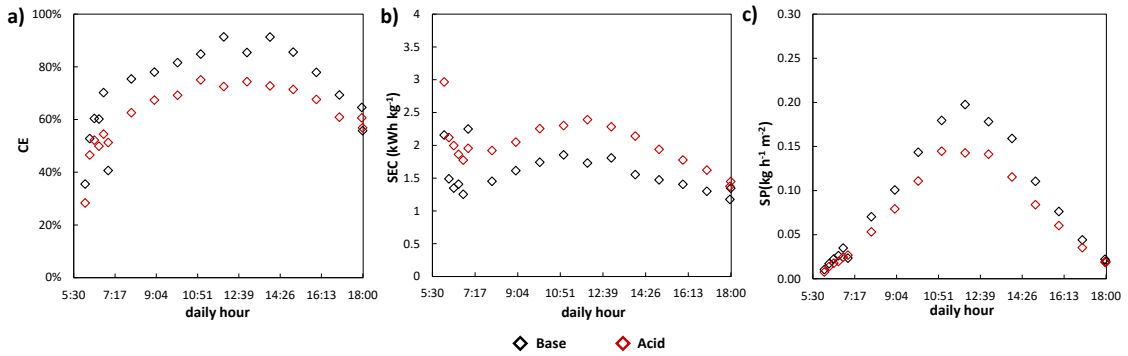

Figure 48. Trends of the main performance indicators during plant operation in summer scenario: a) Current Efficiency; b) Specific Energy Consumption; c) Specific Productivity.

The high value of CE positively affected the other performance indicators such as SEC and SP. However, in the first part of the process test high values of SEC were obtained, equal to 3.0 kWh kg^{-1} and 2.2 kWh kg^{-1} for acid and base, respectively. The minimum SEC values were observed in correspondence with the maximum power resulting equal to 1.8 kWh kg^{-1} for the acid and 1.3 kWh kg^{-1} for the base. In terms of SP, the trends were qualitatively similar to CE. The highest values of SP equal to 0.14 and 0.2 kg h^{-1} m^{-2} for acid and base, respectively, were obtained close to the maximum available power.

3.6.2.5. Winter scenario results

The behaviour of the EDBM pilot under dynamic regimes was further tested simulating in a winter scenario. The results are reported in Figure 49. The operating range was limited to 8 h, with a current density supplied to stack ranging between 80 and 265 A m^{-2}. The composition controller was able to keep the chemical conductivities to their set-point conductivity values (i.e., 175 and 100 mS cm^{-1} for the acid and base, respectively), Figure 49c. The effectiveness of the control action was confirmed by the concentration trends (Figure 49d). Indeed, apart from the start-up phase, a flat trend of concentrations was obtained, equal to 0.5 mol L^{-1} for both chemicals. The trends of the

manipulated variables of the cascade controller are depicted in Figure 49e. Also in this case, the manipulated variable showed a maximum in correspondence of the maximum power. After midday, the flowrates started to decrease, reaching values of 0.42 and 0.52 L min^{-1} for the acid and base, respectively, at 16:00.

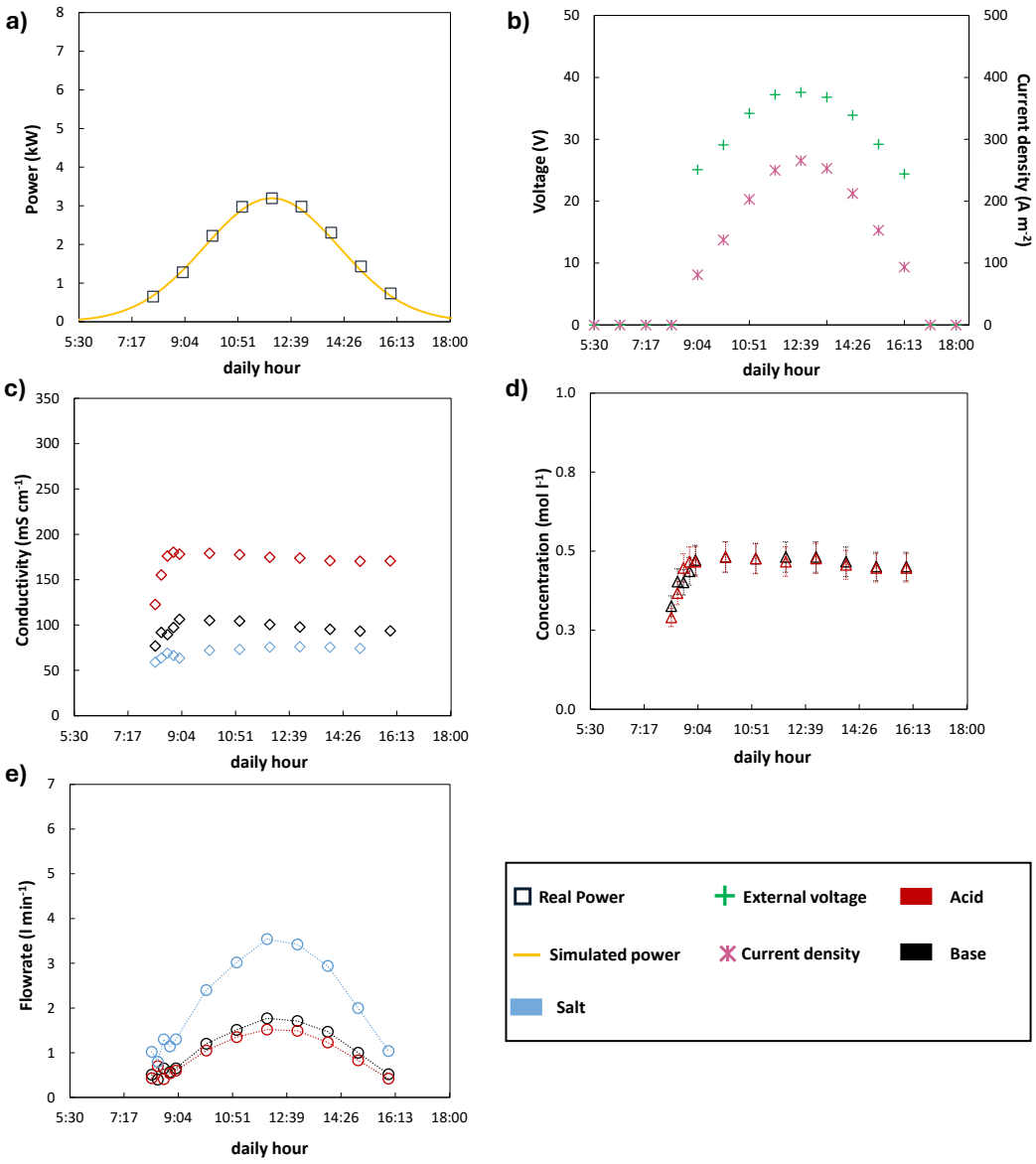

Figure 49. Trends of the main variables during the transient operation of the EDBM unit in winter scenario: a) real and simulated PV-power, b) applied voltage and current density, c) solution conductivities, d) product concentrations, e) solution outlet flowrates.

The performance indicators of the EDBM pilot in winter scenario are reported in Figure 50. The current efficiency increased slowly during the first part of the test due to

the very low current density. Once the set point conductivity had been reached, and the controller had been activated, the current efficiency raised up to values of 70 and 82 % for acid and base, respectively. The SEC exhibited ana slightly decreasing trend along the working day, with average values of 1.9 and 1.6 kWh kg^{-1}. As a consequence of the low current densities, small values of SP were obtained ranging between 0.02-0.08 kg h^{-1} m^{-2} and 0.03-0.11 kg h^{-1} m^{-2} of acid and base, respectively.

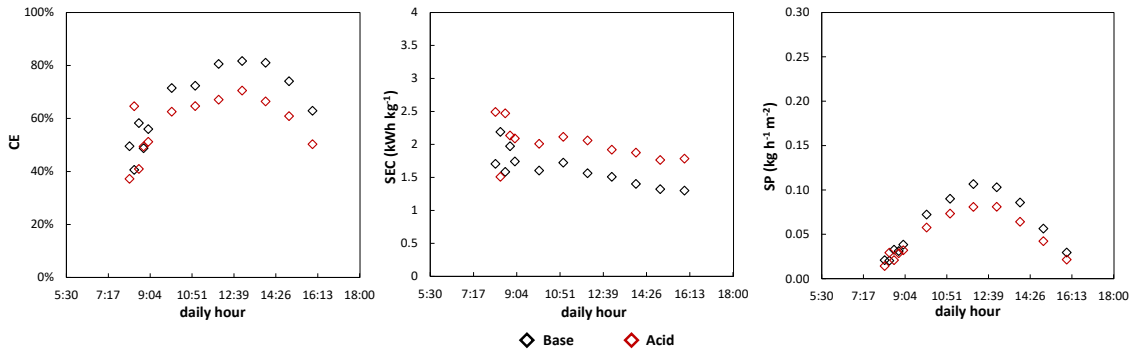

Figure 50. Trends of the main performance indicators during plant operation in winter scenario: a) Current Efficiency; b) Specific Energy Consumption; c) Specific Productivity.

3.6.2.6. Comparison between summer and winter scenarios

A comparison between the summer and winter scenarios is reported in this section. The summer scenario, in Lampedusa, allowed to reach high peak irradiation up to 980 W m^{-2}. On the other hand, in the winter scenario a maximum radiation of 600 W m^{-2} was reached. Consequently, it was also observed a significant drop in the maximum power available, going from a maximum of 6.5 kWp in July to 3.2 kWp in December. This power reduction played a significant role on the maximum current density that was reached in the winter scenario, equal to 265 A m^{-2}. Moreover, the sunny hours decreased significantly from 12 h in July down to 8 h in December. However, in the summer scenario, the power changed rapidly, and acid and base concentrations reached values slightly higher with respect to the set-point value before the maximum, while slightly lower values of concentrations were observed after midday, when the power decreased.

In these conditions, the control system was unable to totally delete the offset since the time required to reach the set-point value was greater than the disturbance variation time. On the other hand, between 11:00 and 13:00, the available power remained almost constant and, consequently, the control system was able to eliminate the offset. In the winter scenario instead, the variation was less rapid thus, the control was able to maintain the concentration constant and equal to the desired value throughout the working day.

Figure 51 shows an overall comparison between the two scenarios considering average parameters. The average available power was found equal to 3.2 and 2 kW for the summer and winter scenarios, respectively. As a consequence, the DC drive control system supplied an 11% higher voltage in the summer scenario compared to the winter one. Thus, the average value of current density resulted equal to 250 and 180 A m^{-2}in summer and winter, respectively. In terms of CE, high values were obtained in both scenarios (higher than 60%), thanks to the target concentration and process configuration used. It is worth noting that in the summer scenario the CE resulted 7% higher. This effect is related to the adoption of the feed and bleed configuration, which offers better performance at higher current densities, as demonstrated in previous works [92], [101]. Concerning the SEC, similar average values were found in the two scenarios. Due to the voltage reduction in winter which balanced the lower current efficiency. Finally, the average SP resulted 25% lower in the winter scenario with respect to the summer one due to the lower average current density.

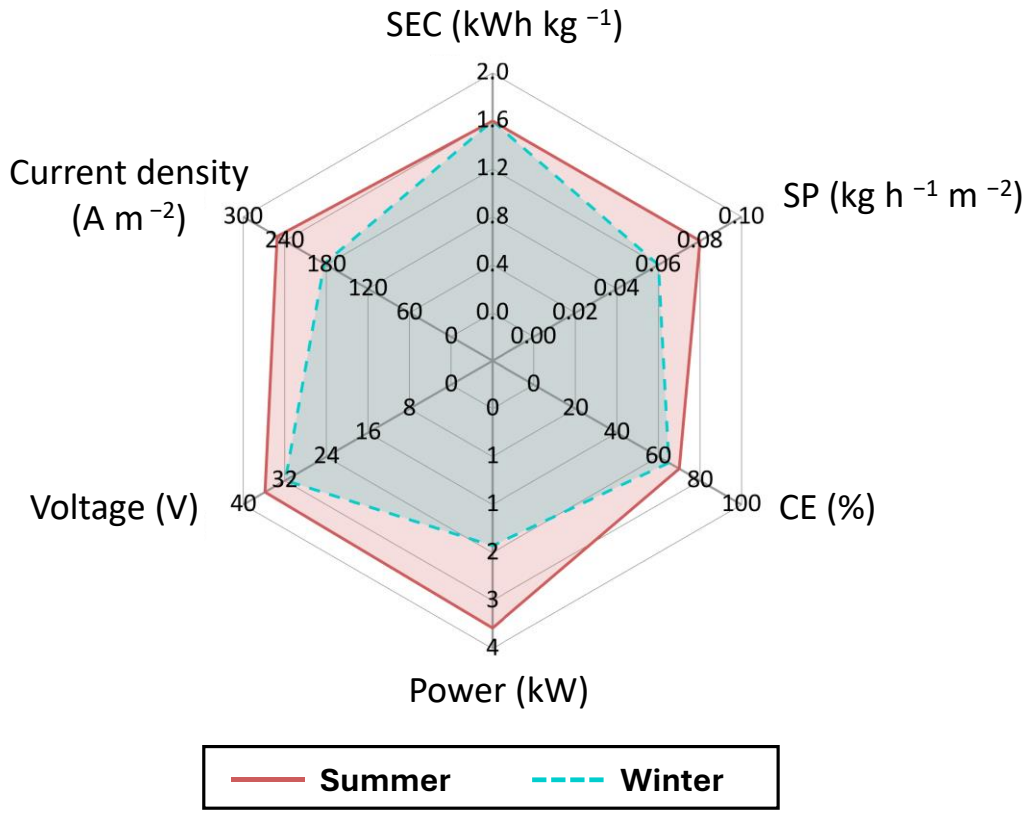

Figure 51. Comparison between the two investigated scenarios with respect to the base product.

These results demonstrated that EDBM technology is perfectly suitable to work in highly transitory regimes like those pertaining to the use of renewable energy sources. Moreover, since the plant exhibits an improved performance with higher energy availabilities, more sophisticated energy supply systems can be considered and integrated (i.e., wind energy from smart grids), especially during the winter season. In this way, stable operation of the system will be guaranteed even during periods of low energy availability through enhanced control strategies.

4. Modelling of EDBM with first principles approaches

In this chapter, the modelling of EDBM is considered utilising traditional approaches based on the physical laws, which describe the mechanisms of the main occurring phenomena. These models are referred to as mechanistic, deterministic or even first principles models [102], [103]. They result the most widely adopted for membrane processes thanks to their reliability and ease of interpretation.

This chapter is divided into steady-state and dynamic modelling of EDBM. Firstly, the utilised multiscale modelling structure is described, and some analyses are conducted focusing mainly on the feed and bleed process configuration. Then, the modifications made to consider also transient conditions were described and the obtained model was utilised to simulate the PV-EDBM system.

4.1 State of the art

Regarding the modelling of EDBM systems, several works have been published, and a comprehensive review has been presented by Culcasi et al. [104]. Apart from a few works that computed local mass balances [104], [105], [106], all the other models reported so far adopted a simplified approach with lumped parameters [107] or the computation of global mass balances [108], [109]. The Nernst-Planck approach is widely used to estimate trans-membrane fluxes [104], [106], [107], while the non-equilibrium thermodynamics (NET) approach is seldom adopted [105]. Concentration polarization causes a difference in concentration between the bulk of the solution and the solution-side of the solution-membrane interface. This effect is caused by the higher transport number of counter-ions in the membrane phase than in the solution phase [40]. To predict this effect, a few studies have applied Donnan equilibria [104], [105], [110]. Additionally, the concentration polarization effect may have significant implications, especially for the

salt compartment, where these phenomena can support the achievement of the diffusion-limited current due to the concentration at the solution side of the solution-membrane interface becoming zero [40]. In addition, osmotic and electro-osmotic water fluxes have rarely been considered, even though they can lead to significant variations in the volumes and concentrations of the solutions [104], [109]. Parasitic currents, also referred to as leakage currents, are detrimental phenomena that reduce the current utilization of the system and are generated by the presence of alternative paths for the ion current. These paths arise from the parallel hydraulic connection between the triplets. Consequently, solution channels of the same type are also connected through collectors and distributors (also known as manifolds), which act as salt-bridges and prevent a portion of the useful ion current from passing through the active membrane area. As a result, the ionic current flowing through the manifolds diminishes the effective current across the membranes responsible for chemicals production and desalination. Therefore, assessing parasitic currents is crucial, especially in industrial applications where energetic consumption is an important consideration. Only one previous study included parasitic currents in an EDBM model [104]. In this previous work it was found that the effect of parasitic currents is exacerbated as the resistance of the cell pack increases [93] and, thus, for industrial scale EDBM stacks their effect must be considered.

Some of the models reported so far in the literature have been validated with experimental results. In Table 14, a list of these models is reported showing the operating conditions and the process configurations adopted to validate them. In some cases, a wide range of current densities was utilized [107], [108], while others adopted only one current density value [104], [109]. In almost all previous studies the range of acid and base concentrations used for validation was between 0.1–1 mol L^{-1}, with only a few exceptions [104], [106]. Moreover, all the studies adopted only closed-loop process configurations

in lab-scale EDBM units. Indeed, the number of triplets installed ranges between 1–5 with an active membrane area in the range of 0.004–0.028 m^2. The EDBM process has been demonstrated to be more effective for low outlet concentrations, up to 1–1.5 mol L^{-1}. At higher concentrations the Nernst potential across the membranes can be significant, leading to high energy consumption. In addition, high current densities cause high ohmic losses and the transport of water inside the BPM can become detrimental. Membrane manufacturers often suggest using a current density sufficiently lower than 1,000 A m^{-2}. All these aspects must be considered to scale-up the EDBM technology and make it an effective and competitive way of producing chemicals *in-situ*.

Table 14. List of the models reported in the literature, showing the processes configurations and operating conditions adopted to validate them in comparison with the present work.

Reference	Validation range						
	Current Density (A m^{-2})	**Voltage (V)**	**Acid Conc. (mol L^{-1})**	**Base Conc. (mol L^{-1})**	**N_{tr}**	**A_m**	**Process Configuration**
Mier et al. [107]	250-1000	-	0.05-1.5	0.05-2.0	1-4	0.01	CL
Gineste et al. [109]	1000	-	0.1-5.8	0.1-5.7	1	0.004	CL
Koter and Warszawski [108]	250-1250	-	0.1-1.4	0.1-1.6	1	0.0049	CL
Leon et al. [106]	-	5	0.05-0.08	0.05-0.08	5	0.028	CL
Culcasi et al. [104]	200	-	0.1-0.8	0.1-0.8	5	0.01	CL
Present model	200-500	30-50	0.05-1	0.05-1	40	0.16	F&B, CL

CL: closed-loop, F&B: feed and bleed.

4.2 Steady-state modelling

In this paragraph, steady-state modelling of the EDBM process is considered, describing the developed multi-scale model and utilising it for analysis of EDBM behaviour and potentials. The results described in this paragraph were published in the article *Multi-scale modelling of an electrodialysis with bipolar membranes pilot plant and economic evaluation of its potential* [57].

4.2.1. Multi-scale model structure

The model developed in this study adopts a multi-scale modelling approach with distributed parameters to simulate the three-chamber EDBM configuration. This configuration is widely adopted for the simultaneous production of chemicals. The model comprises six different sub-models that span five different levels, from the channel/membrane level up to the external circuit level. The solution channels are discretized into 50 domain intervals along the flow direction to eliminate grid dependence issues. However, no discretization is applied in the crossflow direction (i.e., perpendicular to the membrane surface). Concentration gradients, for each discretization domain interval, between the bulk and the membrane/solution interfaces are estimated using polarization coefficients [111]. The multi-scale approach used in this study to simulate EDBM has been previously presented [104]. The approach is here extended to simulate a more intricate EDBM stack configuration, specifically with internal staging, which is of significant interest for industrial applications. The structure of the model used in this study is depicted in Figure 52.

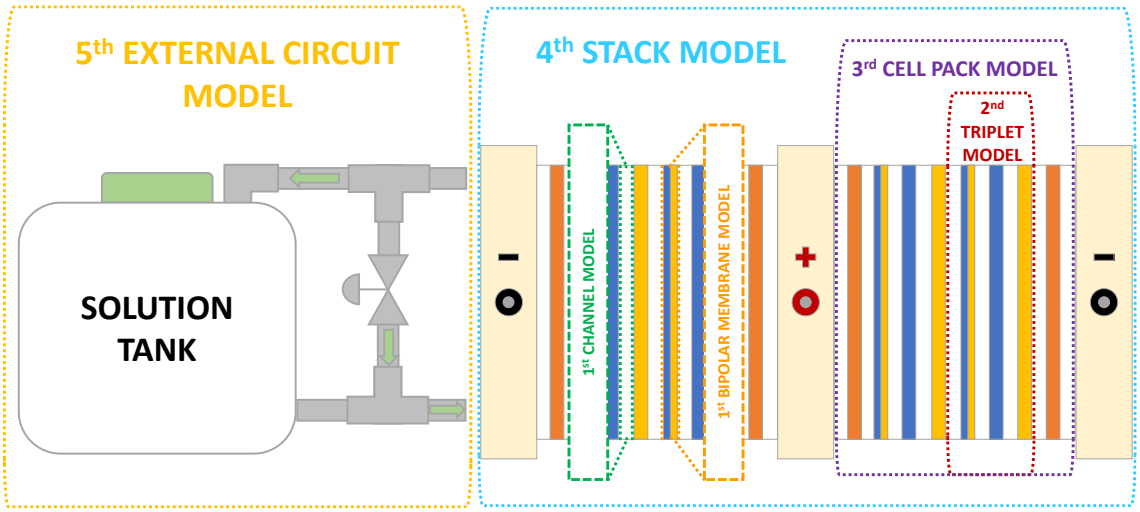

Figure 52. Graphical representation of the multi-scale model structure. Hierarchical levels of the 6 sub-models are represented with the dotted-line areas.

Except for the highest level (i.e., the external circuit model), all other sub-models simulate steady-state operations. The highest model level computes dynamic mass balances in the solutions tanks, accounting for the dynamic behaviour of the EDBM process in closed-loop mode.

A suitable software tool, gPROMS Model Builder® [112], is utilised to integrate and solve all the sub-models. The full model is described in Appendix A, while the following sections present a brief description of each model level, with more details on the levels that are more relevant to the modifications made to extend the previous model to the new simulation scenario.

4.2.1.1. Level 1

This level is composed of two different sub-models: the channel model and the bipolar membrane model. The former evaluates solutions chemical-physical properties, while the latter estimates the limiting current density and ion fluxes through the bipolar membrane.

4.2.1.1.1. The channel model

The channel model evaluates the chemical-physical properties of the solutions, such as electrical conductivity, mass density, viscosity, activity coefficients and ion diffusivity in solution using models from the literature or empirical equations. Sherwood numbers are determined using correlations derived from Computational Fluid Dynamics (CFD) simulations. Further details can be found in [111]. The main modification at this level is the use of the model by McCleskey et al. [113] to determine the electrical conductivities of multi-ion solutions.

The electrical conductivity (σ) of an aqueous solution can be calculated from its chemical composition using the following equation:

$$\sigma = \sum \lambda_i m_i \tag{24}$$

where λ_i is the ionic molal conductivity (S kg m^1 mol^1) and m_i is the molality (mol kg^1) of the *i*-the ion.

The ionic molal conductivity is a function of the temperature and the ionic strength of the solution, through the following equation:

$$\lambda = \lambda^o(T) - \frac{A_{Mc}(T)\, {I_s}^{1/2}}{1+B_{Mc}\, {I_s}^{1/2}} \tag{25}$$

where $\lambda^o$and A_{Mc} are function of the temperature (°C), B_{Mc} is an empirical constant and I_s represents the ionic strength. The latter can be estimated as follows:

$$I_s = \frac{1}{2}\sum m_i\, z_i^2 \tag{26}$$

where z_i is the charge of the *i*-th ion.

McCleskey's model prediction capabilities were tested by conducting some laboratory experimental tests. A total of 10 different solution samples were prepared mixing technical grade chemicals with demineralised water. Specifically, for acid (i.e.,

HCl, ACS reagent 37 wt %, Honeywell, Fluka) and base (i.e., NaOH, technical grade, Inovyn) three samples each were prepared by adding different quantities of sodium chloride (>99.5% purity, Saline di Volterra S.r.l.) (i.e., 0, 0.05 and 0.25 mol L^{-1}) to 1 mol L^{-1} chemical solutions. While four samples were prepared for the salt solution, utilising two different contents of sodium chloride (i.e., 0.5 and 0.7 mol L^{-1}) and by adding different quantities of acid (i.e., 0.1 and 0.2 mol L^{-1}). The choice of preparing these solutions is related to the fact that acid and base products can contain a salt quantity due to the non-perfectly selectivity of the membranes, whilst the salt solution can be acidified due to the passage of protons through the AEM. Thus, the concentration of the prepared solution represents a wide range of possible solutions obtained from the EDBM process. The conductivities of the solutions were measured utilising a conductivity meter WTW Cond3310 (Xylem Analytics Germany Sales GmbH & Co. KG WTW) and compared with the model prediction. The results are shown in Figure 53. A good agreement was found for the tested solutions (maximum deviation equal to 11%), proving the reliability of the model.

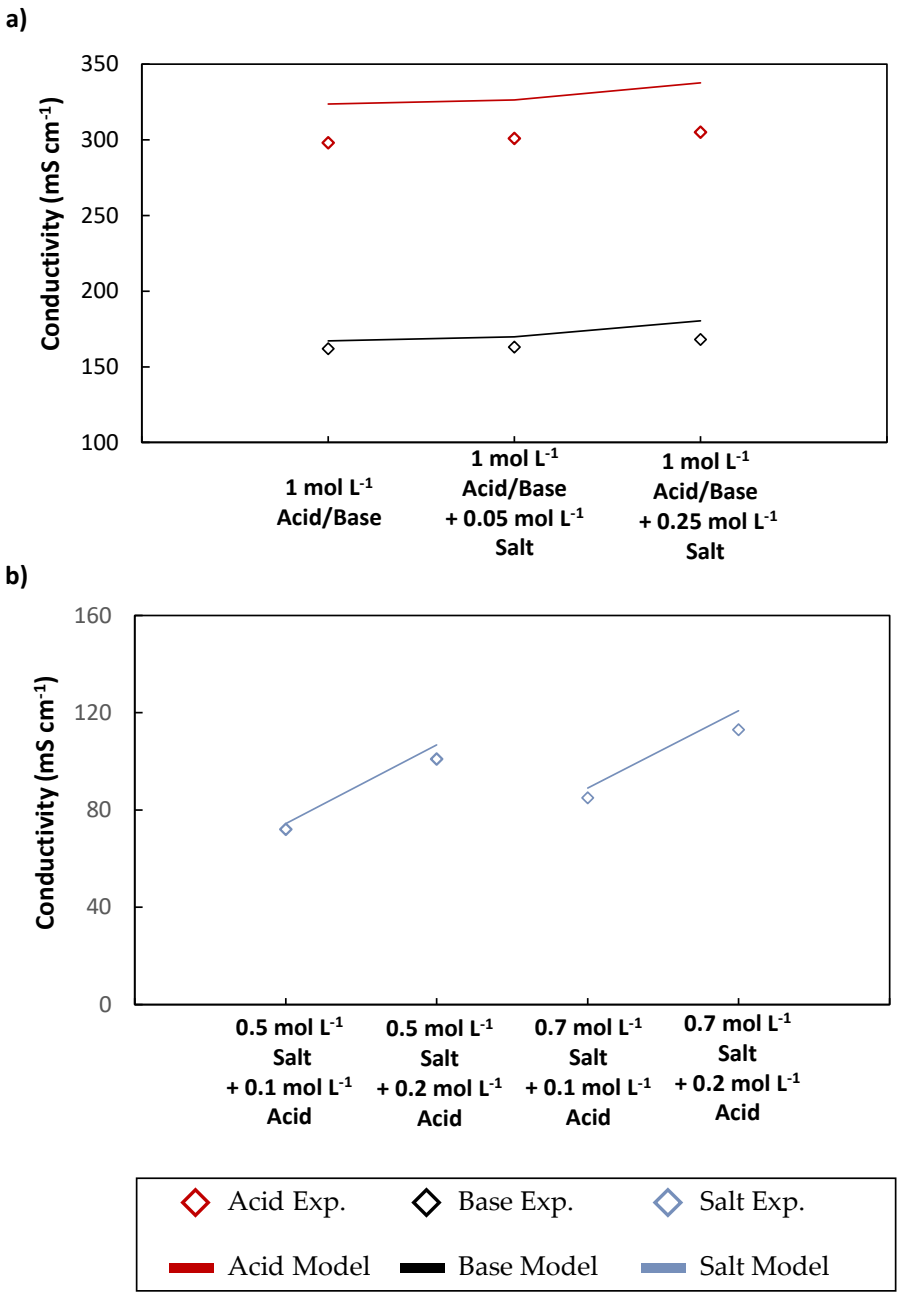

Figure 53. Comparison between McCleskey's model prediction and experimentally measured conductivities.

4.2.1.1.2. The bipolar membrane model

The bipolar membrane model describes the behaviour of the key element of the EDBM process, the bipolar membrane. The approach developed by Strathmann [79] is adopted to estimate the limiting current density and ion fluxes through the two layers of the bipolar membrane. The limiting current density represents the current density at which

all salt ions are removed from the transition region. This value is obtained by computing a mass balance in the transition region and it is then employed in the estimation of the ion migrative fluxes. The model assumes that the ion transport numbers of counter-ion and co-ion are 99% and 1% times the ratio between the limiting current density and the current density, respectively. Moreover, the bipolar membrane is modelled as symmetric thus, the transport numbers of Na^+, Cl^- and H^+ in the CEL are equal to the transport numbers of Cl^-, Na^+, OH^- in the AEL, respectively.

4.2.1.2. Level 2: the triplet model

The triplet model simulates the behaviour of the repetitive unit of the EDBM process. At this level mass balances are computed in each channel, the electrical potential generated across each triplet is evaluated through the Nernst equation, and, finally, the electrical resistance of the entire triplet is estimated as the sum of the membrane resistances and solution resistances in the direction perpendicular to the flow of the solutions.

Mass balances for the acid channels are computed as follows:

$$\frac{\partial Q_a C_{Na^+,a}}{\partial x} = b\, J_{tot,Na^+,a} + \frac{G_{salt,CEL}}{L\ 10^{-3}\ M_{NaCl}} \tag{27}$$

$$\frac{\partial Q_a C_{Cl^-,a}}{\partial x} = b\, J_{tot,Cl^-,a} + \frac{G_{salt,CEL}}{L\ 10^{-3}\ M_{NaCl}} \tag{28}$$

$$\frac{\partial Q_a C_{H^+,a}}{\partial x} = b\, \left(J_{tot,H^+,a} - J_{tot,OH^-,a}\right) \tag{29}$$

$$C_{OH^-,a} = 10^3\ 10^{\left(-14-\log\frac{C_{H^+,a}}{10^3}\right)} \tag{30}$$

$$\frac{\partial Q_a \rho_a}{\partial x} = \left(J_{tot,Na^+,a}\, M_{Na^+} + J_{tot,Cl^-,a}\, M_{Cl^-} + \left(J_{tot,H^+,a} - J_{tot,OH^-,a}\right) M_{H^+}\right) b\ 10^{-3} + \frac{G_{w,a}}{L} + \frac{G_{salt,CEL}}{L} + J_{tot,OH^-,a}\, M_{H_2O}\, b\ 10^{-3} \tag{31}$$

where L, b, d_a are the length, width and thickness of the acid channel, respectively, $C_{i,a}$ is the molar concentration of ion i in the acid channel, Q_a and ρ_a are the volumetric flowrate and mass density of the acid channel, $J_{tot,i,a}$ is the total flux of ion i, $G_{w,a}$ and $G_{salt,\,CEL}$ are the overall water mass flux entering in the acid channel and salt water flux through the CEL layer, M is the molar mass.

Similar equations can be written for the salt channels:

$$\frac{\partial Q_s C_{Na^+,s}}{\partial x} = b\, J_{tot,Na^+,s} \tag{32}$$

$$\frac{\partial Q_s C_{Cl^-,s}}{\partial x} = b\, J_{tot,Cl^-,s} \tag{33}$$

$$\frac{\partial Q_s C_{H^+,s}}{\partial x} = b\left(J_{tot,H^+,s} - J_{tot,OH^-,s}\right) \tag{34}$$

$$C_{OH^-,s} = 10^3\, 10^{\left(-14-\log\frac{C_{H^+,s}}{10^3}\right)} \tag{35}$$

$$\frac{\partial Q_s \rho_s}{\partial x} = \left(J_{tot,Na^+,s}\, M_{Na^+} + J_{tot,Cl^-,s}\, M_{Cl^-} + \left(J_{tot,H^+,s} - J_{tot,OH^-,s}\right) M_{H^+}\right) b\, 10^{-3} + \frac{G_{w,s}}{L} + J_{tot,OH^-,s}\, M_{H_2O}\, b\, 10^{-3} \tag{36}$$

Regarding the base channels, the mass balances are given by:

$$\frac{\partial Q_b C_{Na^+,b}}{\partial x} = b\, J_{tot,Na^+,b} + \frac{G_{salt,AEL}}{L\, 10^{-3}\, M_{NaCl}} \tag{37}$$

$$\frac{\partial Q_b C_{Cl^-,b}}{\partial x} = b\, J_{tot,Cl^-,b} + \frac{G_{salt,AEL}}{L\, 10^{-3}\, M_{NaCl}} \tag{38}$$

$$\frac{\partial Q_b C_{OH^-,b}}{\partial x} = b\left(J_{tot,OH^-,b} - J_{tot,H^+,b}\right) \tag{39}$$

$$C_{H^+,b} = 10^3\, 10^{\left(-14-\log\frac{C_{OH^-,b}}{10^3}\right)} \tag{40}$$

$$\frac{\partial Q_b \rho_b}{\partial x} = \left(J_{tot,Na^+,b}\, M_{Na^+} + J_{tot,Cl^-,b}\, M_{Cl^-} + \left(J_{tot,OH^-,b} - J_{tot,H^+,b}\right) M_{OH^-}\right) b\, 10^{-3} + \frac{G_{w,b}}{L} + \frac{G_{salt,AEL}}{L} + J_{tot,H^+,b}\, M_{H_2O}\, b\, 10^{-3} \tag{41}$$

All other symbols have the same meaning as defined in the previous equations.

The electric potential generated across the IEMs in a triplet can be expressed as

$$E = EMF + \eta_{BL} \tag{42}$$

where EMF is the triplet electromotive force, and η_{BL} accounts for concentration polarization effects in the boundary layers.

The electromotive force is calculated by the Nernst equation

$$E = \sum_{IEMs}\left(-\frac{R_g T}{F}\int_{left,IEM}^{right,IEM}\sum_{ions}\frac{t_i}{z_i}d\,ln\,\alpha_{int,i}\right) \tag{43}$$

where $\alpha_{int,i}$ is the activity of the *i*-th ion at the membrane-solution interface, solution side, $right, IEM$ and $left, IEM$ are the right and the left side of each membrane.

η_{BL} accounts for the non-Ohmic variation of the triplet electric potential due to the effects of concentration polarization in the boundary layers on all the six solution-membrane interfaces

$$\eta_{BL} = -\frac{R_g T}{F}\sum_{int}\sum_{ions}\frac{t_i}{z_i}\ln\theta_{i,sol,int} \tag{44}$$

in which $\theta_{i,sol,int}$ are the polarization coefficients, computed as

$$\left(\theta_{i,sol,int}\right)^{sgn\left(J_{diff,i,sol,int}\right)} = \frac{C_{i,sol,int}}{C_{i,sol}} \tag{45}$$

where $C_{i,sol}$ and $C_{i,sol,int}$ are the concentrations of the *i*-th ion in the so*l* channel (i.e., acid, base or salt) in the bulk and at the solution-membrane interface, respectively, and $sgn\left(J_{diff,i,sol,int}\right)$ is the sign of the diffusive flux of the *i*-th ion at the interface with the membrane, solution side

The triplet electric resistance R (in Ω) is calculated as follows

$$R = \sum_{sol} R_{sol} + \sum_{m} R_{cal} R_m \tag{46}$$

where R_{sol} and R_m are the electrical resistance in the feed channels (i.e., acid, base, and salt) perpendicular to the membranes and the electrical resistance of the membranes (i.e.,

CEM, AEM, and BPM), respectively, and R_{cal} is calibration factor for the membrane resistance.

R_{sol} is calculated as

$$R_{sol} = f_s \frac{d_{sol}}{b\,\Delta x\,\sigma_{sol}} \tag{47}$$

in which f_s is the spacer shadow factor (which can be assumed, for example, equal to the inverse of the volume porosity), b is the channel width, Δx is the length of a discretization interval (e.g., equal to 1/50 of the channel length) and σ_{sol} is the electrical conductivity of the electrolyte solution.

The inputs to this model are membrane and spacer properties. For parameters like thickness, water permeability, and fixed charge density, values previously published in [104] are utilized. While the main features of the spacers, such as thickness as well as porosity in the flow direction and in the plan view, were obtained from the manufacturer. These values are summarized in Table 15. Input parameters to the triplet model. Values for membrane resistances and diffusivity coefficients are obtained from the calibration of the model and they are described in 4.2.3.

Table 15. Input parameters to the triplet model.

Property	Unit	AEM	CEM	AEL	CEL	BPM	Spacers
Thickness	μm	130	130	95	95	190	350
Water permeability	ml bar^{-1} h^{-1} m^{-2}	8	8	-	-	-	-
Fixed charge density	mol m^{-3}	5000	5000	5000	5000	-	-
Porosity flow direction	%	-	-	-	-	-	84
Porosity plan view	%	-	-	-	-	-	64
Areal resistance	Ω m^2	7	6			13	

4.2.1.3. Level 3: the cell pack model

The cell pack model simulates a certain number of triplets connected hydraulically in parallel. The equivalent hydraulic circuit, for all the solutions, is solved by computing mass balances between the channels and the manifolds and assuming a negligible variation in the mass density inside the stack. The following continuity equations can be written for the distributor.

$$Q_{d,1,sol}C_{d,1,i,sol} = \frac{Q_{tot,in,sol}C_{in,i,sol} - Q_{x=0,1,sol}C_{x=0,1,i,sol}}{N_{holes}} \quad (48)$$

$$Q_{d,1,sol} = \frac{Q_{tot,in,sol} - Q_{x=0,1,sol}}{N_{holes}} \quad (49)$$

$$Q_{d,k,sol}C_{d,k,i,sol} = Q_{d,k-1,sol}C_{d,k-1,i,sol} - \frac{Q_{x=0,k,sol}C_{x=0,k,i,sol}}{N_{holes}} \quad (50)$$

$$Q_{d,k,sol} = Q_{d,k-1,sol} - \frac{Q_{x=0,k,sol}}{N_{holes}} \quad (51)$$

$$Q_{d,N,sol}C_{d,N,i,sol} = Q_{dis,N-1,sol}C_{dis,N-1,i,sol} \quad (52)$$

where $C_{d,k,i,sol}$ and $C_{x=0,k,i,sol}$ are the concentration in the distributor in position *k* of ion *i* in the *sol* (i.e., acid, base and salt) compartment and the concentration of ion *i* at the

entrance of *k-th* triplet of the *sol* compartment, $C_{in,i,sol}$ is the inlet concentration of ion *i* in the *sol* compartment, $Q_{tot,in,sol}$ and $Q_{x=0,k,sol}$ are the total flowrate entering in the *sol* compartment and the entering flowrate in *k-th* triplet of the *sol* compartment, N_{holes} in the number of holes in the spacers and $Q_{d,k,sol}$ is the distributor volumetric flowrate in position *k* of the *sol* compartment. Equations (50) and (51) are valid for *k* in the range 2 to N-1, where N is the number of triplets in the cell pack. Constant mass density is considered in equations (49) and (51), since the same solution with fixed concentration is distributed in all the channels.

For the collector, the following equations are utilised:

$$Q_{c,1,sol}\rho_{c,1,sol} = \frac{Q_{x=L,1,sol}\rho_{1,sol}}{N_{holes}} \tag{53}$$

$$Q_{c,k,sol}C_{c,k,i,sol} = \frac{Q_{x=L,k,sol}C_{x=L,k,i,sol}}{N_{holes}} + Q_{c,k-1,sol}C_{c,k-1,i,sol} \tag{54}$$

$$Q_{c,k,sol}\rho_{c,k,sol} = \frac{Q_{x=L,k,sol}\,\rho_{k,sol}}{N_{holes}} + Q_{c,k-1,sol}\rho_{c,k-1,sol} \tag{55}$$

where $Q_{c,k,sol}$ and $Q_{x=L,k,sol}$ are the collector volumetric flowrate in position *k* of the *sol* compartment and the exit flowrate from the *k-th* triplet of the *sol* compartment, $\rho_{c,k,sol}$ and $\rho_{k,sol}$ are the mass density in position *k* of the *sol* collector and the mass density of the of the *sol* compartment in the *k-th* triplet, $C_{c,k,i,sol}$ and $C_{x=L,k,i,sol}$ are the concentration in the collector in position *k* of ion *i* in the *sol* compartment and exit concentration of ion *i* in *k-th* triplet of the *sol* compartment and d_c is the dimeter of the collector. Equations (54) and (55) are valid for *k* in the range 2 to N.

4.2.1.4. Level 4: the stack model

The stack model calculates the solutions resistances in the manifolds and channels and provides the voltage and current profiles along all the triplets installed in the EDBM stack. The voltage profile is used to calculate the voltage applied to the stack. Instead, the

current profile is employed to compute the percentage of unused current due to the parasitic currents effect. The equivalent electrical circuit of the EDBM stack was obtained considering the main features of the internal staging configuration (i.e., a unique manifold and a shared anode between the two cell packs). Figure 54 shows a schematic representation of the equivalent electrical circuit of the stack where only two triplets per cell pack are reported for the sake of simplicity.

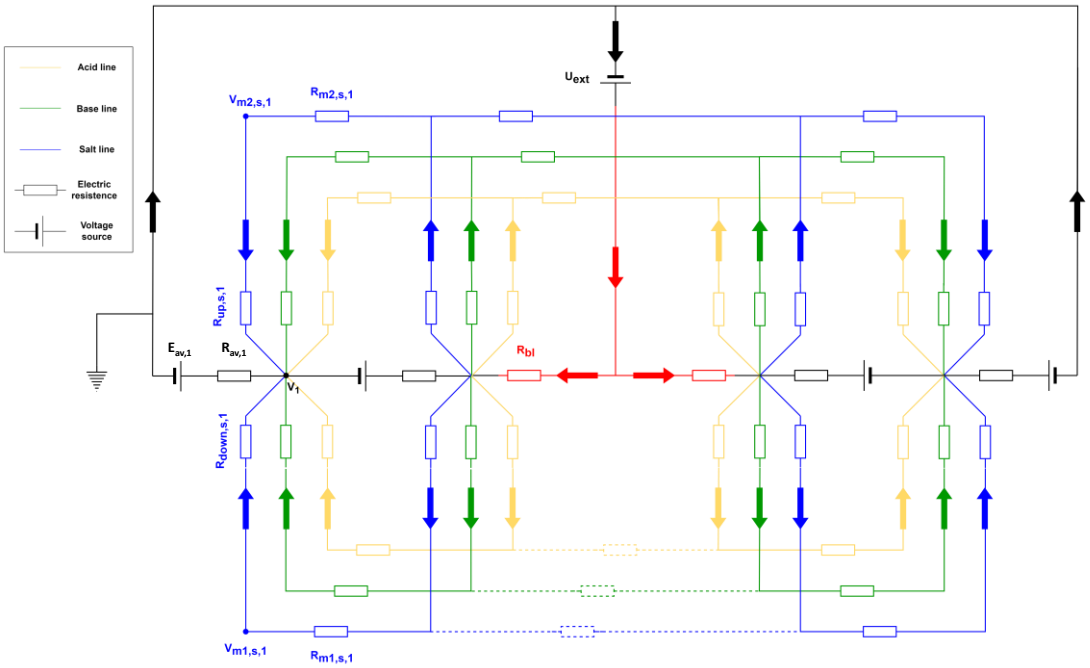

Figure 54. Representation of the equivalent electrical circuit of the EDBM stack, adopting an internal staging configuration with a shared anode. For the sake of clarity, only two repetitive units were represented in each cell pack. R_{bl} represents a lumped parameter known as blank resistance and its meaning and values are described in Appendix A. The dotted lines represent the interruption in manifold 1, allowing the cell packs to work in series.

Each triplet is modelled as a voltage source and an electrical resistance in the direction perpendicular to the membranes. Instead, two longitudinal resistances are assumed in the flow direction. All these electric components are evaluated in the triplet model.

The resistance related to the connection manifolds between two consecutive channels are evaluated through the following equation:

$$R_{m_i,sol,k} = \frac{l_{m_i,k}}{N_{holes}\, S_{m_i}\, \sigma_{m_i,sol,k}} \tag{56}$$

where R is the solution resistance in the manifold m_i (i.e., m_1 or m_2) of the so$l$ (i.e., a, b or s) compartment, in position k (between 1 and N_{tr}-1, where N_{tr} is the total number of triplets in the stack); $l_{m_i,k}$ is the length of the manifold m_i in position k, S_{m_i} is the section of the manifold m_i, $\sigma_{m_i,sol,k}$ is the conductivity of the solution so$l$ in position k in the manifold m_i, N_{holes} is the number of holes in the spacers. It should be noted that each of these resistances represents the equivalent resistance of parallel resistances, equal to the number of holes in the spacers.

The electrode compartments are represented using a lumped parameter known as blank resistance (indicated as R_{bl}) e described in Appendix A. This parameter accounts for: i) standard electrical potentials, ii) over-voltages of the redox reactions occurring at the electrodes, and iii) the ohmic voltage drops due to the two end-membranes (CEMs), the two electrode compartment channels and the additional acid channel installed to better separate the cell packs from the electrodes chambers (see Figure A1). The blank resistance was obtained by performing a laboratory test described in Appendix A. The DC drive that powers the system is represented as an electrical generator.

The hydraulic connections between the two cell packs can be electrically modelled as additional branches of the electric circuit with an electric resistance. The

presence of these electric branches determines the onset of additional parasitic ionic pathways. The cell packs share a central common anode (positive electrode), while two distinct cathodes (negative electrodes) are positioned at the two extremes of the stack. The voltage for both cathodes is considered to be zero (i.e., the ground potential).

This model simulates two manifolds: the lower (designated as 1) and the upper (designated as 2). According to the scheme in Figure 54, an interruption is placed in the anode position of manifold 1, with the two cell packs only connected through manifold 2. This interruption in the manifold 1 is simulated by setting the R_{m_1,sol,N_1} to 10^8 Ω for all three solutions (where N_1 is the number of triplets in the first cell pack). The resistance of manifold 2 denoted as $R_{m_2,sol,N}$, is derived for the three solutions using equation (56), where the length of the linking manifold section connecting the two cell packs, l_{m_2,N_1}, is fixed to 6 cm. This difference in length is due to the presence of the anodic chamber between the cell packs. Due to this different length, this resistance is about two orders of magnitude greater than the other manifolds resistances.

Kirchhoff's and Ohm's laws are applied to the nodes and branches of the equivalent electrical circuit, respectively, to obtain the current and voltage profiles along the entire stack.

For the first cell pack the following equation are employed:

$$I_{m_i,sol,1} = (V_{m_i,sol,2} - V_{m_i,sol,1})/R_{m_i,sol,1} \quad (57)$$

where $I_{m_i,sol,1}$ is the current flowing in the manifold m_i of the *sol* compartment, in position *1* and $V_{m_i,sol,k}$ is the voltage in the manifold m_i of the *sol* compartment in position *k*. For the upper and down branches, the following equation ca be written:

$$I_{up,sol,1} = (V_{m_2so,l,1} - V_1)/R_{up,sol,1} \quad (58)$$

$$I_{down,sol,1} = (V_{m_1,sol,1} - V_1)/R_{down,sol,1} \quad (59)$$

where $I_{x,sol,1}$is the current flowing in the *x* (i.e., *up*, *down*) part of the channel of the *sol* compartment in position *1,* $R_{x,sol,1}$is the resistance of *x* (i.e., *up*, *down*) part of the channel of the *sol* compartment in position *1 and* $V_1$is the voltage of the stack in position 1 (see Figure 54).

$$V_1 = I_1 R_{av,1}/A_m + E_{av,1} \quad (60)$$

where $I_1$is the current flowing between V_1 and the left cathode, $E_{av,1}$and $R_{av,1}$are the average triplet membrane potential and the average cell resistance of the cell in position 1, respectively.

$$I_{k-1} = I_k + \sum_l (I_{up,sol,k-1} + I_{down,sol,k-1}) \quad (61)$$

$$I_{m_1,sol,k-1} = I_{down,sol,k} + I_{m_1,sol,k} \quad (62)$$

$$I_{m_2,sol,k-1} = I_{up,sol,k} + I_{m_2,sol,k} \quad (63)$$

$$I_{m_i,sol,k} = (V_{m_i,sol,k+1} - V_{m_i,sol,k})/R_{m_i,sol,k} \quad (64)$$

$$I_{up,sol,k} = (V_{m_2,sol,k} - V_k)/R_{up,sol,k} \quad (65)$$

$$I_{down,sol,k} = (V_{m_1,sol,k} - V_k)/R_{down,sol,k} \quad (66)$$

$$V_k = V_{k-1} + I_k R_{av,k}/A_m + E_{av,k} \quad (67)$$

The validity interval of equations between (61) and (67)(67) is for *k* [*2* to N_1], where N_1 is the number of triplets installed in the first cell pack.

For the second cell pack the following equation are used:

$$I_{k+2} = I_{k+1} + \sum_l (I_{up,sol,k} + I_{down,sol,k}) \quad (68)$$

$$I_{m_1,sol,k-1} = I_{down,sol,k} + I_{m_1,sol,k} \quad (69)$$

$$I_{m_2,sol,k-1} = I_{up,sol,k} + I_{m_2,sol,k} \quad (70)$$

$$I_{m_i,sol,k} = (V_{m_i,sol,k+1} - V_{m_i,sol,k})/R_{m_i,sol,k} \quad (71)$$

$$I_{up,sol,k} = (V_{m_2,sol,k} - V_{k+1})/R_{up,sol,k} \quad (72)$$

$$I_{down,sol,k} = (V_{m_1,sol,k} - V_{k+1})/R_{down,sol,k} \quad (73)$$

$$V_{k+1} = V_{k+2} + I_{k+2}R_{av,k}/A_m + E_{av,k} \quad (74)$$

The validity interval of equations between (68) and (74) is for k [N_l+*1* to N_{tr}-*1*].

$$I_{N_{tr}+2} = I_{N_{tr}+1} + \sum_l (I_{up,sol,N_{tr}} + I_{down,sol,N_{tr}}) \quad (75)$$

$$I_{m_1,sol,N_{tr}-1} = -I_{down,sol,N_{tr}} \quad (76)$$

$$I_{m_2,sol,N_{tr}-1} = -I_{up,sol,N_{tr}} \quad (77)$$

$$V_{m_1,sol,N_{tr}} - V_{N_{tr}+1} = I_{down,sol,N_{tr}}\, R_{down,sol,N_{tr}} \quad (78)$$

$$V_{m_2,sol,N_{tr}} - V_{N_{tr}+1} = I_{up,sol,N_{tr}}\, R_{up,sol,N_{tr}} \quad (79)$$

$$V_{N_{tr}+1} = I_{N_{tr}+2}R_{av,N_{tr}}/A_m + E_{av,N_{tr}} \quad (80)$$

In the anode position, to connect the two cell packs, the following equation are applied:

$$V_{N_1+1} = U_{ext} \quad (81)$$

$$I_{N_1+1} + I_{N_1+2} = I_{ext} \quad (82)$$

$$I_1 + I_{N_1+2} = I_{ext} \quad (83)$$

$$U_{ext} = R_U\, I_{ext} \quad (84)$$

$$V_{N_1+1} = V_{N_1} + I_{N_1+1}\, R_{bl}/A_m \quad (85)$$

$$V_{N_1+1} = V_{N_1+2} + I_{N_1+2}\, R_{bl}/A_m \tag{86}$$

Where U_{ext} and I_{ext} are the external voltage and current supplied by the DC drive and R_U is the apparent electrical resistance of the entire stack.

Once the current and voltage profiles (i.e., I and V) along the entire stack are determined two key metrics are computed: the percentage of unused current due to parasitic effects and the external voltage applied to the stack.

The percentage of unused current due to parasitic current effects is calculated using the following equation:

$$\eta_I = \frac{A_m\, i - \frac{1}{2}\left(\frac{1}{N_1}\sum_{j=1}^{N_1} I_j + \frac{1}{N_2}\sum_{j=N_1+2}^{N_{tr}+2} I_j\right)}{A_m\, i}\, 100 \tag{87}$$

where N_2 is the number of triplets in the second cell pack.

The voltage applied to the stack is equal to the voltage in the anode position which represents the maximum value observed across the stack.

4.2.1.5. The external hydraulic circuit model

At the highest hierarchical model level, the elements constituting the external hydraulic circuit, including solution tanks, recirculating loops and hydraulic nodes, are simulated. This level differs depending on the process configuration adopted, i.e., closed-loop or feed and bleed.

For the closed-loop configuration, only the solution tanks for acid, base and salt are simulated. Dynamic mass balances are computed, assuming perfect mixing of the solutions. It is noteworthy that the dynamic equations implemented at this level do not make the model fully dynamic as all the other levels simulate steady-state conditions. However, the model can simulate dynamic process configurations, such as the closed-loop, as the dominant dynamic of the system (i.e., the tanks) is simulated.

Dynamic mass balances within the acid and salt storage tanks can be written as follows:

$$\frac{d(\rho_{T,sol} Vt_{sol})}{dt} = Q_{T,in,sol}\, \rho_{T,in,sol} - Q_{T,out,sol}\, \rho_{T,out,sol} \tag{88}$$

$$\frac{d(C_{T,HCl,sol} Vt_{sol})}{dt} = Q_{T,in,sol}\, C_{T,HCl,in,sol} - Q_{T,out,sol}\, C_{T,HCl,out,sol} \tag{89}$$

$$\frac{d(C_{T,NaCl,sol} Vt_{sol})}{dt} = Q_{T,in,sol}\, C_{T,NaCl,in,sol} - Q_{T,out,sol}\, C_{T,NaCl,out,sol} \tag{90}$$

where Vt_{sol} is the solution volume inside the tank, $\rho_{T,sol}$ is the mass density of the solution within the tank, $Q_{T,in,sol}$, $Q_{T,out,sol}$ are the inlet and outlet volume flowrates, respectively, $C_{T,HCl,in,sol}$, $C_{T,HCl,out,sol}$, $C_{T,NaCl,in,sol}$, $C_{T,NaCl,out,sol}$ are the inlet and outlet hydrochloric acid as well as the inlet and outlet sodium chloride concentrations .

For the base storage tank, the following equations can be written as

$$\frac{d(\rho_{T,b} Vt_{b})}{dt} = Q_{T,in,b}\, \rho_{T,in,b} - Q_{T,out,b}\, \rho_{T,out,b} \tag{91}$$

$$\frac{d(C_{T,NaOH,b} Vt_{b})}{dt} = Q_{T,in,b}\, C_{T,NaOH,in,b} - Q_{T,out,b}\, C_{T,NaOH,out,b} \tag{92}$$

$$\frac{d(C_{T,NaCl,b} Vt_{b})}{dt} = Q_{T,in,b}\, C_{T,NaCl,in,b} - Q_{T,out,b}\, C_{T,NaCl,out,b} \tag{93}$$

The feed and bleed configuration is a continuous operating mode and no dynamic equations are implemented. In this case, the recirculation loop from the outlet back to the stack inlet is simulated to increase the residence time of the solution inside the stack. Two hydraulic nodes, for each solution, connecting the recirculating loop to the main flow stream are simulated. Here steady-state mass balances are computed.

For the feed and bleed process configuration, the following equations are employed for the convergent and divergent nodes.

The convergent node represents a mixing element for the entering and the recirculated solution from the stack outlet. The following equations are applied for acid and salt compartments:

$$Q_{cn,sol,out} = Q_{dn,sol,rec} + Q_{sol,in} \tag{94}$$

$$Q_{cn,sol,out}C_{cn,HCl,sol,out} = Q_{dn,sol,rec}C_{dn,HCl,sol,rec} + Q_{sol,in}C_{HCl,sol,in} \tag{95}$$

$$Q_{cn,sol,out}C_{cn,NaCl,sol,out} = Q_{dn,sol,rec}C_{dn,NaCl,sol,rec} + Q_{sol,in}C_{NaCl,sol,in} \tag{96}$$

where $Q_{sol,in}$, $Q_{dn,sol,rec}$, $Q_{cn,sol,out}$ are the volume flowrate entering from the tank, recirculated from the stack outlet and leaving the convergent node, respectively, $C_{HCl,sol,in}$, $C_{dn,HCl,sol,rec}$, $C_{cn,HCl,sol,out}$ are the hydrochloric acid concentration entering from the tank, recirculated from the stack outlet and leaving the convergent node, respectively, $C_{NaCl,sol,in}$, $C_{dn,NaCl,sol,rec}$, $C_{cn,NaCl,sol,out}$ are the sodium chloride concentration entering from the tank, recirculated from the stack outlet and leaving the convergent node, respectively.

For the base compartment, the following equations can be written.

$$Q_{cn,b,out} = Q_{dn,b,rec} + Q_{b,in} \tag{97}$$

$$Q_{cn,b,out}C_{cn,NaOH,b,out} = Q_{dn,b,rec}C_{dn,NaOH,b,rec} + Q_{b,in}C_{NaOH,b,in} \tag{98}$$

$$Q_{cn,b,out}C_{cn,NaCl,b,out} = Q_{dn,b,rec}C_{dn,NaCl,b,rec} + Q_{b,in}C_{NaCl,b,in} \tag{99}$$

For the divergent node, which represents a splitting point between the solution leaving the stack and the solution recirculated to the stack inlet, the following mass balances can be expressed for acid and salt compartments:

$$Q_{dn,sol,in} = Q_{dn,sol,rec} + Q_{sol,out} \tag{100}$$

$$Q_{dn,sol,in}C_{cn,HCl,sol,in} = Q_{dn,sol,rec}C_{dn,HCl,sol,rec} + Q_{sol,out}C_{HCl,sol,out} \tag{101}$$

$$Q_{dn,sol,in}C_{cn,NaCl,sol,in} = Q_{dn,sol,rec}C_{dn,NaCl,sol,rec} + Q_{sol,out}C_{NaCl,sol,out} \tag{102}$$

where $Q_{dn,sol,in}$, $Q_{dn,sol,rec}$, $Q_{sol,out}$ are the volume flowrate leaving the stack, recirculated to the convergent node and entering in the outlet tank, respectively, $C_{dn,HCl,sol,in}$, $C_{dn,HCl,sol,rec}$, $C_{HCl,sol,out}$ are the hydrochloric acid concentration leaving the stack, recirculated to the convergent node and entering in the outlet tank, respectively, $C_{dn,NaCl,sol,in}$, $C_{dn,NaCl,sol,rec}$, $C_{NaCl,sol,out}$ are the sodium chloride concentration leaving the stack, recirculated to the convergent node and entering in the outlet tank, respectively. For the base storage tank, the following equations can be written as

$$Q_{dn,b,in} = Q_{dn,b,rec} + Q_{b,out} \tag{103}$$

$$Q_{dn,b,in}C_{cn,NaOH,b,in} = Q_{dn,b,rec}C_{dn,NaOH,b,rec} + Q_{b,out}C_{NaOH,b,out} \tag{104}$$

$$Q_{dn,b,in}C_{cn,NaCl,b,in} = Q_{dn,b,rec}C_{dn,NaCl,b,rec} + Q_{b,out}C_{NaCl,b,out} \tag{105}$$

4.2.2. Economic model

The economic model evaluates the competitiveness of the EDBM process to produce sodium hydroxide, which results the more profitable product. To this end, the levelized cost of sodium hydroxide (LcoNaOH) is estimated. The LcoNaOH, expressed in € ton^{-1}, represents the minimum sale price of the produced NaOH to guarantee a net present value (NPV) equal to zero at the end of the project life. The model considers all the major components of both capital and operating expenditures. Moreover, the compound interest calculation is applied in determining the LcoNaOH. Several

parameters are employed as model inputs: stack features, capital costs and economic parameters. All the parameters are described in Table 16.

Table 16. Input parameters of the economic model.

	Symbol	Unit	Value/Eq	Reference
Stack Parameter				
Active membrane area	A_m	m^2	0.16	-
Number of triplets in the stack	N_{tr}	-	40	-
Number of stacks in series	N_S	-	1-2	-
Capital Costs				
BPM cost	BPM_{cost}	US$ m^{-2}	300	
AEM/CEM cost	MPM_{cost}	US$ m^{-2}	135	[114]
Spacer cost	S_{cost}	US$ m^{-2}	10	
Economic parameters				
US$/€ conversion	C_{conv}	€ $US\$^{-1}$	0.915	[115]
Electricity price	E_p	€ kWh^{-1}	0.1	[116]
Discount rate	j	%	5	[104]
Membrane and spacers lifetime	M_{lt}	y	5	[117]
Peripherals and electrodes lifetime	PE_{lt}	y	10	
Project lifetime	P_{lt}	y	10	
Performance indicators*				
Specific energy consumption	SEC	kWh kg^{-1}		
Specific productivity	SP	ton y^{-1} m^{-2}		

*Inputs to the economic model obtained from the multi-scale model.

The triplet cost (US$ m^{-2}) is estimated through the following equation:

$$T_{cost} = BPM_{cost} + 2\,MPM_{cost} + 3\,S_{cost} \tag{106}$$

where BPM_{cost} and MPM_{cost} are the cost of bipolar and monopolar membranes respectively and S_{cost} is the spacers cost. A triplet cost of 600 US$ m^{-2} is obtained as a reference value.

The cost of the cell packs installed in the stack (€) is calculated as follows:

$$IM_{cost} = T_{cost} C_{conv} N_{tr} A_m \tag{107}$$

where C_{conv} coverts from US$ to €. The electrodes as well as plates and frames cost can be obtained as a function of the cell packs cost [114].

$$EPF_{cost} = 0.5\, IM_{cost} \tag{108}$$

The total cost of the stack, in €, can be written as:

$$TS_{cost} = IM_{cost} + EPF_{cost} \tag{109}$$

The cost relative to peripheral equipment (i.e., pumps, DC drive, electrical cabinet, monitoring instrumentation and control systems) can be estimated through the following equation:

$$PE_{cost} = 1.2\, TS_{cost}(1 + 0.3(N_s - 1)) \tag{110}$$

where $N_s$is the number of stacks in series. Consequently, adding a second stack in series increases the cost associated with the peripheral equipment by 30%, since some of them are already installed or should only be increased in size.

The initial capital investment (ICI) at the start of the project life is given by:

$$ICI = TS_{cost}N_s + PE_{cost} \tag{111}$$

Often the lifetime of the membranes and spacers M_{lt} is lower than the project lifetime P_{lt}. Subsequently a replacement of the cell packs in necessary at the end of M_{lt}.

Maintenance cost ($Maint_{cost}$) and the Total Energy Consumption (TEC) are considered as operating costs of the EDBM plant. Maintenance cost (€ y^{-1}) are estimated as follows [114]:

$$Maint_{cost} = 0.1\, ICI \tag{112}$$

The total energy consumption (€ ton^{-1}) is calculated using the following equation:

$$TEC = 1.1\, SEC\, E_p 10^3 \tag{113}$$

where E_p is the electricity price, the factor 1.1 accounts for the electrical consumption of the EDBM stack and the peripheral equipment (calculated as 10% of the stack energy consumption [114]), 10^3 coverts the units from € kg^{-1} to € ton^{-1}.

The Process Capacity (PC), expressed in ton y^{-1}, is calculated as follows:

$$PC = SP\ N_{tr} A_m \tag{114}$$

The LcoNaOH is calculated using the following equation:

$$LCoNaOH = \frac{Maint_{cost}}{PC} + TEC + \frac{ICI(1+j)^{P_{lt}} + IM_{cost} N_s (1+j)^{M_{lt}}}{PC \sum_{y=1}^{P_{lt}} (1+j)^{(P_{lt}-y)}} \tag{115}$$

where j is the discount rate.

4.2.3. Model calibration

The model was calibrated with the experimental test in feed and bleed mode to increase its predictive accuracy, accounting for non-ideal phenomena occurring in the EDBM unit, such as internal leakages, pressure differences between channels, membrane deformation and fouling. But also, to account for uncertainties in some membrane properties, such as membrane ion diffusivities and electric resistances.

The parameters used for calibration are: i) an additional term in the Nernst-Planck equation, which accounts for the non-ideal phenomena mentioned above, ii) ion-diffusivities in the membranes, iii) a correction factor for the cell packs resistance.

The Nernst-Planck flux equation is a widely used approach to describe the transport of ions in ion-exchange membranes. Specifically, the ion transport is given by the sum of two contributions: a diffusion term and a migrative term.

$$J_{i,m} = -\sum_j D_{i,j,M} \nabla C_{j,m} + \frac{t_{i,m} i}{z_i F} \tag{116}$$

where $J_{i,m}$ is the total molar flux of the specie i across the generic membrane m (i.e., AEM, CEM or BPM), the sum is extended to all the ionic species, $D_{i,j,m}$ is the cross-diffusion coefficient, $C_{j,MPM}$ is the concentration of the species j in the membrane phase, $t_{i,m}$ is the transport number of the species i in the membrane at the solution-membrane interface, z_i is the valence of ion i.

This equation is derived assuming some standard approximations [118] and consequently, its validity is limited to dilute electrolyte solutions.

The modified Nernst-Planck equation adopted in this work is reported here.

$$J_{tot,i,sol} = J_{ohm,i,sol} + J_{diff,i,sol} + J_{cal,i,sol} \quad (117)$$

where $J_{tot,i,sol}$ is the total flux of the ion i across the two membranes bounding the channel sol (acid, base or salt), $J_{ohm,i,sol}$ and $J_{diff,i,sol}$ are the total ohmic and the total diffusive flux (calculated as described in Appendix A), respectively and $J_{cal,i,sol}$ is the calibration parameter used to correct the Nernst-Plank equation.

There are twelve $J_{cal,i,sol}$ calibration parameters in total, since the ions under consideration are four (Na^+, Cl^-, H^+, OH^-) and the solutions are three (i.e., acid, base and salt). However, certain relationships exist among these parameters. One of these is the mass balance equation between the calibration fluxes of the three solutions flowing in an EDBM stack:

$$J_{cal,i,acid} + J_{cal,i,base} + J_{cal,i,salt} = 0 \quad (118)$$

The second relationship is the electroneutrality requirement between the calibration parameters:

$$\sum J_{cal,i,acid}\, z_i = 0 \quad (119)$$

$$\sum J_{cal,i,base}\, z_i = 0 \quad (120)$$

where the sum is extended to all the ions. The flux calibration parameters and ion-diffusivities used in the model are reported in

Table 17. All the calibration fluxes ranged, in all the cases, from 2% to 7% for the main ion of each compartment compared to the total flux of these ions in the channel.

The ion-diffusivities in the membranes were also obtained from the calibration of the model due to the difficulty in estimating their values from the experimental tests.

Finally, a correction factor for the cell pack areal resistance is considered because a decrease in the apparent stack areal resistance is observed as a function of the current density at a fixed target concentration of the base solution. This reduction is attributed to the membrane resistance, which is the predominant resistance of the stack, and the variations of the solution resistances are considered in the model. In Figure 55, the apparent stack areal resistance is reported as a function of current density for a target concentration of 1 mol L^{-1} NaOH.

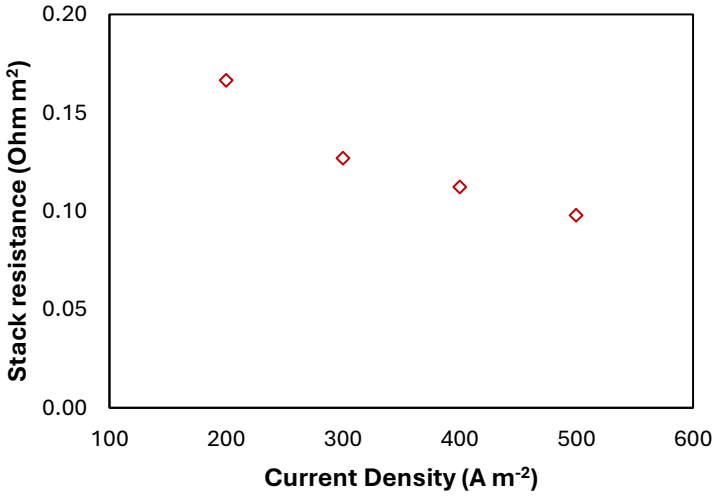

Figure 55. Apparent stack resistance, obtained as the ratio between the external voltage and the current density, as a function of the current density for a fixed target concentration of 1 mol l^{-1} of NaOH, using the feed and process configuration.

The same correction factor for the stack resistance is applied to all the membranes and it is reported as a function of the current density.

$$R_{cal} = 3.7\ 10^{-6}\ i^2 - 4.1\ 10^{-3}\ i + 2.3 \quad (121)$$

Table 17. Calibration parameters adopted in the model to account for non-ideal phenomena such as internal leakages, pressure differences between channel, deformation and fouling of membranes.

	Acid	base	salt		AEM	CEM	AEL	CEL
	(mol m^{-2} s^{-1}) 10^5				(m^2 s^{-1}) 10^{11}			
$J_{cal,sol,Na}$	7	-13.2	6.2	$D_{Na,m}$	3.1	1	4.1	5.7
$J_{cal,sol,Cl}$	-14.2	8.2	5.99	$D_{Cl,m}$	1.6	1.6	2.2	8.5
$J_{cal,sol,OH}$	0.8	-22.4	21.6	$D_{OH,m}$	9.5	7.5	6	6
$J_{cal,sol,H}$	-20.4	-1	21	$D_{H,m}$	7.35	7.1	2	14.6

The above calibration procedure resulted in the simulated vs experimental trend illustrated in Figure 56, where acid and base concentrations as well as the voltage applied to the stack are shown for a feed and bleed operating configuration. The discrepancy between the model results and the experimental values was evaluated, with an average discrepancy of 5% identified across all variables. In all cases, discrepancy values lower than 11% were recorded. When comparing this discrepancy will the experimental error (i.e., 4–5%), the values seem comparable, further confirming the high predictive capability of the model.

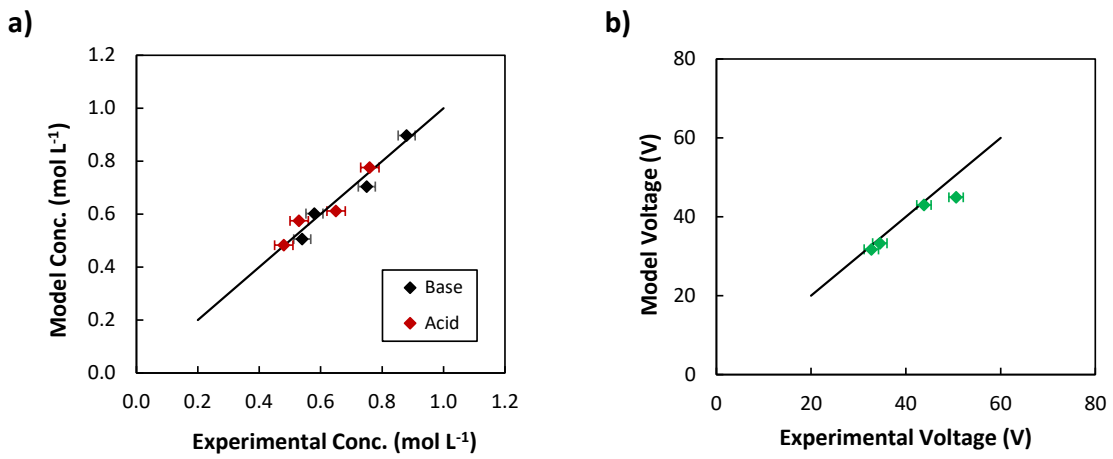

Figure 56. Comparison between experimental and model results in terms of acid and base concentration as well as of voltage applied to the stack.

4.2.4. Model validation

To validate the model calibration, the tests conducted in closed-loop with the EDBM pilot plant were employed. The model was validated under three different process conditions, specifically at current densities of 300, 400 and 500 A m^{-2} (tests described in 3.4). The comparison between the model predictions and experimental results is illustrated in Figure 57. Both chemical concentrations and stack voltage profiles, as functions of time, are presented. The model accurately predicts the concentration profiles and the applied voltage is also well predicted, except for the initial phase of the test. Table 18 reports both the maximum and average discrepancies for performed tests.

Table 18. Average and maximum deviation between model and experimental results and comparison with the experimental error made in measuring concentrations and voltage.

	300 A m^{-2}				400 A m^{-2}				500 A m^{-2}			
	Discrepancy (%)		Exp. Error (%)		Discrepancy (%)		Exp. Error (%)		Discrepancy (%)		Exp. Error (%)	
	Average	Max	Average	Max	Average	Max	Average	Max	Average	Max	Average	Max
C_{acid}	3.2	6.2	3.7	8.0	6.1	8.6	6.7	9.1	3.1	7.0	3.4	6
C_{base}	1.7	2.5	3.7	8.0	3.7	8.1	6.9	9.1	5.3	11	3.3	6
U_{ext}	4.4	21	3.9	4.1	8.4	20	3.4	3.5	4.3	26	3.1	3.3

At 300 A m^{-2}, the maximum discrepancies found for the acid and base profiles resulted 6.2% and 2.5%, respectively. For the voltage profile, a maximum discrepancy of 21 % was observed, but only at the beginning of the voltage profiles when the conditioning of the membranes was not completed. Indeed, before testing the stack was stored in RO permeate (~ 350 μS cm^{-1}) and some time is required after the start-up of the test for the permeate to be replaced by the solutions. Predicting this behaviour using traditional modelling tools is challenging, and a certain membrane conditioning time period should be determined experimentally. Increasing the current density to 400 A m^{-2} does not alter the model predictive capability. Indeed, the average discrepancies ranged between 3.7% and 8.4%. As in the previous test, a maximum voltage discrepancy of 20% was noted at the beginning and can also be attributed to the membranes incomplete conditioning. At 500 A m^{-2}, the maximum current density tested, discrepancies remained lower than 10% apart from the voltage, for which a maximum voltage discrepancy of 26% was observed at the beginning (due to membranes' incomplete conditioning), while on average the discrepancy was 8.4%. It is worth noting that the average discrepancies found resulted comparable with the experimental errors observed in the measurement of these variables, typically between 3–6%.

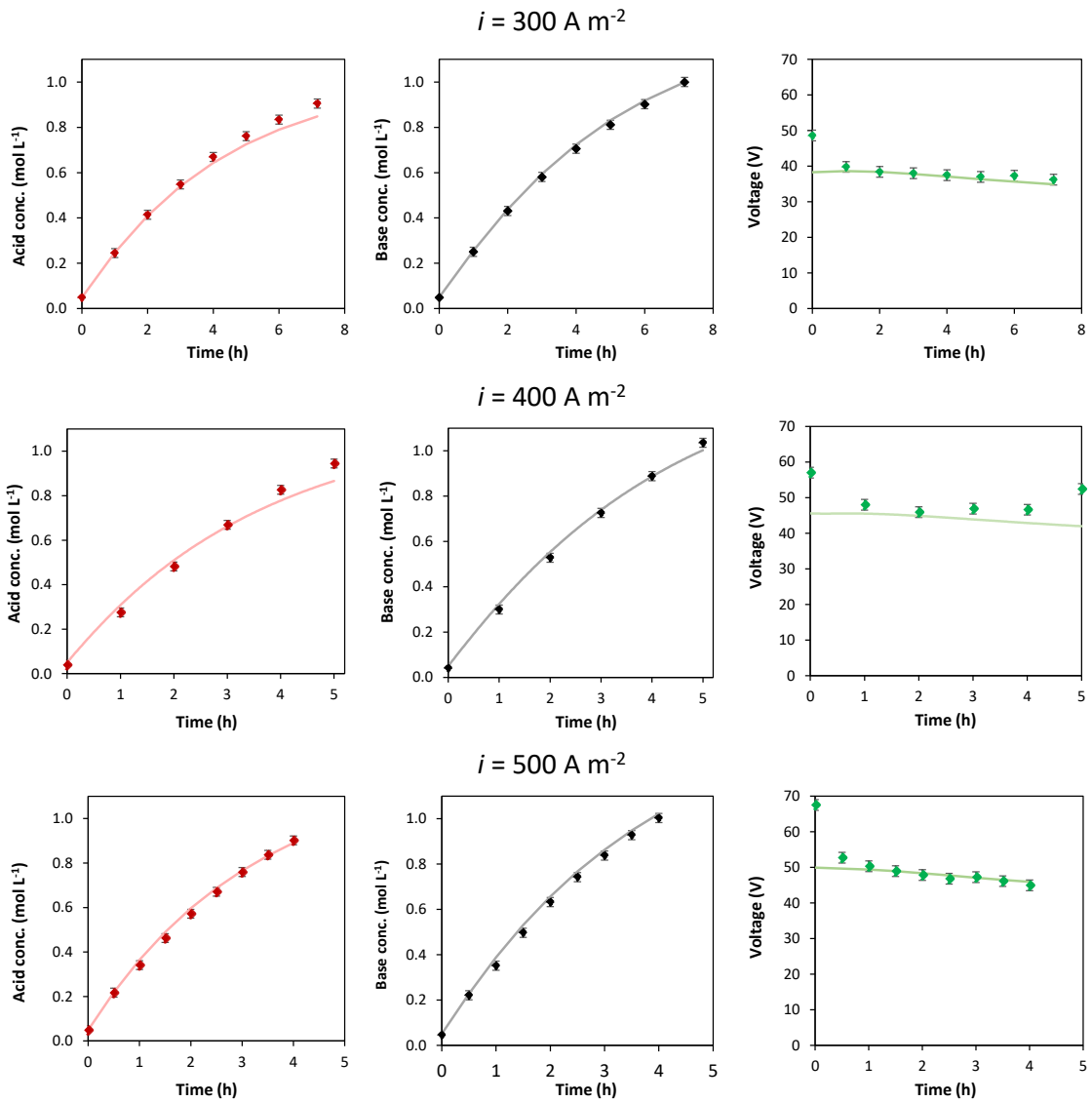

Figure 57. Trends of the main variables of the EDBM process (acid and base concentration as well as voltage applied to the stack) for the three different tests performed in closed-loop mode at constant current densities. Symbols represent experimental results, while the continuous line represents model results.

4.2.5. Electrical profiles and parasitic currents evaluation for the internal staging configuration

In this section, the main output of the stack model, i.e., current and voltage profiles, are shown to better understand how the internal staging configuration works. Additionally, the impact of parasitic currents on the stack performance is also evaluated.

Voltage and current profiles as a function of the number of triples are reported in Figure 58 for a test conducted in feed and bleed mode at 400 A m^{-2} and fixing a target concentration of base of 1 mol L^{-1}. An inlet concentration of 1 mol L^{-1} of NaCl was employed for the salt steam, while, for acid and base lines, water with a low salt content (1 mmol L^{-1} of NaCl) was utilised.

The total current is supplied from the anode to the cell packs, and it is split inversely proportional to the cell pack resistances. This fact can be observed in the current profile (Figure 58a) where two red symbols are shown. The current supplied to the second cell pack was slightly higher due to its lower resistance. Along the cell packs, the current displayed a minimum around the middle, at triplets 11 and 30 for the first and second cell packs, respectively. Moving from the anode to the cathode, the current divides in each triplet and a certain portion flows through parasitic paths (manifolds and channels) instead of passing through the active membrane area. The observed minimum in the current profile for each cell pack is correlated to the relative weight of the cell pack resistance and the resistance of the parasitic pathways in each stack position (i.e., in each triplet). At the end of the cell packs (cathode side), the electrical current in the final triplets (i.e., 1 and 40) equals that reaching the cathode. Ultimately, the sum of the currents in the two cathodes is equal to the total current supplied to the stack.

The voltage profile was determined by setting the cathode voltage to zero and evaluating the voltage drop across each triplet of the cell pack and its respective cathode. The trend was almost symmetric between the two cell packs, with small changes due to the difference in the conductivities of the solutions flowing inside. The red symbol in Figure 58b represents the anode voltage, i.e., the external voltage applied to the stack.

For the current profile depicted in Figure 58b the percentage of unused current due to parasitic currents was evaluated using equations (87). This value represents the

percentage reduction of the average current utilized by the stack to produce chemicals compared to the total current supplied by the DC drive. A value of 3.1% was found for the entire stack while at minimum points of the current profile local unused current values of 4.5% and 4.7% were found for the first and second cell packs, respectively. These low values resulted from the small number of triplets present in each cell pack and from the well-designed EDBM stack in terms of channel length and manifold diameter. Consequently, it can be stated that the internal staging configuration with a shared anode effectively allows for a reduction of the parasitic currents, despite the linking manifold, and minimises the capital expenditure compared to the use of two separate EDBM stacks in series.

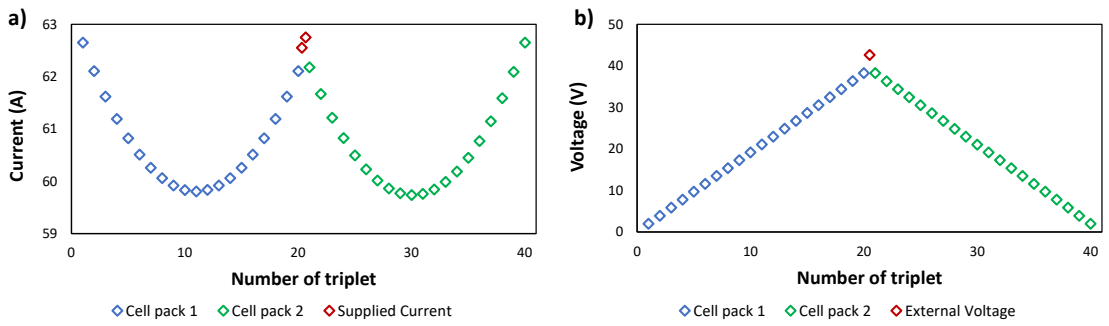

Figure 58. Current and voltage profiles along the entire EDBM stack obtained with the model. The blue and green symbols represent the first and the second cell pack, respectively; the red symbols represent the anode, which supplies the current to both cell packs. The voltage read at the anode is equal to the external voltage (the voltage in the cathodes is assumed equal to 0). The profiles were obtained at 400 A m^{-2}, fixing the target concentration of NaOH to 1 mol l^{-1}.

4.2.6. Techno-economic analysis of EDBM potential

In this section, the validated model is used to conduct a sensitivity analysis based on the main process variables and, secondly, an economic evaluation of the Levelized Cost of sodium hydroxide (LcoNaOH). In both cases, the feed and bleed process configuration was used as it is attractive for industrial applications.

The sensitivity analysis investigates the effect of varying current density and target concentration of sodium hydroxide on the key performance indicators of the EDBM

process, (described in section 2.5). The variation range of these operating variables was selected to offer insights pertinent to industrial applications. The target concentration varied between 0.5–1 mol L^{-1} aligning with the interests of various applications highlighted in section 1.2 The current density, instead, was tested between 320–600 A m^{-2}, which guarantees high specific productivity (SP), reasonable ohmic loss and safe conditions for the bipolar membranes. Also in this case, an inlet concentration of 1.0 mol L^{-1} of NaCl was employed for the salt steam, while, for acid and base lines, water with a low salt content (1 mmol L^{-1} of NaCl) was utilised, emulating RO permeate. Different target concentrations were obtained by changing the outlet flow rates from the entire EDBM unit while maintaining constant flowrates through the stack (constant channels flow velocities) equal to 5 L min^{-1}. The outlet flowrates of acid and base were maintained equal whereas the salt outlet flowrate was twice as high reaching up to 4.4 L min^{-1}. For values of chemicals outlet flowrates higher than 2.2, the salt outlet flowrate was maintained constant at 4.4 L min^{-1}. In the simulated conditions, the limiting current density, calculated with the Strathmann's approach (Section 4.2.1.1.2), was considerably lower compared to the applied current density, with value up to 20 A m^{-2}. The results of the sensitivity analysis are reported in Figure 59 in terms of key performance indicators.

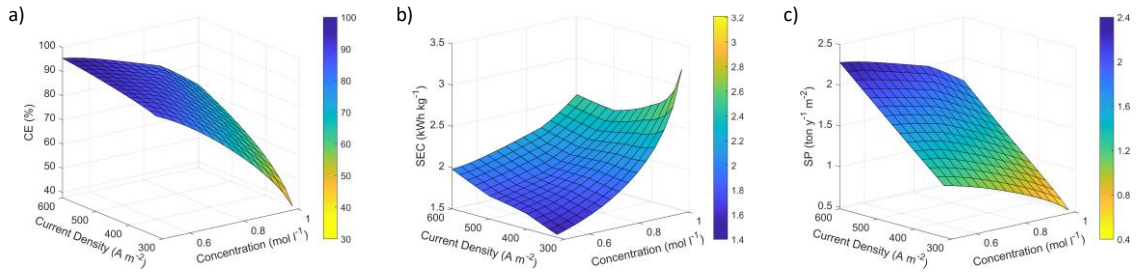

Figure 59. Trends of key performance indicators, CE, SEC and SP, as a function of current density and target concentration of sodium hydroxide.

The Current Efficiency (CE) shows a decreasing trend as the target concentration rises at a fixed current density. Instead, it increases when the current density rises at

a constant target concentration. The decrease as the concentration rises could be easily explained: by increasing the sodium hydroxide target concentration at a constant current density the average concentration in the base channel increases. This in turn results in a greater concentration difference across the CEM (and similarly across the AEM) thereby intensifying the diffusive flux of hydroxide ions to the salt channel. The rise in current efficiency, at a constant target concentration, by increasing the current density is less intuitive. This phenomenon is strictly related to the simulated process configuration, in which both the outlet concentration and flowrate that pass through the stack remain fixed for the base stream. Therefore, when increasing the current density the EDBM system increases its productivity reducing the concentration of the base stream at the stack inlet. This has a positive effect on the current efficiency due to the lower average concentration of NaOH in the base channel, which decreases the diffusive phenomena across the CEM. At 600 A m^{-2} the highest current utilisation is observed, with values in the range 72–95%, while, reducing the current density to 320 A m^{-2}, gives a CE between 38% and 88%.
The SEC depends directly on the voltage applied to the stack and inversely on the current efficiency. The voltage in turn shows an increase with the current density while its dependence on the base concentration is inversely proportional and quite weak. This is a consequence of the dominant resistance of the system which is the resistance of the cell packs. Overall, the SEC shows an increase with the concentration due to the dominant effect of the decreasing CE while its trend as a function of the current density is more complex because both voltage and CE play a counteracting role.

Two different trends of SEC as a function of the current density are observed depending on the target concentration of sodium hydroxide. At low concentration (i.e, lower than 0.8 mol L^{-1}) an increasing trend with the current is observed, while a trend with a minimum is observed at a high concentration (i.e, higher than 0.8 mol L^{-1}). For

low target concentration of sodium hydroxide, the effect of the voltage is dominant in the SEC. In contrast both the effects of voltage and CE become significant at high concentrations and a minimum value is observed around 500 A m^{-2}. The minimum values observed for the SEC are in the range 1.5–2.5 kWh kg^{-1} for target concentration between 0.5 mol L^{-1} and 1 mol L^{-1}, respectively.

The SP behaviour is quite similar to that observed for the CE. Under a constant current density, the SP and CE show a proportional relationship. When the current density is not fixed, the SP depends both on the CE and the current density. Maximum values between 2.3 ton y^{-1} m^{-2} and 1.7 ton y^{-1} m^{-2} are observed at 600 A m^{-2}, for sodium hydroxide concentration in the range 0.5–1 mol L^{-1}.

The economic analysis (Figure 60) evaluates the LcoNaOH using the same operating conditions applied in the sensitivity analysis, considering variable current density and target concentration of NaOH. Additionally, the effect of varying the specific cost of electricity and the triplet cost on the LcoNaOH is examined for three different NaOH target concentrations, namely: 0.5, 0.75 and 1 mol L^{-1}.

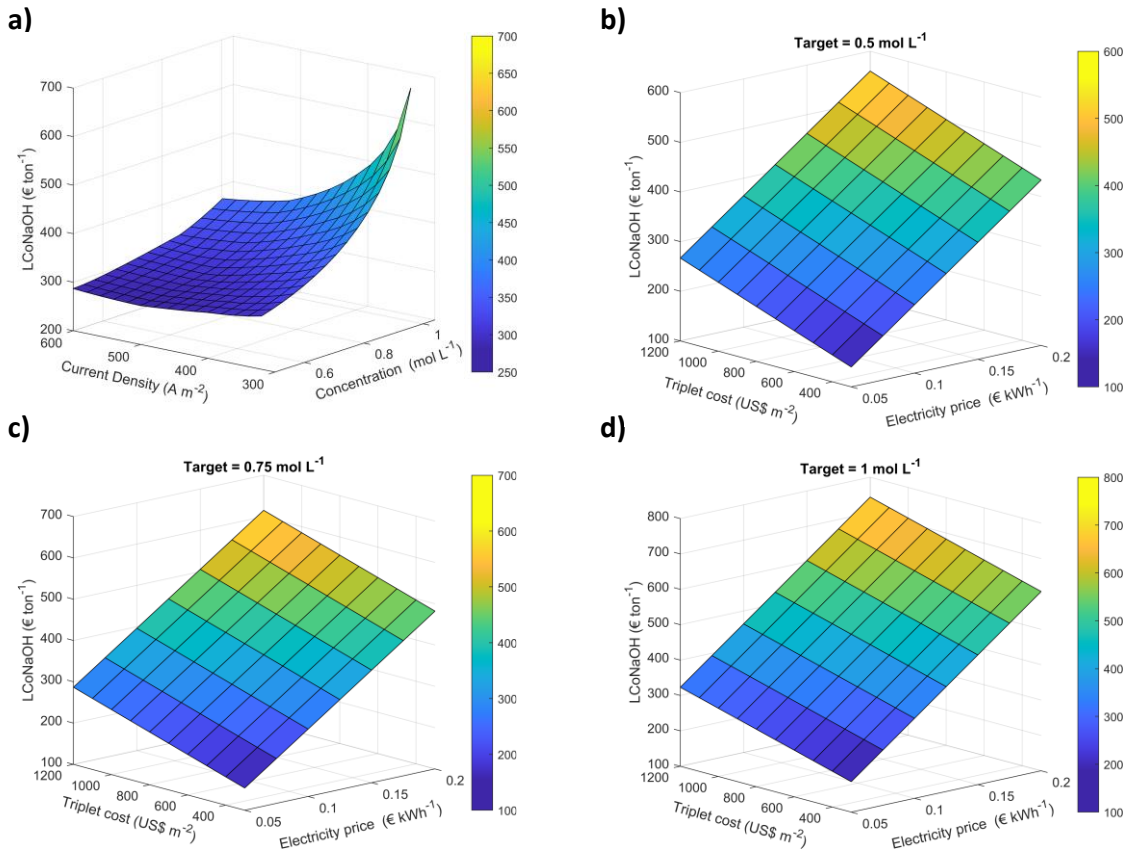

Figure 60. a) Levelized cost of sodium hydroxide (LcoNaOH) as a function of NaOH target concentration and current density for a fixed triplet cost (600 US$ m^{-2}) and electricity price (0.1 € kWh^{-1}). b) variation of LcoNaOH with electricity price and triplet cost, for the target concentration of 0.5 mol L^{-1}, c) 0.75 mol L^{-1} and d) 1 mol L^{-1}. Current density is fixed to 500, 520 and 600 A m^{-2}, for cases b, c and d, respectively.

The LcoNaOH rises with increasing concentration due to the decreasing CE of the process. At 320 A m^{-2}, the obtained values of LcoNaOH are in the range 310–680 € ton^{-1}, while lower values, in the range 290–370 € ton^{-1}, are observed at 600 Am^{-2}, for the entire range of concentration studied (0.5–1 mol L^{-1}). Raising the current density, a minimum can be identified for target concentrations lower than 0.86 mol L^{-1}, while a decreasing trend is observed for higher NaOH concentrations. The minimum lies between 500 A m^{-2} and 560 A m^{-2}, with LcoNaOH values in the range 280–320 € ton^{-1} (NaOH concentration in the range 0.5-0.86 mol L^{-1}). The observed minimum results from the counteracting effects of TEC and PC on the LcoNaOH. The TEC is associated with the SEC while the PC is linearly proportional to the SP. In fact, in the region of the low

concentration values (< 0.8 mol L^{-1}), the SEC shows an increasing trend with the current density, which, in turn, produces an increase in the TEC. In the same region, the SP shows a growing trend with the current density, which produces an increase in the PC.
For high NaOH concentrations (> 0.8 mol L^{-1}), the TEC variation becomes dominant on the LcoNaOH, especially at low current densities. On the other side, the PC shows an increasing trend with current density, resulting in a noticeable downward trend of LcoNaOH.

From Figure 60b, c, d, it is evident that E_p has a dominant effect on the LcoNaOH, while the triplet cost has a lower influence. Interestingly, in the most favourable conditions, indicating a scenario with low electricity and membrane costs, a production cost below 150 € ton^{-1} of NaOH can be achieved when a target of 0.5 mol L^{-1} is fixed, while increasing the target to 1 mol L^{-1} the minimum in LCoNaOH rises to 180 € ton^{-1}. All that shows that the current price of membranes enables the production of valuable chemicals at a cost lower than the current market price of NaOH , ranging between 360 € ton^{-1} and 680 € ton^{-1} [119], [120]. Moreover, the obtained production costs result comparable or even lower to those already reported in the literature, in the range 340-370 € ton^{-1} [104], [121], for similar concentrations of sodium hydroxide.

4.2.7. Preliminary analysis of multi-stage EDBM potential

As an example of the use of the presented model for process intensification analysis, a double-stage EDBM unit has been simulated in similar operating conditions. Specifically, two stacks with equal features as the one described in section 3.1, are connected in serial arrangement as indicated in Figure 61.

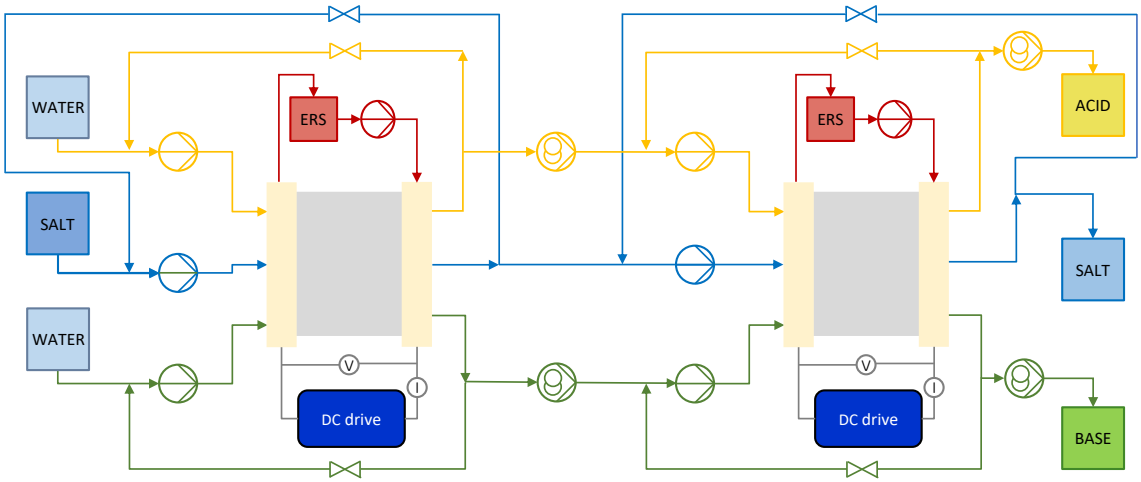

Figure 61. Schematic representation of the simulated double-stage EDBM configuration.

The same inlet concentrations and outlet flowrate ratio (described in 4.2.6) were employed for acid, base and salt lines. The outlet streams from the first stack are directly sent to the second stack, while the flowrate in the recirculating loop is chosen to maintain the same channel speed in the two stacks (i.e., 2.6 cm s^{-1}).

The double-stage configuration enables to distribute the concentration variation of the produced chemicals, in a way that the operating conditions of each stack can be optimised for that specific variation. In this case, the system is employed to produce 1 mol L^{-1} NaOH, fixing the outlet concentration of each stack equal to 0.6 mol L^{-1} and 1 mol L^{-1} for the first stack and second stack, respectively. The choice of a higher concentration variation (from ~0 to 0.6 mol L^{-1}) in the first stack, is due to the higher CE at lower concentration, which allows to produce more product in the first stage. The operating conditions of the first stack are those identified as optimal in the economic analysis above. For the second stack, inlet/outlet concentrations are fixed, while the current density is determined by the model itself.

The results of the analysis are reported in Table 19, showing a comparison with a single stage EDBM unit used to produce the same target. As expected, the first stage works much more efficiently than the single unit, due to the lower average concentration

in the channels. Instead, in the second stage, a slightly poorer performance is observed, due to the higher average concentration inside the base channel (0.88 mol L^{-1} compared to 0.83 mol L^{-1}). However, comparing the overall performance of the double stage with the single stage, an important improvement in all energetic performance indicators can be observed, with an 8% reduction in SEC and a 4% increase in CE. The SP shows a slight reduction (6%), but this effect is attenuated by the doubled total membrane area. Finally, comparing the two configurations in terms of LCoNaOH, a reduction of 10% is observed for the double stage, highlighting the benefits of using multi-stage EDBM to reduce the production cost of NaOH.

Table 19. Comparison between single and double-stage EDBM's configurations for a target concentration of 1 mol L^{-1} NaOH. The performances of each stage as well as the overall are reported for the base stream.

EDBM Configuration	**Stage**	**Target (mol L^{-1})**	**i (A m^{-2})**	**SEC (kWh kg^{-1})**	**CE (%)**	**SP (ton y^{-1} m^{-2})**	**LCoNaOH (€ ton^{-1})**
Single stage	-	1	600	2.5	72	1.7	372
Double stage	1	0.6	500	1.8	90	1.8	-
	2	1	573	2.9	61	1.4	-
	Overall	1	-	2.3	75	1.6	334

4.3 Dynamic modelling

A dynamic model of the EDBM process has been developed to effectively simulate and study its behaviour under transient regimes, considering the inertia of the system in response to variations. Transient regimes are common in the field of renewable energy sources and load levelling in power stations thus, the importance of developing a dynamic model. To the best of the author's knowledge, no previous fully dynamic EDBM models have been developed and validated.

4.3.1. Multi-scale model modification

This section describes the modification made to the steady-state model described in 4.2 in order to predict also transient regimes.

4.3.1.1. Level 1: the channel model and the bipolar membrane model

At the first level, no modifications were made with respect to the model described in 4.2.1.1.

4.3.1.2. Level 2: the triplet model

At this level, mass balance are computed for each channel, considering all the entering or leaving fluxes to obtain concentration profiles along the channels. The modification involves the introduction of the accumulation term in the mass balances. The mass balances for the acid channels are calculated as follows:

$$b\ d_a \frac{\partial C_{Na^+,a}}{\partial t} + \frac{\partial Q_a C_{Na^+,a}}{\partial x} = b\ J_{tot,Na^+,a} + \frac{G_{salt,CEL}}{L\ 10^{-3}\ M_{NaCl}} \quad (122)$$

$$b\ d_a \frac{\partial C_{Cl^-,a}}{\partial t} + \frac{\partial Q_a C_{Cl^-,a}}{\partial x} = b\ J_{tot,Cl^-,a} + \frac{G_{salt,CEL}}{L\ 10^{-3}\ M_{NaCl}} \quad (123)$$

$$b\ d_a \frac{\partial C_{H^+,a}}{\partial t} + \frac{\partial Q_a C_{H^+,a}}{\partial x} = b\ \left(J_{tot,H^+,a} - J_{tot,OH^-,a}\right) \quad (124)$$

$$C_{OH^-,a} = 10^3\ 10^{\left(-14-\log\frac{C_{H^+,a}}{10^3}\right)} \quad (125)$$

$$\frac{\partial Q_a \rho_a}{\partial x} = \left(J_{tot,Na^+,a}\, M_{Na^+} + J_{tot,Cl^-,a}\, M_{Cl^-} + \left(J_{tot,H^+,a} - J_{tot,OH^-,a}\right) M_{H^+}\right) b\, 10^{-3} + \frac{G_{w,a}}{L} + \frac{G_{salt,CEL}}{L} + J_{tot,OH^-,a}\, M_{H_2O}\, b\, 10^{-3} \quad (126)$$

where L, b, d_a are the length, width and thickness of the acid channel, respectively, $C_{i,a}$ is the molar concentration of ion i in the acid channel, Q_a and ρ_a are the volumetric flowrate and mass density of the acid channel, $J_{tot,i,a}$ is the total flux, $G_{w,a}$ and $G_{salt,\ CEL}$ are the overall water mass flux entering in the acid channel and salt water flux through the CEL layer, M is the molar mass.

Similar equations can be written for the salt channels:

$$b\, d_s \frac{\partial C_{Na^+,s}}{\partial t} + \frac{\partial Q_s C_{Na^+,s}}{\partial x} = b\, J_{tot,Na^+,s} \quad (127)$$

$$b\, d_s \frac{\partial C_{Cl^-,s}}{\partial t} + \frac{\partial Q_s C_{Cl^-,s}}{\partial x} = b\, J_{tot,Cl^-,s} \quad (128)$$

$$b\, d_s \frac{\partial C_{H^+,s}}{\partial t} + \frac{\partial Q_s C_{H^+,s}}{\partial x} = b\left(J_{tot,H^+,s} - J_{tot,OH^-,s}\right) \quad (129)$$

$$C_{OH^-,s} = 10^3\, 10^{\left(-14-\log\frac{C_{H^+,s}}{10^3}\right)} \quad (130)$$

$$\frac{\partial Q_s \rho_s}{\partial x} = \left(J_{tot,Na^+,s}\, M_{Na^+} + J_{tot,Cl^-,s}\, M_{Cl^-} + \left(J_{tot,H^+,s} - J_{tot,OH^-,s}\right) M_{H^+}\right) b\, 10^{-3} + \frac{G_{w,s}}{L} + J_{tot,OH^-,s}\, M_{H_2O}\, b\, 10^{-3} \quad (131)$$

Regarding the base channels, the mass balances are given by:

$$b\, d_b \frac{\partial C_{Na^+,b}}{\partial t} + \frac{\partial Q_b C_{Na^+,b}}{\partial x} = b\, J_{tot,Na^+,b} + \frac{G_{salt,AEL}}{L\, 10^{-3}\, M_{NaCl}} \quad (132)$$

$$b\, d_b \frac{\partial C_{Cl^-,b}}{\partial t} + \frac{\partial Q_b C_{Cl^-,b}}{\partial x} = b\, J_{tot,Cl^-,b} + \frac{G_{salt,AEL}}{L\, 10^{-3}\, M_{NaCl}} \quad (133)$$

$$b\, d_b \frac{\partial C_{OH^-,b}}{\partial t} + \frac{\partial Q_b C_{OH^-,b}}{\partial x} = b\left(J_{tot,OH^-,b} - J_{tot,H^+,b}\right) \quad (134)$$

$$C_{H^+,b} = 10^3\, 10^{\left(-14-\log\frac{C_{OH^-,b}}{10^3}\right)} \quad (135)$$

$$\frac{\partial Q_b \rho_b}{\partial x} = \left(J_{tot,Na^+,\mathrm{b}}\, M_{Na^+} + J_{tot,Cl^-,\mathrm{b}}\, M_{Cl^-} + \left(J_{tot,OH^-,\mathrm{b}} - J_{tot,H^+,\mathrm{b}}\right) M_{OH^-}\right) b\, 10^{-3} + \frac{G_{w,\mathrm{b}}}{L} + \frac{G_{salt,AEL}}{L} + J_{tot,H^+,\mathrm{b}}\, M_{H_2O}\, b\, 10^{-3} \quad (136)$$

all other symbols have the same meaning as defined in the previous equations.

An assumption made in deriving the above equations is that the variation in mass density over time is negligible. Specifically, the mass density is calculated at the channel entrance and it is maintained constant along the channel. This assumption is reasonable since a small amount of ions are dissolved in solutions and, consequently, the mass density remains nearly constant (variations lower than 1% are expected).

4.3.1.3. Level 3: the cell pack model

Also in the cell pack model, the accumulation term was introduced in mass balances to consider unsteady-state conditions in the manifolds (i.e., collector and distributor). For the distributor, the following equations can be written as follows:

$$\frac{\pi {d_d}^2}{4}\delta \frac{dC_{d,1,i,sol}}{dt} = \frac{Q_{tot,in,sol}C_{in,i,sol} - Q_{x=0,1,sol}C_{x=0,1,i,sol}}{N_{holes}} - Q_{d,1,sol}C_{d,1,i,sol} \quad (137)$$

$$Q_{d,1,sol} = \frac{Q_{tot,in,sol} - Q_{x=0,1,sol}}{N_{holes}} \quad (138)$$

$$\frac{\pi {d_d}^2}{4}\delta \frac{dC_{d,k,i,sol}}{dt} = Q_{d,k-1,sol}C_{d,k-1,i,sol} - \frac{Q_{x=0,k,sol}C_{x=0,k,i,sol}}{N_{holes}} + -Q_{d,k,sol}C_{d,k,i,sol} \quad (139)$$

$$Q_{d,k,sol} = Q_{d,k-1,sol} - \frac{Q_{x=0,k,sol}}{N_{holes}} \quad (140)$$

$$Q_{d,N,sol}C_{d,N,i,sol} = Q_{dis,N-1,sol}C_{dis,N-1,i,sol} \quad (141)$$

where d_d and δ are the diameter of the distributor and the thickness of a triplet, $C_{d,k,i,sol}$ and $C_{x=0,k,i,sol}$ are the concentration in the distributor in position *k* of ion *i* in the *sol* (i.e., acid, base and salt) compartment and the concentration of ion *i* at the entrance of *k-th* triplet of the *sol* compartment, $C_{in,i,sol}$ is the inlet concentration of ion *i* in the *sol*

compartment, $Q_{tot,in,sol}$ and $Q_{x=0,k,sol}$ are the total flowrate entering in the *sol* compartment and the entering flowrate in *k-th* triplet of the *sol* compartment, N_{holes} in the number of holes in the spacers and $Q_{d,k,sol}$ is the distributor volumetric flowrate in position *k* of the *sol* compartment. Equations (139) and (140) are valid for *k* in the range 2 to N-1, where N is the number of triplets in the cell pack. Constant mass density is considered in equations (138) and (140), since the same solution with fixed concentration is distributed in all the channels.

For the collector, the following equations are utilised:

$$Q_{c,1,sol}\rho_{c,1,sol} = \frac{Q_{x=L,1,sol}\rho_{1,sol}}{N_{holes}} \tag{142}$$

$$\frac{\pi {d_c}^2}{4}\delta\frac{dC_{c,k,i,sol}}{dt} = \frac{Q_{x=L,k,sol}C_{x=L,k,i,sol}}{N_{holes}} + Q_{c,k-1,sol}C_{c,k-1,i,sol} + -Q_{c,k,sol}C_{c,k,i,sol} \tag{143}$$

$$Q_{c,k,sol}\rho_{c,k,sol} = \frac{Q_{x=L,k,sol}\,\rho_{k,sol}}{N_{holes}} + Q_{c,k-1,sol}\rho_{c,k-1,sol} \tag{144}$$

where $Q_{c,k,sol}$ and $Q_{x=L,k,sol}$ are the collector volumetric flowrate in position *k* of the *sol* compartment and the exit flowrate from the *k-th* triplet of the *sol* compartment, $\rho_{c,k,sol}$ and $\rho_{k,sol}$ are the mass density in position *k* of the *sol* collector and the mass density of the of the *sol* compartment in the *k-th* triplet, $C_{c,k,i,sol}$ and $C_{x=L,k,i,sol}$ are the concentration in the collector in position *k* of ion *i* in the *sol* compartment and exit concentration of ion *i* in *k-th* triplet of the *sol* compartment and d_c is the dimeter of the collector. Equations (143) and (144) are valid for *k* in the range 2 to N.

4.3.1.4. Level 4: the stack model

At the fourth level, no modifications were made with respect to the model described in 4.2.1.4.

4.3.1.5. Level 5: the external hydraulic circuit model

In addition to the dynamics of the EDBM stack, it is essential to consider the dynamic of the external hydraulic circuit composed of tubes. Indeed, in feed and bleed process configuration the recirculating loops significantly impact the dynamic of EDBM process. Therefore, it is important to account for the total volume of tubes connecting the stack outlet and inlet. To this end, two tubes for each compartment are introduced, after the convergent node and before the divergent node, in the simulated process flow sheet and unsteady-state mass balances are computed utilising the following equations:

$$\frac{\pi {D_{tube}}^2}{4}\frac{\partial C_{cn,i,sol,out}}{\partial t} + Q_{cn,sol,out}\frac{\partial C_{cn,i,sol,out}}{\partial x} = 0 \quad (145)$$

$$\frac{\pi {D_{tube}}^2}{4}\frac{\partial C_{dn,i,sol,in}}{\partial t} + Q_{dn,sol,in}\frac{\partial C_{dn,i,sol,in}}{\partial x} = 0 \quad (146)$$

where D_{tube} is the internal diameter of the tube, $C_{cn,i,sol,out}$ and $C_{cd,i,sol,in}$ are the molar concentration of ion *i* in the *sol* line exiting from the convergent node and entering in the divergent node, $Q_{cn,sol,out}$ and $Q_{dn,sol,out}$ are the volumetric flowrate in the *sol* line exiting from the convergent node and entering in the divergent node.

4.3.2. Dynamic model validation

In order to validate the developed dynamic model of the EDBM process, the pilot plant described in section 3.1 was adopted, using the feed and bleed process configuration. Step variations in the chemical volumetric flowrates and in the current density were considered. To verify the prediction capabilities of the model, it is essential to compare the entire process dynamic from one steady-state condition to another. Instead of collecting a large number of samples at high frequency, which can introduce errors, the model was validated in terms of chemical conductivities. Indeed, conductivities can be utilised as an effective inferential variables to online monitor the concentration of electrolytic solutions, as observed in previous sections. For the validation test a synthetic

sodium chloride solution, with 1 mol L^{-1} concentration, was employed in the salt compartment and RO permeate (~ 350 μS cm^{-1}) was fed to the acid and alkaline compartments, adopting the feed and bleed process configuration. In this way, chemicals with a high purity are expected, thereby enhancing the reliability of using the conductivity for model validation. The results of the model validation are reported in Figure 62. The left side of the figure refers to a step variation in the outlet chemical volumetric flowrates, from 2 L min^{-1} to 1 L min^{-1}, as shown in Figure 62a. The corresponding variation in the outlet chemical concentrations and conductivity are shown in Figure 62b and Figure 62c, respectively. The time span depicted is sufficient to reach the new steady-state condition. Three samples were collected in the stable zones and manual titrations were performed. The results were compared with the trends predicted by the model showing very similar values. Finally, the conductivity trends obtained from online conductivity meters were compared with those predicted by the model. Interestingly, the model accurately captures the entire dynamic for both products. On the right side of Figure 62, the validation for a step change in current density from 400 A m^{-2} to 200 A m^{-2} is shown. The results are presented in a similar way as those for the step change in the flowrates. In this case as well, the model shows good agreement with the experimental results in terms of steady-state outlet concentrations and conductivity trends. In all the cases, discrepancies lower than 15 % were observed, demonstrating the high fidelity of the model.

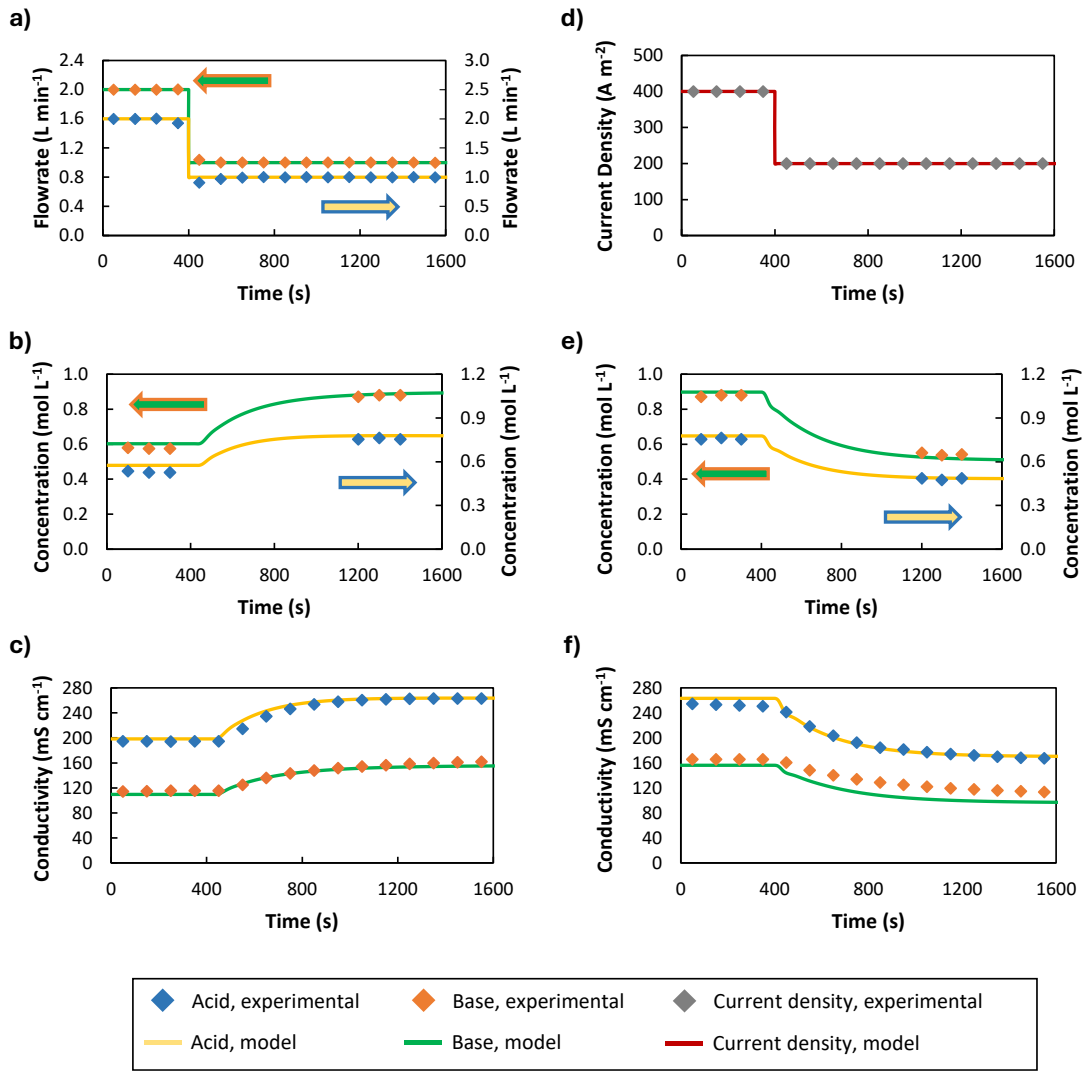

Figure 62. Validation of the dynamic model utilising a first principles approach. a) trends of the chemical flowrates, b) chemical outlet concentrations profiles and c) chemical outlet conductivities trends due to the step variation in the chemical flowrate; d) trend of the current density, e) chemical outlet concentrations profiles and f) chemical outlet conductivities trends due to the step variation in the current density.

4.3.3. Analysis of the dynamic behaviour of EDBM

The developed dynamic model was utilised to conduct a time response analysis of the EDBM system for the step variation in the current density and in the outlet flowrate of products. The analysis was performed adopting the continuous feed and bleed process configuration and the results are reported for the alkaline product, which represents the more profitable one. However, analogous results are expected for the acid, since it shows the same functional dependence on the current density and on the corresponding outlet

flowrate. The simulations were carried out utilising the layout of the EDBM pilot plant described in section 3.1, in terms of geometry and installed membrane area. The inlet concentration and operating conditions fixed during the simulation are summarised in Table 20.

Table 20. Inlet concentrations and operating conditions set in the model during the simulations.

	Compartment		
	Acid	**Base**	**Salt**
$C_{HCl,sol,in}$ (mol m^{-3})	1	0	1
$C_{NAOH,sol,in}$ (mol m^{-3})	0	1	0
$C_{NaCl,sol,in}$ (mol m^{-3})	3	3	1000
$Q_{sol,in}$ (mol m^{-3})	5	5	5

The simulations were conducted at constant outlet base flowrate during the step variation in the current density and *vice versa*. The outlet flowrates of acid and base were maintained equal whereas the saline solution outlet flowrate was twice as high reaching up to 4.4 L min^{-1}. Step variations of different amplitudes (i.e., ±12.5 ±25, ±50) were considered, starting from two different initial conditions: i) 400 A m^{-2} of current density and 2.7 L min^{-1} of outlet base flowrate, ii) 200 A m^{-2} of current density and 1.1 L min^{-1} of outlet base flowrate. Both conditions correspond to an outlet base concentration of 0.5 mol L^{-1}. The response time was calculated as the time needed to reach 98% of the new steady-state concentration after the step change. The results of the analysis are shown in Figure 63.

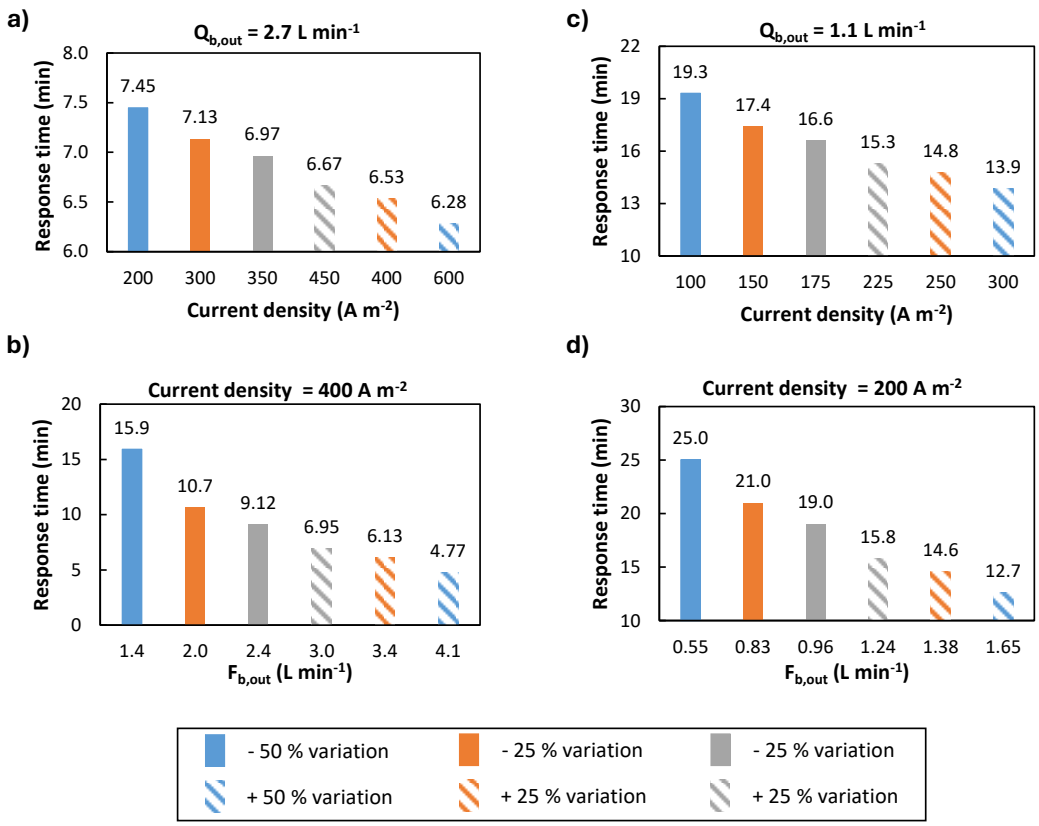

Figure 63. Starting from initial condition of 400 A m^{-2} of current density and 2.7 L min^{-1} of outlet base flowrate: a) step variations in the current density at constant flowrate of 2.7 L min^{-1}, b) step variation in the outlet base flowrate at constant current density of 400 A m^{-2}; Starting from initial condition of 200 A m^{-2} of current density and 1.1 L min^{-1} of outlet base flowrate: c) step variations in the current density at constant flowrate of 1.1 L min^{-1}, d) step variation in the outlet base flowrate at constant current density of 200 A m^{-2}.

Interestingly, the results proved that moving towards higher current densities leads to a reduction in response time for both initial conditions. This effect could be related to the higher rate of protons and hydroxide ions generation, which allows to achieve quicker the new outlet concentration. It should be noted how a low value of the outlet base flowrate severely affects the response time, Figure 63c. Indeed, this is also related to the employed process configuration (i.e., feed and bleed) which slows down the dynamic of the system as the recirculated base flowrate increases (i.e., lower outlet base flowrate). This effect can be observed also from Figure 63b and Figure 63. These charts depict a significant response time reduction as the new outlet flowrates moves towards higher values. The combined action of high current density and elevated outlet base flowrate can

reduce the response time down to 5 min, whilst the response time can increase up to 25 min in the case of reduced current density and low base outlet flowrate. This analysis gives an indication of the response time of the system as the operating conditions vary which can be used in the design of control systems for coupling EDBM with non-stationary energy sources.

4.3.4. Simulation of EDBM powered by renewable energy sources

As an application of the developed dynamic model, the coupling of the EDBM process with a photovoltaic (PV) system was considered to further reduce the carbon footprint of this process. A solar panel model, available in the literature, was utilised to reproduce the electrical and thermal behaviour of this element. The EDBM process was operated in continuous feed and bleed mode, and a proportional-integral (PI) feedback controller was developed to maintain constant chemical concentrations despite the variations in available power. The results confirmed the versatility of this process, which is able to work also with non-stationary energy sources maintaining high performance.

4.3.4.1.1. The solar panel model

To simulate solar panel modules an integrated thermal and electric model was employed. The model is derived from existing photovoltaic simulators available in the literature. Specifically, the electrical behaviour of the module is modelled through the commonly used single-diode approach [42]. This approach utilises five parameters, which are not provided in the manufacturer's datasheet, and must be extracted from other information available. In this case, a simplified method reported by Ibrahim and Anani is adopted [122], in which two of the parameters are neglected (i.e., the series and the shunt resistances). On the other hand, the dynamic thermal behaviour of the module is reproduced with the approach of Torres-Lobera and Valkealahti [123]. In this approach, the module temperature is calculated by solving a heat balance, accounting for the heat

exchange of the module with its environment (i.e., due to convection and long-wave radiation).

4.3.4.1.2. Solar irradiation data and sizing of the solar field

Solar irradiation data were taken from the European PV-GIS platform [100]. Average daily irradiation data in a specific month were obtained considering Palermo (i.e., latitude/longitude of 38.104/13.349) as location and choosing clear sky irradiance as well as fixing a plane slope of 30° and azimuth of 0°. To simulate the coupled PV-EDBM system in different irradiation scenarios, four months were selected to represent the four seasons: January for Winter, April for Spring, July for Summer, and October for Autumn. PV-GIS platform data are available with a frequency of one hour thus, gaussian curves were utilised to fit the data and implemented in the process simulator. In this way, much smaller time discretion can be used in the process simulator to effectively study the EDBM process powered by a solar energy source.

The utilised gaussian curves have the following expression:

$$f_{gauss} = A_{gauss} \exp\left(\frac{-(3600\ t - B_{gauss})^2}{2\ C_{gauss}{}^2}\right) \quad (147)$$

where A_{guass}, B_{guass} and C_{guass} are the gaussian constants and t is the process time is seconds. The gaussian constants obtained from the fitting process are reported in Table 21.

Table 21. Gaussian constants utilised to fit PV-GIS data.

Season	A_{gauss}	B_{gauss}	C_{gauss}
Winter	540	11	2.3
Spring	800	11	2.8
Summer	950	11	2.85
Autumn	700	10.5	2.5

In Figure 64 the comparison between PV-GIS data points and fitting curves.

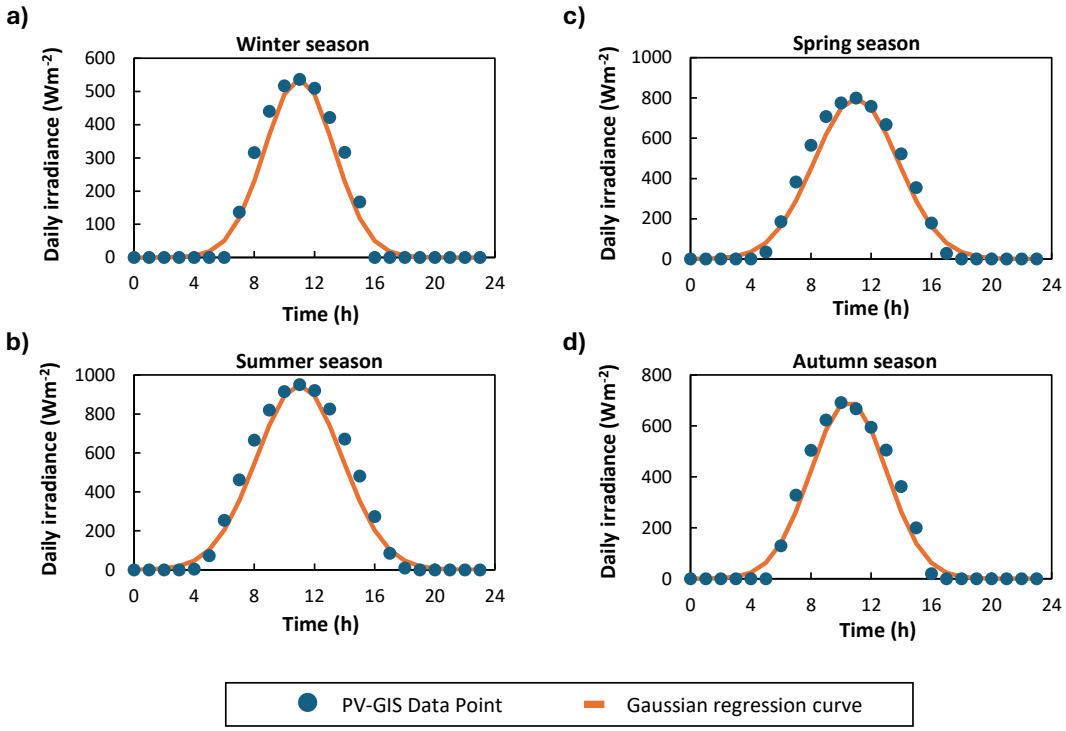

Figure 64. Comparison between PV-GIS data points and fitting gaussian curves. PV-GIS refer to Palermo (i.e., latitude/longitude of 38.104/13.349) as location and choosing clear sky irradiance as well as a fixed plane slope of 30° and azimuth of 0°.

The PV module selected to power the EDBM unit is a monocrystalline Glass-Glass 430 W TEN HCD (Solarday®, Italy). The main characteristics of the module are

reported in Table 22. The dimension of the solar field requires the definition of the number of modules arranged in parallel and in series. The maximum power consumed by EDBM as well as the corresponding current and voltage were considered for the dimension of the solar field, corresponding to ~11 kW, 192 A (i.e., 600 A m^{-2}) and 57 V, respectively. Finally, a total of 14 modules were arranged in series and 2 in parallel, enabling to power the system up to ~12 kW (i.e., 186 A and 65 V). The maximum power points of the EDBM unit and of the solar field resulted quite close to each other, thus guaranteeing that the coupled system is well dimensioned.

Table 22. Main characteristics of the monocrystalline module Glass-Glass 430 W TEN HCD (Solarday®, Italy). The reported values were obtained in standard test conditions (STC): 1000 W m^{-2} of solar irradiance, Air Mass (AM) 1.5 spectrum, and a cell temperature of 77 °F(25 °C).

Characteristic	Value	Units
Peak Power (P_{max})	430	W
Voltage P_{max} (V_{mpp})	32.31	V
Current P_{max} (I_{mpp})	13.32	A
Open circuit voltage (V_{oc})	38.31	V
Short-circuit current (I_{sc})	14.13	A
Efficiency (η)	22	%
Temperature Coeff. Of V_{oc} (μ_V)	-0.25	% $°C^{-1}$
Temperature Coeff. Of I_{sc} (μ_I)	0.05	% $°C^{-1}$
Number of cells (N_{cell})	108	-
Length (L_{mod})	1134	mm
Height (H_{mod})	1722	mm
Width (W_{mod})	35	mm

4.3.4.1.3. Development of the EDBM feedback control system

An important aspect of coupling EDBM with renewable energy sources is the development of control systems which maintain constant outlet product concentrations despite the fluctuations in the power supply. Two different control systems must be designed to effectively control the acid and alkaline products. As manipulated variables of these control loops, the outlet flowrates of products were utilised since the existent strong correlations between outlet concentration and flowrate of the same product. The current density, which has also a significant correlation with the product concentrations, was considered as a disturbance as it varies when employing renewable energy sources. However, online measurement of outlet product concentrations is not feasible, requiring samples to be collected and analysed offline. A potential solution to this problem is the use of electrical conductivities as an indirect measure of product concentrations. Indeed, the solution conductivities can be easily measured online and employed in product quality control. On the other hand, the conductivity measure can be utilised in the case of electrolytic solutions with high purity, because the conductivity is an overall measure and does not allow to consider ion contribution to the total solution conductivity. Hydrochloric acid and sodium hydroxide solutions have electrical conductivities in the ranges 160–340 mS cm^{-1} and 90–180 mS cm^{-1}, respectively, for product concentrations in the range 0.5–1 mol L^{-1}, at ambient temperature. A low sodium chloride contamination, which has lower conductivity (i.e., 50–80 mS cm^{-1} at ambient temperature) in the same range of concentrations, is expected in a well performing system, thus guaranteeing the effectiveness of this measuring method for product quality controllers.

Step tests were performed varying the outlet chemicals flowrates, in the range ±12.5 % – ±50 %, at fixed current density (i.e., 400 A m^{-2}) and monitoring the dynamic

responses of the outlet conductivities. From the analysis described in section 4.3.3., it was observed that the response time of the system is in the range 5-16 min, depending on the outlet flowrate value. Consequently, the total simulated time was set to 16 min. The results of the step tests are shown in Figure 65. Notably, the EDBM system exhibits a non-linear behaviour. For example, step variations in the outlet chemical flowrates of equal magnitude but opposite directions, result in outlet conductivities that are asymmetrical relative to the starting value. This effect can be also observed by plotting the outlet concentration trends due to the step variations.

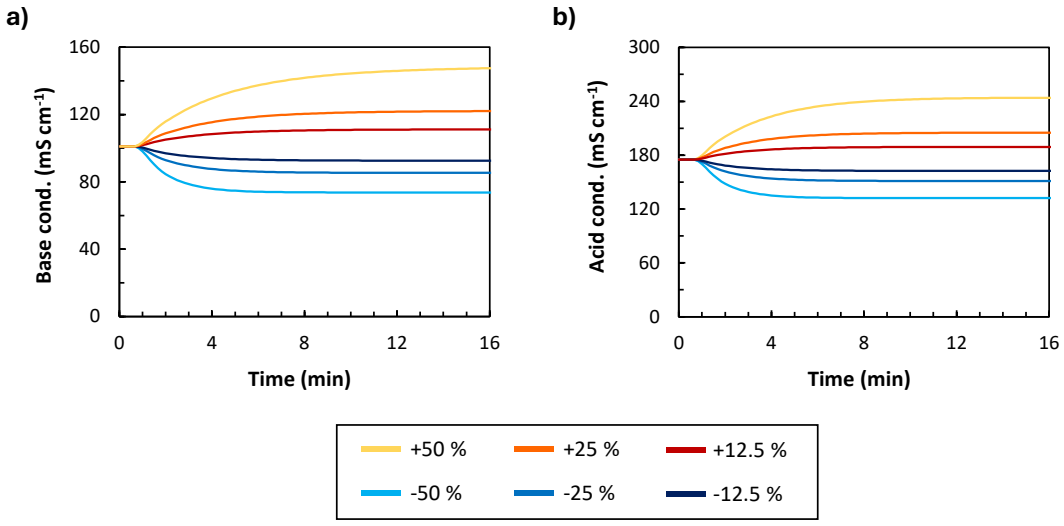

Figure 65. Trends of: a) outlet base conductivity due to step variations in the outlet base flowrate, b) outlet acid conductivity due to step variations in the outlet acid flowrate. All the step tests were performed at a constant current density of 400 A m^{-2}, starting from constant acid, base and salt outlet flowrate of 2.5 L min^{-1}, 2.5 L min^{-1} and, 4.2 L min^{-1}, adopting the continuous feed and bleed configuration.

Proportional-integral (PI) feedback controllers were designed adopting the Internal Model Control (IMC) method. Each dynamic response to step variations was approximated with first-order plus dead time transfer function. The controller parameters were calculated utilising IMC tables [124] and utilising the calculated transfer function constants (i.e., gain, time constant and dead time). All the obtained control parameters of a specific product were averaged between those obtained for each step test, to obtain controllers which perform well in the entire range of operating conditions. Finally, an

online tuning was performed, reducing the obtained gain values to have a more robust response, Table 23.

Table 23. Average control parameters obtained from the IMC method and final version obtained from a fine tuning for product quality controllers.

	Base Controller		**Acid Controller**	
	Average	Final	Average	Final
$K_c \left(\frac{L\,cm}{\min mS}\right)$	-0.057	-0.035	-0.034	-0.025
$\tau_c\,(s)$	187	190	163	160

4.3.4.1.4. Testing of the PV-EDBM integrated system

The dynamic EDBM model, the PV modules simulator and the product quality controller were implemented in the process simulator (i.e., gPROMS Model Builder®) and PV-EDBM integrated system was tested in four different irradiation scenarios: i) winter, ii) spring, iii) summer and iv) autumn. The feed and bleed process configuration allows the system to work in a wide range of chemical outlet flowrates, between 0.5–4.5 L min^{-1} at fixed channel speed of 2.7 cm s^{-1}. The minimum irradiation to start the system was selected to guarantee product concentrations equal to 0.5 mol L^{-1} at the minimum flowrate (i.e., 0.5 L min^{-1}). The solar radiation which enables to reach this condition is around 220 W m^{-2}, corresponding to a total generated power of approximately 1.3 kW. The simulation starts at the daily time at which the minimum solar radiation is available, and it ends when the same solar radiation is reached in the decreasing part of the fitted gaussian curve. The simulated process time varies significantly depending on the scenario, ranging from 9.7 h in summer to 6.1 h in winter. The set point fixed in the product quality controller were 175 mS cm^{-1} and 95 mS cm^{-1} for acid and base,

respectively. These values approximatively correspond to a product concentration of 0.5 mol L^{-1} with low salt contamination at ambient temperature. The results of the PV-EDBM integration are reported in Figure 66.

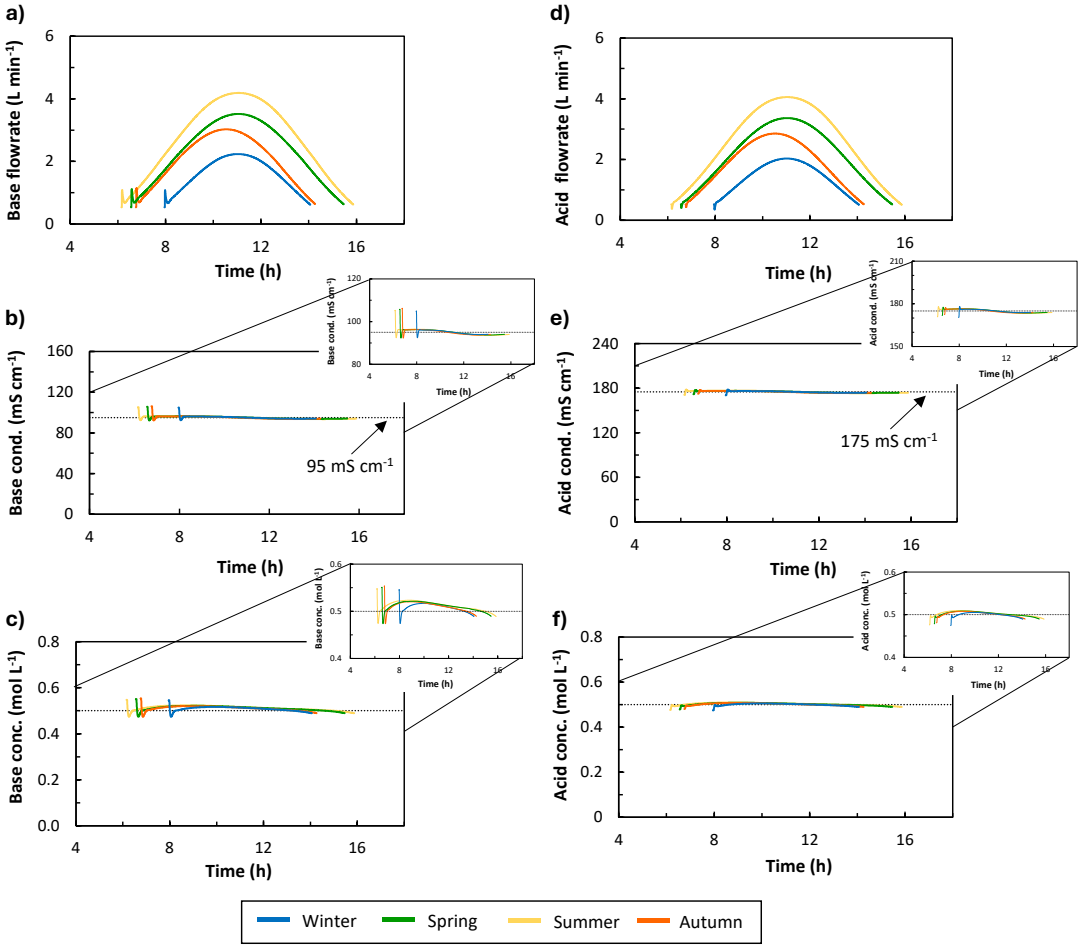

Figure 66. Simulation of the integrated PV-EDBM system for the four different irradiation scenarios (i.e., winter, spring, summer and autumn). The represent trends are a) the outlet flowrate from the base compartment; b) the outlet conductivity of the base product; c) the outlet concentration of the base product; d) the outlet flowrate from the acid compartment; b) the outlet conductivity of the acid product; c) the outlet concentration of the acid product. The outlet salt flowrate was maintained twice the value of the base outlet flowrate up to the value of 4.2 L min^{-1}, for higher value it remained constant.

It could be observed from Figure 66a that the outlet flowrate varies with a gaussian trend as the available power, from a minimum of around 0.5 L min^{-1} to a maximum of 4.2 L min^{-1} in the summer scenario. The maximum outlet base flowrates reached in the other scenarios resulted equal to 2.2 L min^{-1}, 3.0 L min^{-1} and 3.5 L min^{-1} 2.2 L min^{-1}, in winter, autumn and spring respectively. The obtained maximum flowrates correspond to

a percentage of utilisation of the EDBM unit ranging from 43 % in winter up to 92 % in summer. From Figure 66b it could be seen that the conductivity controllers effectively maintain the set point in all the scenarios. Also in terms of alkaline concentration, an almost constant value was reached, demonstrating that the conductivity controller can be utilised to control the product concentration. A slightly higher concentration was observed at the beginning of the tests because minimum power was selected to reach a concentration of both chemicals at least equal to 0.5 mol L^{-1}, but, in general, the base product is produced with a higher efficiency leading to a higher concentration at the beginning of the test. From Figure 66d it could be observed that the same consideration can be applied also to the acid product, but with slightly lower flowrates. The maximum outlet flowrate varies from 2 L min^{-1} to 4.1 L min^{-1}, in winter and summer, respectively. Almost overlapped trends of acid conductivities and concentrations were registered compared to the set point and the target concentration, respectively.

These results confirmed what was already observed in section 3.6.2 for the EDBM pilot plant despite the higher range of current density investigated (up to 600 A m^{-2}). Thus, proving the effectiveness of the developed simulation tools. The PI linear control enables to effective control the system products quality in all the scenarios, suggesting that the PV-EDBM systems can be easily operated in an industrial context also adopting traditional reliable control strategies. The developed modelling tools can be utilised to solve optimisation problems that can arise in the design of EDBM systems powered by variable energy sources in order to minimise the cost of the produced chemicals.

5. Modelling of EDBM with Artificial neural networks

The improvement in computational capacity along with the broad availability of data (the era of big data) has promoted the adoption of machine learning techniques across a variety of fields, from industry to law [125]. In this chapter, the potential of applying these techniques to model the Electrodialysis with Bipolar Membranes process is evaluated under both steady-state and dynamic conditions. The described activities were conducted during two research periods at the University College London (UCL), London (UK).

Artificial neural networks (ANN) are biologically inspired learning algorithms that have recently been utilised as an alternative way to model complex non-linear processes [126]. This modelling technique does not require the formulation of physical equations to describe a process, and thus it falls under the category of *black-box* models [102]. Instead, the knowledge of the process is reconstructed from available data, through a suitable training procedure. The data are usually divided into two groups: inputs and outputs data, and a relationship between inputs and outputs variable is created [127].

Among the advantages of employing ANN there are: i) the capability of capturing complex non-linear relationships between process variables; ii) the ability to model multiple-inputs multiple-outputs systems; iii) the reduced computational time requirements; iv) the possibility of incorporating dynamic elements (i.e., delays or feedback loops) to simulated un-steady-state conditions; v) the ease of updating the current model with new data. However, some limitations also exist that complicate the use of this powerful modelling approach. These include i) the need for a high-quality dataset, with significant variability and volume; ii) the lack of standardised procedures to select network type and structure (e.g., number of nodes and hidden layers); iii) the over-fitting problem that severely affects the performance of this type of models, that can be

mitigated with appropriate training procedure; iv) the under-fitting issue, caused by convergence to a local minimum in the objective function.

5.1 Literature review

Over the last three decades, several studies have been conducted in modelling membrane-based processes adopting ANN. Microfiltration (MF) is a pressure-driven filtration process that uses porous membranes to separate suspended particles, with a size in the range 0.1–1 μm, from a liquid [128]. During the operations, particles deposit on the membrane surface and inside the membrane itself, reducing the permeate flux. Thus, it results important to predict this reduction to stop the operation on time for cleaning procedure or membranes replacement. Jokić et al. [129] proposed a feed-forward ANN to model a cross-flow microfiltration modelling unit, utilised for *bacillus velezensis* cultivation broth filtration. A network architecture with one hidden layer and five inputs (i.e., process time, transmembrane pressure, superficial feed velocity, superficial air velocity, and presence of static mixer) was adopted to predict the permeate flux. Experimental data, obtained using a single channel ceramic membrane, were employed to develop the model. A coefficient of determination (R^2) value of 0.992 was obtained over the entire dataset, proving the successful application of the ANN model. Hamachi et al. [130] utilised a recurrent artificial neural networks to obtain a dynamic model of a cross-flow MF unit for bentonite suspension treatment. The network, trained on experimental data, is capable of predicting the deposit thickness and the permeate flux, using one hidden layer and three inputs (i.e., concentration, crossflow velocity and transmembrane pressure). Comparing model results and experimental data, it could be observed that the model is able to predict the time trend of both outputs, with relative error lower than 7 % and 20% for the permeate flux and the deposit thickness, respectively. Nanofiltration (NF) is a pressure-driven filtration process that uses

membranes with pore size in the range 1–10 nm, intermediate between ultrafiltration and reverse osmosis [127]. Al-Zoubi et al. [131] developed ANN models to predict the NF process performance. The data used to develop the model were obtained from experimental tests, using three different nanofiltration membranes (NF90, NF270, and N30F) and different salts (KCl, Na2 SO4, and MgSO4). The models adopt the same network architecture with three inputs (feed pressure, permeate flux and salt concentrations) and one hidden layer, and can predict membrane rejections. The ANN models effectively tracked the nonlinear behaviour of rejection vs. pressure and rejection vs. permeate flux, with deviations lower than 8%. Shim et al. [132] developed a recurrent deep neural network model to investigate the variations in NF performance and fouling growth. Laboratory-scale experiments were conducted and 2D images were acquired via optical coherence tomography to quantify the layer of cake formed on the membrane surface. The network architecture consists of seven different layers, six inputs (operating conditions, process time and fluorescence excitation-emission matrix, and two outputs (permeate flux and fouling thickness). The model exhibits satisfying performance, with R^2>0.97 in the validation set. Membrane Distillation (MD), which combines the use of thermal energy for heating the feed and a hydrophobic membrane to separate the vapour from the concentrated brine [133], has been also modelled utilising ANN. Indeed, Porrazzo et al. [134] presented a non-recurring feedforward dynamic network to describe the behaviour of a solar-powered MD unit. The structure of the network presents one hidden layer and three inputs (i.e., radiation, feed flowrate and inlet temperature of the cold channel) to predict the distillate flowrate. The data used to develop the network were recorded from a six days experimental campaign with the MD unit. Values of the regression coefficient (Reg) higher than 0.95 were obtained for the validation and testing sets. Regarding the adoption of ANN to predict the behaviour of the electrodialysis

(ED) process, a few works are available. Sadrzadeh et al. [135] applied ANN to predict the removal of Pb^{2+} ions from wastewater through ED. A feedforward network was select, utilising two hidden layers, four inputs (i.e., voltage, flowrate, temperature and concentration) and predicting the separation percentage of Pb^{2+} ions or, alternatively, the current efficiency. The network was trained and verified adopting experimental data obtained from a laboratory scale ED unit. The authors claim that values of relative error of about 1% were obtained for most of the data. In another work, Jing et al. [136] modelled the separation percentage of sodium chloride solution in an ED unit. A feedforward neural network was adopted and trained on experimental data utilising different training algorithms (i.e., adaptive learning rate method and flexible back propagation algorithm). The network uses one hidden layer, four inputs (i.e., feed concentration, dilute flowrate, temperature and voltage) and predicts one output (i.e., the separation percentage). A good correlation was found with all the tested training algorithms, with value of Reg higher than 0.98. Table 24 summarises the main neural network models architecture utilised in membrane processes and their performance. To the best of the author's knowledge, no application of ANN for predicting EDBM behaviour was reported in the literature. Thus, suggesting the possibility of extensively investigate this interesting filed.

Table 24. Application of artificial neural network models in membrane processes. The main characteristics of the model architectures as well data information and performance assessment are reported.

Reference	Membrane process	Network model	Data type	N. of data	N. Hidden layer	Inputs	Outputs	Performance assessment
Jokić et al.	MF	FFNN	Experimental data points	1115	1	5	1	R^2, MSE
Hamachi et al.	MF	NAR neural network	Experimental data points	4900 training 1750 testing	1	3	2	Relative error
Al-Zoubi et al.	NF	FFNN	Experimental data points	6 training 12 verification	1	3	1	Relative error
Shim et al.	NF	LSTM	Experimental data points + 2D images	960 training 420 verification	7	6	2	R^2, MSE
Porrazzo et al.	MD	NION	Experimental data points	540	1	3	1	Reg, MSE
Sadrzadeh et al.	ED	FFNN	Experimental data points	50 training 11 validation 10 testing	2	4	1	Relative error, MSE
Jing et al.	ED	FFNN	Experimental data points	270	1	4	1	Reg, R^2, MSE

FFNN: FeedForward Neural Network
NAR: Nonlinear AutoRegressive
LSTM: Long-Short Term Memory
NION: Nonlinear Input Output Network
MSE: Mean Squared Error

5.2 Background

This section introduces some fundamental aspects of modelling steady-state and transient processes with artificial neural networks.

5.2.1. Network architecture

Artificial neural networks are black box models capable of reproducing nonlinear relationships between inputs and outputs. Their structure is composed of processing elements, indicated as nodes, neurons or perceptrons [137]. A single input node is schematically represented in Figure 67. The input of the node, *p*, is multiplied by a constant factor *w*, known as input weight, and sent to the summation element along with a bias, *bi*. The result of the summation, called net input, is passed through a transfer function (or activation function), which calculates the output of the node, *a*.

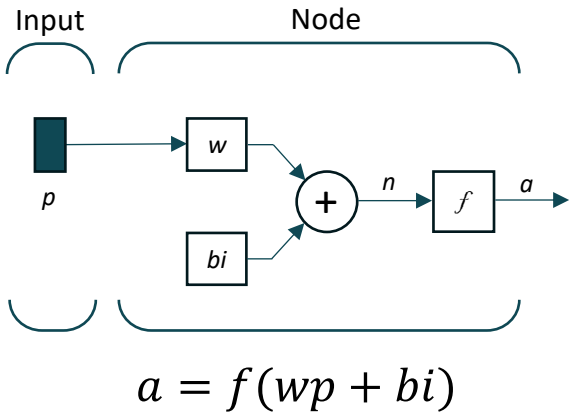

Figure 67. Representation of a single input node. Adapted from [138].

The input weight and the bias are the adjustable parameters of the node. They are usually initialised before the training process starts, and then their values are updated, depending on a certain learning rule, during the training phase. The transfer function is a bounded continuous function, which could be linear or nonlinear. It is selected in the design phase and it remains fixed during the training phase. A variety of transfer functions

are commonly utilised depending on the application. It is worth noting that a nonlinear transfer function enables the network to reproduce the nonlinear behaviour of a system. The most widely used transfer functions are depicted in Figure 68.

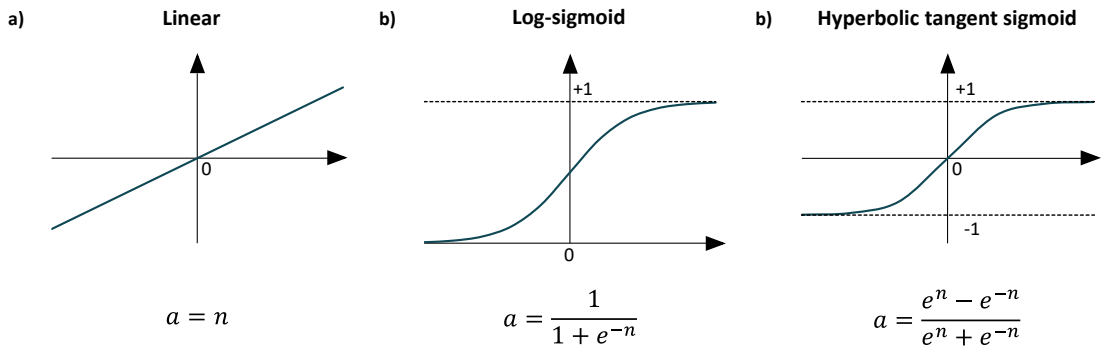

Figure 68. Trends and equations of typical adopted transfer functions. "a" represents the output of the node, while "n" is the result of the summation element (net input).

To improve the prediction capabilities several nodes can be arranged in parallel into a *network layer*. In a network layer composed of *s* nodes, each of the *r* inputs is linked to all the nodes through weights. A matrix of weights, *W*, with *s* rows and *r* columns, can be used to contain the weight values obtained. Similarly, it is possible to define an s-rows vector, *bi*, which contains the bias value of each node. The schematic representation of an artificial neural network layer is shown in Figure 69.

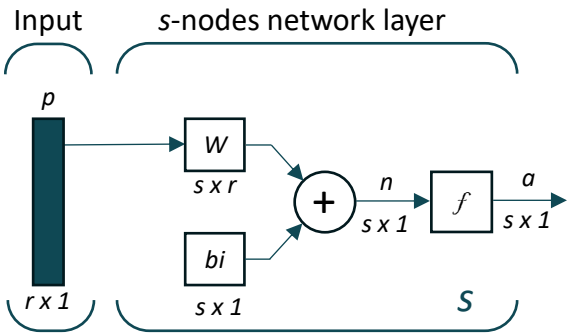

$$a = f(Wp + bi)$$

Figure 69. Representation of an s-nodes network layer. The matrix of weights "W" and the bias vector "bi" represent the adjustable parameters of the network layer.

The performance of an ANN model can be also enhanced by adding other layers of nodes in a series arrangement. This configuration results particularly suitable to predict complex behaviours, thanks also to the possibility of adopting different transfer functions in each layer. The last layer of a network, whose outputs are the network outputs, is denoted as the *output layer*, whilst the other layers are indicated as *hidden layers*. A simplified representation of a three-layer network is reported in Figure 70

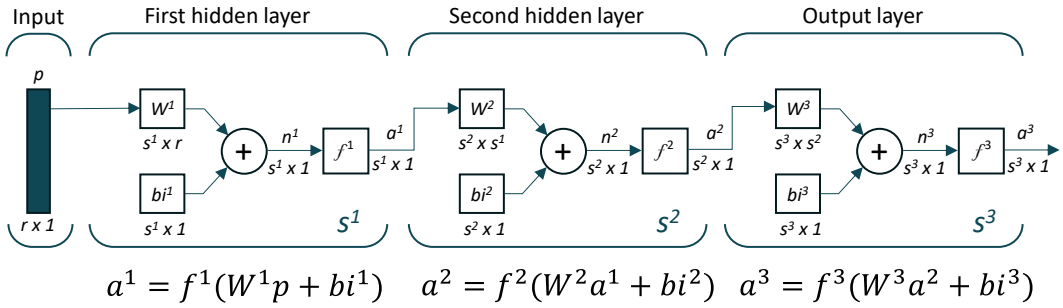

Figure 70. Representation of a three-layer network. The second hidden and the output layer utilise as input the output from the previous layer. Each layer has a set of adjustable parameters (W and bi) indicated with a superscript which refers to the layer.

In a layer, the output of each node is linked with all the node inputs of the following layer. On the other hand, there are no connections between node outputs of the same layer or with node inputs different from the following layer. This kind of network is known as feedforward [139]. It should be noted that the number of nodes in the output layer is equal to the number of outputs of the ANN model. Thus, its value is already determined and only the hidden layer nodes number should be defined in the design phase of the network. Moreover, the transfer function of the output layer depends on the output type of the ANN model. Usually, if the model produces output values in a wide range, the linear transfer function is used.

5.2.2. Dynamic networks

Dynamic networks represent a particular class of artificial neural networks in which the *time* plays a key role. These networks incorporate dynamic elements, such as

delays, integrators and feedback loops, which enable the network to reproduce time-dependent behaviours. Specifically, the output of the network can depend on both previous and current inputs as well as on previous outputs and states of the network [138].

The main dynamic elements used in a network are illustrated in Figure 71. The Tapped Delay Line (TDL) element (Figure 71a), in which the delay value, *dy*, is selected, produces a dy-rows vector which contains the delayed input, from time step *1* (t-1, first row) to time step *dy* (t-dy, dy-row). A vector of initial condition, a_0, is specified to provide values of the input vector at time zero. This is done by removing the first dy-rows from the dataset and saving their values in a_0. The integrator element (Figure 71b) calculates the integral of the input variable from time zero to current time, providing an initial condition a_0. A feedback loop is introduced in a network to estimate the output of the network from previous output values (Figure 71c). This element is essential to predict non-linear behaviour since their time evolution depends on the position from which the process starts. It should be noted that this loop presents a TDL element as only the past outputs can be employed to predict the new output. The past outputs are connected, through weight, to the first hidden layer, thus used as additional inputs. A feedback loop can also connect the first hidden layer with the outputs from this layer or from other hidden layers, referred to as states. In general, networks with feedback connection loops are referred to as *recurrent*[130] .

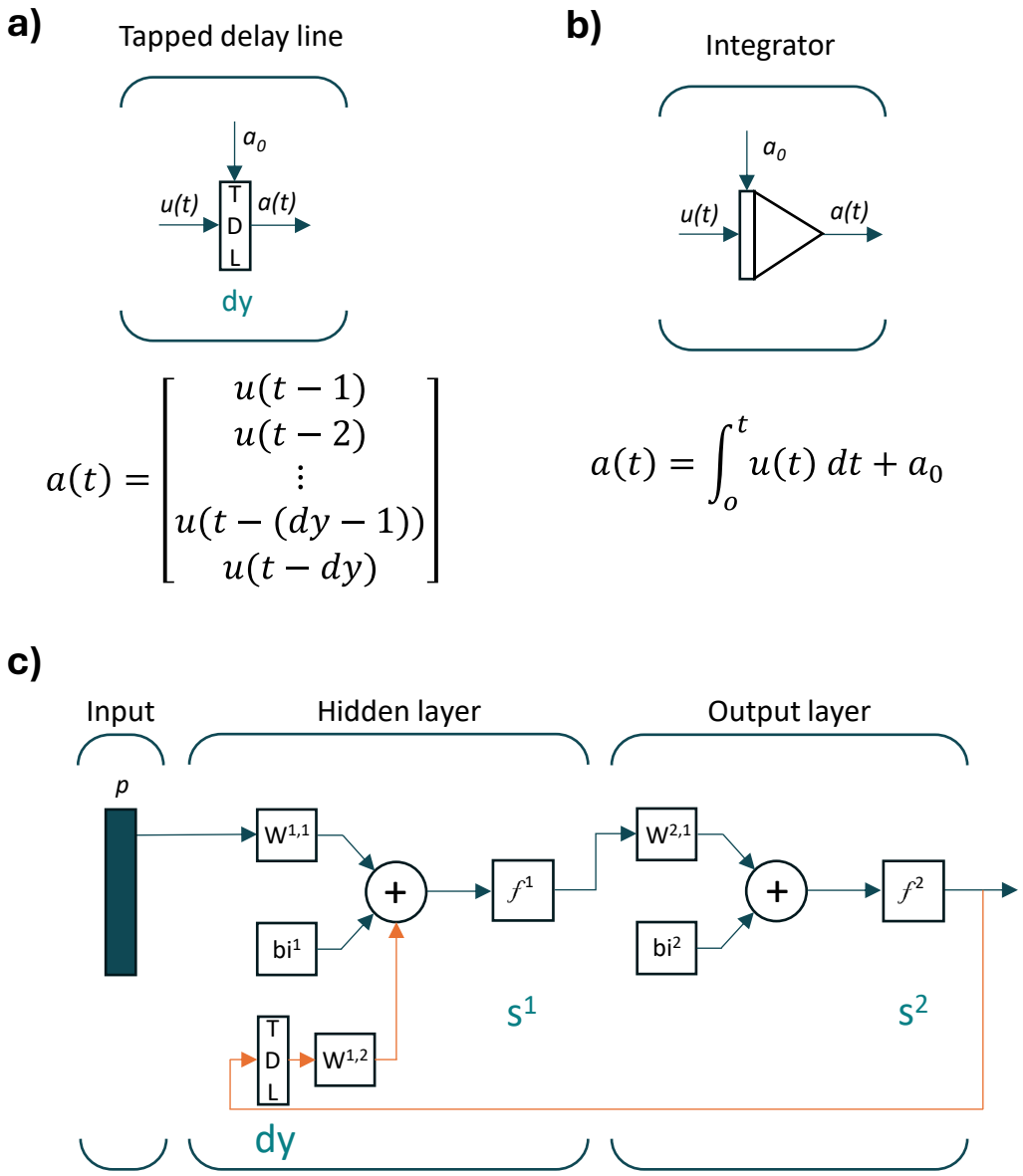

Figure 71. Elements used to convert static networks into dynamic: a) tapped delay line, which produces a delayed input vector; b) integrator, which integrates the input variable from time 0 to the current time step; c) feedback loop, which is used to estimate future output of the network from previous outputs.

5.3 Steady-state modelling

The experimental data collected with the EDBM pilot plant, described in chapter 3, were utilised to develop a steady-state ANN model. Data-driven models require well distributed, high quality and abundant data to show good performance. In this case, the feed and bleed process configuration was chosen as the majority of the tests were conducted with this configuration thus, a larger dataset could be employed for the development of the model. Considering the whole set of operating conditions investigated in feed and bleed, a total number of 34 data points (one for each steady-state condition) were registered, adopting a synthetic solution (i.e., 1 mol L^{-1} of sodium chloride). The distribution of these data, in terms of current density, is reported in Table 25.

Table 25. Number of operating conditions evaluated in feed and bleed mode for fixed current density. Both conventional and unconventional schemes (salt solution also in the chemicals compartments) are shown. These operating conditions refer to chemical concentrations in the range 0.3-1.2 mol L^{-1}.

	Current density (A m^{-2})			
	200	300	400	500
Conventional scheme	3	1	13	1
Unconventional schemes	8	0	8	0

As can be observed from Table 25, the operating conditions are not uniformly distributed between current densities for the convention scheme, as most of them utilised a current density of 400 A m^{-2}. On the other hand, a uniform distribution is available for unconventional schemes between 200 and 400 A m^{-2}. In all the cases the number of evaluated operating conditions results rather restricted. This is related to the fact that the feed and bleed configuration is a continuous operating mode and once the operating conditions are set, the system reaches a stable condition (i.e., steady-state). Thus, if

several data are collected at different time, they result almost unchanged. This limit the information that can be acquired in a single test, also because several minutes (i.e., 5-30 min) are necessary to move from a stable condition to another. From the literature review summarised in Table 24, it was possible to note that larger datasets are commonly used, in the range 71-6650 points, with only one exception [131]. The complexity of the network (number of inputs, outputs, nodes and layers) depends on the available data. A good rule of thumb is to employ a network with a number of parameters which is similar to the number of available data points [138]. This produces a network with high generalization capabilities thus, avoiding the undesired overfitting problem.

It was decided to model the conventional EDBM scheme utilising ANN, as this scheme presents a wider range of application and a lower complexity compared to the unconventional scheme. To develop an EDBM neural network model it is important to define the input and output variables needed to comprehensively describe the EDBM system. To this end, several measured variables can be used, also depending on the measurement instrumentations available. Aiming to reduce the complexity of the model, the most significant variables were considered. Specifically, outlet chemical concentration and voltage were used as model output, while, as inputs, the outlet flowrates and current density supplied to the system were adopted. The outputs were selected to evaluate chemical concentrations reached and the electrical energy consumed by the system. On the other hand, the inputs were chosen to provide the variables with a greater impact on the output, while are commonly set during EDBM operation. It is important to note that the use of the outlet flowrates allows to correctly account for the quantity of the produced chemicals as well as provides an indication of the water consumption (needed for the acid and base compartments). A negligible variation between inlet and outlet flowrate of the same compartment can be assumed for the feed and bleed configuration.

Due to the importance of a uniform distribution of the data across the input and output range, it was decided to use only the data referred to a current density of 400 A m^{-2} (i.e., 13 data points). In this case the number of network inputs can be reduced to 3 (i.e., acid, base and salt outlet flowrates) as the current density remains constant across all the data, thus do not providing any information to the network. The architecture of the network in reported in Figure 72.

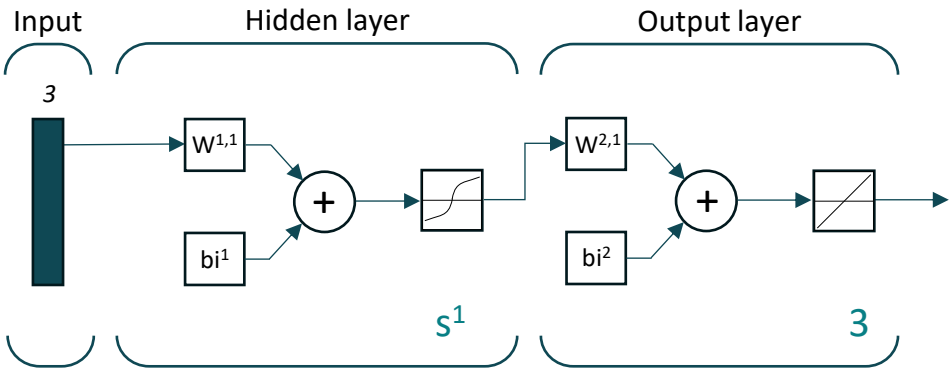

Figure 72. Structure of the artificial network utilised to model the steady-state behaviour of EDBM adopting a conventional feed and bleed configuration. The 3 network inputs represent the outlet flowrate of acid, base and salt compartments, while the 3 network outputs are acid and base concentrations and voltage.

A single hidden layer was utilised as it results sufficient in most applications [140], but also to reduce the number of network parameters. As transfer functions in the hidden and in the output layer, sigmoid and linear transfer functions were adopted, respectively. To define the number of nodes in the hidden layer different networks were trained by changing the number of nodes between 1 and 3, to limit the number of parameters up to 24 (s^1=3). To train the feedforward network, *MATLAB's fitnet function* was utilised, adopting the Bayesian Regularization training algorithm. This algorithm is recommended for small dataset because the validation set is not needed to stop the train and to reduce overfitting problems [138]. The data were manually distributed into two sets: training, and testing sets. A total of 10 data were used for the training, while 3 data were employed for testing the network. This data distribution between the sets prevents

that in the testing sets there are data point which are out of the training range, since neural networks are not able to efficient with extrapolation processes [141]. As a cost function the Mean Squared Error (MSE) was employed, defined as follows:

$$MSE = \frac{1}{N_{tp}} \sum_{k=1}^{N_{tp}} (a(k) - h(k))^2 \tag{148}$$

where *a(k)* represents the *k-th* predicted value and *h(k)* is the desired value. The summation is extended to the number of training point (i.e., N_{tp}). To account for the 3 outputs an average MSE was used. Moreover, to avoid issues related to the different scale of inputs and outputs, they were rescaled in the range 0-1, dividing them by their maximum value (all the input variables are positive values). This enables to reduce the effect of higher relative importance due to higher absolute value. A random weight initialisation was utilised, with values also in the range 0-1. Once satisfying performance had been achieved, the network was retrained using as initial values the weights obtained from the previous training. The best performance was obtained with a network with 2 nodes in the hidden layer (i.e., corresponding to a total number of weights equal to 17), with a value of MSE = 0.00129. The trend of the MSE during the training processes is reported in Figure 73.

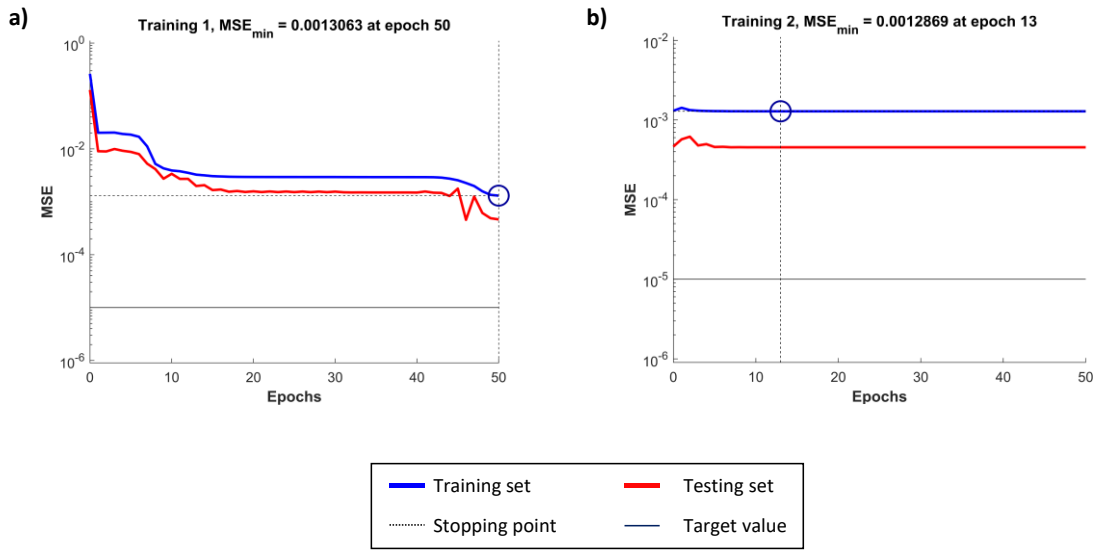

Figure 73. Trend of the mean squared error as a function of epochs during the training phase. In figure a) a random initialization is used, while in figure b) the weights were initialised with the value obtained from the previous training. Bayesian Regularization is used as a training algorithm.

It could be observed from Figure 73a that the MSE decreases with the number of epochs (i.e., the number of iterations of the training algorithm) for both data sets, suggesting the absence of overfitting. The best performance is obtained at epoch 50, which was set as the maximum number of epochs. A second training was conducted to see whether further improvement could be achieved, Figure 73b. The minimum MSE was obtained at epoch 13, with a slightly lower value compared to the previous training. In Figure 74 the predictions of the trained network are compared with the output experimental data (i.e., desired values).

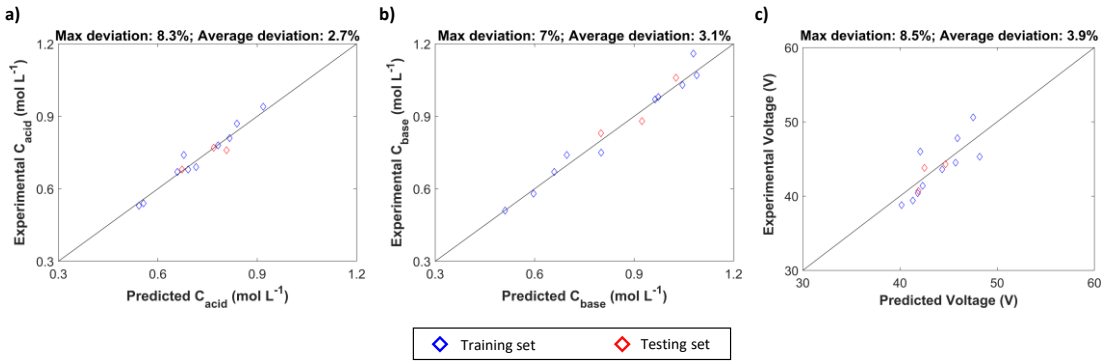

Figure 74. Comparison between network predictions (x-axis) and experimental values (y-axis) for training and testing sets: a) acid concentration; b) base concentration; c) external applied voltage. The network structure is the following: 3 inputs, 1 hidden layer with 2 nodes and 3 outputs.

As could be observed from Figure 74 the network shows satisfying performance for all the output, despite its quite simple structure. Indeed, the average discrepancy (i.e., relative error) between experimental data and model prediction is lower than 4 %, with a maximum value lower the 8.6 % in all the cases.

These results suggest that a reduced number of data can be sufficient to develop steady-state networks, also for complex non-linear processes such as EDBM. This model presents a low computational demand compared to first principles models thus, representing a flexible tool for on-site evaluation. As an example, the operating conditions needed for certain target specifications can be found with the ANN model and then set in the EDBM unit. A larger dataset can be adopted to investigate a wider range of operating conditions (by varying also the current density) maintaining high performance.

5.4 Dynamic modelling

Artificial neural networks are also suitable for predicting the performance variation of a system with time. This aspect has led to several applications in the field of membrane processes to predict fouling effects, which represent the deposit of substances onto membrane surfaces and/or into their pores [142]. This is crucial to plan membranes cleaning in place and maximize their lifespan. Different approaches have been utilised so far: i) the adoption of a static network, introducing the process time as an additional input; ii) the use of a dynamic network with a feedback loop from the network outputs to its inputs; iii) the utilisation of both dynamic network and introducing the time as input. Regarding the first approach, it has been proven to be effective to predict the permeate flux [129] or water permeability constant decline [141] as a function of the process time. The main advantage of this approach is to generate easy to train networks, adopting a standard approach. As a drawback, it could be used only for those processes that present always the same time evolution, as in the case of performance decline due to

fouling. The second approach, overcome this limit by utilising dynamic networks. As mentioned in section 5.2.2, these networks present dynamic elements, such as delays and feedback loops, which enable to describe complex dynamic behaviour, without the use of the process time as additional inputs. This guarantees, higher generalisation performance and the capability of predicting processes with different time evolution. Hamachi et al. [130] effectively employed a recurrent network to model two different time behaviour of deposit thickness on the membrane surface (i.e., quasi-parabolic and quasi-linear) with the same network. The third approach results similar to the first approach, showing the same drawback. On the other hand, the use of a more complicated network enabled to describe more intricate processes. This approach was adopted by Geissler et al. [143] to model the permeability decline during operation of filtration process in membrane bioreactor systems. An Elman network, which presents a single hidden layer and a feedback connection between the hidden layer outputs and its inputs, was developed utilising 9 operational parameters as inputs (between them the filtration time). An average relative error of 2.7 % was found, highlighting the prediction capability of this network.

To model the EDBM time evolution, due to the different temporal trends of the system that can arise from the adoption of renewable energy sources or variable target concentrations during operation, it was decided to develop a general neural network model adopting the second approach (i.e., dynamic network without the use of the process time as additional inputs). The network must predict increasing and decreasing trends towards the new stable condition, due to the variation of different outputs. Moreover, significantly different time constants can be observed between the output s (e.g., voltage and chemical concentrations), but also between inputs and outputs due to the inertia of the system. Thus, a dynamic neural network, with a feedback loop from the output layer to the inputs of the hidden layer (known as Jordan network) was selected, considering

also the possibility of adding tapped delay lines for the inputs. The results described in this paragraph were published in the article *Dynamic Modelling of Electrodialysis with Bipolar Membranes using NARX Recurrent Neural Networks* [144]

To train the network it was decided to use the data obtained from the experimental campaigns conducted with the EDBM pilot plant described in chapter 3. Unfortunately, due to problems with the acquisition of some variables, such as flowrates, voltage and current, it was not possible to use a significant part of the available data. Once the signal problems had been solved, due to the assistance of a technician, other experimental campaign campaigns were conducted but the number of acquired data was reduced because an expected problem with the stack occurred, due to the formation of chlorine compounds in the electrode compartments, which led to degradation of end-membranes and electrodes cases. For these reasons, it was decided to generate the needed amount of data utilising the validated dynamic model described in section 4.3. The model was used to simulate the EDBM pilot plant (FT-ED 1600-3 FuMA-Tech GmbH) operated in feed and bleed process configuration for all the lines (i.e., acid, base, and salt). Four different datasets were generated by varying the operating conditions as a function of time and observing the dynamic response of the system. Fixed inlet concentrations of the solutions were used in all the datasets. A concentration of 1 mol L^{-1} of NaCl was employed for the salt steam, while, for acid and base lines, water with a low salt content (1 mmol L^{-1} of NaCl) was utilized. Outlet acid and base flowrate were maintained constant to each other, while a constant ratio of 1.5 was kept between outlet salt and acid flowrate. This represents typical operating conditions in feed and bleed mode [97]. Step changes were given to the outlet flowrates of the solutions and to the current density, also at the same time, to investigate several operating conditions of interest for industrial applications. For each dataset consecutive changes were simulated with alternating periods of stable

conditions (40 min) to observe the system behaviour, adopting a discretization time of 1 min. A graphical representation of the generated datasets as a function of the operating conditions is shown in Figure 75.

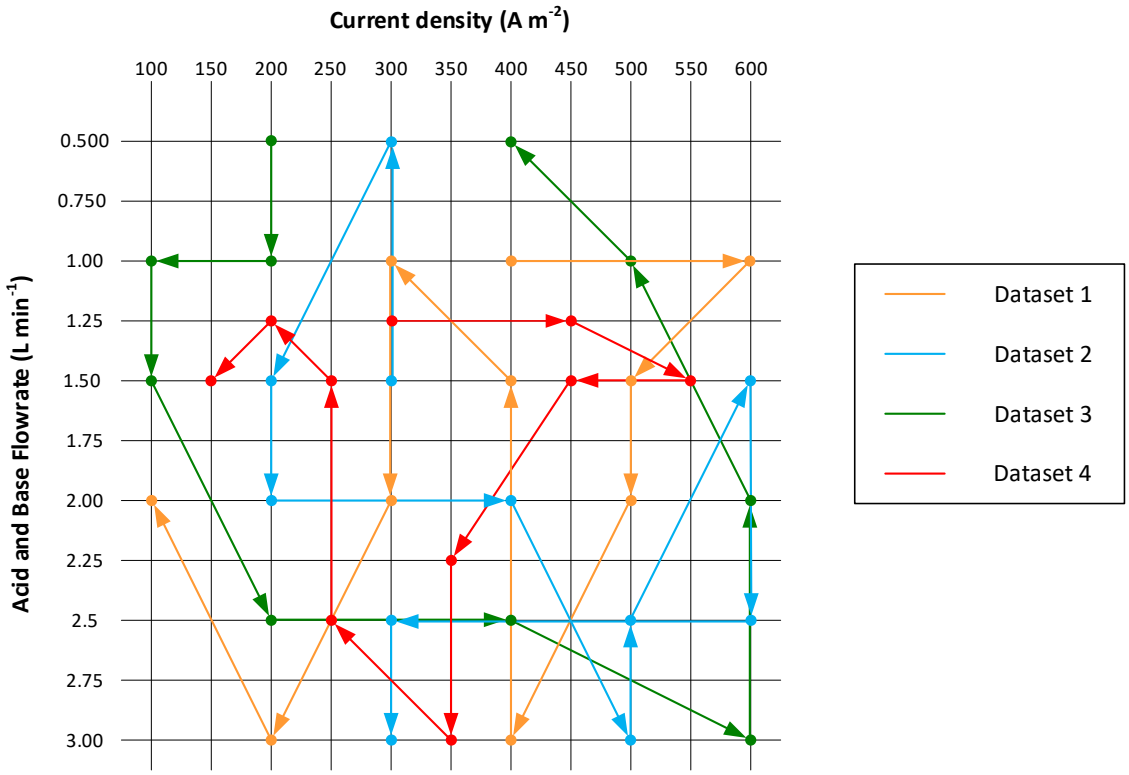

Figure 75. Representation of the generated datasets with the validated dynamic model adopting a first principles approach. Each point represents a steady-state condition, while the arrows, connecting the points represent a variation in the operating conditions toward the new steady-state condition.

From Figure 75 it can be noted that each dataset contains different steady-state conditions, represented by coloured dots. The dataset 4 evaluates values of flowrates and current densities (i.e., 0.75, 1.25,…, 2.25, 2.75 L min^{-1}, and 150, 250,…, 450, 500 A m^{-2}) which were not considered in the first three datasets. Indeed, this dataset was created to externally test the generalization capability of the network, while the first three datasets were adopted for the training phase. Additional information about the datasets is reported in Table 26.

Table 26. Additional information about the four datasets.

Dataset	N. data points	Duration (h)	N. step changes
1	357	5.95	9
2	422	7.03	10
3	376	6.27	9
4	376	6.27	9

The choice of utilising three different datasets for the training instead of one larger dataset had the objective of reproducing situations that can happen during experimental campaigns. Moreover, the datasets utilised for the training process present a different number of data points and, a as consequence, a dissimilar duration.

The variables subjected to step changes represent the inputs of the network, while as output physically meaningful and easy to measure online variables were selected. In particular, the outlet conductivity of the acid and alkaline solutions as well as the voltage applied to the stack were chosen. Acid and base conductivities were here adopted as inferential variables for an online indication of the concentration obtained, as the salt contamination of acid and base product is negligible. The structure of the dynamic network utilised to model the EDBM pilot plant is reported in Figure 76. This network, known as Jordan network, belongs to a class of nonlinear autoregressive models with exogenous inputs (NARX). NARX artificial neural networks have been successfully implemented in many dynamic systems with complex nonlinearities, such as hysteresis phenomena [145].

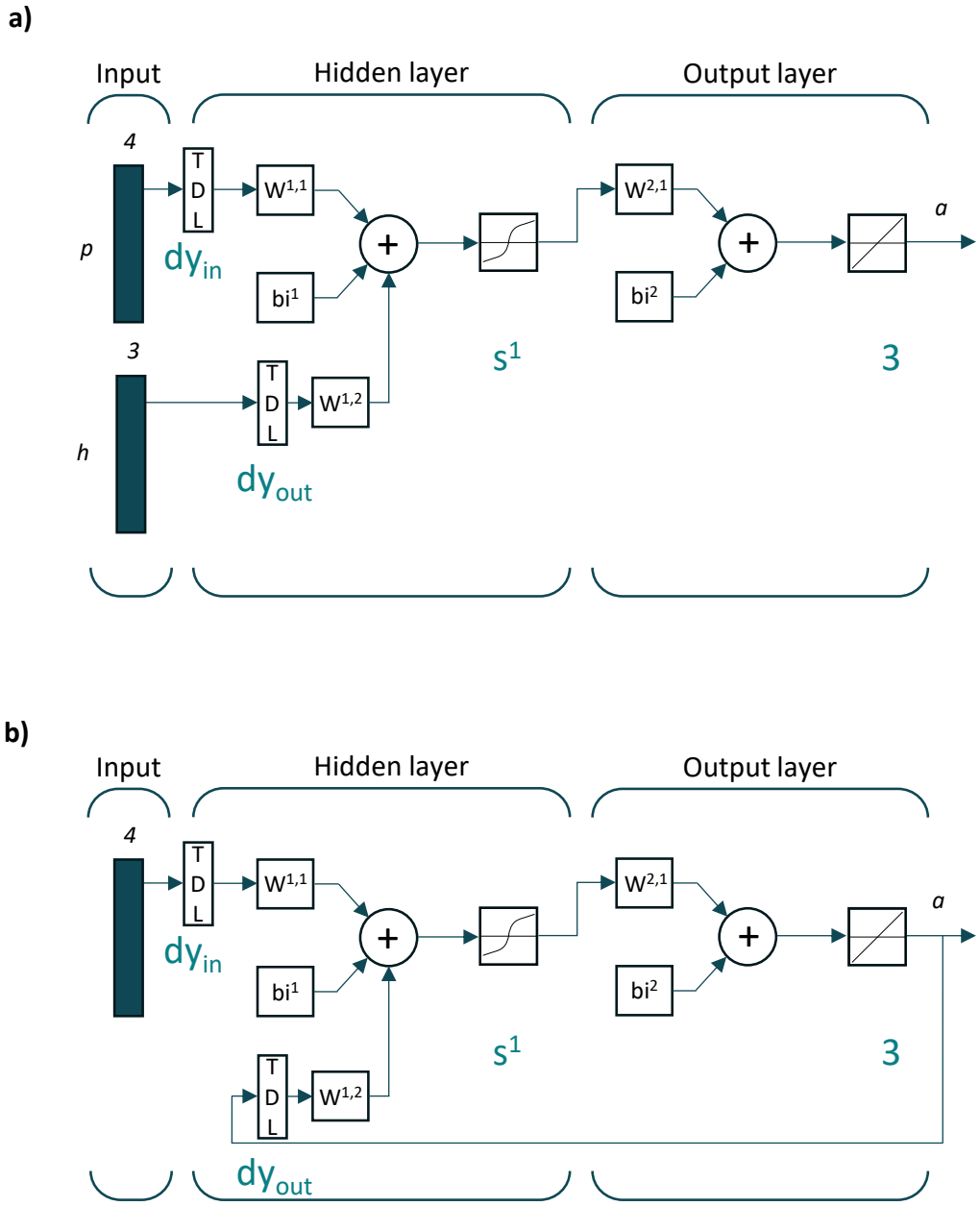

Figure 76. Structure of the artificial network utilised to model the dynamic behaviour of EDBM adopting a Jordan configuration. This network belongs to the class of NARX neural networks, The 4 inputs represent the outlet flowrate of acid, base and salt compartments as well as the current density, while the 3 network outputs are acid and base conductivities and voltage. a) series-parallel configuration, adopted for the training phase; b) parallel configuration, employed for multi-step ahead predictions.

The network structure presents four inputs, one hidden layer, and three outputs. The Elliot symmetric sigmoid and the linear function were adopted as activation functions for the hidden layer and the output layer, respectively. The number of nodes in the hidden layer, the order of the Tapped Delay Line (TDL) of input and output must be selected for

NARX neural network. The mean squared error was used as a cost function to train the network.

To train the NARX network, MATLAB's Neural net time series toolbox was employed. The structure described above was implemented and the Levenberg-Marquardt training algorithm was used. Three different datasets (i.e., datasets 1 to 3) were employed for the training phase, employing the *catsamples* function. Whist dataset 4 was adopted for subsequent testing. The NARX network was trained in series-parallel configuration (also known as open loop, Figure 76a), while its performance was evaluated using the parallel configuration (also known as closed loop, Figure 76b) for multi-step ahead predictions. Initialization of the network weight was adopted to avoid instability issues in closed loop. The Levenberg-Marquardt training algorithm was employed. The training data were randomly divided into three subsets: training, validation and testing subsets. In particular, 70 % of the data was used for training, 15% for validation and the remaining 15% for verification, adopting block of data (i.e., divideblock option) instead of random division (i.e., dividerand option). It is important to note that this division is useful to stop the training phase. Indeed, the training phase stops at the number of epochs at which the error in the validation set starts to increase and the weights and biases determined at that point are selected.

To define the number of nodes in the hidden layer and the order of TDL of inputs and outputs, different networks were trained by changing the number of nodes between 1 and 15 as well as the number of TDL of the outputs between 1 and 5. The MSE obtained in dataset 4 was calculated using the network in a parallel configuration and predicting the entire dataset. The average value of MSE between all the outputs was adopted as the evaluation criterion of the network performance. The best performance was obtained for a NARX network with 5 nodes and a TDL of 2 for the output. Finally, it was checked

whether an increase in performance could be obtained using a non-zero value for the TDL of the input, and values between 1 and 3 were investigated. No improvements were observed, consequently a zero order TDL was used for the input. In Figure 77, the trend of the MSE during the training processes is reported along with the obtained network structure in a parallel configuration.

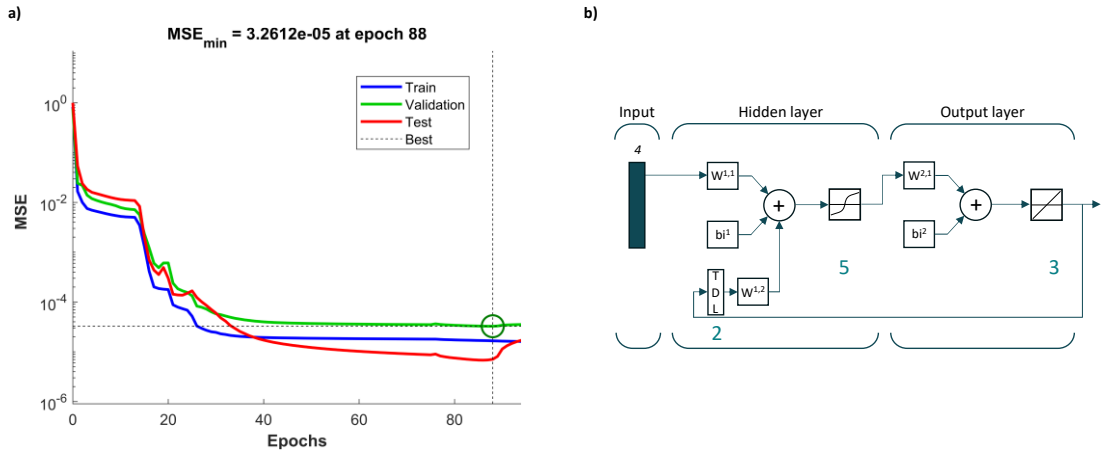

Figure 77. a) trends of MSE as a function of the number of epochs during the training phase. It is important to that the minimum in the validation dataset is adopted as stopping criteria (Levenberg-Marquardt training algorithm); b) obtained structure of the NARX network in a parallel configuration.

The generalization performance of the NARX network in predicting dataset 4 are shown in Figure 78. As it can be observed the NARX network, in parallel configuration and doing multi-step ahead predictions, is able to reliably predict the entire dataset 4. The dynamics of all the EDBM outputs were accurately predicted despite the much faster behaviour of the voltage compared to the conductivities. The local discrepancy between the predicted value and the true value was evaluated. Average values lower than 0.5 % were found for all the outputs, while maximum error resulted lower than 5 %, demonstrating the high generalization capability of the NARX networks on new data (i.e., unseen in the training phase).

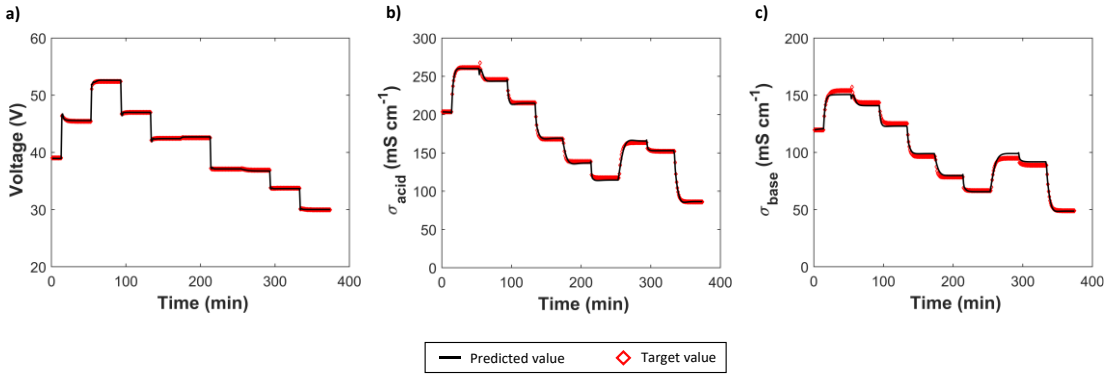

Figure 78. Comparison between the NARX prediction and the true value for dataset 4. The NARX neural network was employed in closed loop mode for multi-step ahead prediction. The time-dependent profiles are shown for: a) voltage applied to the stack, b) outlet conductivity of the acid line and c) outlet conductivity of the base line.

Finally, as external testing of the network performance it was decided to compare the prediction of the network with the real data obtained from the EDBM pilot plant, Figure 79. It can be observed that the network is capable of preproduce the dynamic trend with good agreement for all the outputs, showing a maximum deviation of 15 %. A slight underestimation of the voltage is observed in the first part of the voltage trend that can be related to the higher salt conversion reached in the salt compartment, which leads to an increase of the stack resistance (i.e., an increase of the channel and membrane resistances).

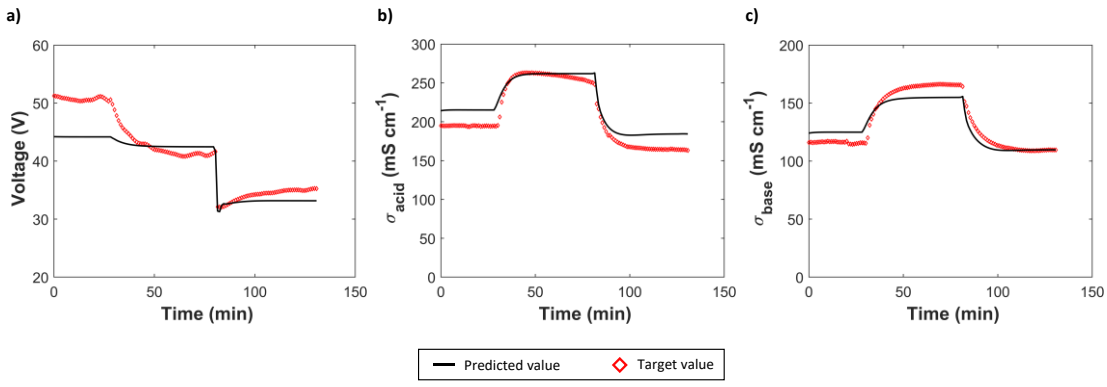

Figure 79. Comparison between the NARX prediction and the real data obtained from the EDBM pilot plant. The NARX neural network was employed in closed loop mode for multi-step ahead prediction. The time-dependent profiles are shown for: a) voltage applied to the stack, b) outlet conductivity of the acid line and c) outlet conductivity of the base line.

These results show the effectiveness of NARX networks in describing complex nonlinear electro-membrane systems, suggesting that they can be used for advanced control systems (such as model predictive control) and to optimize the EDBM process also in transitory scenarios. Moreover, these results suggest that if a similar amount of real data is available, NARX networks can be effectively used to develop a high-fidelity model considering also of non-ideal phenomena and thermal effects, usually neglected in first principles approaches.

6. *Modelling of EDBM with hybrid approaches*

To comprehensively evaluate EDBM modelling approaches, in addition to first principles and data-driven models, it was decided to also test hybrid approaches that combine both model types. Hybrid models, also known as grey-box models, can leverage the advantage of both approaches, retaining physical meaning while accounting for non-ideal phenomena which are difficult to describe. The interaction between mechanistic and data-driven models in hybrid models can vary depending on the objective and the complexity of the process. In general, hybrid models can be categorised into serial and parallel structures [146], as shown in Figure 80.

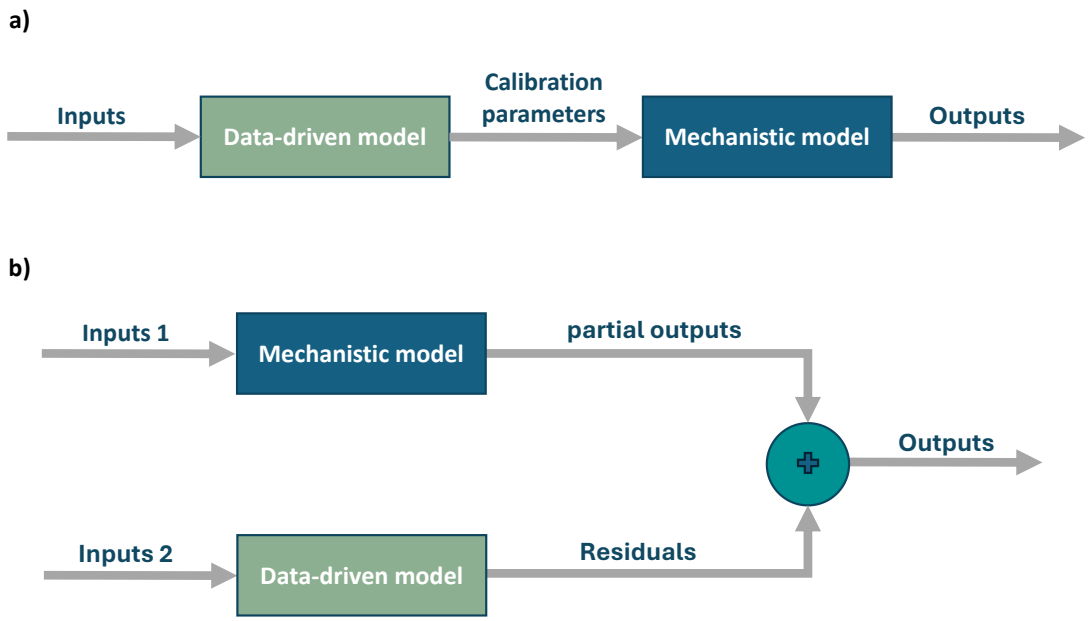

Figure 80. Hybrid model structures: a) serial; b) parallel. Adapted from [146].

In a series structure, the data-driven model is utilised to estimate calibration parameters required by the mechanistic model to solve the physico-chemical equations. These parameters are often not constant across the entire range of operating conditions and can be influenced by several variables. Therefore, the data-driven model helps to map these complex dependencies. In a parallel structure, the two models work in synergy to

predict the final outputs. The same inputs can be provided to both models, or they can be fed with diverse inputs. Typically, data-driven models are employed to estimate complex phenomena that are not accounted for by the mechanistic model [147].

6.1 State of the art

A few hybrid models have been developed in the field of membrane processes, considering mainly filtration processes. Rall et al. [148] developed a serial structure hybrid model, integrating membrane synthesis (data-driven) and process plant (mechanistic) models. A single NF unit is simulated in this case. The process plant model solves mass balances, describes the behaviour of a feed pump and considers also cost correlations. The membrane synthesis model estimates salt retention and membrane permeability, utilising membrane properties as inputs. Specifically, two different ANN models were developed, one for each output of the synthesis model. These outputs are shared with the process plant model. The whole process is optimized considering two objectives: i) minimal annual operation costs, ii) minimal permeate concentration. This hybrid model expands the number of variables that can be changed to obtain favourable results. Lower impurities at comparable costs were found compared to a commercially available nanofiltration membrane. Liu et al. [149] developed a hybrid model with a parallel structure to predict short-term fouling formation in an ultrafiltration unit. A Gaussian process regression model (GPRM) was adopted as a data-driven model. As a first principles model, a simple model based on the Darcy's equation was utilised to describe filtration and backwash phases. This equation contains the hydraulic resistance, which varies from cycle to cycle for both filtration and backwash phases due to fouling. The parameters were obtained from the model solving a minimisation problem (comparing the estimated transmembrane pressure with the measured one) at the end of a cycle. Thus, the parameters estimated at the end of a cycle were used in the subsequent

cycle leading to inaccurate predictions. The data-driven model supports the mechanistic model, compensating for these mismatches. The adoption of this hybrid model leads to a significant improvement in transmembrane prediction (R^2=0.96) compared to the first principles model (R^2=0.5). Hwang et al. [150] proposed a hybrid model with a parallel structure. As a first principles model, they applied the Hagen–Poiseuille equation along with filtration models (cake formation) to predict the performance of a hollow fiber microfiltration membrane, in terms of transmembrane pressure. As a data-driven model, ANN models were developed: i) the first ANN model predicts the transmembrane pressure starting from six inputs, mainly operating conditions; ii) the second ANN model estimates the specific flux and a fouling index utilizing six inputs which refer to feed water quality. Thus, with this hybrid model, it was possible to predict the transmembrane pressure and membrane filtration capability (i.e., specific flux and fouling index) simultaneously. The comparison of the hybrid model calculations with experimental results revealed good agreement, suggesting that the hybrid model can be useful in evaluating membrane fouling characteristics.

This literature review proved the effectiveness of hybrid models in predicting the behaviour of membrane processes. Although they have proposed to predict the effect of fouling, their capability can be also used to improve the estimation of process performance in those membrane processes in which fouling has a limited impact.

6.2 Steady-state modelling: conventional scheme

The possibility of using a hybrid model to predict the behaviour of EDBM was investigated for the feed and bleed configuration, in steady-state conditions. A parallel structure was considered as it results the most widespread in the literature. As data-driven model a feedforward neural network was employed. To train the network, the data collected for the conventional feed and bleed scheme at 400 A m^{-2} (Table 25) were

utilised. Specifically, these data were compared with the mechanistic model (MM) predictions and their difference was calculated (experimental – MM prediction), indicated as deviation. The network has three inputs, which are the solution flowrates, and predicts voltage as well as acid and base product concentrations. The input and output variables (i.e., the deviations) utilised to train the network were scaled utilising the following approach [141].

$$v_{scaled} = \frac{v - v_{av}}{v_{std}} \tag{149}$$

where v represents the generic input or output variable, v_{ave} is the average value of v and v_{std} is the standard deviation of v. The unscaled outputs assume both positive and negative values in a limited range thus, increasing the complexity of the network. Thus, this scaling strategy is convenient, leading to inputs and outputs with unit standard deviation which can assume positive and negative values. The data were divided into two sets, training (10 data points) and testing (3 data points), and the Bayesian regularization algorithm was utilised during the training process due to the reduced number of data points. The trend of the MSE a s function of the number of epochs and the structure of the network selected are shown in Figure 81.

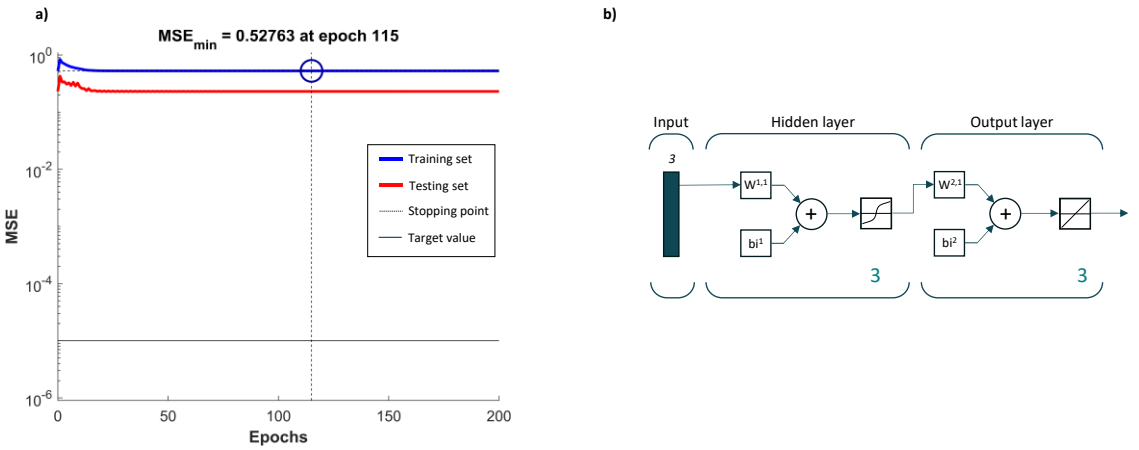

Figure 81. a) trends of MSE as function of the number of epochs during the training phase; b) obtained structure of the feedforward neural network.

The best results in terms of minimum percentual error between predicted and target deviation values in the whole dataset were obtained with a single hidden layer network with three nodes. As stopping criteria for the training process the minimum MSE in the training set was considered (Figure 81a). The comparison between the network predictions and the target values, in terms of deviation (experimental – MM prediction), is shown in Figure 82 for the three network outputs.

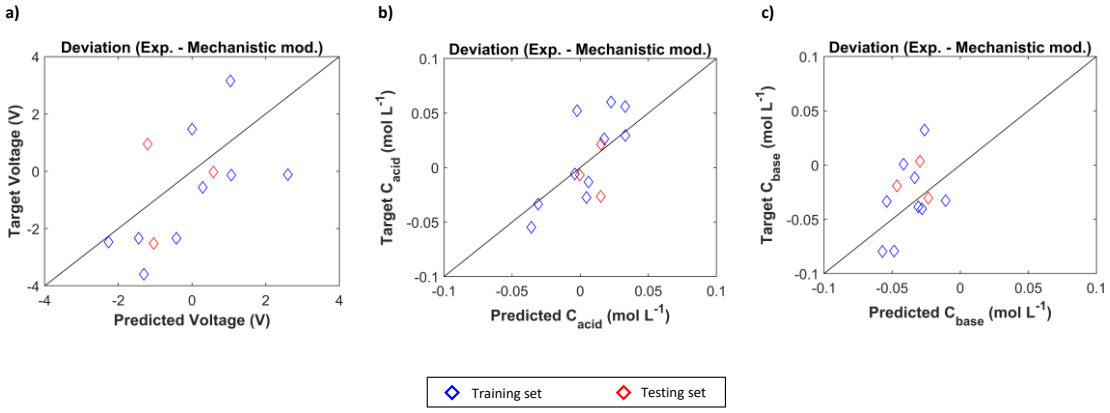

Figure 82. Comparison between network protection and target values of deviation (Experimental value- Mechanistic model prediction) for training and testing sets. The network structure is the following: 3 inputs, 1 hidden layer with 3 nodes and 3 outputs.

As can be observed from Figure 82 the network is not able to reach a perfect data regression for all the outputs. This fact is related to the quite low absolute values of the

target outputs, which in turn depends on the elevated prediction capability of the mechanistic model (average discrepancy between 4 % and 5 %). The deviation values result in some cases comparable with the experimental error thus, better regression of the ANN model would lead to an overfitting of the data. In Figure 82, instead, the errors found in training and testing data are comparable and the trend of the MSE is similar for training and testing sets (Figure 81a), proving the reliability of the data-driven model.

Connecting the developed ANN model with the first principles model developed in section 4.2, the hybrid model (HM) was made and its predictions were evaluated, Figure 83a and b. A good agreement between experimental values and hybrid model predictions is observed for the three outputs, with discrepancies always lower than 10% (dashed black lines). More in detail, average discrepancies between 2.7 % and 3.7 % were registered, which results slightly lower compared to the MM model (in the range 4-5 %), Figure 83c and d. Whilst, a maximum discrepancy lower than 8 % was found for the hybrid, compared to 14 % registered for the MM. Fore sake of convenience, also the predictions of the pure data-driven ANN model developed in 5.3 (i.e., trained with experimental data) in comparison with the experimental values are shown in Figure 83e and f. The ANN model alone shows intermediate performance between the hybrid and mechanistic models, with maximum and average discrepancy equal to 9.3 and 3.7 %, respectively.

These results proved that ANN can effectively compensate the prediction of the MM for those operating conditions in which its results less accurate, leading to improved protection. This means that the ANN model is considering those unideal phenomena, which are difficult to model with first principles approaches, such as leakages, undesired fluxes as well as variations in membrane and fluid properties, etc.

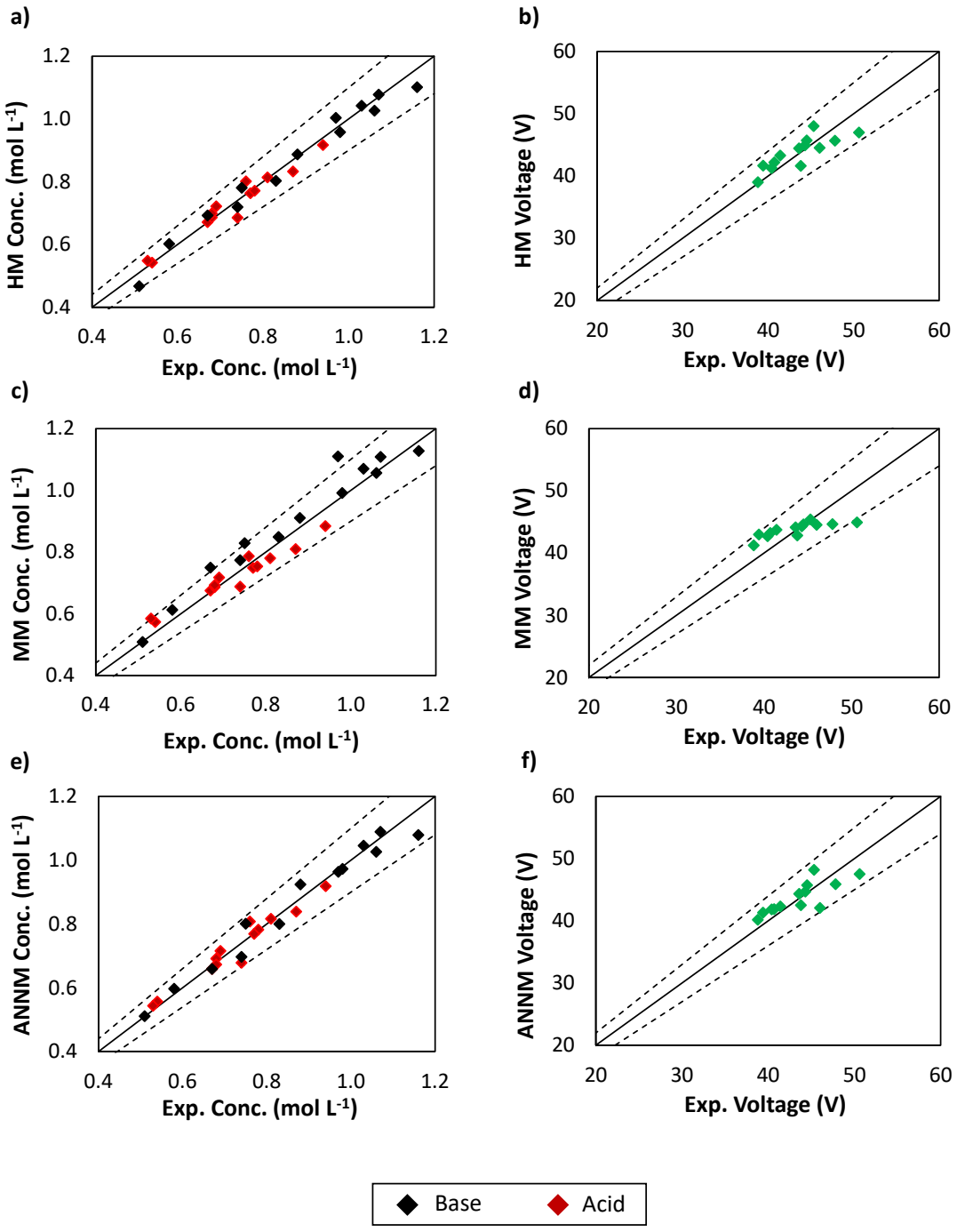

Figure 83. Parity plots comparing experimental and model results in terms of acid and base concentration as well as of voltage applied to the stack: a) and b) hybrid model with a parallel structure (mechanistic model plus artificial neural network model); c) and d) mechanistic model developed in section 4.2; e) and f) artificial neural network model obtained in section 5.3. The dashed black lines represent percentual discrepancy of +10 % and – 10%.

6.3 Steady-state modelling: non-conventional schemes

To further prove the capability of hybrid approaches in describing complex processes, non-conventional feed and bleed schemes were considered. These schemes have been introduced in section 3.5.1 and consist of feeding a brine solution also in the chemical compartments (one at a time or both) to reduce water consumption. The production of alkaline or acid brine is accompanied, but a more complex process is obtained. Indeed, the presence of salt in the acid and base chambers exacerbates the salt transport inside the bipolar membrane and increases the salt-limiting current density, but also competitive ions transport is obtained through the monopolar membranes.

The network structure changed considerably compared to the conventional scheme. Indeed, the number of network inputs passed from 3 to 6. As additional inputs, the current density and the presence of brine in the acid and base compartments were considered. For the latter, the presence was indicated with value 1, while the absence of salt was indicated with 0. The same network outputs were maintained compared to the conventional scheme.

As for conventional schemes, the network was trained using deviation values with experimental and mechanistic model (experimental – MM prediction). Input and output variables (i.e., the deviations) utilised to train the network were scale utilising Eq. (149). The data were divided into two sets, training (12 data points) and testing (4 data points), and the Bayesian regularization algorithm was utilised during the training process. The trend of the MSE as a function of the number of epochs and the structure of the network selected, also with 3 nodes in the hidden layer, are shown in Figure 84.

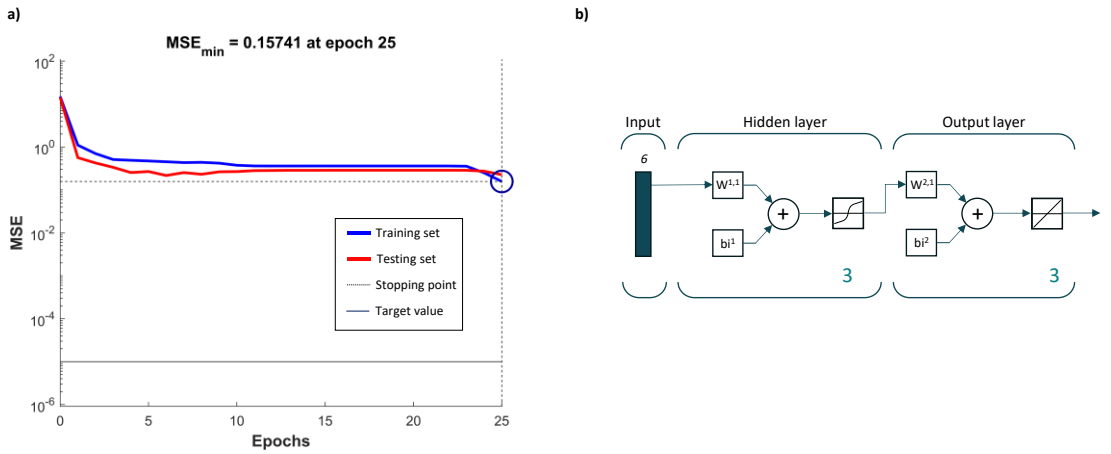

Figure 84. a) trends of MSE as a function of the number of epochs during the training phase; b) obtained structure of the feedforward neural network.

The comparison between the network predictions and the target values, in terms of deviation (experimental – MM prediction), is depicted in Figure 85.

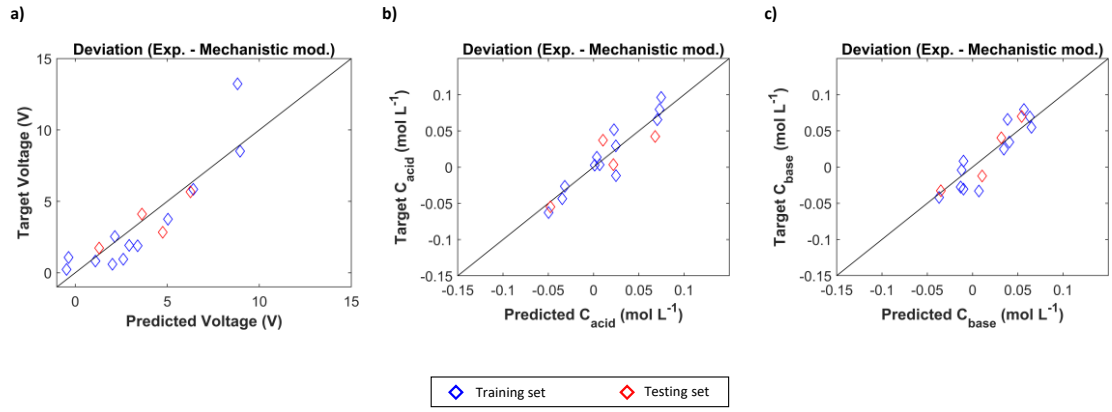

Figure 85. Comparison between network protection and target values of deviation (Experimental value- Mechanistic model prediction) for training and testing sets in the case of non-conventional schemes. The network structure is the following: 6 inputs, 1 hidden layer with 3 nodes and 3 outputs.

Fairly good agreement was observed between network prediction and deviation values for the three outputs, with similar results for testing and training sets. Also in this case, a comparison between the obtained hybrid model and the mechanistic model was made in terms of final output variables. The results are reported in Figure 86.

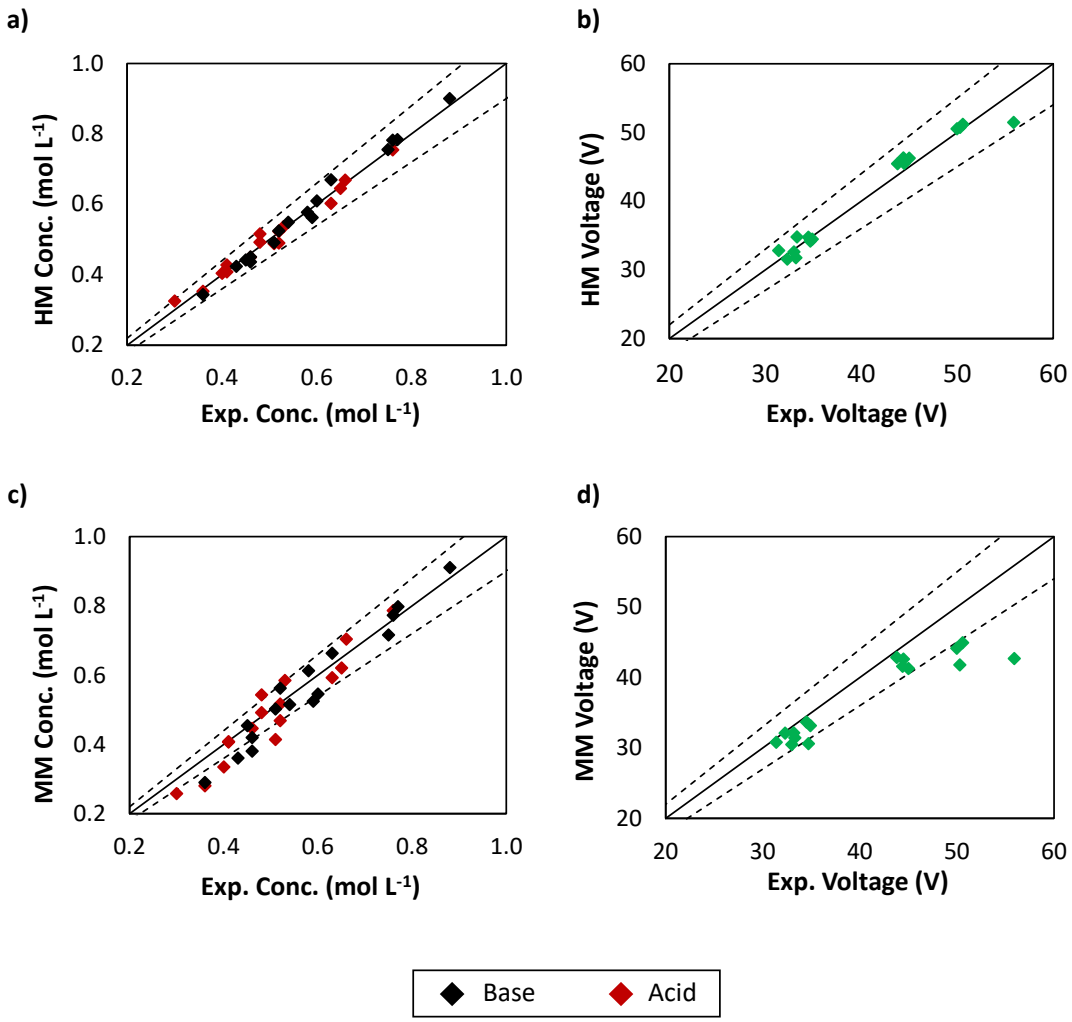

Figure 86. Parity plots comparing experimental and model results in terms of acid and base concentration as well as of voltage applied to the stack for the non-conventional feed and bleed schemes: a) and b) hybrid model with a parallel structure (mechanistic model plus artificial neural network model); c) and d) mechanistic model developed in section 4.2. The dashed black lines represent percentual discrepancy of +10 % and – 10%.

From Figure 86 a remarkable improvement of the prediction capability could clearly observed when passing from the mechanistic to the hybrid model. Indeed, all the data points are contained between the dashed black line which represents discrepancies of +10 % and – 10%. Specifically, average discrepancies between 2.6 % and 3.0 % were obtained for the HM, whilst the MM shows significantly higher values, in the range 7.6-8.3. In terms of maximum discrepancy, the improvement results more evident. Indeed, a value of 7.9 % was obtained for the HM compared to 24% for the MM.

These results proved the wide range of applicability of the hybrid model, suggesting that their effectiveness could be crucial for those complex processes for which the mechanistic models exhibit reduced prediction capability.

Conclusions

This PhD thesis aimed to study the behaviour of Electrodialysis with bipolar membrane process to promote its adoption at industrial level. To this end, different strategies were followed: experimental investigation and the development of high fidelity modelling tools.

An overview of EDBM potential in addressing modern sustainability challenges was presented in Chapter 1 highlighting the importance of further studies and optimisations. Chapter 2 provides an in-depth background on EDBM, starting with its history and reaching the latest research challenges.

Chapter 3 describes the wide experimental investigation conducted with a semi-industrial scale EDBM pilot plant. Firstly, the design and assembly phases of the pilot were briefly described, highlighting the flexibility to operate in a wide range of operating conditions and process configurations. Secondly, the experimental investigation conducted on the Island of Lampedusa, where the Water Mining treatment chain was located, was described. Following a few preliminary tests, which aimed to verify the correct functioning of the unit and to define the operative range of the unit, several research investigations were conducted. A comparison between three different process configurations was carried out, considering both discontinuous operating mode (i.e., closed-loop and fed-batch) and continuous (i.e., partial feed bleed). The results demonstrate the behaviour of the EDBM unit depends on the adopted operating condition and process configuration. The analysis suggests that the partial feed and bleed mode should be preferred in an industrial context since it combines high performance at elevated current density with continuous production. Therefore, for further experimental analyses, this process configuration was employed. Novel schemes for brine valorisation,

adopting the feed and bleed configuration, were tested to reduce water consumption and improve the brine treatment capacity of the process. The results indicate that feeding a brine in one of the chemical compartments, leads to performance reduction between 9 and 14% in terms of concentration, at 400 A m^{-2}, for the base production. While a significant lower performance was observed when feeding the brine in both chemical compartments, with reduction up to 44%. The adoption of these schemes should be economically evaluated considering water cost reduction and environmental benefits obtained from a larger volume of treaded brine. An innovative process configuration, indicated as WSD, was tested for the first time. A remarkable improvement in performance was observed with respect to the non-conventional schemes, reaching comparable performance with the conventional feed and bleed at high target concentrations or even slightly better. This process configuration should be preferred in all the fields in which acid brines could be tolerated, such as in the desalination compartment. Risk mitigation strategies were found to ensure a safe operation of the EDBM system with real brines: i) adoption of ion-exchange resins; ii) automatic switch-off of the system and reduction of the maximum absolute operating voltage of the electrodes; iii) installation of a heat exchanger and of a stripping column; iv) free chlorine content of ERS monitoring and ERS replacement. These strategies should be strictly followed to avoid irreversible stack damages. Comparing the performance of the system with artificial and real brines, on a parity base of conductivity, no significant variations were observed, proving the effectiveness of the process in working also with real multi-ionic solutions. Two different control strategies (i.e., flowrate and pressure control) were tested for the feed and bleed configurations. In the presence of non-uniform pressure losses between the compartments, the pressure control strategy must be adopted. Indeed, improvements in concentration and KPIs up to 40% were registered moving from

flowrate to pressure control mode for the EDBM pilot plant fed with a real brine. This effect was related to the minimization of convective fluxes between compartments through membranes. These results highlighted the adaptability of the EDBM process in real industrial scenarios, showcasing the technology potential within MLD and ZDL treatment chains for the recovery of high value-added materials. Finally, the use of photovoltaic modules was considered to power the EDBM pilot plant, which requires the adoption of control strategies to maintain constant product concentrations. These results of the tests suggested that the EDBM technology combined with control strategies is particularly suitable for working with variable energy sources and maintaining constant products, thanks also to the adopted feed and bleed configuration. This positively reduces the environmental footprint of the process as well as the cost of the produced chemicals.

In Chapter 4, a comprehensive multi-scale model capable of simulating EDBM units, also with complex stack configuration (i.e. internal staging), was developed. The model was validated by adopting two process configurations (i.e., closed-loop and feed and bleed) with experimental data coming from the EDBM pilot plant. Discrepancies between 2 and 14% were obtained. This validation allows the model to provide reliable results when simulating industrial scale stacks. The internal staging configuration was analysed from an electrical point of view, deriving an *ad hoc* equivalent electrical circuit (i.e., stack model) to show current and voltage profiles along the entire stack. The effect of parasitic currents on the stack performance was analysed to understand if the linking manifold could promote this detrimental effect. It was observed that the unused current due to parasitic effects was limited suggesting that this stack layout can be adopted to reduce the cost of the most expensive electrode (i.e., the anode). A techno-economic analysis was conducted for the feed and bleed process configuration. The economic analysis evaluated the Levelized Cost of sodium hydroxide (LCoNaOH) at different

process conditions changing the current density and the target concentration of sodium hydroxide. A LCoNaOH between 280–380 € ton^{-1} depending on the target concentration was found. Scale-up potentials of the model were shown simulating a double stage EDBM unit with two stacks in series. The overall performance was compared with a single stage EDBM unit working at the same target concentration. The results showed higher performance for the double stage, with a reduction of 10% in the LCoNaOH. These results suggest that the number of stages can be optimised to further reduce the cost of the products. Moreover, a dynamic version of the multi-scale model was developed to predict also nonstationary conditions of the EDBM unit. The model was utilised to study the dynamic behaviour of the system in terms of response time to step variations. The results proved that moving towards higher current densities or larger outlet chemical flowrates leads to a reduction in response time. This effect could be related to the higher rate of protons and hydroxide ions production and to the reduction of the residence time of the solution inside the stack. The combined action of high current density and elevated outlet chemical flowrates can reduce the response time down to 5 min, so these conditions should be maintained when working in fast transient regimes. As an application of the developed dynamic model, the coupling of the EDBM process with a photovoltaic system was considered. The results showed that the conductivity control effectively maintains the set point in all the scenarios. Also, in terms of chemical concentrations, an almost constant value was reached, demonstrating that the conductivity controller can be utilised to keep stable product concentrations. These results confirmed what was already observed in the experimental investigation despite the higher range of current density investigated (up to 600 A m^{-2}). Thus, proving the effectiveness of developed modelling simulation tools, that can be used for solving dynamic optimisation problems aiming to maximise the use of the available power or minimise the product costs.

Chapter 5 describes the adoption of artificial neural networks to model the EDBM process. This innovative modelling approach was evaluated for the first time considering both steady-state and transient operating modes. Firstly, a steady-state network was developed to simulate the EDBM process in conventional feed and bleed mode. Experimental data collected with the EDBM pilot plant were utilised to this end. Due to the reduced number of available data, a simple structure network with one hidden layer was utilised and the best performance, in terms of mean squared error, was found for two nodes in the hidden layer. The model can predict the voltage applied to the stack and the chemical concentrations starting from the set outlet flowrates at a fixed current density (i.e., 400 A m^{-2}). Comparing the predictions of the trained network with the experimental data, an average discrepancy lower than 4% was found, with a maximum value lower the 8.6 % in all the cases. These results suggested a slight improvement in prediction performance compared to the multi-scale model with a first principles approach. Thus, a reduced amount of data can be sufficient to develop an effective steady-state network to model complex non-linear processes such as EDBM. This low computational demand model can be utilised for on-site evaluations and/or for optimising the operating conditions. A recurrent dynamic network, NARX, was adopted to predict the transient behaviour of the EDBM pilot plant in feed and bleed operation mode. Due to some difficulties in collecting a large amount of data with the pilot plant, it was decided to utilise the available dynamic model with a first principles approach to generate data. Four different datasets were generated simulating consecutive step changes with alternating periods of stable conditions. A network architecture with four inputs, four outputs and one hidden layer was employed. The best number of nodes and the order of tapped delay line of input and output were determined by evaluating different architectures. The best performance was obtained for a NARX network with 5 nodes, a

TDL of 2 for the output and a zero order TDL for the input. The generalization performance of the NARX network in predicting a new dataset was evaluated, showing an average discrepancy value lower than 0.5 % and a maximum discrepancy lower than 5 %, demonstrating the high generalisation capability of the NARX networks on novel data. This model can be adopted for advanced control strategies of the process such as model predictive control.

Chapter 6 pertains to the modelling of EDBM employing hybrid data-driven and first principles approaches. The feed and bleed process configuration was considered in steady-state conditions for both conventional a non-conventional schemes. A parallel structure was adopted for the hybrid model in both cases. The neural network model, adopted as data-driven model, was trained with deviation values between experimental and mechanistic model predictions. For the conventional scheme, the network was made of a single hidden layer of three nodes, three inputs (i.e., solutions flowrates), and three outputs (i.e., voltage and chemical concentrations). A good agreement between experimental values and hybrid model predictions was observed, with discrepancies lower than 10% and average values in the range 2.7-3.7 %. This performance resulted slightly superior compared to the two types of models utilised alone. In addition to the conventional scheme, non-conventional schemes were considered and a hybrid model was developed changing the neural network model. Additional inputs (i.e., current density and the presence of brine in the acid and base compartments) were adopted compared to conventional schemes, while the same number of nodes in the hidden layers and number of outputs were used. Comparing the prediction capability with the first principles model a significant improvement in the performance was obtained, with a maximum discrepancy reduction from 24% to 7.9 %. These results proved that data-driven models, such as neural networks, can effectively compensate the mechanistic model deviations, leading to

improved protection. Hybrid models appear more effective for those cases in which a higher deviation between mechanistic models and experimental results is observed, due to simplifying assumptions in the occurring phenomena.

The results presented in this PhD thesis have shown the potential of the Electrodialysis with Bipolar Membrane process in different fields. Further studies should focus on real brines, developing appropriate modelling tools, and on the optimisation of the operating conditions and stack design to further reduce the chemical production cost. Moreover, the coupling of EDBM with other variable energy sources, such as smart grids, should be considered developing also optimising control strategies. This will widespread EDBM use in different contexts.

List of ISI publications

- Cassaro, C., **Virruso, G**., Culcasi, A., Cipollina, A., Tamburini, A., & Micale, G. (2023). Electrodialysis with Bipolar Membranes for the Sustainable Production of Chemicals from Seawater Brines at Pilot Plant Scale. ACS Sustainable Chemistry and Engineering, 11(7), 2989–3000. https://doi.org/10.1021/acssuschemeng.2c06636;
- Herrero-Gonzalez, M., López, J., **Virruso, G**., Cassaro, C., Tamburini, A., Cipollina, A., Cortina, J. L., Ibañez, R., & Micale, G. (2023). Analysis of Operational Parameters in Acid and Base Production Using an Electrodialysis with Bipolar Membranes Pilot Plant. Membranes, 13(2). https://doi.org/10.3390/membranes13020200;
- Morgante, C., Vassallo, F., Cassaro, C., **Virruso, G**., Diamantidou, D., Van Linden, N., Trezzi, A., Xenogianni, C., Ktori, R., Rodriguez, M., Micale, G., & Xevgenos, D. (2024). Pioneering minimum liquid discharge desalination: A pilot study in Lampedusa Island. Desalination, 581. https://doi.org/10.1016/j.desal.2024.117562;
- **Virruso, G**., Cassaro, C., Culcasi, A., Cipollina, A., Tamburini, A., Bogle, I. D. L., & Micale, G. D. M. (2024). Multi-scale modelling of an electrodialysis with bipolar membranes pilot plant and economic evaluation of its potential. Desalination, 583, 117724. https://doi.org/10.1016/j.desal.2024.117724.

List of non-ISI publications

- **Virruso, G**., Cassaro, C., Tamburini, A., Cipollina, A., & Micale, G. D. M. (2023). Performance Evaluation of an Electrodialysis with Bipolar Membranes Pilot Plant Operated in Feed & Bleed Mode. Chemical Engineering Transactions, 105, pp. 73 - 78, https://doi.org/10.3303/CET23105013;
- Cassaro, C., **Virruso, G**., Cipollina, A., Fagiolini, A., Tamburini, A., & Micale, G. (2024). Coupling Electrodialysis with bipolar membranes with renewable energies through advanced control strategies. In Computer Aided Chemical Engineering (Vol. 53). https://doi.org/10.1016/B978-0-443-28824-1.50330-6;
- **Virruso, G**., Cassaro, C., Ashraf, W. M., Tamburini, A., Dua, V., Bogle, I. D. L., Cipollina, A., & Micale, G. (2024). Dynamic Modelling of Electrodialysis with Bipolar Membranes using NARX Recurrent Neural Networks. In Computer Aided Chemical Engineering (Vol. 53). https://doi.org/10.1016/B978-0-443-28824-1.50031-4.

Submitted papers

- **Virruso G**., Cassaro C., Vassallo F., Filingeri A., Pellegrino A., Tamburini A., Cipollina A., Micale G. A pilot plant investigation on real seawater brine valorisation via electrodialysis with bipolar membranes. Journal of Water Process Engineering.
- Cassaro C., **Virruso G**., Cipollina A., Fagiolini A., Tamburini. A., Micale G. Enhanced schemes for brine valorisation via ElectroDialysis with Bipolar Membranes powered by Renewable Energy. ACS Omega

Papers in preparations

- Calogero Cassaro, **Giovanni Virruso**, Andrea Cipollina, Alessandro Tamburini, Giorgio Micale, Novel approaches for valorisation of waste brines at pilot scale for circular economy perspective.
- **Giovanni Virruso**, Calogero Cassaro, Andrea Culcasi, Andrea Cipollina, Alessandro Tamburini, Giorgio Micale, Dynamic modelling of electrodialysis with bipolar membranes at industrial scale for the sustainable production of chemicals from brines

Abstract at international conferences

- **Giovanni Virruso**, Andrea Culcasi, Andrea Cipollina, Alessandro Tamburini, Giorgio Micale, Simulation-based Design of a Bipolar Membranes Electrodialysis Unit for Chemicals Production from Brines, Collection: Congresso Nazionale GRICU 2022 Organization: GRICU. AIDIC DOI: 10.3303/BOA2201;
- Calogero Cassaro, **Giovanni Virruso**, Andrea Culcasi, Andrea Cipollina, Alessandro Tamburini, Giorgio Micale, Electrodialysis with bipolar Membranes for the sustainable production of chemicals from seawater brines at pilot plant scale, Desalination for the Environment Clean Water and Energy, https://hdl.handle.net/10447/659073;
- Fabrizio Vassallo, Carmelo Morgante, Calogero Cassaro, **Giovanni Virruso**, Dionysia Diamantidou, Niels Van Linden, Giuseppe. Scelfo, Alessandro. Tamburini, Serena. Randazzo, Alessandro Trezzi, Andrea Cipollina, Giorgio Micale, Dimitris Xevgenos, Minimum Liquid Discharge desalination: a pilot study in Lampedusa island, Desalination for the Environment Clean Water and Energy, https://hdl.handle.net/10447/619697;
- **Giovanni Virruso**, Calogero Cassaro, Andrea Culcasi, Andrea Cipollina, Alessandro Tamburini, Giorgio Micale, Dynamic modelling of electrodialysis with bipolar membranes at industrial scale for the sustainable production of chemicals from brines, 14th European Congress of Chemical Engineering and 7th European Congress of Applied Biotechnology, https://hdl.handle.net/10447/620782;
- **Giovanni Virruso**, Calogero Cassaro, Andrea Culcasi, Andrea Cipollina, Alessandro Tamburini, Giorgio Micale, Modelling of large scale Electrodialysis with Bipolar Membranes processes using a multi-scale approach with validation at pilot plant scale, 6th International Conference on Desalination using Membrane Technology, https://hdl.handle.net/10447/620784
- **Giovanni Virruso**, Calogero Cassaro, Andrea Culcasi, Andrea Cipollina, Alessandro Tamburini, Giorgio Micale, Electrodialysis with bipolar membranes for the sustainable production of chemicals from seawater brines at pilot plant scale, 2nd International Conference On Energy, Environment & Digital Transition, https://hdl.handle.net/10447/660633;
- Calogero Cassaro, **Giovanni Virruso**, Fabrizio Vassallo, Antonia Filingeri, Alessandra Pellegrino, Andrea Cipollina, Alessandro Tamburini, Giorgio Micale, Brine Valorisation via Extensive Operation of a pilot-scale ElectroDialysis with Bipolar Membranes (EDBM), Euromed 2024 – Desalination for clean water and energy, https://hdl.handle.net/10447/659074;

- **Giovanni Virruso**, Waqar Muhammad Ashraf, Calogero Cassaro, Alessandro Tamburini, Vivek Dua, I. David L. Bogle, Andrea Cipollina, Giorgio Micale, Dynamic modelling of electrodialysis with bipolar membranes unit using NARX recurrent neural networks, European Symposium on Computer Aided Process Engineering and International Symposium on Process Systems Engineering (ESCAPE34 - PSE24), https://iris.unipa.it/handle/10447/658958
- Cassaro, C., **Virruso, G**., Cipollina, A., Fagiolini, A., Tamburini, A., & Micale, G. Coupling Electrodialysis with bipolar membranes with renewable energies through advanced control strategies, European Symposium on Computer Aided Process Engineering and International Symposium on Process Systems Engineering (ESCAPE34 - PSE24), https://hdl.handle.net/10447/660653;
- **Giovanni Virruso**, Andrea Culcasi, Alessandro Tamburini, Andrea Cipollina, Giorgio Micale, Energy analysis of electrodialisys with bipolar membranes for chemicals production, EUROMEMBRANE 2024 https://iris.unipa.it/handle/10447/658473.

Submitted abstract for oral presentations

- **Giovanni Virruso**, Calogero Cassaro, Andrea Culcasi, Andrea Cipollina, Alessandro Tamburini, Giorgio Micale, Dynamic modelling of electrodialysis with bipolar membranes at industrial scale for the sustainable production of chemicals from brines, 14th European Congress of Chemical Engineering and 7th European Congress of Applied Biotechnology, https://hdl.handle.net/10447/620782
- **Giovanni Virruso**, Calogero Cassaro, Andrea Culcasi, Andrea Cipollina, Alessandro Tamburini, Giorgio Micale, Modelling of large scale Electrodialysis with Bipolar Membranes processes using a multi-scale approach with validation at pilot plant scale, 6th International Conference on Desalination using Membrane Technology, https://hdl.handle.net/10447/620784
- **Giovanni Virruso**, Waqar Muhammad Ashraf, Calogero Cassaro, Alessandro Tamburini, Vivek Dua, I. David L. Bogle, Andrea Cipollina, Giorgio Micale, Dynamic modelling of electrodialysis with bipolar membranes unit using NARX recurrent neural networks, European Symposium on Computer Aided Process Engineering and International Symposium on Process Systems Engineering (ESCAPE34 - PSE24), https://iris.unipa.it/handle/10447/658958
- **Giovanni Virruso**, Andrea Culcasi, Alessandro Tamburini, Andrea Cipollina, Giorgio Micale, Energy analysis of electrodialisys with bipolar membranes for chemicals production, EUROMEMBRANE 2024 https://iris.unipa.it/handle/10447/658473.

Acknowledgements

I would like to thank my supervisor, Prof. Giorgio Micale, whose office door has always been open to suggest and help me in many situations, and for his vast generosity. Many thanks to Prof. Andrea Cipollina, who supervised all my PhD activities providing useful pieces of advice and stimulus for the research. Many thanks also to Prof. David Bogle for supporting me in learning a new modelling approach with all his experience and for his valuable feedback on all my research activities. Thanks to Prof. Alessandro Tamburini for his pieces of advice on research and tutoring activities. Thanks also to Dr. Andrea Culcasi for his insights about mechanistic models.

A huge thank you to my girlfriend Angela for sharing with me this path at any moment, always encouraging and helping me during difficulties with love.

I would like to thank my mother for always supporting me with kindness, gentleness and helpfulness.

Many thanks to Calogero Cassaro for his sincere friendship.

I would like to also Tonino, Pietro, Giuseppe, Martina, Giusy and Salvo for their affection and closeness.

Finally, I would like to thank my colleagues from Università degli Studi di Palermo and from University College London and all the wonderful people met during this PhD.

References

[1] European Commission, “Grant Agreement number- N° 869474 -WATER-MINING,” 2020. doi: https://doi.org/10.3030/869474.

[2] I. Manisalidis, E. Stavropoulou, A. Stavropoulos, and E. Bezirtzoglou, “Environmental and Health Impacts of Air Pollution: A Review,” *Front Public Health*, vol. 8, 2020, doi: 10.3389/fpubh.2020.00014.

[3] European Commission, “Il Green Deal europeo,” 2019, [Online]. Available: https://eur-lex.europa.eu/legal-content/EN/TXT/?qid=1588580774040&uri=CELEX:52019DC0640

[4] C. Fernandez-Gonzalez, A. Dominguez-Ramos, R. Ibañez, and A. Irabien, “Electrodialysis with Bipolar Membranes for Valorization of Brines,” *Separation and Purification Reviews*, vol. 45, no. 4, pp. 275–287, 2016, doi: 10.1080/15422119.2015.1128951.

[5] Muhammad Yaqub and W. Lee, “Zero-liquid discharge (ZLD) technology for resource recovery from wastewater: A review,” *Science of the Total Environment*, vol. 681, pp. 551–563, 2019, doi: 10.1016/j.scitotenv.2019.05.062.

[6] T. Tong and M. Elimelech, “The Global Rise of Zero Liquid Discharge for Wastewater Management: Drivers, Technologies, and Future Directions,” *Environ Sci Technol*, vol. 50, no. 13, pp. 6846–6855, 2016, doi: 10.1021/acs.est.6b01000.

[7] D. Puyol, D. J. Batstone, T. Hülsen, S. Astals, M. Peces, and J. O. Krömer, “Resource recovery from wastewater by biological technologies: Opportunities, challenges, and prospects,” *Front Microbiol*, vol. 7, no. JAN, 2017, doi: 10.3389/fmicb.2016.02106.

[8] A. Panagopoulos and K.-J. Haralambous, “Minimal Liquid Discharge (MLD) and Zero Liquid Discharge (ZLD) strategies for wastewater management and resource

recovery-Analysis, challenges and prospects," *J Environ Chem Eng*, vol. 8, no. 5, 2020, doi: 10.1016/j.jece.2020.104418.

[9] A. Panagopoulos, "Techno-economic assessment of zero liquid discharge (ZLD) systems for sustainable treatment, minimization and valorization of seawater brine," *J Environ Manage*, vol. 306, p. 114488, Mar. 2022, doi: 10.1016/J.JENVMAN.2022.114488.

[10] Z. Wang, A. Deshmukh, Y. Du, and M. Elimelech, "Minimal and zero liquid discharge with reverse osmosis using low-salt-rejection membranes," *Water Res*, vol. 170, 2020, doi: 10.1016/j.watres.2019.115317.

[11] G. Cipolletta, N. Lancioni, Ç. Akyol, A. L. Eusebi, and F. Fatone, "Brine treatment technologies towards minimum/zero liquid discharge and resource recovery: State of the art and techno-economic assessment," *J Environ Manage*, vol. 300, 2021, doi: 10.1016/j.jenvman.2021.113681.

[12] D. G. Randall, J. Nathoo, and A. E. Lewis, "A case study for treating a reverse osmosis brine using Eutectic Freeze Crystallization-Approaching a zero waste process," *Desalination*, vol. 266, no. 1–3, pp. 256–262, 2011, doi: 10.1016/j.desal.2010.08.034.

[13] A. Panagopoulos, K.-J. Haralambous, and M. Loizidou, "Desalination brine disposal methods and treatment technologies - A review," *Science of the Total Environment*, vol. 693, 2019, doi: 10.1016/j.scitotenv.2019.07.351.

[14] F. Vassallo *et al.*, "A pilot-plant for the selective recovery of magnesium and calcium from waste brines," *Desalination*, vol. 517, 2021, doi: 10.1016/j.desal.2021.115231.

[15] A. Kumar *et al.*, “Metals Recovery from Seawater Desalination Brines: Technologies, Opportunities, and Challenges,” *ACS Sustain Chem Eng*, vol. 9, no. 23, pp. 7704–7712, 2021, doi: 10.1021/acssuschemeng.1c00785.

[16] Z. Ye *et al.*, “An integrated process for removal and recovery of Cr(VI) from electroplating wastewater by ion exchange and reduction–precipitation based on a silica-supported pyridine resin,” *J Clean Prod*, vol. 236, 2019, doi: 10.1016/j.jclepro.2019.117631.

[17] H. A. Arafat, *Desalination sustainability: A technical, socioeconomic, and environmental approach*. 2017.

[18] C. Morgante *et al.*, “Influence of Operational Strategies for the Recovery of Magnesium Hydroxide from Brines at a Pilot Scale,” *Ind Eng Chem Res*, vol. 61, no. 41, pp. 15355–15368, 2022, doi: 10.1021/acs.iecr.2c02935.

[19] W. Jin, M. Hu, Z. Sun, C.-H. Huang, and H. Zhao, “Simultaneous and precise recovery of lithium and boron from salt lake brine by capacitive deionization with oxygen vacancy-rich CoP/Co<inf>3</inf>O<inf>4</inf>-graphene aerogel,” *Chemical Engineering Journal*, vol. 420, 2021, doi: 10.1016/j.cej.2020.127661.

[20] M. Lu, L. Shao, Y. Yang, and P. Li, “Simultaneous Recovery of Lithium and Boron from Brine by the Collaborative Adsorption of Lithium-Ion Sieves and Boron Chelating Resins,” *Ind Eng Chem Res*, vol. 62, no. 3, pp. 1508–1522, 2023, doi: 10.1021/acs.iecr.2c03650.

[21] M. AzadiAghdam, A. Achilli, S. A. Snyder, and J. Farrell, “Increasing water recovery during reclamation of treated municipal wastewater using bipolar membrane electrodialysis and fluidized bed crystallization,” *Journal of Water Process Engineering*, vol. 38, 2020, doi: 10.1016/j.jwpe.2020.101555.

[22] N. Adiba *et al.*, "Multi-stage membrane integrated system to achieving low-mixed-salt-discharge of high-salinity mining wastewater: System design and experimental validation," *Chemical Engineering Research and Design*, vol. 202, pp. 12–22, 2024, doi: 10.1016/j.cherd.2023.12.015.

[23] G. Jiang, H. Li, M. Xu, and H. Ruan, "Sustainable reverse osmosis, electrodialysis and bipolar membrane electrodialysis application for cold-rolling wastewater treatment in the steel industry," *Journal of Water Process Engineering*, vol. 40, 2021, doi: 10.1016/j.jwpe.2021.101968.

[24] X. Zhao *et al.*, "Zero Liquid Discharge and Resource Treatment of Low-Salinity Mineralized Wastewater Based on Combing Selectrodialysis with Bipolar Membrane Electrodialysis," *Separations*, vol. 10, no. 4, 2023, doi: 10.3390/separations10040269.

[25] A. Kumar, F. Du, and J. H. Lienhard, "Caustic Soda Production, Energy Efficiency, and Electrolyzers," *ACS Energy Lett*, vol. 6, no. 10, pp. 3563–3566, 2021, doi: 10.1021/acsenergylett.1c01827.

[26] "Chlor-alkali industry review 2021-2022." Accessed: Aug. 26, 2023. [Online]. Available: https://chlorineindustryreview.com

[27] P. ; F. T. ; C. L. C. ; L. ke, B. ; S. R. ; N. T. ; Z. E. ; B. R. Chlorine. Schmittinger, *Ullmann's Encyclopedia of Industrial Chemistry*. Wiley, 2003. doi: 10.1002/14356007.

[28] G. P. Thiel, A. Kumar, A. Gómez-González, and J. H. Lienhard, "Utilization of Desalination Brine for Sodium Hydroxide Production: Technologies, Engineering Principles, Recovery Limits, and Future Directions," *ACS Sustain Chem Eng*, vol. 5, no. 12, pp. 11147–11162, 2017, doi: 10.1021/acssuschemeng.7b02276.

[29] S. S. Madaeni and S. Samieirad, “Chemical cleaning of reverse osmosis membrane fouled by wastewater,” *Desalination*, vol. 257, no. 1–3, pp. 80–86, 2010, doi: 10.1016/j.desal.2010.03.002.

[30] J. R. Davis, Y. Chen, J. C. Baygents, and J. Farrell, “Production of Acids and Bases for Ion Exchange Regeneration from Dilute Salt Solutions Using Bipolar Membrane Electrodialysis,” *ACS Sustain Chem Eng*, vol. 3, no. 9, pp. 2337–2342, 2015, doi: 10.1021/acssuschemeng.5b00654.

[31] Eusalt, “Caustic soda uses.” Accessed: Aug. 26, 2023. [Online]. Available: https://eusalt.com/about-salt/salt-uses/industry/

[32] J. Shen, C. Zhao, G. Liu, and C. Chen, “Enhancing the Performance on Anaerobic Digestion of Vinegar Residue by Sodium Hydroxide Pretreatment,” *Waste Biomass Valorization*, vol. 8, no. 4, 2017, doi: 10.1007/s12649-016-9666-2.

[33] W. Ye *et al.*, “Environmental evaluation of bipolar membrane electrodialysis for NaOH production from wastewater: Conditioning NaOH as a CO2 absorbent,” *Sep Purif Technol*, vol. 144, pp. 206–214, 2015, doi: 10.1016/j.seppur.2015.02.031.

[34] M. Yoo, S. J. Han, and J. H. Wee, “Carbon dioxide capture capacity of sodium hydroxide aqueous solution,” *J Environ Manage*, vol. 114, 2013, doi: 10.1016/j.jenvman.2012.10.061.

[35] OxyChem, “Hydrochloric Acid Handbook.” Accessed: Aug. 28, 2023. [Online]. Available: https://www.oxy.com/siteassets/documents/chemicals/products/chlor-alkali/Hydrochloric_Acid_Handbook.pdf

[36] Foodcom, “Hydrochloric Acid: applications in the food and pharmaceutical industries.” Accessed: Oct. 15, 2023. [Online]. Available: https://foodcom.pl/en/hydrochloric-acid-applications-in-the-food-and-pharmaceutical-industries/

[37] A. Culcasi, R. Gueccia, S. Randazzo, A. Cipollina, and G. Micale, “Design of a novel membrane-integrated waste acid recovery process from pickling solution,” *J Clean Prod*, vol. 236, 2019, doi: 10.1016/j.jclepro.2019.117623.

[38] A. Mirwan, M. D. Putra, J.-C. Liu, Susianto, A. Altway, and R. Handogo, “Aluminum leaching from water treatment sludge using hydrochloric acid and kinetic study,” *Environmental Science and Pollution Research*, vol. 27, no. 20, pp. 25553–25562, 2020, doi: 10.1007/s11356-020-08922-x.

[39] Purolite, “C104Plus and C104EPlus Hydrogen Cycle Operation Hydrochloric or Sulfuric Acid Regeneration.”

[40] H. Strathmann, *Ion-Exchange Membrane Separation Processes*, First edit. Elsevier B.V., 2004.

[41] M. Herrero-Gonzalez, P. Diaz-Guridi, A. Dominguez-Ramos, R. Ibañez, and A. Irabien, “Photovoltaic solar electrodialysis with bipolar membranes,” *Desalination*, vol. 433, pp. 155–163, 2018, doi: 10.1016/j.desal.2018.01.015.

[42] M. Herrero-Gonzalez, A. Culcasi, A. Tamburini, R. Ibañez, A. Cipollina, and G. Micale, “Techno-economic feasibility of photovoltaic solar electrodialysis with bipolar membranes,” *Desalination*, vol. 582, 2024, doi: 10.1016/j.desal.2024.117624.

[43] J. A. (Abbé) Nollet, “Investigations on the causes for the ebullition of liquids,” *J Memb Sci*, vol. 100, no. 1, pp. 1–3, 1995, doi: 10.1016/0376-7388(94)00224-M.

[44] Ostwald W., “Elektrische Eigenschaften Halbdurchlassiger Scheidewande,” *Z. Physik. Cheime*, vol. 6, pp. 71–82, 1890.

[45] Donnan F.G., “Theory of Membrane Equilibria and Membrane Potentials in the Presence of Non-dialyzing Electrolytes,” *Z. Elektrochem.*, vol. 17, pp. 572–581, 1911.

[46] K. H. Meyer and W. Straus, “La perméabilité des membranes VI. Sur le passage du courant électrique à travers des membranes sélectives,” *Helv Chim Acta*, vol. 23, no. 1, pp. 795–800, 1940, doi: 10.1002/hlca.19400230199.

[47] J. B. Farrell and R. N. Smith, “Process applications of electrodialysis,” *Ind Eng Chem*, vol. 54, no. 6, pp. 29–35, 1962, doi: 10.1021/ie50630a004.

[48] V. J. Frilette, “Preparation and characterization of bipolar ion-exchange membranes,” *Journal of Physical Chemistry*, vol. 60, no. 4, pp. 435–439, 1956, doi: 10.1021/j150538a013.

[49] K. Nagasubramanian, F. P. Chlanda, and K. J. Liu, “Use of bipolar membranes for generation of acid and base - an engineering and economic analysis,” *J Memb Sci*, vol. 2, no. C, 1977, doi: 10.1016/S0376-7388(00)83237-8.

[50] L. Bazinet, F. Lamarche, and D. Ippersiel, “Bipolar-membrane electrodialysis: Applications of electrodialysis in the food industry,” *Trends Food Sci Technol*, vol. 9, no. 3, pp. 107–113, 1998, doi: 10.1016/S0924-2244(98)00026-0.

[51] F. Giacalone *et al.*, “Exergy analysis of electrodialysis for water desalination: Influence of irreversibility sources,” *Energy Convers Manag*, vol. 258, 2022, doi: 10.1016/j.enconman.2022.115314.

[52] H. Strathmann, “Electrodialysis, a mature technology with a multitude of new applications,” *Desalination*, vol. 264, no. 3, pp. 268–288, 2010, doi: 10.1016/j.desal.2010.04.069.

[53] L. Gurreri, A. Tamburini, A. Cipollina, and G. Micale, “Electrodialysis applications in wastewater treatment for environmental protection and resources recovery: A systematic review on progress and perspectives,” Jul. 01, 2020, *MDPI AG*. doi: 10.3390/membranes10070146.

[54] A. Campione *et al.*, "A hierarchical model for novel schemes of electrodialysis desalination," *Desalination*, vol. 465, pp. 79–93, 2019, doi: 10.1016/j.desal.2019.04.020.

[55] R. Pärnamäe *et al.*, "Bipolar membranes: A review on principles, latest developments, and applications," 2021. doi: 10.1016/j.memsci.2020.118538.

[56] Y. Tanaka, *Ion Exchange membranes: Fundamentals and Applications*. Amsterdam: Elsevier B.V., 2007.

[57] G. Virruso *et al.*, "Multi-scale modelling of an electrodialysis with bipolar membranes pilot plant and economic evaluation of its potential," *Desalination*, vol. 583, p. 117724, Aug. 2024, doi: 10.1016/j.desal.2024.117724.

[58] A. Culcasi *et al.*, "Towards sustainable production of minerals and chemicals through seawater brine treatment using Eutectic freeze crystallization and Electrodialysis with bipolar membranes," *J Clean Prod*, vol. 368, 2022, doi: 10.1016/j.jclepro.2022.133143.

[59] H. Wang *et al.*, "Bipolar membrane electrodialysis: A promising paradigm for caustic soda production," *AIChE Journal*, vol. 70, no. 1, 2024, doi: 10.1002/aic.18260.

[60] G. S. Trivedi, B. G. Shah, S. K. Adhikary, and R. Rangarajan, "Studies on bipolar membranes Part III: Conversion of sodium phosphate to phosphoric acid and sodium hydroxide," *React Funct Polym*, vol. 39, no. 1, pp. 91–97, 1999, doi: 10.1016/s1381-5148(97)00159-4.

[61] M. A. B. Ali, M. Rakib, S. Laborie, Ph. Viers, and G. Durand, "Coupling of bipolar membrane electrodialysis and ammonia stripping for direct treatment of wastewaters containing ammonium nitrate," *J Memb Sci*, vol. 244, no. 1–2, pp. 89–96, 2004, doi: 10.1016/j.memsci.2004.07.007.

[62] K. N. Mani, “Electrodialysis water splitting technology,” *J Memb Sci*, vol. 58, no. 2, pp. 117–138, 1991, doi: 10.1016/S0376-7388(00)82450-3.

[63] H. Ren, Q. Wang, X. Zhang, R. Kang, S. Shi, and W. Cong, “Membrane fouling caused by amino acid and calcium during bipolar membrane electrodialysis,” *Journal of Chemical Technology and Biotechnology*, vol. 83, no. 11, pp. 1551–1557, 2008, doi: 10.1002/jctb.1969.

[64] H. Ma, S. Yue, H. Li, Q. Wang, and M. Tu, “Recovery of lactic acid and other organic acids from food waste ethanol fermentation stillage: Feasibility and effects of substrates,” *Sep Purif Technol*, vol. 209, pp. 223–228, 2019, doi: 10.1016/j.seppur.2018.07.031.

[65] E. Gyo Lee, S.-H. Moon, Y. Keun Chang, I.-K. Yoo, and H. Nam Chang, “Lactic acid recovery using two-stage electrodialysis and its modelling,” *J Memb Sci*, vol. 145, no. 1, pp. 53–66, 1998, doi: 10.1016/S0376-7388(98)00065-9.

[66] G. S. Trivedi, B. G. Shah, S. K. Adhikary, V. K. Indusekhar, and R. Rangarajan, “Studies on bipolar membranes. Part II - Conversion of sodium acetate to acetic acid and sodium hydroxide,” *React Funct Polym*, vol. 32, no. 2, pp. 209–215, 1997, doi: 10.1016/S1381-5148(96)00088-0.

[67] X. Tongwen and Y. Weihua, “Citric acid production by electrodialysis with bipolar membranes,” *Chemical Engineering and Processing*, vol. 41, no. 6, pp. 519–524, 2002, doi: 10.1016/S0255-2701(01)00175-1.

[68] X. Zhang, W. Lu, H. Ren, and W. Cong, “Recovery of glutamic acid from isoelectric supernatant using electrodialysis,” *Sep Purif Technol*, vol. 55, no. 2, pp. 274–280, 2007, doi: 10.1016/j.seppur.2006.11.017.

[69] F. Alvarez, R. Alvarez, J. Coca, J. Sandeaux, R. Sandeaux, and C. Gavach, "Salicylic acid production by electrodialysis with bipolar membranes," *J Memb Sci*, vol. 123, no. 1, pp. 61–69, 1997, doi: 10.1016/S0376-7388(96)00197-4.

[70] H. Grib, L. Bonnal, J. Sandeaux, R. Sandeaux, C. Gavach, and N. Mameri, "Extraction of amphoteric amino acids by an electromembrane process. pH and electrical state control by electrodialysis with bipolar membranes," *Journal of Chemical Technology and Biotechnology*, vol. 73, no. 1, pp. 64–70, 1998, doi: 10.1002/(SICI)1097-4660(199809)73:1<64::AID-JCTB933>3.0.CO;2-F.

[71] J.-H. Choi, S.-J. Oh, and S.-H. Moon, "Structural effects of ion-exchange membrane on the separation of L-phenylalanine (L-Phe) from fermentation broth using electrodialysis," *Journal of Chemical Technology and Biotechnology*, vol. 77, no. 7, pp. 785–792, 2002, doi: 10.1002/jctb.638.

[72] K. N. Mani, F. P. Chlanda, and C. H. Byszewski, "Aquatech membrane technology for recovery of acid/base values for salt streams," *Desalination*, vol. 68, no. 2–3, pp. 149–166, 1988, doi: 10.1016/0011-9164(88)80051-1.

[73] K. N. Mani and F. P. Chlanda, "SOXAL**t**m FLUE GAS DESULFURIZATION PROCESS - RESULTS OF LAB AND PILOT STUDIES.," 1985, pp. 177–196.

[74] G. P. ZEMEL, C. A. SIMS, M. R. MARSHALL, and M. BALABAN, "Low pH Inactivation of Polyphenoloxidase in Apple Juice," *J Food Sci*, vol. 55, no. 2, pp. 562–563, 1990, doi: 10.1111/j.1365-2621.1990.tb06813.x.

[75] J. S. Tronc, F. Lamarche, and J. Makhlouf, "Effect of pH Variation by Electrodialysis on the Inhibition of Enzymatic Browning in Cloudy Apple Juice," *J Agric Food Chem*, vol. 46, no. 3, pp. 829–833, 1998, doi: 10.1021/jf970642e.

[76] L. Bazinet, F. Lamarche, R. Labrecque, and D. Ippersiel, “Effect of KCl and Soy Protein Concentrations on the Performance of Bipolar Membrane Electroacidification,” *J Agric Food Chem*, vol. 45, no. 7, pp. 2419–2425, 1997, doi: 10.1021/jf970004w.

[77] L. Bazinet, F. Lamarche, and D. Ippersiel, “Ionic balance: a closer look at the K+ migrated and H+ generated during bipolar membrane electro-acidification of soybean proteins,” *J Memb Sci*, vol. 154, no. 1, pp. 61–71, Mar. 1999, doi: 10.1016/S0376-7388(98)00281-6.

[78] A. Filingeri *et al.*, “In-depth insights on multi-ionic transport in Electrodialysis with bipolar membrane systems,” *Chemical Engineering Journal*, vol. 468, 2023, doi: 10.1016/j.cej.2023.143673.

[79] H. Strathmann, J. J. Krol, H.-J. Rapp, and G. Eigenberger, “Limiting current density and water dissociation in bipolar membranes,” *J Memb Sci*, vol. 125, no. 1, pp. 123–142, 1997, doi: 10.1016/S0376-7388(96)00185-8.

[80] R. Pärnamäe *et al.*, “The acid–base flow battery: Sustainable energy storage via reversible water dissociation with bipolar membranes,” *Membranes (Basel)*, vol. 10, no. 12, pp. 1–20, 2020, doi: 10.3390/membranes10120409.

[81] A. Culcasi, L. Gurreri, A. Tamburini, A. Cipollina, and G. Micale, “Effect of design features and operating conditions on the performance of a bipolar membrane-based acid/base flow battery,” *Chem Eng Trans*, vol. 86, pp. 1387–1392, 2021, doi: 10.3303/CET2186232.

[82] E. Al-Dhubhani, R. Pärnamäe, J. W. Post, M. Saakes, and M. Tedesco, “Performance of five commercial bipolar membranes under forward and reverse bias conditions for acid-base flow battery applications,” *J Memb Sci*, vol. 640, 2021, doi: 10.1016/j.memsci.2021.119748.

[83] H. Ruan *et al.*, “Capturing CO2 with NaOH solution from reject brine via an integrated technology based on bipolar membrane electrodialysis and hollow fiber membrane contactor,” *Chemical Engineering Journal*, vol. 450, p. 138095, Dec. 2022, doi: 10.1016/j.cej.2022.138095.

[84] C. W. Hwang *et al.*, “Process design for lithium recovery using bipolar membrane electrodialysis system,” *Sep Purif Technol*, vol. 166, pp. 34–40, 2016, doi: 10.1016/j.seppur.2016.03.013.

[85] C. Jiang, Y. Wang, Q. Wang, H. Feng, and T. Xu, “Production of lithium hydroxide from lake brines through electro-electrodialysis with bipolar membranes (EEDBM),” *Ind Eng Chem Res*, vol. 53, no. 14, pp. 6103–6112, 2014, doi: 10.1021/ie404334s.

[86] A. Pellegrino *et al.*, “Hydrogen-Electrodialysis with Bipolar Membrane (H-EDBM): First experiments and preliminary economic evaluation,” *Desalination*, vol. 592, 2024, doi: 10.1016/j.desal.2024.118169.

[87] G. Scelfo *et al.*, “Demonstration of ultra-high-water recovery and brine concentration in a prototype evaporation unit: Towards zero liquid discharge desalination,” *Sep Purif Technol*, vol. 354, 2025, doi: 10.1016/j.seppur.2024.129427.

[88] Giovanni Virruso, “Modellazione multiscala e scale-up di unità di elettrodialisi con membrane bipolari per la produzione di chemicals,” Università degli Studi di Palermo, Palermo, 2021.

[89] “Google Earth.” Accessed: Oct. 19, 2024. [Online]. Available: https://www.google.it/intl/it/earth/index.html

[90] M. Herrero-Gonzalez *et al.*, “Analysis of Operational Parameters in Acid and Base Production Using an Electrodialysis with Bipolar Membranes Pilot Plant,” *Membranes (Basel)*, vol. 13, no. 2, 2023, doi: 10.3390/membranes13020200.

[91] S. A. Mareev *et al.*, “A comprehensive mathematical model of water splitting in bipolar membranes: Impact of the spatial distribution of fixed charges and catalyst at bipolar junction,” *J Memb Sci*, vol. 603, 2020, doi: 10.1016/j.memsci.2020.118010.

[92] C. Cassaro, G. Virruso, A. Culcasi, A. Cipollina, A. Tamburini, and G. Micale, “Electrodialysis with Bipolar Membranes for the Sustainable Production of Chemicals from Seawater Brines at Pilot Plant Scale,” *ACS Sustain Chem Eng*, vol. 11, no. 7, pp. 2989–3000, 2023, doi: 10.1021/acssuschemeng.2c06636.

[93] A. Culcasi *et al.*, “Ionic shortcut currents via manifolds in reverse electrodialysis stacks,” *Desalination*, vol. 485, 2020, doi: 10.1016/j.desal.2020.114450.

[94] H. R. Yang *et al.*, “Bipolar membrane electrodialysis for sustainable utilization of inorganic salts from the reverse osmosis concentration of real landfill leachate,” *Sep Purif Technol*, vol. 308, Mar. 2023, doi: 10.1016/j.seppur.2022.122898.

[95] C. Huang and T. Xu, “Electrodialysis with bipolar membranes for sustainable development,” *Environ Sci Technol*, vol. 40, no. 17, pp. 5233–5243, 2006, doi: 10.1021/es060039p.

[96] A. Filingeri *et al.*, “Acid/Base Production via Bipolar Membrane Electrodialysis: Brine Feed Streams to Reduce Fresh Water Consumption,” *Ind Eng Chem Res*, vol. 63, no. 7, pp. 3198–3210, Feb. 2024, doi: 10.1021/acs.iecr.3c03553.

[97] C. Cassaro, G. Virruso, A. Cipollina, A. Fagiolini, A. Tamburini, and G. Micale, *Coupling Electrodialysis with bipolar membranes with renewable energies*

through advanced control strategies, vol. 53. 2024. doi: 10.1016/B978-0-443-28824-1.50330-6.

[98] M. Reig, S. Casas, C. Valderrama, O. Gibert, and J. L. Cortina, "Integration of monopolar and bipolar electrodialysis for valorization of seawater reverse osmosis desalination brines: Production of strong acid and base," *Desalination*, vol. 398, pp. 87–97, Nov. 2016, doi: 10.1016/j.desal.2016.07.024.

[99] M. Herrero-Gonzalez, P. Diaz-Guridi, A. Dominguez-Ramos, A. Irabien, and R. Ibañez, "Highly concentrated HCl and NaOH from brines using electrodialysis with bipolar membranes," *Sep Purif Technol*, vol. 242, 2020, doi: 10.1016/j.seppur.2020.116785.

[100] European Commission, "PHOTOVOLTAIC GEOGRAPHICAL INFORMATION SYSTEM (PV-GIS)." Accessed: Oct. 06, 2024. [Online]. Available: https://re.jrc.ec.europa.eu/pvg_tools/en/

[101] G. Virruso, C. Cassaro, A. Tamburini, A. Cipollina, and G. D. M. Micale, "Performance Evaluation of an Electrodialysis with Bipolar Membranes Pilot Plant Operated in Feed & Bleed Mode," *Chem Eng Trans*, vol. 105, pp. 73–78, 2023, doi: 10.3303/CET23105013.

[102] M. Asghari, A. Dashti, M. Rezakazemi, E. Jokar, and H. Halakoei, "Application of neural networks in membrane separation," *Reviews in Chemical Engineering*, vol. 36, no. 2, pp. 265–310, 2020, doi: 10.1515/revce-2018-0011.

[103] Anders. Rasmuson, B. Andersson, L. Olsson, and R. Andersson, *Mathematical Modeling in Chemical Engineering*. Cambridge: Cambridge University Press, 2014.

[104] A. Culcasi, L. Gurreri, A. Cipollina, A. Tamburini, and G. Micale, "A comprehensive multi-scale model for bipolar membrane electrodialysis (BMED),"

Chemical Engineering Journal, vol. 437, p. 135317, Jun. 2022, doi: 10.1016/J.CEJ.2022.135317.

[105] A. Ortega *et al.*, "Modelling water dissociation, acid-base neutralization and ion transport in bipolar membranes for acid-base flow batteries," *J Memb Sci*, vol. 641, 2022, doi: 10.1016/j.memsci.2021.119899.

[106] T. León, J. López, R. Torres, J. Grau, L. Jofre, and J.-L. Cortina, "Describing ion transport and water splitting in an electrodialysis stack with bipolar membranes by a 2-D model: Experimental validation," *J Memb Sci*, vol. 660, 2022, doi: 10.1016/j.memsci.2022.120835.

[107] M. P. Mier, R. Ibañez, and I. Ortiz, "Influence of ion concentration on the kinetics of electrodialysis with bipolar membranes," *Sep Purif Technol*, vol. 59, no. 2, pp. 197–205, 2008, doi: 10.1016/j.seppur.2007.06.015.

[108] S. Koter and A. Warszawski, "A new model for characterization of bipolar membrane electrodialysis of brine," *Desalination*, vol. 198, no. 1–3, pp. 111–123, 2006, doi: 10.1016/j.desal.2006.09.016.

[109] J. L. Gineste, G. Pourcelly, Y. Lorrain, F. Persin, and C. Gavach, "Analysis of factors limiting the use of bipolar membranes: A simplified model to determine trends," *J Memb Sci*, vol. 112, no. 2, pp. 199–208, 1996, doi: 10.1016/0376-7388(95)00284-7.

[110] Y. Wang, A. Wang, X. Zhang, and T. Xu, "Simulation of electrodialysis with bipolar membranes: Estimation of process performance and energy consumption," *Ind Eng Chem Res*, vol. 50, no. 24, pp. 13911–13921, 2011, doi: 10.1021/ie200467s.

[111] A. Culcasi, L. Gurreri, A. Zaffora, A. Cosenza, A. Tamburini, and G. Micale, "On the modelling of an Acid/Base Flow Battery: An innovative electrical energy

storage device based on pH and salinity gradients," *Appl Energy*, vol. 277, p. 115576, Nov. 2020, doi: 10.1016/j.apenergy.2020.115576.

[112] Siemens, "gPROMS – Digital Process Twin technology." Accessed: Oct. 08, 2024. [Online]. Available: https://www.siemens.com/global/en/products/automation/industry-software/gproms-digital-process-design-and-operations.html

[113] R. B. McCleskey, D. K. Nordstrom, J. N. Ryan, and J. W. Ball, "A new method of calculating electrical conductivity with applications to natural waters," *Geochim Cosmochim Acta*, vol. 77, pp. 369–382, Jan. 2012, doi: 10.1016/J.GCA.2011.10.031.

[114] C. Lei *et al.*, "Comparative study on the production of gluconic acid by electrodialysis and bipolar membrane electrodialysis: Effects of cell configurations," *J Memb Sci*, vol. 608, p. 118192, Aug. 2020, doi: 10.1016/J.MEMSCI.2020.118192.

[115] "XE currency converter ." Accessed: Aug. 16, 2023. [Online]. Available: https://www.xe.com/currencyconverter/convert/?Amount=1&From=EUR&To=USD

[116] "Eurostat, Electricity price statistics." Accessed: Aug. 15, 2023. [Online]. Available: https://ec.europa.eu/eurostat/databrowser/view/NRG_PC_205/default/table?lang=en

[117] H.-J. Lee, F. Sarfert, H. Strathmann, and S.-H. Moon, "Designing of an electrodialysis desalination plant," *Desalination*, vol. 142, no. 3, pp. 267–286, 2002, doi: 10.1016/S0011-9164(02)00208-4.

[118] J. A. M. K. Kontturi, L. Murtomäki, *Ionic Transport Processes*. Oxford University Press, 2008. [Online]. Available: https://oxford.universitypressscholarship.com/view/10.1093/acprof:oso/9780199533817.001.0001/acprof-9780199533817

[119] W. Zhang *et al.*, "Process Economic Evaluation of Resource Valorization of Seawater Concentrate by Membrane Technology," *ACS Sustain Chem Eng*, vol. 5, no. 7, pp. 5820–5830, 2017, doi: 10.1021/acssuschemeng.7b00555.

[120] Y. Cao, M. Kasaeian, H. Abbasspoor, M. Shamoushaki, M. A. Ehyaei, and S. Abanades, "Energy, exergy, and economic analyses of a novel biomass-based multigeneration system integrated with multi-effect distillation, electrodialysis, and LNG tank," *Desalination*, vol. 526, 2022, doi: 10.1016/j.desal.2022.115550.

[121] O. S. L. Bruinsma, D. J. Branken, T. N. Lemmer, L. van der Westhuizen, and S. Rossouw, "Sodium sulfate splitting as zero brine process in a base metal refinery: Screening and optimization in batch mode," *Desalination*, vol. 511, Sep. 2021, doi: 10.1016/j.desal.2021.115096.

[122] H. Ibrahim and N. Anani, "Evaluation of Analytical Methods for Parameter Extraction of PV modules," in *Energy Procedia*, 2017, pp. 69–78. doi: 10.1016/j.egypro.2017.09.601.

[123] S. Armstrong and W. G. Hurley, "A thermal model for photovoltaic panels under varying atmospheric conditions," *Appl Therm Eng*, vol. 30, no. 11–12, pp. 1488–1495, 2010, doi: 10.1016/j.applthermaleng.2010.03.012.

[124] I.-L. Chien and P. S. Fruehauf, "Consider IMC tuning to improve controller performance," *Chem Eng Prog*, vol. 86, no. 10, pp. 33–41, 1990.

[125] C. Xiouras, F. Cameli, G. L. Quilló, M. E. Kavousanakis, D. G. Vlachos, and G. D. Stefanidis, "Applications of Artificial Intelligence and Machine Learning

Algorithms to Crystallization," *Chem Rev*, vol. 122, no. 15, pp. 13006–13042, 2022, doi: 10.1021/acs.chemrev.2c00141.

[126] C. J. Harris, M. Brown, K. M. Bossley, D. J. Mills, and F. Ming, "Advances in neurofuzzy algorithms for real-time modelling and control," *Eng Appl Artif Intell*, vol. 9, no. 1, pp. 1–16, 1996, doi: 10.1016/0952-1976(95)00059-3.

[127] J. Jawad, A. H. Hawari, and S. Javaid Zaidi, "Artificial neural network modeling of wastewater treatment and desalination using membrane processes: A review," *Chemical Engineering Journal*, vol. 419, 2021, doi: 10.1016/j.cej.2021.129540.

[128] R. W. Baker, *Membrane Technology and Applications*, Second. London: Wiley, 2012. doi: 10.1002/9781118359686.

[129] A. Jokić *et al.*, "Dynamic modeling using artificial neural network of bacillus velezensis broth cross-flow microfiltration enhanced by air-sparging and turbulence promoter," *Membranes (Basel)*, vol. 10, no. 12, pp. 1–14, 2020, doi: 10.3390/membranes10120372.

[130] M. Hamachi, M. Cabassud, A. Davin, and M. Mietton Peuchot, "Dynamic modelling of crossflow microfiltration of bentonite suspension using recurrent neural networks," *Chemical Engineering and Processing: Process Intensification*, vol. 38, no. 3, pp. 203–210, 1999, doi: 10.1016/S0255-2701(99)00004-5.

[131] H. Al-Zoubi, N. Hilal, N. A. Darwish, and A. W. Mohammad, "Rejection and modelling of sulphate and potassium salts by nanofiltration membranes: neural network and Spiegler-Kedem model," *Desalination*, vol. 206, no. 1–3, pp. 42–60, 2007, doi: 10.1016/j.desal.2006.02.060.

[132] J. Shim, S. Park, and K. H. Cho, "Deep learning model for simulating influence of natural organic matter in nanofiltration," *Water Res*, vol. 197, 2021, doi: 10.1016/j.watres.2021.117070.

[133] A. Cipollina, A. Di Miceli, J. Koschikowski, G. Micale, and L. Rizzuti, "CFD simulation of a membrane distillation module channel," *Desalination Water Treat*, vol. 6, no. 1–3, pp. 177–183, Jun. 2009, doi: 10.5004/DWT.2009.664.

[134] R. Porrazzo, A. Cipollina, M. Galluzzo, and G. Micale, "A neural network-based optimizing control system for a seawater-desalination solar-powered membrane distillation unit," *Comput Chem Eng*, vol. 54, pp. 79–96, 2013, doi: 10.1016/j.compchemeng.2013.03.015.

[135] M. Sadrzadeh, T. Mohammadi, J. Ivakpour, and N. Kasiri, "Separation of lead ions from wastewater using electrodialysis: Comparing mathematical and neural network modeling," *Chemical Engineering Journal*, vol. 144, no. 3, pp. 431–441, 2008, doi: 10.1016/j.cej.2008.02.023.

[136] G. Jing, W. Du, and Y. Guo, "Studies on prediction of separation percent in electrodialysis process via BP neural networks and improved BP algorithms," *Desalination*, vol. 291, pp. 78–93, 2012, doi: 10.1016/j.desal.2012.02.002.

[137] W. M. Ashraf and V. Dua, "Artificial intelligence driven smart operation of large industrial complexes supporting the net-zero goal: Coal power plants," *Digital Chemical Engineering*, vol. 8, 2023, doi: 10.1016/j.dche.2023.100119.

[138] Martin T. Hagan, Howard B. Demuth, Mark Hudson Beale, and Orlando De Jesús, "Neural Network Design 2nd Edition."

[139] Bellini Alessandro and Guidi Andrea, Eds., *Python and machine learning*. Milano: McGraw-Hill Education (Italy) S.r.l., 2022.

[140] N. Shojai Kaveh, S. N. Ashrafizadeh, and F. Mohammadi, "Development of an artificial neural network model for prediction of cell voltage and current efficiency in a chlor-alkali membrane cell," *Chemical Engineering Research and Design*, vol. 86, no. 5, pp. 461–472, 2008, doi: 10.1016/j.cherd.2007.12.009.

[141] M. Barello, D. Manca, R. Patel, and I. M. Mujtaba, “Neural network based correlation for estimating water permeability constant in RO desalination process under fouling,” *Desalination*, vol. 345, pp. 101–111, 2014, doi: 10.1016/j.desal.2014.04.016.

[142] C. Niu, X. Li, R. Dai, and Z. Wang, “Artificial intelligence-incorporated membrane fouling prediction for membrane-based processes in the past 20 years: A critical review,” *Water Res*, vol. 216, 2022, doi: 10.1016/j.watres.2022.118299.

[143] S. Geissler, T. Wintgens, T. Melin, K. Vossenkaul, and C. Kullmann, “Modelling approaches for filtration processes with novel submerged capillary modules in membrane bioreactors for wastewater treatment,” *Desalination*, vol. 178, no. 1-3 SPEC., pp. 125–134, 2005, doi: 10.1016/j.desal.2004.11.032.

[144] G. Virruso *et al.*, *Dynamic Modelling of Electrodialysis with Bipolar Membranes using NARX Recurrent Neural Networks*, vol. 53. 2024. doi: 10.1016/B978-0-443-28824-1.50031-4.

[145] H. Wang and G. Song, “Innovative NARX recurrent neural network model for ultra-thin shape memory alloy wire,” *Neurocomputing*, vol. 134, pp. 289–295, 2014, doi: 10.1016/j.neucom.2013.09.050.

[146] C. F. Galinha and J. G. Crespo, “From black box to machine learning: A journey through membrane process modelling,” *Membranes (Basel)*, vol. 11, no. 8, 2021, doi: 10.3390/membranes11080574.

[147] M. L. Thompson and M. A. Kramer, “Modeling chemical processes using prior knowledge and neural networks,” *AIChE Journal*, vol. 40, no. 8, pp. 1328–1340, 1994, doi: 10.1002/aic.690400806.

[148] D. Rall *et al.*, “Simultaneous rational design of ion separation membranes and processes,” *J Memb Sci*, vol. 600, 2020, doi: 10.1016/j.memsci.2020.117860.

[149] Y. Liu, C.-P. Chou, J. Chen, and J.-Y. Lai, “Active learning assisted strategy of constructing hybrid models in repetitive operations of membrane filtration processes: Using case of mixture of bentonite clay and sodium alginate,” *J Memb Sci*, vol. 515, pp. 245–257, 2016, doi: 10.1016/j.memsci.2016.05.057.

[150] T.-M. Hwang, H. Oh, Y.-J. Choi, S.-H. Nam, S. Lee, and Y.-K. Choung, “Development of a statistical and mathematical hybrid model to predict membrane fouling and performance,” *Desalination*, vol. 247, no. 1–3, pp. 210–221, 2009, doi: 10.1016/j.desal.2008.12.025.

[151] M. Laliberté and W. E. Cooper, “Model for calculating the density of aqueous electrolyte solutinos,” *J Chem Eng Data*, vol. 49, no. 5, pp. 1141–1151, 2004, doi: 10.1021/je0498659.

[152] K. S. Pitzer and G. Mayorga, “Thermodynamics of electrolytes. II. Activity and osmotic coefficients for strong electrolytes with one or both ions univalent,” *Journal of Physical Chemistry*, vol. 77, no. 19, pp. 2300–2308, 1973, doi: 10.1021/j100638a009.

[153] K. S. Pitzer and J. J. Kim, “Thermodynamics of Electrolytes. IV. Activity and Osmotic Coefficients for Mixed Electrolytes,” *J Am Chem Soc*, vol. 96, no. 18, pp. 5701–5707, 1974, doi: 10.1021/ja00825a004.

Nomenclature

Acronyms/abbreviations

2D	Two-dimensional
3D	Three-dimensional
A	Artificial brine
ABFB	Acid–base flow battery
AC	Alternating current
AEL	Anion exchange layer
AEM	Anion exchange membrane
ANN	Artificial neural network
ANNM	Artificial neural network model
BPM	Bipolar membrane
CAD	Computer aided design
CE	Current efficiency
CEL	Cation exchange layers
CEM	Cation exchange membrane
CFD	Computational fluid dynamics
CL	Closed-loop
DC	Direct current
DSA	Dimensionally stable anode
ED	Electrodialysis
EDBM	Electrodialysis with bipolar membranes
EP	Evaporative pond
ERS	Electrodes rinse solution
F	Flowrate control strategy
F&B	Feed and Bleed
FFNN	Feedforward neural network
GPRM	Gaussian process regression model
H2ccys	Carbocysteine
HB	Hybrid model
HDPE	High-densitypolyethylene
H-EDBM	Electrodialysis with bipolar membranes for hydrogen production
IBC	Intermediate bulk containers
ICI	Initial capital investment
IEM	Ion-exchange membrane
IEX	Ion-exchange resins
KPI	Key performance indicator

LCoNaOH	Levelized cost of sodium hydroxide
LSTM	Long-short term memory
MD	Membrane Distillation
MED	Multiple effect distillation
MF	Microfiltration
MF-PFR	Multiple feed plug flow reactor
MLD	Minimum liquid discharge
MM	Mechanistic model
MPC	Model predictive control
MPM	Monopolar membrane
MSE	Mean squared error
NAR	Nonlinear autoregressive
NARX	Nonlinear autoregressive models with exogenous inputs
NET	non-equilibrium thermodynamics
NF	Nanofiltration
NION	Nonlinear input output network
NPV	Net present value
P	Pressure control strategy
PC	Process capacity
PFD	Process flow diagram
PI	Proportional-integral
PK	Aliphatic polyketone
PLC	Programmable logic controller
PP	Polypropylene
PTFE	Polytetrafluoroethylene
PV	Photovoltaic
PVC	Polyvinyl chloride
PV-EDBM	Electrodialysis with bipolar membranes powered by photovoltaic modules
R	Real brine
REF	Reference scheme
RES	Renewable energy source
RO	Reverse osmosis
SCADA	Supervisory control and data acquisition
SEC	Specific energy consumption
SED	Selectrodialysis
SP	Specific productivity
SSS	Salt-salt-salt scheme
SWS	Salt-water-salt scheme
TDL	Tapped delay line
TEC	Total energy consumption
TRL	Technology readiness level

UF	Ultrafiltration
WSD	Without salt discharge configuration
WSS	Water-salt-salt scheme
ZLD	Zero liquid discharge

Symbols

a (-)	Node output
a_0 (-)	Initial condition
A_{gauss} (-)	Gaussian constant A
A_m (m^2)	Active membrane area
A_{Mc} (-)	McCleskey model's constant
AEM_{cost} (US$ m^{-2})	Anion exchange membrane cost
b (m)	Channel width
B_{Mc} (-)	McCleskey model's constant
b_1 (-)	first Sherwood number correlation coefficient
b_2 (-)	second Sherwood number correlation coefficient
B_{gauss} (-)	Gaussian constant B
b_i (-)	Bias vector
BPM_{cost} (US$ m^{-2})	Bipolar membrane cost
C (mol L^{-1}) or (mol m^{-3})	Molar concentration
C_{conv} (€ US$$^{-1}$)	US$/€ conversion
C_{gauss} (-)	Gaussian constant C
CEM_{cost} (US$ m^{-2})	Anion exchange membrane cost
d (m)	Channel thickness
D (m^2 s^{-1})	Diffusion coefficient
d^c (-)	Collector diameter
d_d (-)	Distributor diameter
D_{tube} (m)	Internal diameter of the tube
dy (-)	Delay value
E (V)	Triplet membrane potential
E_p (€ kWh^{-1})	Electricity price
EMF (V)	Triplet electromotive force
EPF_{cost} (€)	Electrodes and plates and frames cost
f (-)	Activation function
F (C mol^{-1})	Faraday constant
f_{gauss} (-)	Gaussian function
f_s (-)	spacer shadow factor
G (kg s^{-1})	Mass flowrate

h (m)	Desired value
H_{mod} (mm)	PV module height
i (A m^{-2})	Current density
I (A)	Generic current
I_ext (A)	External current
i_{lim} (A m^{-2})	Limiting current density
I_{mpp} (A)	PV module current at P_{max}
I_s (mol kg^{-1})	Ionic strength
I_{sc} (A)	PV module short-circuit current
ICI (€)	Anion exchange membrane cost
IM_{cost} (€)	Cell packs installed in the stack cost
j (%)	Discount rate
J (mol m^{-2} s^{-1})	Molar flux
k (-)	Generic triplet (mechanistic model), generic predicted value (ANN model)
K_c (L cm min^{-1} mS^{-1})	Controller gain
k_ζ (-)	regression coefficient
l (m)	Generic length
L (m)	Channel length
L_{mod} (mm)	PV module length
M (g mol^{-1})	Molar mass
m (mol kg^{-1})	Molality
M_{lt} (y)	Membranes and spacers lifetime
$Maint_{cost}$ (€)	Maintenance cost
MPM_{cost} (US$ m^{-2})	Monopolar membranes cost
n (-)	Net input
N (-)	Generic number of triplets
N_1 (-)	Number of triplets in the first cell pack
N_2 (-)	Number of triplets in the second cell pack
N_{cell} (-)	PV module number of cells
n_h (-)	hydration number
N_{holes} (-)	Number of holes in the spacers
N_{packs} (-)	Number of cell packs installed in the stack
N_s (-)	Number of stacks in series
N_{tp} (-)	Number of training point
N_{tr} (-)	Number of triplets
P (%)	Purity
p (-)	Node input
P_{lt} (y)	Project lifetime
P_{max} (W)	PV module peak power
PC (ton y^{-1})	Process capacity

PE_{cost} (€)	Peripheral equipment cost
PE_{lt} (y)	Peripheral equipment and electrodes lifetime
Q (L min^{-1})	Volumetric flowrate
r (-)	Number of network inputs
R (Ω)	Generic electrical resistance
R^2 (-)	coefficient of determination
R_g (J K^{-1} mol^{-1})	Ideal gas constant
R_U (V)	Apparent electrical resistance of the stack
Re (-)	Reynolds number
Reg (-)	Regression coefficient
s (-)	Number of nodes in a layer
S (m^{-2})	Generic section
S_{cost} (US$ m^{-2})	Spacer cost
Sc (-)	Schmidt number
Sel (%)	Apparent membrane selectivity
Sh (-)	Sherwood number
Sp (%)	Speciation
T (K) or (°C)	Temperature
t (s)	Process time
T_{cost} (US$ m^{-2})	Triplet cost
t_i (-)	Ion transport number
TEC (€ ton^{-1})	Total energy consumption
TS_{cost} (€)	Total cost of the stack
u (-)	Generic variable
U_{ext} (V)	External voltage
v (-)	Generic input or output variable
V (V)	Generic voltage
V_{mpp} (V)	PV module voltage at P_{max}
V_{oc} (V)	PV module open circuit voltage
Vol_{tra} (m3)	BPM transition region (interlayer) volume
Vt (m3)	Solution volume inside the tank
w (-)	Weight
W (-)	Matrix of weights
W_{mod} (mm)	PV module width
x (m)	Discretised channel length
z (-)	Ion charge

Greek letters

α (mol m^{-3})	Ion activity
δ (m)	Thickness of a triplet
Δx (m)	Discretization interval length
η (%)	PV module efficiency
η_{BL} (V)	Potential due to concentration polarization effects in boundary layers
η_I (%)	Unused current due to parasitic currents effect
ϑ (-)	Polarization coefficient
λ (S kg m^{-1} mol^{-1})	Ionic molal conductivity
λ^o (-)	McCleskey's model constant
μ_I (% $°C^{-1}$)	Temperature Coeff. Of I_{sc}
μ_V (% $°C^{-1}$)	Temperature Coeff. Of V_{oc}
ρ (kg m^{-3})	Mass density
σ (S m^{-1}) or (mS cm^{-1})	Electrical conductivity
τ_c (s)	Controller integral time
τ_p (-)	Yield
ξ (-)	Generic physical property

Subscripts and superscripts

a	acid
AEM	Anion exchange membrane
ani	Anions
av	Average
b	base
BPL	Bipolar membrane layer
BPM	Bipolar membrane
c	Collector
cal	calibration
cat	Cations
CEM	Cation exchange membrane
ch	channel
cn	Convergent node
co	co-ion
ct	counter-ion
d	Distributor
diff	Diffusive
dn	Divergent node
down	Lower branch
i	Generic ion specie
IEM	Ion-exchange membrane
in	Inlet
int	Interface
k	Generic triplet in the stack
m	Membrane (i.e., AEM, CEM or BPM)
m_i	Manifold (i.e., $m_1$or m_2)
MPM	Monopolar membrane
ohm	Ohmic
out	Outlet
p	Product
r	Reagent
rec	Recirculated
ref	Reference
s	salt
sol	Solution (i.e., *acid*, *base* or *salt*)
std	Standard deviation
t	Generic time instant
T	Tank

tot	Total
tra	Transition region
up	Upper branch
w	Water

Appendix A

Description of the multi-scale model

The mathematical model of the EDBM used for this study was partially developed in previous works [104], [111] and it is here described comprehensively in detail for the reader's convenience.

Level 1

The channel model

Mass density is calculated following the Laliberté's model [151]. Ion activity and osmotic coefficients are evaluated adopting the Pitzer virial equations for multi-electrolyte solutions [152], [153].

The electrical conductivity of multi-ion solution is estimated through the model of McCleskey et al. [113].

The electrical conductivity (σ) of an aqueous solution can be calculated from its chemical composition using the following equation:

$$\sigma = \sum \lambda_i m_i \tag{150}$$

Where λ_i is the ionic molal conductivity (S kg m^1 mol^1) and m_i is the molality (mol kg^1) of the i-the ion. The ionic molal conductivity is a function of the temperature and the ionic strength of the solution, though the following equation:

$$\lambda = \lambda^o(T) - \frac{A_{Mc}(T)\ {I_s}^{1/2}}{1 + B_{Mc}\ {I_s}^{1/2}} \tag{151}$$

Where $\lambda^o$and A_{Mc} are function of the temperature (°C), B_{Mc} is an empirical constant and I_s represents the ionic strength. The latter can be estimated as follows:

$$I_s = \frac{1}{2}\sum m_i\ z_i^2 \tag{152}$$

Where z_i is the charge of the i-th ion.

For the generic physical property obtained from OLI studio, correlations assume the following general expression.

$$\zeta_l = k_{\zeta,l,1} C_{i,l} + k_{\zeta,l,2} C_{j,l} + k_{\zeta,l,3} \tag{153}$$

where ζ_l is the considered physical property ζ (i.e., dynamic viscosity μ or ions diffusivity D) in the solution l (i.e., acid, base or salt), $k_{\zeta,l,1}$, $k_{\zeta,l,2}$ and $k_{\zeta,l,3}$ are the regression coefficients, $C_{i,l}$ is the molar concentration of the ion i, and $C_{j,l}$ is the molar concentration of the ion j, expressed in mol m^{-3} (see Table A). All the regression coefficients are computed at 25 °C.

The following correlation was adopted for the Sherwood number (Sh) for the fully developed region:

$$\mathrm{Sh} = (b_1 \cdot \mathrm{Re} + b_2) \left(\frac{\mathrm{Sc}}{\mathrm{Sc}_{ref}} \right)^{0.5} \tag{154}$$

where Re is the Reynolds number, Sc is the Schmidt number, Sc_{ref} is a reference value for the Schmidt number (equal to ~615), and the other symbols indicate coefficients depending on the geometry.

A woven spacer with 90° angled filaments, pitch to height ratio equal to 2, and flow attack angle of 45° was considered. For this configuration, the following values of the coefficients were derived from CFD simulations [111] (Re<30): $b_1 = 2.81$, and $b_2 = 14.5$.

Table A1. List of the physical properties in the acid (a), base (b) and salt (s) solution and the regression coefficients used to compute them by Equation (153).

	ζ	l	i	j	$k_{\zeta,l,1}$	$k_{\zeta,l,2}$	$k_{\zeta,l,3}$
Dynamic	μ	a	H^+	-	2.8E-9	0	0.928E-3
viscosity	μ	s	H^+	-	2.8E-9	0	0.928E-3
(Pa s)	μ	b	OH^-	-	0.215E-6	0	0.927E-3
Ion diffusivity	D_H	a	H^+	-	-1E-13	0	2E-9
(m s^{-2})	D_{Na}	a	Na^+	-	-5E-14	0	1E-9
	D_{OH}	a	OH^-	-	0	0	4E-9
	D_{Cl}	a	Cl^-	-	-7E-14	0	2E-9
	D_H	s	H^+	-	-1E-13	0	2E-9
	D_{Na}	s	Na^+	-	-5E-14	0	1E-9
	D_{OH}	s	OH^-	-	-1E-13	0	5E-9
	D_{Cl}	s	Cl^-	-	-7E-14	0	2E-9
	D_H	b	H^+	-	0	0	8E-9
	D_{Na}	b	Na^+	-	-2E-13	0	1E-9
	D_{OH}	b	OH^-	-	-5E-13	0	5E-9
	D_{Cl}	b	Cl^-	-	-2E-13	0	2E-9

The bipolar membrane model

The mass balance in the BPM interlayer is calculated as:

$$Vol_{tra}\frac{dC_{Na,tra}}{dt} = A_m\left(J_{ohm,Na,AEL} + J_{ohm,Na,CEL} + J_{diff,Na,AEL} + J_{diff,Na,CEL}\right) \quad (155)$$

where Vol_{tra} is the BPM transition region (interlayer) volume, $C_{Na,tra}$ is the sodium ion concentration in the interlayer, A is the membrane area, $J_{ohm,Na,AEL}$ and $J_{ohm,Na,CEL}$ are the Ohmic fluxes of sodium ions in the AEL and CEL respectively, $J_{diff,Na,AEL}$ and $J_{diff,Na,CEL}$ are the diffusive fluxes of sodium ions in the AEL and CEL, respectively.
In fact, following the Strathmann's assumption, the bipolar membrane is modelled as symmetrical. Ohmic and diffusive fluxes are calculated as follows:

$$J_{ohm,Na,AEL} = \frac{t_{Na,AEL}\, i_{lim}}{z_{Na}\, F} \quad (156)$$

$$J_{ohm,Na,CEL} = -\frac{t_{Na,CEL}\, i_{lim}}{z_{Na}\, F} \quad (157)$$

$$J_{diff,Na,AEL} = D_{NaCl}\frac{C_{Na,AEL,ch}-C_{Na,AEL,tra}}{d_{AEL}} \quad (158)$$

$$J_{diff,Na,CEL} = D_{NaCl}\frac{C_{Na,CEL,ch}-C_{Na,CEL,tra}}{d_{CEL}} \quad (159)$$

in which i_{lim} is the limiting current density, $t_{Na,AEL}$ and $t_{Na,CEL}$ are the sodium ion transport numbers in the two layers of the BPM, z_{Na} is the sodium ion valence, F is the Faraday constant, D_{NaCl} is the salt diffusion coefficient (i.e., 2×10^{-11} m^2 s^{-1}), $C_{Na,AEL,ch}$ and $C_{Na,CEL,ch}$ are the sodium ion concentrations in the AEL and CEL layers, respectively, at the channel side, $C_{Na,AEL,tra}$ and $C_{Na,CEL,tra}$ are the sodium ion concentration in the AEL and CEL layers, respectively, at the transition region, and d_{AEL} and d_{CEL} are thicknesses of the AEL and CEL, respectively.

The sodium and chloride ion transport numbers are related to i_{lim} as:

$$t_{Na,AEL} = 0.01 \cdot abs\left(\frac{i_{lim}}{i}\right) \quad (160)$$

$$t_{Cl,AEL} = 0.99 \cdot abs\left(\frac{i_{lim}}{i}\right) \quad (161)$$

in which i is the cell current density, which is greater than or equal to i_{lim}.

Accordingly, the hydroxide ion transport number $t_{OH,AEL}$ is calculated as

$$t_{OH,AEL} = 1 - t_{Na,AEL} - t_{Cl,AEL} \quad (162)$$

Given that the bipolar membrane is modelled as symmetrical, the following equalities apply:

$$t_{Na,CEL} = t_{Cl,AEL} \quad (163)$$

$$t_{Cl,CEL} = t_{Na,AEL} \quad (164)$$

$$t_{H,CEL} = t_{OH,AEL} \quad (165)$$

The Ohmic flux of hydroxide ions through the CEL, as well as of proton ions through the AEL, are neglected, and thus their transport numbers as co-ions are null.

The following Donnan equilibrium is applied at each BPM layer (BPL) - solution interface:

$$\frac{R_g T}{z_{Na} F} ln \frac{C_{Na,sol,int}}{C_{Na,BPL,int}} = \frac{R_g T}{z_{Cl} F} ln \frac{C_{Cl,sol,int}}{C_{Cl,BPL,int}} \quad (166)$$

where $C_{i,sol,int}$ and $C_{i,BPL,int}$ are the ion concentrations at the solution-BPM interface on the channel (*ch*) or on the transition region (*tra*) side and BPM-layer side, respectively. R_g is the gas constant and T is the temperature.

The electro-neutrality within the BPM layers is considered with the general expression:

$$X_{BPL} + \sum C_{co,BPL} = \sum C_{ct,BPL} \quad (167)$$

where X_{BPL} is the fixed charge group concentration in the BPL, and $C_{co,BPL}$ and $C_{ct,BPL}$ are the co-ion and counter-ion concentrations in BPL phase.

At the membrane-solution interface on the interlayer side, the following assumptions are used:

$$C_{Na,CEL,tra} = X_{BPL} \quad (168)$$

$$C_{Na,AEL,tra} = 0 \quad (169)$$

i_{lim} is obtained by solving the set of equations shown above, with the following condition:

$$C_{Na,tra} = 0 \quad (170)$$

The salt mass flux (G_{salt}) due to the migration of sodium and chloride ions through the bipolar membrane layers is computed as follows:

$$G_{salt,BPL} = -\frac{(t_{Na,BPL} + t_{Cl,BPL})\, i}{2F} M_{NaCl} \cdot 10^{-3} \quad (171)$$

where M_{NaCl} is the molar mass of the sodium chloride.

Level 2: the triplet model

The ion transport through the membrane is given by the sum of the diffusive and Ohmic terms and follows the general expression

$$J_{i,m} = -\sum_j D_{i,j,m} \nabla C_{j,m} + \frac{t_{i,m}\, i}{z_i\, F} \quad (172)$$

in which $J_{i,m}$ is the total molar flux of the *i*-th ion across the generic membrane *m* (i.e., CEM, AEM or BPM), $D_{i,j,m}$ is the cross-diffusion coefficient (defined later), $C_{j,m}$ is the

concentration in the membrane phase of the *j*-th ion, $j = 1,2, \dots, n$ (where n is the number of ion species), $t_{i,m}$ is the transport number of the *i*-th ion within the membrane, i is the current density, z_i is the ion charge and F is the Faraday constant. $J_{i,m}$ is positive if entering the channel, negative if exiting the channel.

The overall Ohmic fluxes of the species *i* across the two membranes bounding the three compartments can be calculated as

$$J_{ohm,i,a} = \frac{(t_{i,CEL} - t_{i,AEM})i}{z_i F} \tag{173}$$

$$J_{ohm,i,b} = \frac{(t_{i,CEM} - t_{i,AEL})i}{z_i F} \tag{174}$$

$$J_{ohm,i,s} = \frac{(t_{i,AEM} - t_{i,CEM})i}{z_i F} \tag{175}$$

where $J_{ohm,i,a}$, $J_{ohm,i,b}$, $J_{ohm,i,s}$ are the overall Ohmic fluxes of each acid, base and salt channels respectively, $t_{i,CEL}$, $t_{i,AEL}$, $t_{i,CEM}$, $t_{i,AEM}$ are the transport numbers of the *i*-th ion in the cation and anion exchange layers of the bipolar membrane and in the cation and anion exchange membranes, respectively. $J_{ohm,i,sol}$ are positive if entering the channels, negative otherwise.

The ion transport numbers in the membranes are given by

$$t_{i,m} = \frac{{z_i}^2 D_{i,m} \overline{C_{i,m}}}{\sum_j {z_j}^2 D_{j,m} \overline{C_{j,m}}} \tag{176}$$

in which $D_{i,m}$ is the diffusion coefficient of the *i*-th ion, and $\overline{C_{i,m}}$ is the average ion concentration within the membrane.

The following *n*-1 Donnan equilibrium equations at the membrane-solution interfaces are applied

$$\frac{R_g T}{z_i F} ln \frac{C_{i,sol,int}}{C_{i,m,int}} = \frac{R_g T}{z_{i+1} F} ln \frac{C_{i+1,sol,int}}{C_{i+1,m,int}} \tag{177}$$

where $C_{i,sol,int}$ and $C_{i,m,int}$ are the ion concentrations at the interface on the solution and membrane side, respectively, R_g is the gas constant and T is the temperature.

Moreover, the electro-neutrality within the membrane is considered with the general expression:

$$X_m + \sum C_{co,m} = \sum C_{ct,m} \tag{178}$$

where X_m is the fixed charge group concentration in the IEM, $C_{co,m}$ and $C_{ct,m}$ are the co-ion and counter-ion concentrations in the membrane phase.

The diffusive flux of the ion species *i* through a membrane *m* is

$$J_{diff,i,m} = -\sum_j D_{i,j,m} \nabla C_{j,m} \tag{179}$$

where the cross-diffusion coefficients $D_{i,j,m}$ are expressed as follows:

$$D_{i,j,m} \equiv D_{i,m}\delta_{ij} + \frac{t_{i,m}}{z_i} z_j \left(D_{i,m} - D_{j,m}\right). \tag{180}$$

The total *i*-th ion flux across the two membranes bounding each channel $J_{tot,i,sol}$ is calculated as

$$J_{tot,i,sol} = J_{ohm,i,sol} + J_{diff,i,sol} + J_{cal,i,sol} \tag{181}$$

$$J_{tot,i,sol} = J_{ohm,i,sol} + J_{diff,i,sol} + J_{cal,i,sol} \tag{182}$$

where $J_{tot,i,sol}$ is the total flux of the ion *i* across the two membranes bounding the channel *sol* (acid, base or salt), $J_{ohm,i,sol}$ and $J_{diff,i,sol}$ are the total ohmic and the total diffusive flux, respectively and $J_{cal,i,sol}$ is the calibration parameter used to correct the Nernst-Plank equation.

From the mass balance equation between the calibration fluxes of the three solutions flowing in an EDBM stack it follows:

$$J_{cal,i,a} + J_{cal,i,b} + J_{cal,i,s} = 0 \tag{183}$$

The second relationship is the electroneutrality requirement between the calibration parameters:

$$\sum J_{cal,i,a}\, z_i = 0 \tag{184}$$

$$\sum J_{cal,i,b}\, z_i = 0 \tag{185}$$

where z_i is the charge of the ion *i,* and the sum is extended to all the ions.

The osmotic fluxes are generated by the osmotic pressure difference across the membrane. In formulae:

$$G_{osm,a} = -\frac{\rho_w L_p (\pi_{osm,a,2} - \pi_{osm,s,1})}{3.6\ 10^9} \quad (186)$$

$$G_{osm,b} = -\frac{\rho_w L_p (\pi_{osm,b,1} - \pi_{osm,s,2})}{3.6\ 10^9} \quad (187)$$

where $G_{osm,a}$, $G_{osm,b}$ are the osmotic mass fluxes of the acid and base channels, expressed in kg m^{-2} s^{-1} , ρ_w is the water mass density at 25°C in kg m^{-3}, L_p is the Osmotic permeability (expressed in ml m^{-2} h^{-1} bar^{-1}), $\pi_{osm,a,2}$, $\pi_{osm,s,1}$, are osmotic pressures at the left and right side respectively of the AEM and $\pi_{osm,b,1}$, $\pi_{osm,s,2}$ are those of the CEM (all expressed in bar). $G_{osm,sol}$ is negative when entering the channel, positive otherwise. The electro-osmotic fluxes can be calculated as

$$G_{e.osm,sol} = 10^{-3}\ M_{H_2O}\ \sum_i J_{i,sol}\, n_{h,i} \quad (188)$$

where M_{H_2O} is the molar mass of water in g mol^{-1} and $n_{h,i}$ is the number of water molecules with the solvation shell per each ion.

In the acid and base compartments, the stoichiometric water flux through the BPM due to the water dissociation is

$$G_{split,sol} = -\frac{t_{H/OH,IEL}\, i}{2F} M_{H_2O} \cdot 10^{-3} \quad (189)$$

where $t_{H/OH,IEL}$ is the transport number of proton or hydroxide ion in the CEL or AEL of the BPM, respectively $G_{split,sol}$.

The overall water mass fluxes $G_{w,sol}$ (positive when entering the channel, negative otherwise) for the acid and base channels are evaluated according to the equations

$$G_{w,sol} = G_{e.osm,sol} - G_{osm,sol} + G_{split,sol} \quad (190)$$

The water mass flux for the salt channels is related to the water fluxes calculated for the acid and base compartments

$$G_{w,s} = -G_{w,a} - G_{w,b} \quad (191)$$

The electric potential generated across the IEMs in the triplet E can be written as

$$E = EMF + \eta_{BL} \tag{192}$$

Where EMF is the triplet electromotive force that would be generated by the membranes in contact with the bulk solutions, and η_{BL} is the contribution to E due to concentration polarization boundary layers.

The electromotive force is calculated by Nernst equation

$$E = \sum_{IEMs}\left(-\frac{R_g T}{F}\int_{left,IEM}^{right,IEM}\sum_{ions}\frac{t_i}{z_i} d\ ln\ \alpha_{int,i}\right) \tag{193}$$

where $\alpha_{int,i}$ is the activity of the *i*-th ion at the membrane-solution interface, solution side, $right, IEM$ and $left, IEM$ are the right and the left side of each membrane.

η_{BL} accounts for the non-Ohmic variation of the triplet electric potential due to the effects of concentration polarization in the boundary layers on all the six solution-membrane interfaces

$$\eta_{BL} = -\frac{R_g T}{F}\sum_{int}\sum_{ions}\frac{t_i}{z_i}\ln\theta_{i,sol,int} \tag{194}$$

in which $\theta_{i,sol,int}$ are the polarization coefficients, computed as

$$\left(\theta_{i,sol,int}\right)^{sgn\left(J_{diff,i,sol,int}\right)} = \frac{C_{i,sol,int}}{C_{i,sol}} \tag{195}$$

where $C_{i,sol}$ and $C_{i,sol,int}$ are the concentrations of the *i*-th ion in the so*l* channel (i.e., acid, base or salt) in the bulk and at the solution-membrane interface, respectively, and $sgn\left(J_{diff,i,sol,int}\right)$ is the sign of the diffusive flux of the *i*-th ion at the interface with the membrane, solution side

Imposing the continuity of the total flux at the interface, it can be calculated as

$$J_{diff,i,sol,int} = J_{diff,i,m} + \frac{\left(t_{i,m} - t_{i,sol}\right) i}{F} \tag{196}$$

where $t_{i,sol}$ is the ion transport number in the solution

$$t_{i,sol} = \frac{{z_i}^2 D_{i,sol} C_{i,sol}}{\sum_j {z_j}^2 D_{j,sol} C_{j,sol}} \tag{197}$$

in which $D_{i,sol}$ is the ion diffusion coefficient of the i-th ion in the solution. From the definition of the Sherwood number, it follows that the polarization coefficient can be calculated as

$$\theta_{i,sol,int} = \left(1 - \frac{J_{diff,i,sol,int}\ 2\ d_{sol}}{\mathrm{Sh}_{sol,int}\ D_{i,sol}\ C_{i,sol}}\right)^{sgn\left(J_{diff,i,sol,int}\right)} \tag{198}$$

where d_{sol} is the spacer thickness and $\mathrm{Sh}_{sol,int}$ is the Sherwood number in the considered interface, which is evaluated by CFD correlations.

The triplet electric resistance R (in Ω) is calculated as follows

$$R = \sum_{sol} R_{sol} + \sum_{m} R_{cal} R_m \tag{199}$$

where R_{sol} and R_m are the electrical resistance in the feed channels (i.e., acid, base, and salt) perpendicular to the membranes and the electrical resistance of the membranes (i.e., CEM, AEM, and BPM), respectively and R_{cal} is calibration factor for the membrane resistance.

R_l are calculated as

$$R_{sol} = f_s \frac{d_{sol}}{b\ \Delta x\ \sigma_{sol}} \tag{200}$$

in which f_s is the spacer shadow factor (which can be assumed, for example, equal to the inverse of the volume porosity), b is the channel width, Δx is the length of a discretization interval (e.g., equal to 1/30 of the channel length) and σ_l is the electrical conductivity of the electrolyte solution.

Mass balances for the channels line are:

$$b\ d_a \frac{\partial C_{Na^+,a}}{\partial t} + \frac{\partial Q_a C_{Na^+,a}}{\partial x} = b\ J_{tot,Na^+,a} + \frac{G_{salt,CEL}}{L\ 10^{-3}\ M_{NaCl}} \tag{201}$$

$$b\ d_a \frac{\partial C_{Cl^-,a}}{\partial t} + \frac{\partial Q_a C_{Cl^-,a}}{\partial x} = b\ J_{tot,Cl^-,a} + \frac{G_{salt,CEL}}{L\ 10^{-3}\ M_{NaCl}} \tag{202}$$

$$b\ d_a \frac{\partial C_{H^+,a}}{\partial t} + \frac{\partial Q_a C_{H^+,a}}{\partial x} = b\left(J_{tot,H^+,a} - J_{tot,OH^-,a}\right) \tag{203}$$

$$C_{OH^-,a} = 10^3\ 10^{\left(-14-\log\frac{C_{H^+,a}}{10^3}\right)} \tag{204}$$

$$\frac{\partial Q_a \rho_a}{\partial x} = \left(J_{tot,Na^+,a}\, M_{Na^+} + J_{tot,Cl^-,a}\, M_{Cl^-} + \left(J_{tot,H^+,a} - J_{tot,OH^-,a}\right) M_{H^+}\right) b\, 10^{-3} + \frac{G_{w,a}}{L} + \frac{G_{salt,CEL}}{L} + J_{tot,OH^-,a}\, M_{H_2O}\, b\, 10^{-3} \quad (205)$$

where L, b, d_a are the length, width and thickness of the acid channel, respectively, $C_{i,a}$ is the molar concentration of ion i in the acid channel, Q_a and ρ_a are the volumetric flowrate and mass density of the acid channel, $J_{tot,i,a}$ is the total flux, $G_{w,a}$ and $G_{salt,\ CEL}$ are the overall water mass flux entering in the acid channel and salt water flux through the CEL layer, M is the molar mass.

Similar equations can be written for the salt channels:

$$b\, d_s \frac{\partial C_{Na^+,s}}{\partial t} + \frac{\partial Q_s C_{Na^+,s}}{\partial x} = b\, J_{tot,Na^+,s} \quad (206)$$

$$b\, d_s \frac{\partial C_{Cl^-,s}}{\partial t} + \frac{\partial Q_s C_{Cl^-,s}}{\partial x} = b\, J_{tot,Cl^-,s} \quad (207)$$

$$b\, d_s \frac{\partial C_{H^+,s}}{\partial t} + \frac{\partial Q_s C_{H^+,s}}{\partial x} = b\left(J_{tot,H^+,s} - J_{tot,OH^-,s}\right) \quad (208)$$

$$C_{OH^-,s} = 10^3\, 10^{\left(-14-\log\frac{C_{H^+,s}}{10^3}\right)} \quad (209)$$

$$\frac{\partial Q_s \rho_s}{\partial x} = \left(J_{tot,Na^+,s}\, M_{Na^+} + J_{tot,Cl^-,s}\, M_{Cl^-} + \left(J_{tot,H^+,s} - J_{tot,OH^-,s}\right) M_{H^+}\right) b\, 10^{-3} + \frac{G_{w,s}}{L} + J_{tot,OH^-,s}\, M_{H_2O}\, b\, 10^{-3} \quad (210)$$

Regarding the base channels, the mass balances are given by:

$$b\, d_b \frac{\partial C_{Na^+,b}}{\partial t} + \frac{\partial Q_b C_{Na^+,b}}{\partial x} = b\, J_{tot,Na^+,b} + \frac{G_{salt,AEL}}{L\, 10^{-3}\, M_{NaCl}} \quad (211)$$

$$b\, d_b \frac{\partial C_{Cl^-,b}}{\partial t} + \frac{\partial Q_b C_{Cl^-,b}}{\partial x} = b\, J_{tot,Cl^-,b} + \frac{G_{salt,AEL}}{L\, 10^{-3}\, M_{NaCl}} \quad (212)$$

$$b\, d_b \frac{\partial C_{OH^-,b}}{\partial t} + \frac{\partial Q_b C_{OH^-,b}}{\partial x} = b\left(J_{tot,OH^-,b} - J_{tot,H^+,b}\right) \quad (213)$$

$$C_{H^+,b} = 10^3\, 10^{\left(-14-\log\frac{C_{OH^-,b}}{10^3}\right)} \quad (214)$$

$$\frac{\partial Q_b \rho_b}{\partial x} = \left(J_{tot,Na^+,\mathrm{b}}\, M_{Na^+} + J_{tot,Cl^-,\mathrm{b}}\, M_{Cl^-} + \left(J_{tot,OH^-,\mathrm{b}} - J_{tot,H^+,\mathrm{b}}\right) M_{OH^-}\right) b\, 10^{-3} + \frac{G_{w,\mathrm{b}}}{L} + \frac{G_{salt,AEL}}{L} + J_{tot,H^+,\mathrm{b}}\, M_{H_2O}\, b\, 10^{-3} \quad (215)$$

All other symbols have the same meaning as defined in the previous equations.

An assumption made in deriving the above equations is consider a negligible mass density variation over time. This assumption results reasonable since a low amount of ions are dissolved in solution and, consequently, the mass density is almost constant.

Level 3: the cell pack model

For the distributor, the following equations can be written as follows:

$$\frac{\pi {d_{dis}}^2}{4}\delta \frac{dC_{dis,1,i,sol}}{dt} = \frac{Q_{tot,in,sol}C_{in,i,sol} - Q_{0,1,sol}C_{0,1,i,sol}}{N_{holes}} - Q_{dis,1,sol}C_{dis,1,i,sol} \quad (216)$$

$$Q_{dis,1,sol} = \frac{Q_{tot,a} - Q_{0,1,sol}}{N_{holes}} \quad (217)$$

$$\frac{\pi {d_{dis}}^2}{4}\delta \frac{dC_{dis,k,i,sol}}{dt} = -\frac{Q_{0,k,sol}C_{0,k,i,sol}}{N_{holes}} + Q_{dis,k-1,sol}C_{dis,k-1,i,sol} - + Q_{dis,k,sol}C_{dis,k,i,sol} \quad (218)$$

$$Q_{dis,k,sol} = Q_{dis,k-1,sol} - \frac{Q_{0,k,sol}}{N_{holes}} \quad (219)$$

$$Q_{dis,N,sol}C_{dis,N,i,sol} = Q_{dis,N-1,sol}C_{dis,N-1,i,sol} \quad (220)$$

where d_{dis} and δ are the dimeter of the distributor and the thickness of a triplet, $C_{dis,k,i,sol}$ and $C_{0,k,i,sol}$ are the concentration in the distributor in position *k* of ion *i* in the *sol* (i.e., acid, base and salt) compartment and inlet concentration of ion *i* in *k-th* triplet of the *sol* compartment, $C_{in,i,sol}$ is the inlet concentration of ion *i* in the *sol* compartment, $Q_{tot,in,sol}$ and $Q_{0,k,sol}$ are the tot flowrate entering in the *sol* compartment and the inlet flowrate in *k-th* triplet of the *sol* compartment, N_{hole}s in the number of holes in the spacers and $Q_{dis,k,sol}$ is the distributor volumetric flowrate in position *k* of the *sol* compartment. Equations (218) and (219) are valid for *k* in the range 2 to N-1, where N is the number of triplets in

the cell pack. Constant mass density is considered in equation (217) and (219), since the same solution with fixed concentration is distributed in all the channels.

For the collector, the following equations are utilised:

$$Q_{col,1,sol}\rho_{col,1,sol} = \frac{Q_{1,1,sol}\rho_{1,sol}}{N_{holes}} \tag{221}$$

$$\frac{\pi {d_{col}}^2}{4}\delta\frac{dC_{col,k,i,sol}}{dt} = \frac{Q_{1,k,sol}C_{1,k,i,sol}}{N_{holes}} + Q_{col,k-1,sol}C_{col,k-1,i,sol} - \\ +Q_{col,k,sol}C_{col,k,i,sol} \tag{222}$$

$$Q_{col,k,sol}\rho_{col,k,sol} = \frac{Q_{1,k,sol}\,\rho_{k,sol}}{N_{holes}} + Q_{col,k-1,sol}\rho_{col,k-1,sol} \tag{223}$$

where $Q_{col,k,sol}$ and $Q_{1,k,sol}$ are the volumetric flowrate in position k of the *sol* collector and the outlet flowrate from the *k-th* triplet of the *sol* compartment, $\rho_{col,k,sol}$ and $\rho_{k,sol}$ are the mass density in position k of the *sol* collector and the mass density of the the *k-th* triplet of the *sol* compartment, $C_{col,k,i,sol}$ and $C_{1,k,i,sol}$ are the concentration in the collector in position k of ion i in the *sol* compartment and outlet concentration of ion i in *k-th* triplet of the *sol* compartment and d_{col} is the dimeter of the collector. Equations (222) and (223) are valid for k in the range 2 to N.

Level 4: the stack model

Kirchhoff's and Ohm's laws were applied to the independent nodes and branches of the equivalent electrical circuit, respectively, to obtain the current and voltage profiles along the entire stack.

The resistance related to the connection manifolds between two consecutive channels are evaluated through the following equation:

$$R_{m_i,sol,k} = \frac{l_{m_i,k}}{N_{holes}\,S_{m_i}\,\sigma_{m_i,sol,k}} \tag{224}$$

where R is the solution resistance in the manifold m_i (i.e., m_1 or m_2) of the so*l* (i.e., *a*, *b* or *s*) compartment, in position k (between *1* and N_{tr}-*1*, where N_{tr} is the total number of

triplets in the stack); $l_{m_i,k}$ is the length of the manifold m_i in position k, S_{m_i} is the section of the manifold m_i, $\sigma_{m_i,sol,k}$ is the conductivity of the solution so*l* in position k in the manifold m_i, N_{holes} is the number of holes in the spacers. It should be noted that each of these resistances represents the equivalent resistance of parallel resistances, equal to the number of holes in the spacers.

The electrode compartments are represented using a lumped parameter known as blank resistance, expressed as follows for the stack described in section 3.1:

$$R_{bl} = 0.4024\ i^{-0.6018} \tag{225}$$

For the first cell pack the following equation are employed:

$$I_{m_i,sol,1} = (V_{m_i,sol,2} - V_{m_i,sol,1})/R_{m_i,sol,1} \tag{226}$$

Where $I_{m_i,sol,1}$ is the current flowing in the manifold m_i of the *sol* compartment, in position *1* and $V_{m_i,sol,k}$ is the voltage in the manifold m_i of the *sol* compartment in position k. For the upper and down branches, the following equation ca be written:

$$I_{up,sol,1} = (V_{m_2so,l,1} - V_1)/R_{up,sol,1} \tag{227}$$

$$I_{down,sol,1} = (V_{m_1,sol,1} - V_1)/R_{down,sol,1} \tag{228}$$

where $I_{x,sol,1}$is the current flowing in the x (i.e., *up*, *down*) part of the channel of the *sol* compartment in position *1,* $R_{x,sol,1}$is the resistance of x (i.e., *up*, *down*) part of the channel of the *sol* compartment in position *1 and* $V_1$is the voltage of the stack in position 1 (see Figure 54).

$$V_1 = I_1 R_{av,1}/A_m + E_{av,1} \tag{229}$$

where $I_1$is the current flowing between V_1 and the left cathode, $E_{av,1}$and $R_{av,1}$are the average triplet membrane potential and the average cell resistance of the cell in position 1, respectively.

$$I_{k-1} = I_k + \sum_l (I_{up,sol,k-1} + I_{down,sol,k-1}) \quad (230)$$

$$I_{m_1,sol,k-1} = I_{down,sol,k} + I_{m_1,sol,k} \quad (231)$$

$$I_{m_2,sol,k-1} = I_{up,sol,k} + I_{m_2,sol,k} \quad (232)$$

$$I_{m_i,sol,k} = (V_{m_i,sol,k+1} - V_{m_i,sol,k})/R_{m_i,sol,k} \quad (233)$$

$$I_{up,sol,k} = (V_{m_2,sol,k} - V_k)/R_{up,sol,k} \quad (234)$$

$$I_{down,sol,k} = (V_{m_1,sol,k} - V_k)/R_{down,sol,k} \quad (235)$$

$$V_k = V_{k-1} + I_k R_{av,k}/A_m + E_{av,k} \quad (236)$$

The validity interval of equations between (230) and (236) is for **k** [*2* to N_1], where N_1 is the number of triplets installed in the first cell pack.

For the second cell pack the following equation are used:

$$I_{k+2} = I_{k+1} + \sum_l (I_{up,sol,k} + I_{down,sol,k}) \quad (237)$$

$$I_{m_1,sol,k-1} = I_{down,sol,k} + I_{m_1,sol,k} \quad (238)$$

$$I_{m_2,sol,k-1} = I_{up,sol,k} + I_{m_2,sol,k} \quad (239)$$

$$I_{m_i,sol,k} = (V_{m_i,sol,k+1} - V_{m_i,sol,k})/R_{m_i,sol,k} \quad (240)$$

$$I_{up,sol,k} = (V_{m_2,sol,k} - V_{k+1})/R_{up,sol,k} \quad (241)$$

$$I_{down,sol,k} = (V_{m_1,sol,k} - V_{k+1})/R_{down,sol,k} \quad (242)$$

$$V_{k+1} = V_{k+2} + I_{k+2} R_{av,k}/A_m + E_{av,k} \quad (243)$$

The validity interval of equations between (237) and (243) is for **k** [N_1+*1* to N_{tr}-*1*].

$$I_{N_{tr}+2} = I_{N_{tr}+1} + \sum_l (I_{up,sol,N_{tr}} + I_{down,sol,N_{tr}}) \quad (244)$$

$$I_{m_1,sol,N_{tr}-1} = -I_{down,sol,N_{tr}} \quad (245)$$

$$I_{m_2,sol,N_{tr}-1} = -I_{up,sol,N_{tr}} \quad (246)$$

$$V_{m_1,sol,N_{tr}} - V_{N_{tr}+1} = I_{down,sol,N_{tr}} R_{down,sol,N_{tr}} \quad (247)$$

$$V_{m_2,sol,N_{tr}} - V_{N_{tr}+1} = I_{up,sol,N_{tr}} R_{up,sol,N_{tr}} \quad (248)$$

$$V_{N_{tr}+1} = I_{N_{tr}+2} R_{av,N_{tr}}/A_m + E_{av,N_{tr}} \quad (249)$$

In the anode position, to connect the two cell packs, the following equation are applied:

$$V_{N_1+1} = U_{ext} \quad (250)$$

$$I_{N_1+1} + I_{N_1+2} = I_{ext} \quad (251)$$

$$I_1 + I_{N_1+2} = I_{ext} \quad (252)$$

$$U_{ext} = R_U I_{ext} \quad (253)$$

$$V_{N_1+1} = V_{N_1} + I_{N_1+1} R_{bl}/A_m \quad (254)$$

$$V_{N_1+1} = V_{N_1+2} + I_{N_1+2} R_{bl}/A_m \quad (255)$$

Where U_{ext} and I_{ext} are the external voltage and current supplied by the Dc drive and R_U is the apparent electrical resistance of the entire stack.

Once current and voltage profile (i.e., I and V) along the entire stack were determined two key metrics are computed: the percentage of unused current due to parasitic effects and the external voltage applied to the stack.

Level 5: the external hydraulic circuit model

For the closed-loop configuration, only the solution tanks for acid, base and salt are simulated. Dynamic mass balances are computed, assuming perfect mixing of the solutions. It is noteworthy that the dynamic equations implemented at this level do not

make the model fully dynamic as all the other levels simulate steady-state conditions. However, the model can simulate dynamic process configurations, such as the closed-loop, as the dominant dynamic of the system (i.e., the tanks) is simulated.

Dynamic mass balances within the acid and salt storage tanks can be written as follows:

$$\frac{d(\rho_{T,sol} Vt_{sol})}{dt} = Q_{T,in,sol}\, \rho_{T,in,sol} - Q_{T,out,sol}\, \rho_{T,out,sol} \tag{256}$$

$$\frac{d(C_{T,HCl,sol} Vt_{sol})}{dt} = Q_{T,in,sol}\, C_{T,HCl,in,sol} - Q_{T,out,sol}\, C_{T,HCl,out,sol} \tag{257}$$

$$\frac{d(C_{T,NaCl,sol} Vt_{sol})}{dt} = Q_{T,in,sol}\, C_{T,NaCl,in,sol} - Q_{T,out,sol}\, C_{T,NaCl,out,sol} \tag{258}$$

where Vt_{sol} is the solution volume inside the tank in m^3, $\rho_{T,sol}$ is the mass density of the solution within the tank, $Q_{T,in,sol}$, $Q_{T,out,sol}$ are the inlet and outlet volume flowrates, respectively, $C_{T,HCl,in,sol}$, $C_{T,HCl,out,sol}$, $C_{T,NaCl,in,sol}$, $C_{T,NaCl,out,sol}$ are the inlet and outlet hydrochloric acid and the inlet and outlet sodium chloride concentrations (all expressed in mol m^{-3}).

For the base storage tank, the following equations can be written as

$$\frac{d(\rho_{T,b} Vt_{b})}{dt} = Q_{T,in,b}\, \rho_{T,in,b} - Q_{T,out,b}\, \rho_{T,out,b} \tag{259}$$

$$\frac{d(C_{T,NaOH,b} Vt_{b})}{dt} = Q_{T,in,b}\, C_{T,NaOH,in,b} - Q_{T,out,b}\, C_{T,NaOH,out,b} \tag{260}$$

$$\frac{d(C_{T,NaCl,b} Vt_{b})}{dt} = Q_{T,in,b}\, C_{T,NaCl,in,b} - Q_{T,out,b}\, C_{T,NaCl,out,b} \tag{261}$$

The feed and bleed configuration is a continuous operating mode and no dynamic equations are implemented. In this case, the recirculation loop from the outlet back to the stack inlet is simulated to increase the residence time of the solution inside the stack. Two

hydraulic nodes, for each solution, connecting the recirculating loop to the main flow stream are simulated. Here steady-state mass balances are computed.

For the feed and bleed process configuration the following equation are employed for the convergent and divergent nodes.

Convergent node:

$$Q_{cn,sol,out} = Q_{dn,sol,rec} + Q_{sol,in} \tag{262}$$

$$Q_{cn,sol,out}C_{cn,HCl,sol,out} = Q_{dn,sol,rec}C_{dn,HCl,sol,rec} + Q_{sol,in}C_{HCl,sol,in} \tag{263}$$

$$Q_{cn,sol,out}C_{cn,NaCl,sol,out} = Q_{dn,sol,rec}C_{dn,NaCl,sol,rec} + Q_{sol,in}C_{NaCl,sol,in} \tag{264}$$

where $Q_{sol,in}$, $Q_{dn,sol,rec}$, $Q_{cn,sol,out}$ are the volume flowrate entering from the tank, recirculated from the stack outlet and leaving the convergent node, respectively, $C_{HCl,sol,in}$, $C_{dn,HCl,sol,rec}$, $C_{cn,HCl,sol,out}$ are the hydrochloric acid concentration entering from the tank, recirculated from the stack outlet and leaving the convergent node, respectively, $C_{NaCl,sol,in}$, $C_{dn,NaCl,sol,rec}$, $C_{cn,NaCl,sol,out}$ are the sodium chloride concentration entering from the tank, recirculated from the stack outlet and leaving the convergent node, respectively.

For the base storage tank, the following equations can be written as

$$Q_{cn,b,out} = Q_{dn,b,rec} + Q_{b,in} \tag{265}$$

$$Q_{cn,b,out}C_{cn,NaOH,b,out} = Q_{dn,b,rec}C_{dn,NaOH,b,rec} + Q_{b,in}C_{NaOH,b,in} \tag{266}$$

$$Q_{cn,b,out}C_{cn,NaCl,b,out} = Q_{dn,b,rec}C_{dn,NaCl,b,rec} + Q_{b,in}C_{NaCl,b,in} \tag{267}$$

For the divergent node the following mass balances can be expressed for acid and salt compartment:

$$Q_{dn,sol,in} = Q_{dn,sol,rec} + Q_{sol,out} \quad (268)$$

$$Q_{dn,sol,in}C_{dn,HCl,sol,in} = Q_{dn,sol,rec}C_{dn,HCl,sol,rec} + Q_{sol,out}C_{HCl,sol,out} \quad (269)$$

$$Q_{dn,sol,in}C_{dn,NaCl,sol,in} = Q_{dn,sol,rec}C_{dn,NaCl,sol,rec} + Q_{sol,out}C_{NaCl,sol,out} \quad (270)$$

where $Q_{dn,sol,in}$, $Q_{dn,sol,rec}$, $Q_{sol,out}$ are the volume flowrate leaving the stack, recirculated to the convergent node and entering in the exit tank, respectively, $C_{dn,HCl,sol,in}$, $C_{dn,HCl,sol,rec}$, $C_{HCl,sol,out}$ are the hydrochloric acid concentration leaving the stack, recirculated to the convergent node and entering in the exit tank, respectively, $C_{dn,NaCl,sol,in}$, $C_{dn,NaCl,sol,rec}$, $C_{NaCl,sol,out}$ are the sodium chloride concentration leaving the stack, recirculated to the convergent node and entering in the exit tank, respectively. For the base storage compartment, the following equations can be written as

$$Q_{dn,b,in} = Q_{dn,b,rec} + Q_{b,out} \quad (271)$$

$$Q_{dn,b,in}C_{cn,NaOH,b,in} = Q_{dn,b,rec}C_{dn,NaOH,b,rec} + Q_{b,out}C_{NaOH,b,out} \quad (272)$$

$$Q_{dn,b,in}C_{dn,NaCl,b,in} = Q_{dn,b,rec}C_{dn,NaCl,b,rec} + Q_{b,out}C_{NaCl,b,out} \quad (273)$$

Two tubes for each compartment are introduced, after the convergent node and prior to the divergent node, in the simulated process flow sheet and unsteady-state mass balances are computed utilising the following equations:

$$\frac{\pi {D_{tube}}^2}{4}\frac{\partial C_{cn,i,sol,out}}{\partial t} + Q_{cn,sol,out}\frac{\partial C_{cn,i,sol,out}}{\partial x} = 0 \quad (274)$$

$$\frac{\pi {D_{tube}}^2}{4}\frac{\partial C_{dn,i,sol,in}}{\partial t} + Q_{dn,sol,in}\frac{\partial C_{dn,i,sol,in}}{\partial x} = 0 \quad (275)$$

where D_{tube} is the internal diameter of the tube, $C_{cn,i,sol,out}$ and $C_{cd,i,sol,in}$ are the molar concentration of ion *i* in the *sol* line exiting from the convergent node and entering in the divergent node, $Q_{cn,sol,out}$ and $Q_{dn,sol,out}$ are the volumetric flowrate in the *sol* line exiting from the convergent node and entering in the divergent node.

Blank resistance

The blank resistance is a lumped parameter that accounts for the voltage drop in the electrode compartment. It is often employed in electro-membrane processes where the effects of the electrodes are not of primary importance and can be represented by a single parameter. This resistance accounts for the standard potential and overvoltage of the electrode's reactions, as well as for the resistance of the end-membranes and solution channels associated with the electrode compartments.

For the stack described in section 3.1, a sodium sulphate solution is employed as the electrode rinse solution. This salt is used to increase the conductivity of the electrodes rinse solution (ERS) compartments, but it remains chemically inert from a reaction point of view. The redox reactions are the production of hydrogen and oxygen.

At the cathode the production of hydrogen is obtained though the following electro-chemical reaction:

$$H^+ + e \leftrightarrows \frac{1}{2} H_2 \tag{276}$$

while at the anode oxygen is produced according to:

$$2H_2 0 \rightleftarrows O_2 + 4e + 4H^+ \tag{277}$$

A blank resistance test was conducted employing a lab-scale EDBM (FT-ED-100, Fumatech BWT Gmbh, Germany) unit. The choice of using a lab-scale EDBM unit instead of the semi-industrial unit was due to the difficulty of disassembling and assembling the larger unit. Moreover, the blank resistance is usually obtained as a lumped value expressed as areal resistance and it generally causes a small variation of the overall stack voltage of about 10%. Consequently, it is sufficient to have a rough estimate for modelling purposes. The laboratory unit has an active membrane area of 10 × 10 cm^2 and

includes PVC/ECTFE woven spacers (thickness = 480 μm). The electrode compartments' configuration consists of two ERS compartments adjacent to the electrodes, two end-membranes (CEM, FUMASEP® FKB-PK) and an acid compartment between the two end-membranes. A schematic representation of the electrode cell test set-up is reported in Figure A1a. The configuration of the ERS compartments mimics that of the semi-industrial unit simulated in this study. A DC power supply (1902B, B&K precision) was used to power the EDBM unit. Two multimeters (Fluke 175) were connected to measure the electrical current and voltage provided by the power supply to the stack.

The tests were conducted utilizing solutions. Specifically, the ERS was prepared using demineralized water and adding 35.5 g L^{-1} of Na_2SO_4 (technical grade, CR GRUPO CRIMIDESA). The acid solution was prepared from demineralized water, adding HCl (ACS Reagent 37%, Honeywell, Fluka) to reach a concentration of 0.5 mol L^{-1}. This acid concentration is representative of an intermediate condition of a closed-loop test, in which the acid concentration varies in the range of 0.05–1 mol L^{-1}. The solutions were fed into the stack using two peristaltic pumps (YT15, BT601S Lead Fluid, CO LTD, China) and adopting an open-loop configuration. The flow rates of the solutions were chosen to guarantee a channel flow velocity of 2.7 cm/s, which is the same as that used for the tests with the semi-industrial unit.

During the blank resistance tests the current density supplied to the stack was varied between 50 and 500 A m^{-2}, in increments of 50 A m^{-2}. 3–5 minutes were allowed between adjustments to ensure that the steady-state condition was reached. At each steady-state, both voltage and current data were recorded. The apparent specific areal stack resistance was calculated by dividing the voltage by the current density for each steady-state condition. The trend of blank resistance as a function of the current density is reported in Figure A1b.

A regression curve, fitted to the experimental data, was used in the model to predict the electrode voltage drops.

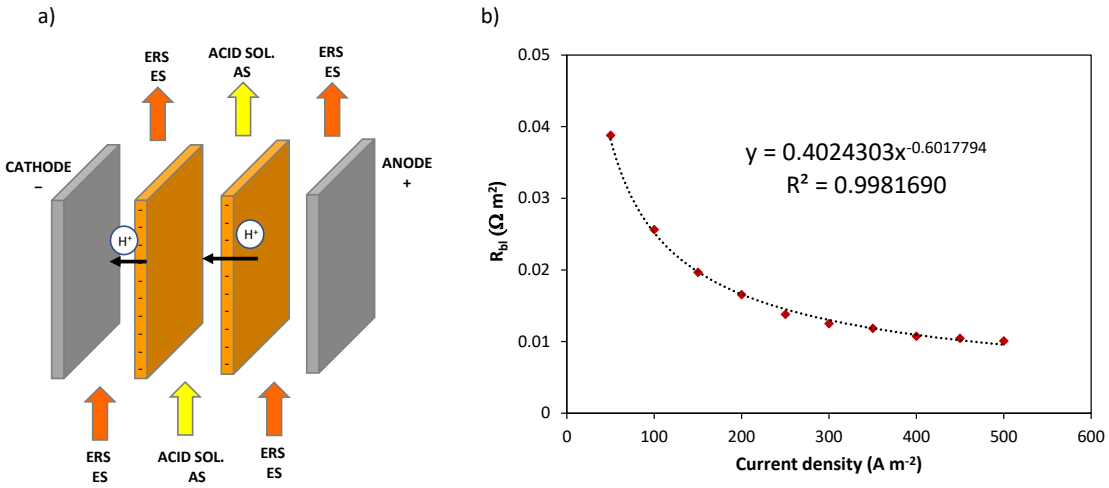

Figure A1. a) configuration of the electrodes compartments of the stack described in section 2.1, with two end-membranes (CEM) and three channels (two ERS and one acidic). b) experimental trend of the blank resistance as a function of the current density. The regression curve employed in the model to account for the blank resistance is shown.